AN ABSTRACT OF THE DISSERTATION OF

Mahshid Mohammadi for the degree of Doctor of Philosophy in Mechanical Engineering presented on June 12, 2014.

Title: Design of a Single Lamina for a Microchannel Dialyzer with a Focus on Bubble Removal

Abstract approved:

Kendra V. Sharp

A microchannel-based hemodialyzer offers a novel approach to hemodialysis practice and holds many promises for improving dialysis treatment efficiency and quality of life for kidney patients. The hollow fiber hemodialyzer, a conventional dialysis device, has certain limitations including non-uniformity of the dialysate flow path which necessitates the use of a high dialysate flow rate. In the microchannel-based design, successive stacked layers alternate between blood flow and dialysate flow. A flat porous membrane between these layers allows for the transport of toxins from the blood side to the dialysis fluid side. This design improves mass transfer characteristics and enables the use of lower dialysate to blood flow rate ratios suitable for a home hemodialysis system. One of the current issues in microchannel dialyzer is the emergence of bubbles through blood-outgassing and air ingress. This dissertation provides an in-depth study of the bubble pinning phenomenon and the impact of the geometrical design of a single lamina of the microchannel dialyzer on bubble removal.

Our primary method to facilitate bubble mitigation in the system is increasing the surface hydrophilicity by applying polyethylene oxide (PEO) coating on internal surface of polycarbonate laminas. The effects of contact angle hysteresis and contact line (pinning) forces as well as the dewetting velocity on bubble stagnation have been studied. A theoretical model that estimates the required pressure drop along the length of a stagnant bubble to overcome pinning forces to stimulate motion has been developed. The model has been validated by experimental results. The model demonstrates that the use of highly hydrophilic surfaces is a robust approach to reducing both pinning and capillary forces and subsequently bubble clogging in microfluidic systems.

The geometrical design must exhibit low resistance for bubble mitigation while maintaining a relatively uniform flow distribution between channels for efficient mass transfer. A single lamina of the microchannel dialyzer under development at OSU is comprised of an inlet manifold, an outlet manifold and a parallel microchannel array; the manifolds feature a micropost arrangement that supports the membrane. The overall manifold geometry was designed for uniform flow distribution while the suggested arrangement of microposts inside the manifolds was aimed at exhibiting low bubble retention. For all the experiments in this dissertation, water has been used as the working fluid; however, for the selection of the microchannel size and velocity conditions, considerations for preventing blood hemolysis under shear stress were taken into account. Furthermore, the anticipated differences between an air-water system and an air-blood system have been discussed.

Design of a Single Lamina for a Microchannel Dialyzer with a Focus on Bubble Removal

by

Mahshid Mohammadi

A DISSERTATION

submitted to

Oregon State University

in partial fulfillment of

the requirements for the

degree of

Doctor of Philosophy

Presented June 12, 2014

Commencement June 2015

Doctor of Philosophy dissertation of Mahshid Mohammadi presented on June 12, 2014.

APPROVED:

Major Professor, representing Mechanical Engineering

Head of the School of Mechanical, Industrial and Manufacturing Engineering

---

Dean of the Graduate School

I understand that my dissertation will become part of the permanent collection of Oregon State University libraries. My signature below authorizes release of my dissertation to any reader upon request.

Mahshid Mohammadi, Author

ACKNOWLEDGEMENTS

I would like to thank my advisor Dr. Kendra Sharp for her support and for giving me the opportunity to be a part of this great project, and thanks to the National Institutes of Health (NIH) for funding this project.

Thanks to my committee members, Dr. Goran Jovanovic, Dr. Deborah Pence, Dr. Sourabh Apte, and to my GCR Dr. Windy Baltzer for their time and guidance. Thanks to Dr. James Liburdy, Dr. Joseph McGuire, and Dr. Karl "Rat" Schilke for always answering my questions with patience and a smile. I have learned much from you all.

Thanks to the project PI Dr. Brian Paul and fellow students Spencer Porter, Keely Heintz, Venkata Rajesh Saranam, Agnieszka Truszkowska, and Daniel Peterson for their collaborations. Special thanks to Dustin Ward and Patrick McNeff for assisting with the clamp system and microfabrication.

Thanks to my MIME friends for their friendship, encouragement, and help on so many levels during my time at OSU: Preeti Mani, Ruander Cardenas, Mohammad Ghazvini, Nathan Germann, Erfan Rasouli, Thomas Mosier, Eden Durant, Chris Stull, and Logan Strid.

Thanks to Frederick Atadana for lots of laughs and for making the lab a happier place to work. Thanks for all the encouragements in your special fun ways.

Thanks to Matthew Coblyn for being a great teammate and friend. You were always willing to help with whatever was going on and I am very grateful for that. Thanks for listening to my never ending sad stories. I couldn't ask for a better teammate. You are awesome.

Thanks to my mom, Azra, for being the best mom. Thanks for having confidence in me, even when I don't. Thanks to my dad, my brother, my sisters, and my sweet nephew for their telephone calls and encouraging words.

Finally, I would like to thank my loving husband, Mohammad "Hadi" Tabatabaee. Words cannot express my gratitude for everything you have done for me over the last couple of years. Thanks for listening and discussing ideas, for proofreading all of my papers, for making hundreds of cups of tea to keep me going, and for doing all those crazy dances for me to make me happy. Thanks for driving up to Portland and back home every day for 14 months to be with me, and for visiting me every other week these past few months that you had to be in Davis. You are the best thing that ever happened to me. You are my happiness.

TABLE OF CONTENTS

Page

1 INTRODUCTION 2

2 BUBBLE BLOCKAGE IN MICROCHANNELS.....10

2.1 INTRODUCTION.....11

2.2 THEORETICAL MODEL: THE ROLE OF CONTACT LINE FORCES ON BUBBLE BLOCKAGE.....16

2.2.1 Differentiation between capillary and pinning forces 22

2.2.2 Capillary pressure 23

2.3 THEORETICAL MODEL VALIDATION 24

2.3.1 Experimental setup and procedure 25

2.3.2 Results.....28

2.4 EFFECT OF PEO COATING ON BUBBLE MOVABILITY IN MICROCHANNELS 36

2.5 THE MERIT OF STUDYING AN AIR-WATER MODEL SYSTEM.....39

2.6 A BLOCKAGE-FREE MULTICHANNEL ARRAY.....41

3 SHEAR-INDUCED BLOOD DAMAGE IN MICROCHANNELS ...44

3.1 BLOOD COMPONENTS.....44

3.2 BLOOD FLOW IN MICROCHANNELS.....46

TABLE OF CONTENTS (Continued)

Page

3.2.1 Cell-free layer 47

3.2.2 Fahraeus-Lindqvist effect 47

3.2.3 Non-Newtonian behavior 49

3.3 SHEAR EFFECTS ON RED BLOOD CELLS 50

3.3.1 Shear effects on red blood cell deformability 51

3.3.2 Hemolysis 52

3.4 SHEAR EFFECTS ON PLATELETS 54

3.5 SHEAR EFFECTS ON WHITE BLOOD CELLS 57

3.6 SHEAR STRESS IN RECTANGULAR MICROCHANNELS 58

3.6.1 Estimation of the maximum shear stress for blood flow in microchannels 62

3.7 LIMITATION ON DEVICE DEPTH BASED ON CONSIDERATION OF BLOOD DAMAGE 64

4 SELECTION OF GEOMETRICAL PARAMETERS FOR MICROCHANNELS 67

4.1 MASS TARANSFER 67

TABLE OF CONTENTS (Continued)

Page

4.1.1 Mass transfer model....68

4.1.2 Influence of channel length on mass transfer....72

4.1.3 Influence of channel depth on mass transfer....75

4.1.4 Influence of channel width on mass transfer....78

4.1.5 Influence of velocity on mass transfer....79

4.2 PRESSURE DROP....80

4.3 BUBBLE MOVABILITY....83

4.4 SUMMARY....84

4.5 MAXIMUM CHANNEL WIDTH TO PREVENT MEMBRANE SAGGING....85

4.6 DECISION MAKING AND OPTIMIZATION....87

4.6.1 Objective....88

4.6.2 Constraints....88

4.6.3 Methods....90

5 EXPERIMENTAL FACILITY AND METHODS....92

5.1 TEST SECTION....92

5.2 LAMINA FABRICATION....96

TABLE OF CONTENTS (Continued)

Page

5.2.1 Method A 96

5.2.2 Method B....98

5.3 MEMBRANE PREPARATION....99

5.4 IMAGING SYSTEM 100

5.5 IMAGE PROCESSING 102

5.5.1 Calibration uncertainty....103

5.5.2 Thresholding uncertainty 106

6 MANIFOLD DESIGN: FLOW UNIFORMITY 109

6.1 INTRODUCTION....109

6.2 CFD MODELING 118

6.2.1 Selection of structural parameters 121

6.3 VERIFICATION AND VALIDATION 123

6.3.1 Verification study 123

6.3.2 Validation study....125

6.3.3 Correlations used in validation study 126

TABLE OF CONTENTS (Continued)

Page

6.3.4 Comparison between the simulation results and analytical/experimental correlations 128

6.4 CFD SIMULATION RESULTS 129

6.4.1 Effect of microchannel dimensions on flow uniformity and pressure drop 131

6.4.2 Effect of manifold asymmetry on flow distribution 135

6.4.3 Effect of channel spacing on flow uniformity 138

6.4.4 Effect of corner angle and vertical corner spacing on flow uniformity and pressure drop 139

6.4.5 Influence of flow rate on the observed flow uniformity trends 143

6.5 CONCLUSIONS 145

7 MANIFOLD DESIGN: MICROPOST ARRANGEMENT 148

7.1 CLOGGING PRESSURE OF BUBBLES MOVING THROUGH CONTRACTIONS 148

7.2 LITERATURE REVIEW: PRESSURE DROP IN A MICROPOST ARRAY 152

7.3 CLOGGING PRESSURE FOR A BUBBLE PASSING A CONTRACTION BETWEEN MICROPOSTS 161

TABLE OF CONTENTS (Continued)

Page

7.4 PREFERENTIAL BUBBLE PATHS IN DIFFERENT STAGGERED ARRANGEMENTS 167

7.5 STATISTICAL COMPARISON OF BUBBLE RETENTION BETWEEN ARRANGEMENTS WITH $\theta < 60^{\circ}$ AND $120^{\circ} < \theta$ 172

7.5.1 Experimental procedure 174

7.5.2 Image processing 175

7.5.3 Results 178

7.6 BUBBLE BREAKUP AND STAGNATION 183

7.7 SIDE PINNING FORCES IN PARALLEL ARRANGEMENT 185

7.8 MINIMUM REQUIRED POST DIAMETER IN PARALLEL ARRANGEMENT 191

7.9 COMPARISON OF BUBBLE RETENTION IN MANIFOLDS WITH DIFFERENT POST ARRAYS 192

7.9.1 Triangular manifolds with elongated posts 194

7.9.2 Triangular manifolds with tilted parallel post arrangements (TPPA) 196

7.9.3 Triangular manifolds with parallel post arrangement (PPA) 197

7.9.4 Triangular manifolds with equilateral post arrangement (EPA) 199

7.9.5 Summary and conclusions 200

TABLE OF CONTENTS (Continued)

Page

8 CONCLUSIONS AND FINAL REMARKS 203

8.1 SUMMARY 203

8.2 MAJOR CONTRIBUTIONS 206

8.3 RECOMMENDATIONS FOR FUTURE WORK 208

LIST OF PUBLICATIONS AND PRESENTATIONS 211

BIBLIOGRAPHY 212

APPENDICES 223

LIST OF FIGURES

Figure Page

Figure 1: a) A conventional hollow fiber hemodialyzer and b) a close up view of the fibers....3

Figure 2: Cross-section of a single filtration unit of the microchannel hemodialyzer ...4

Figure 3: Laminated-sheet structure of a microchannel dialyzer with double-sided laminas 5

Figure 4: Dewetting velocity with which the dry patch opens up 13

Figure 5: Bubbles with different wetting conditions: a) dry bubble, b) consecutive images of a hybrid bubble, and c) lubricated bubble, reproduced with permission from Cubaud and Ho [21]....15

Figure 6: Dry stationary bubbles in a microchannel array where clear channels act as a bypass for the flow. Upon stagnation, small droplets start to condense and enlarge on the channel walls inside the saturated bubbles; the picture was taken 17 minutes after stagnation....16

Figure 7: Surface tension forces acting on a triple contact line 17

Figure 8: Pinning forces resisting motion under the action of a piston in a circular tube, adapted from de Gennes et al. [22] 17

Figure 9: a) Side view of a stationary bubble and forces applied on it by the pressure field and the channel walls, b and c) channel cross section at the left contact line with and without liquid in the corner regions, respectively, note that the dotted border is not a part of the triple contact line but rather a gas liquid interface, d) a moving bubble with a convex back interface 18

Figure 10: Progression of bubble shape with increasing velocity: a) dry dynamic bubble, b) thin film forming, c) lubricated bubble, and d) bullet-shaped lubricated bubble, adapted from Jensen [29]....24

LIST OF FIGURES (Continued)

Figure Page

Figure 11: Experimental setup for pressure measurements 26

Figure 12: Variation in the contact angles during the motion, a and b are images of one bubble and c and d are images of another. a) concave back interface, c) convex back interface, b and d) nearly flat back interfaces and unequal front contact angles at the side walls 29

Figure 13: Pressure difference across the length of the crawling bubble 30

Figure 14: Pressure readings prior to bubble injection 31

Figure 15: Comparison between the model's predictions and the measured pressures for the 6 sets of experiments. There could be a large difference between the concave and convex back model predictions. 32

Figure 16: Comparison between the measured pressure and the matching models' prediction. There are four irregular occurrences that have a slightly convex back interface but match the concave back model's prediction better.....33

Figure 17: Normalized models' predictions based on the measured pressure 33

Figure 18: Pressure fluctuations that might be caused by the syringe pump 34

Figure 19: Consecutive images of dewetting on the coated surface.....38

Figure 20: Scanning electron micrograph of blood cells. From left to right: human erythrocyte (RBC), thrombocyte (platelet), leukocyte (WBC), from Wikimedia Commons 45

Figure 21: An estimation of the relative viscosity of red cell suspensions perfused through tubes of different diameters for *Hct*= 0.45, adapted from Pries et al. [37] 48

Figure 22: Shear-thinning behavior of blood at low shear rates, adapted from Merrill [36].....50

LIST OF FIGURES (Continued)

Figure Page

Figure 23: Dependence of the viscosity of blood on shear rate, adapted from Kwak and Kiris [54] 50

Figure 24: The locus of onset of hemolysis and onset of serotonin release from platelet upon aggregation. Estimates of stress levels in cardiac valves and the normal blood circulation system are also shown (dyne/cm^2 = 0.1 Pa), reproduced with permission from Hellums [44] 57

Figure 25: Aspect ratio of a rectangular microchannel.....58

Figure 26: A sample shear rate profile in a $200\ \mu m \times 100\ \mu m$ channel.....59

Figure 27: An illustration of the dependence of maximum shear stress on aspect ratio and depth of channels.....63

Figure 28: Maximum shear stress in the square channel (SC) and parallel plate (PP) geometry for a wide range of velocities and device depths. Dashed lines represent square channels and continuous lines represent parallel plates.....64

Figure 29: Two-dimensional computational domain, in a three-dimensional domain the width of the channel would be normal to the page 69

Figure 30: Concentration profile around a membrane (K<1).....72

Figure 31: Urea fractional removal in channels with different lengths 74

Figure 32: Normalized concentration of urea along the centerlines of channels with different lengths.....75

Figure 33: Urea fractional removal at varying channel depths 77

Figure 34: Effect of channel depth on mass transfer rate.....77

Figure 35: Effect of velocity on fractional removal and mass transfer rate.....79

LIST OF FIGURES (Continued)

Figure Page

Figure 36: Influence of channel depth on the pressure drop per unit length of channel for a velocity of 1 cm/s....82

Figure 37: Membrane deflection due to the ultrafiltration pressure....86

Figure 38: Exploded view of the test section....93

Figure 39: A close-up view of the exploded test section....94

Figure 40: A close-up view of the compressed test section....94

Figure 41: Experimental setup....96

Figure 42: Lamina fabrication steps, method A....97

Figure 43: Image of microchannels and microposts fabricated by method A....98

Figure 44: Lamina fabrication steps, method B....99

Figure 45: Images of a) microchannels (in the darker color) and b) microposts fabricated by method B....99

Figure 46: Imaging system....101

Figure 47: Uncertainty across the image for the micro-Nikkor lens a) an image of the resolved grid, b) the centroid locations of a small section of the grid, c) contour of lens distortion across the image, and d) image distortion rate due to optical aberration...105

Figure 48: The final image of a spherical bubble as the outcome of the various paths light takes when interacting with the bubble....107

Figure 49: Maximum angle of incident light....108

LIST OF FIGURES (Continued)

Figure Page

Figure 50: a) Laminated-sheet structure, reproduced with permission from Pan et al. [89] and b) manifold categorization based on the flow direction, adapted from Webb [91] 112

Figure 51: Schematic view of the microstructure including geometrical parameters 118

Figure 52: a) The mesh near the entrance of the channel and b) The mesh of the inlet tube 120

Figure 53: Effect of grid size in the inlet manifold on flow distribution 125

Figure 54: Velocity profiles along the length of the microchannel 129

Figure 55: Effect of channel dimension on flow uniformity. For parameter definition, refer to Table 12 comparative study 1. 132

Figure 56: a) Effect of channel dimensions on total pressure drop and b) effect of channel dimensions on average pressure loss in the inlet manifold. For parameter definition, refer to Table 12, comparative study number 1. 134

Figure 57: Effect of channel dimension on the ratio of the pressure loss in the microchannels to the total pressure drop. For parameter definition, refer to Table 12, comparative study 1 135

Figure 58: a) Effect of inlet manifold magnification on flow distribution and b) effect of outlet manifold magnification on flow distribution. For parameter definition, refer to Table 12, comparative study 2 137

Figure 59: Effect of channel spacing on flow uniformity. For parameter definition, refer to Table 12, comparative study 3 138

Figure 60: Effect of manifold corner angle and vertical corner spacing on flow uniformity, a) case (a) and b) case (b). For parameter definition, refer to Table 12, comparative study 4 (a) and 4 (b) 140

LIST OF FIGURES (Continued)

Figure Page

Figure 61: Effect of manifold corner angle and vertical corner spacing on pressure drop throughout the device related to case (a). For parameter definition, refer to Table 12 comparative study 4 (a) 142

Figure 62: Effect of manifold corner angle and vertical corner spacing on flow uniformity for case (a) geometry, a) at the flow rate of 6 ml/min and b) at the flow rate of 1.5 ml/min. For parameter definition, refer to Table 12, comparative study 5 (a) and 5 (b) 144

Figure 63: Bubble moving through a tapered contraction, adapted from Jensen et al. [27] 150

Figure 64: Staggered post arrangement: S_T , S_L, and S_D represent the transverse, longitudinal, and diagonal pitches, respectively. The height of the post is defined by h normal to the page. 154

Figure 65: Velocity contour in the simulation domain, the pressure drop over the length of the middle row is measured for a range of inlet velocities 156

Figure 66: Comparison of pressure drop through a single row in a staggered array from analytical correlation for 2D parallel plates (PP) with the inlet velocity of $U_{\max}$, 3D CFD, and Tamayol et al.'s correlation [114] 160

Figure 67: Classification of bubbles based on their size relative to the open space between posts 161

Figure 68: Side and top views of a small dry bubble confined between parallel plates 162

Figure 69: Medium bubbles passing through contractions, bubbles with a flat back interface experience the largest capillary pressure 163

Figure 70: Bubbles prefer to proceed through the larger contractions 167

LIST OF FIGURES (Continued)

Figure Page

Figure 71: Relative size of openings in a staggered arrangement is determined by the top angle of the hexagon 168

Figure 72: Categorizing staggered arrangements into six groups based on the top angle of the hexagon 168

Figure 73: Preferential bubble paths through different arrangements depends on the relative size of openings. Large arrows present the more noticeable bubble trajectories and small arrows shows the less frequent paths. For a given cell, green spacings are larger than the red ones. 169

Figure 74: Preferential bubble paths for a) equilateral arrangements, b) arrangements with $60^\circ < \theta < 120^\circ$, and c) arrangements with $120^\circ < \theta$ and $\theta < 60^\circ$ 171

Figure 75: a) Image of the lamina filled with water, b) dimensions of the unit cells in the studied arrangements and c) a Zescope image of the middle part of the lamina connecting the two arrangements 173

Figure 76: a) Normalized image after cropping, b) normalized five-piece image after subtraction from the background, c) thresholded (binarized) pieces, and d) labeled bubbles 177

Figure 77: Remaining bubbles in the lamina at different flow rates 178

Figure 78: Blockage percentage vs. flow rate, small dots represent the blockage percentages in the set of experiments while large symbols represent the average blockage percentage at each flow rate 179

Figure 79: Average number of stagnant bubbles vs. flow rate.....180

Figure 80: Average size of stagnant bubbles vs. flow rate 181

Figure 81: Median size of stagnant bubbles vs. flow rate.....182

LIST OF FIGURES (Continued)

Figure Page

Figure 82: Remaining bubbles in the lamina at the flow rate of 13 ml/min after pausing the flow, note the bubbles that are pressed against the posts in the left arrangement 182

Figure 83: Strangling of a bubble on a post side in a) an arrangement with $120^\circ < \theta$ and b) an arrangement with $\theta = 90^\circ$ (flow direction: left to right).....184

Figure 84 : A large bubble leaving several small and medium bubbles behind (flow direction: left to right). Spaces behind the posts are sweet spots for stagnation when bubbles take meandering paths.....184

Figure 85: a) Large stagnant bubbles pressed against the posts in equilateral arrangements at a flow rate of 13 ml/min, and b) the same bubbles expanded after pausing the flow.....185

Figure 86: Variation in the thickness of the side contact lines during motion as an indication for the existence of side pinning forces 186

Figure 87: Median length of stagnant bubbles vs. flow rate in parallel arrangement.187

Figure 88: Schematic of a bubble side incursion into longitudinal openings. The interstitial space inside a longitudinal opening is shown with diagonal pattern. 188

Figure 89: Stationary bubbles in an arrangement with elongated posts, note the large number of small bubbles remaining in the manifolds.....195

Figure 90: Variations in the direction of the flow paths in a right triangular manifold with a corner angle of 25 degrees and no posts.....195

Figure 91: Stationary bubbles in the tilted parallel post arrangement 197

Figure 92: Stationary bubbles in the parallel post arrangement (PPA) at the flow rate of 1.95 ml/min 198

Figure 93: Stationary bubbles in the equilateral post arrangement (EPA).....199

LIST OF FIGURES (Continued)

Figure Page

Figure 94: The blockage percentage in the inlet and outlet manifolds of the studied designs: tilted parallel post arrangement (TPPA), parallel post arrangement (PPA), equilibrium post arrangement (EPA) 201

LIST OF TABLES

Table Page

Table 1: Details of the six sets of experiments.....30

Table 2: Contact angles on uncoated and coated embossed polycarbonate sheets.....37

Table 3: Estimation of the minimum allowable channel depth for various flow velocities.....65

Table 4: Boundary conditions for Navier-Stokes equations 70

Table 5: Boundary conditions for mass transfer equations.....72

Table 6: Effect of channel structural parameters and velocity on the studied design elements.....85

Table 7: Specifications of the Navitar lens and the FOV of the imaging system.....102

Table 8: Reviewed studies on manifold and microchannel structures.....114

Table 9: Grid convergence study on a single 200-μm square channel with Re=8 124

Table 10: Grid convergence study on the inlet manifold.....125

Table 11: Comparison between the numerical results and theoretical estimations....129

Table 12: Structural parameters of the microchannels and manifolds in different studies, number of channels = 20, channel length = 2 cm 130

Table 13: Friction factor correlations for staggered array of short tubes between parallel plates.....155

Table 14: Parameters used in CFD simulations.....160

LIST OF TABLES (Continued)

Table Page

Table 15: Dimensions of the geometrical features in the studied manifolds 200

LIST OF APPENDICES

Appendix		Page
A.	Uncertainty in pressure measurements and model's prediction	224
B.	Dewetting velocity measurment	228
C.	Slip boundary condition at bubble interface	231
D.	Drawings of the test section pieces	233
E.	Positive capillary pressure at the beginning of a contraction	238
F.	Matlab image processing codes	242
G.	Drawings of the post arrangements in the manifolds	247

LIST OF APPENDIX FIGURES

Figure Page

Figure B-1: Dewetting velocity on the uncoated polycarbonate surface 230

Figure B-2: Dewetting velocity on the PEO coated surface 230

Figure E-1: The top view of the studied geometry 239

Figure E-2: Variation in the capillary pressure vs. position of the front contact line.240

Figure E-3: Variation in the capillary pressure vs. position of the back contact line.241

LIST OF APPENDIX TABLES

Table Page

Table A-1: Properties of the pressure transducer 225

Table B-1: Data used for the calibration of the dewetting images 229

NOMENCLATURE

A	Cross sectional area of bubble
C	Molar concentration
Ca	Capillary number
D	Diffusion coefficient
E	Tensile module
E_{in}	Vertical spacing at the corner of the inlet manifold
E_{out}	Vertical spacing at the corner of the outlet manifold
F	Force
FR	Fractional removal of solute
I	Moment of inertia
K	Partition coefficient
L	Length
L_c	Channel length
L_e	Entrance length of channel
N	Number of channels
N_x	Number of elements in the width of channel
N_y	Number of elements in the depth of channel
N_z	Number of elements in the length of channel
N_{row}	Number of rows in a micropost array
$\overrightarrow{N}$	Mass transfer flux
P	Pressure
Pe	Peclet number
Q	Flow rate

NOMENCLATURE (Continued)

Re	Reynolds number
S_L	Longitudinal post spacing
S_T	Transverse post spacing
S_D	Diagonal post spacing
U	Velocity
W_c	Microchannel width
W_s	Channel spacing
W_t	Total width of the manifold
d	Diameter
d_{eff}	Effective dynamic diameter of the corner flow
d_h	Hydraulic diameter of the rectangular channel
e	Liquid film thickness
e_{ij}	Strain rate tensor
f	Fanning friction factor
g	Gravitational acceleration
h	Microchannel height or distance between parallel plates
k	Dewetting coefficient
l	Length
$\dot{m}$	Mass transfer rate
n	The boundary normal pointing out of the domain
r	Radius
r_D	Radius of the bubble in the diagonal opening between posts

NOMENCLATURE (Continued)

r_L	Radius of the bubble in the longitudinal opening between posts
s	Length of the contact line
u	Velocity
t	Time
t_m	Membrane thickness
w	Microchannel width
z	Longitudinal distance from the beginning of the channel
Greek symbols	
Δ	Difference
α	Aspect ratio of the channel
δ	Deflection
δ_{ij}	Kronecker Delta operator
θ	Contact angle
θ_l	Lateral angle of a bubble in parallel post arrangement
θ_t	Tapering angle
ε	Uncertainty
σ, σ_{lg}	Liquid-gas surface tension
σ_{sg}	Gas-solid surface free energy
σ_{sl}	Liquid-solid surface free energy
σ_{ij}	Stress tensor
$\sigma_U\%$	Standard deviation of the normalized velocities of the channels

NOMENCLATURE (Continued)

$\lvert\dot{\gamma}\rvert$	Magnitude of shear rate tensor
κ^{-1}	Capillary length $\kappa^{-1} = \sqrt{\sigma / \rho g}$
ρ	Density
τ	Shear stress
μ	Dynamic viscosity
μ'	Viscosity ratio, $\mu' = \mu / \mu_{eff}$
ϕ	Porosity of a micropost array
φ	Post density, $\varphi = 1 - \phi$

Subscripts

D	Dynamic
L	Left
C	Center
R	Right
adv	Advancing
app	Apparent
b	Bubble
cap	Capillary
clog	Clogging
crit	Critical
cont	Contraction
dew	Dewetting
equ	Equilibrium
eff	Effective

NOMENCLATURE (Continued)

fd	Fully developed region
g	Gas
I	At the interface
in	Inlet boundary
inc	Side incursion
J	Channel number
L	Liquid
max	Maximum
mean	Average
out	Outlet boundary
pin	Pinning
rec	Receding
rel	Relative
row	Along a row
wall	Wall
0	Specified

DESIGN OF A SINGLE LAMINA FOR A MICROCHANNEL DIALYZER WITH A FOCUS ON BUBBLE REMOVAL

1 INTRODUCTION

Bubble clogging in microchannels is a well-known problem in microfluidics. Immobile bubbles induce strong resistance effects on the flow within the channels and may disturb performance and reduce the efficiency of the device. Bubble blockage is one of the current challenges in the microchannel-based hemodialysis system currently being developed at Oregon State University as a potential alternative for current hemodialysis systems.

Patients suffering from end-stage renal disease (ESRD) need to undergo 3 – 4 hours of hemodialysis treatment approximately three times a week. The heavy treatment schedule disturbs the patients' everyday life. Patients usually feel ill before the treatment due to toxin buildup in the blood and dizzy afterwards due to the rapid fluctuation in blood composition during the treatment [1]. The 5-year survival rate of hemodialysis patients is only about 36% [2]. A long-duration (6 – 8 hours) home hemodialysis system for usage on a nightly basis could improve the patient's quality of life and the outcome of the therapeutic dialysis [3]. The microchannel-based hemodialysis system is aimed at establishing a viable home dialysis system.

A hollow-fiber hemodialyzer as employed in a conventional dialysis device, has certain limitations including non-uniformity of the dialysate flow which necessitates the use of a high dialysate flow rate [4, 5]. High dialysate consumption is one of the barriers for operation of hemodialyzers at home.

Figure 1 presents a conventional hemodialyzer; blood passes through semi-permeable fibers and dialysate flows across the fibers in the opposite direction. The fibers are flexible and may be moved by the dialysate flow; this causes flow maldistribution and may create stagnant regions within the dialyzer cylinder. The uneven spacing of the fibers hinders diffusion from the membrane to the dialysate [5]. A high dialysate flow rate (generally two or more times the flow rate of the blood) is required to maintain a large enough concentration gradient between the blood and the dialysate to compensate for the high mass-transfer resistance. On average, a 3.5-hour conventional hemodialysis treatment consumes about 105 liters of dialysate [6].

a

b

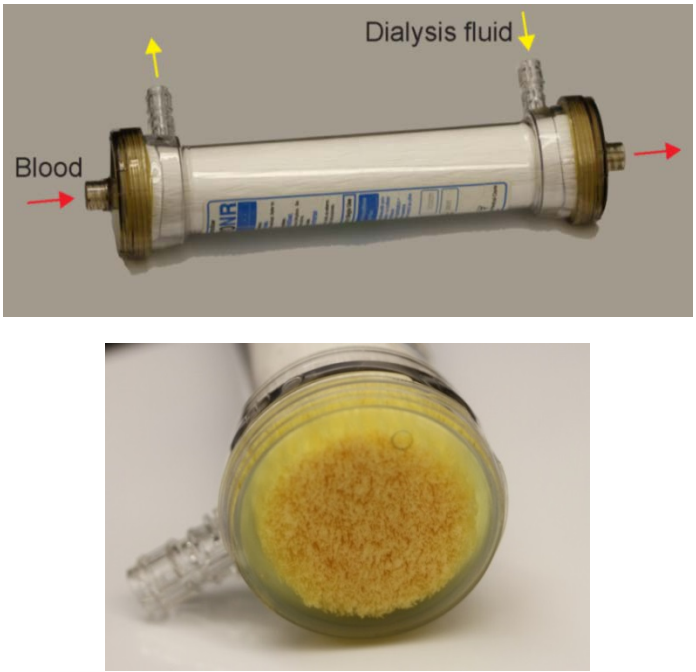

Figure 1: a) A conventional hollow fiber hemodialyzer and b) a close up view of the fibers

The microchannel-based hemodialyzer offers a novel approach to hemodialysis practice and holds many promises to improve kidney patients' quality of life and dialysis treatment efficiency. Each layer of the microchannel-based design consists of an array of microchannels and inlet and outlet manifolds. The layers are fabricated in polycarbonate. A porous membrane (Gambro AN69 ST) between these layers, as shown in Figure 2, allows for the transport of toxins from the blood side to the dialysate side. The use of a microchannel and flat membrane geometry significantly improves the mass transfer characteristics and enables the design of a smaller unit with lower dialysate to blood flow rate ratios.

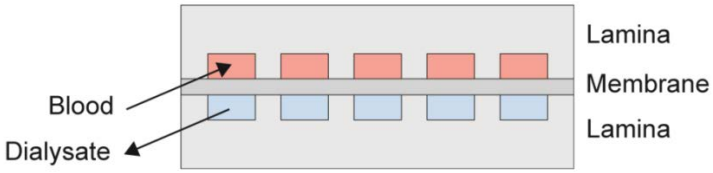

Figure 2: Cross-section of a single filtration unit of the microchannel hemodialyzer

To achieve a higher filtration capacity, successive stacked layers alternate between blood flow and dialysate flow as shown in Figure 3. The envisioned long-term goal of this project is to enable patients to take a 6 to 8 hour dialysis treatment every night at home when sleeping using a microchannel hemodialyzer device.

One of the current issues with the microchannel-based dialyzer is the presence of bubbles. The planar size of these bubbles can vary from 5 micrometers to a couple of centimeters. Out-gassing from the blood stream and diffusion of gases through the dialyzer membrane are causes of the formation of the microbubbles $(< 20\ \mu m)$.

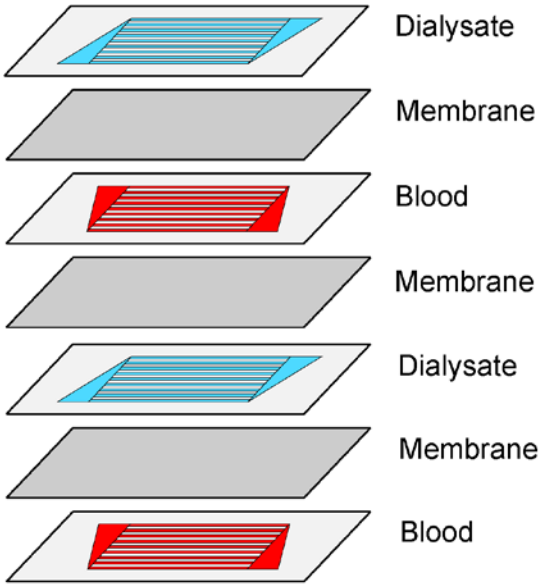

Figure 3: Laminated-sheet structure of a microchannel dialyzer with double-sided laminas

Microbubbles are most commonly found on the blood side of the membrane since protein molecules stabilize the bubble interface. Macrobubbles, sizing from 20 μm to several centimeters, may appear on both sides of the membrane. Possible sources for the appearance of macrobubbles include large microchannel machining errors, faulty membranes, material failure, and errors in the assembly process; they can also get introduced into the system while connecting/disconnecting tubing to the valves, pumps, etc. Both types of bubbles, either in the manifold or in the channels, create stagnant regions of fluid, which results in flow maldistribution and lower mass transfer efficiency. The presence of stagnant regions can also promote coagulation due to surface interactions as well as blood cell damage. It is important to note that blood goes through air detector and air trap systems before returning to the patient's body.

In this thesis, the bubble blockage phenomenon in general microfluidics systems has been studied in depth. For the first time, an estimation of the required pressure difference across the bubble length to overcome contact line (pinning) forces and initiate motion is presented. The model is validated with experimental results from an air-water system. Moreover, the importance of the surface hydrophilicity and the contact angle hysteresis on bubble retention behavior in microfluidic systems is clarified.

Two approaches are taken for bubble management in the microchannel dialyzer. The first approach is the immobilization of pendant polyethylene oxide (PEO) chains on fluid-contacting surfaces which makes the polycarbonate surfaces more hydrophilic. The coating provides two critical functionalities as well. First, the pendant PEO brush strongly inhibits protein adsorption and cell adhesion. Second, anticoagulant activity can be functionalized by coupling an active heparin derivative to the ends of the PEO chains [1]. These latter functionalities are crucial for the microchannel dialyzer; however, they are mentioned here for completeness and are not the focus of the present context.

Prior statistical studies have shown that bubbles are less prone to getting stuck in an array of PEO coated microchannels compared to an uncoated array. The hypothesis that the PEO coating promotes a fast passage of bubbles in the system has been proven experimentally by showing the reduced dewetting velocity on the coated surface which results in a higher probability of bubbles remaining lubricated. Furthermore,

using the insight gained from the theoretical model the underlying reasons for the positive effect of PEO coating on bubble movability by reducing the receding and advancing contact angles are revealed and explained.

The second approach to bubble management involves designing an effective manifold geometry for bubble elimination, so bubbles are less likely to get stuck in the manifold and remain in the system. To support the membrane and prevent membrane sagging, the manifold regions have to be filled with structural features. Bubbles have to overcome large capillary and pinning forces to move through these features. The design of a micropost array that exhibits low bubble retention characteristic is of great interest and is one the objectives of this work.

Chapter 2 focuses on bubble blockage in microchannels. A theoretical model is proposed for the first time that estimates the pressure difference required across the length of a stagnant bubble to overcome the contact line forces and stimulate motion. The model has been validated by experimental results.

Since we are in the early stages of development of the microchannel dialyzer, all of the experiments for this thesis were conducted with deionized water, not blood. However, the differences we expect to see between the behavior of bubbles in water and blood have been explained in chapter 2. Furthermore, necessary considerations to prevent blood damage in the device have been taken into account and explained in chapter 3.

In chapter 4, a general guideline that describes the effect of channel structural parameters and flow velocity in each channel on mass transfer, pressure drop, and bubble movability is provided. Furthermore, potential objective and constraint functions for a design optimization have been suggested. Only an optimization approach is able to determine the optimum values of the design parameters in such a convoluted nonlinear design problem with multiple constraints.

Chapter 5 describes the experimental facility including the imaging system for bubble retention studies in the microchannels of a single lamina along with the fabrication and assembly of the lamina.

The microchannel dialyzer should be designed to have a relatively uniform flow distribution among individual channels within a microchannel array. Flow uniformity as one of the factors affecting the performance of laminated structured micro-devices has been discussed in chapter 6. Based on current literature, we have concluded that right triangular manifolds can distribute the flow more uniformly than other types of manifolds. Furthermore, the impacts of the geometry of the right triangular manifold and the dimensions of microchannels on the desired uniformity have been investigated. Obviously, bubble retention in the manifold region disturbs any uniform flow distribution achieved through designing a manifold for uniformity of single phase flow.

Structural features must be distributed in the manifold areas to support the membrane and prevent membrane sagging. In chapter 7 preferential bubble paths in different

staggered arrangements of microposts have been identified. Statistical studies revealed that the frequency of the bubble breakup, the size of the remaining bubbles in the system, and the bubble blockage percentage are related to the geometrical arrangement of the microposts. The developed design concepts have been used in designing manifolds featuring micropost arrangements that exhibit low bubble retention.

Finally, chapter 8 presents the scientific and technical contributions of this work and recommendations for future work.

2 BUBBLE BLOCKAGE IN MICROCHANNELS

This chapter highlights the influence of contact line forces on the mobility of dry bubbles in microchannels. Bubbles moving at velocities less than the dewetting velocity of liquid on the surface are essentially dry. In the absence of thin liquid films around the bubbles, contact line (pinning) forces and sometimes the capillary pressure gradient induced by pinning act on the bubbles and resist motion. A lack of sufficient driving force (e.g. external pressure) brings a dry bubble to stagnation. A theoretical model that estimates the required pressure difference across the length of a stagnant bubble to overcome the contact line forces and stimulate motion is proposed. To validate our theory, the pressure required to move a dry bubble in a square microchannel exhibiting contact angle hysteresis has been measured. The experimental results are in agreement with the model's prediction.

The model presented herein and also the aforementioned velocity conditions suggest that the use of highly hydrophilic surfaces is a robust approach to reducing bubble clogging in microfluidic systems.

Three final sections of this chapter discuss specific subjects related to bubbles in our microchannel hemodialysis application: the effect of PEO coating on bubble movability in microchannels, the value of studying an air-water system prior to an air-blood system, and the conditions that result in a blockage-free multichannel system.

2.1 INTRODUCTION

Bubble clogging in microchannels is a well-known problem in microfluidics. Immobile bubbles induce strong resistance effects on the flow in the channels and may disturb the performance and reduce the efficiency of the device [7]. Therefore, management of gas bubbles is an important matter for microfluidic devices. The emergence of the bubbles can be caused by various factors, e.g., simply by diffusion of air into the device or by the degassing of the liquid due to temperature or pressure variations. Vibration can stimulate the formation of the bubbles as well [8]. Bubbles can also get introduced into the system while connecting or disconnecting tubing to the valves, pumps, etc. Overall, the chances of the appearance of unwanted bubbles in microfluidic devices are relatively high in practice. Furthermore, bubbles may be generated as a reaction product in the device, e.g. the production of carbon dioxide during the oxidation of methanol on the anode side of a micro direct methanol fuel cell (μDMFC) [9]. Two-phase flow micro-heat exchangers and condensers may also deal with the bubble removal problems [10-12].

Some of the methods suggested for facilitating bubble removal in microchannels include the use of T-shaped non clogging microchannels [13], tapered structures [7], hydrophilic-hydrophobic patterning [14], and hydrophobic porous membranes [15, 16].

Most of the previous studies attributed the lack of motion of stagnant bubbles to resistant capillary forces related to pressure differences across the front and back

interfaces [8, 17-20]. Herein we investigate pinning forces along *triple* contact lines as another factor hindering the motion of dry bubbles. Note that lubricated bubbles have no triple contact line and do not experience pinning.

To the best of authors' knowledge, the only study to account for the pinning forces acting on a bubble in the force balance is a study by Metz et al. [7]. They modeled the forces acting on a moving bubble in a microchannel as the superposition of the capillary force, viscous drag, the drag induced due to thin film deposition, pinning forces, and contact angle dynamic forces. Their simple model for the pinning forces linearly correlates this force to a constant pinning coefficient, the length of the gas bubble contact line, and the surface tension. For their experiments, the pinning coefficient and subsequently the pinning force turned out to be negligible which was attributed to the high surface quality of the glass channels and the disappearance of contact lines in lubricated bubbles.

Elongated bubbles moving in microfluidic systems are not always lubricated. The existence of lubricating films around bubbles in a partially wetting microchannel depends on bubble velocity, dewetting velocity, length of the bubbles, and the microchannel cross-sectional dimensions. [21]

Dewetting refers to the spontaneous withdrawal of a liquid film from a partially wetting surface [22]. On a totally wetting substrate, a film is always stable while on a partially wetting surface, thin films below a critical thickness are metastable and may

dewet by nucleation and the growth of a dry zone, as shown in Figure 4. The critical thickness for an ideal surface is given by

$$e_{crit} = 2\kappa^{-1}\sin\left(\theta_{equ}/2\right) \tag{1}$$

where κ^{-1} is the capillary length defined by $\sqrt{\sigma/\rho g}$ [22]. Non-ideal surfaces which are marred by chemical or physical surface irregularities exhibit contact angle hysteresis. For non-ideal surfaces the critical thickness is given by

$$e_{crit} = 2\kappa^{-1}\sin\left(\theta_{rec}/2\right) \tag{2}$$

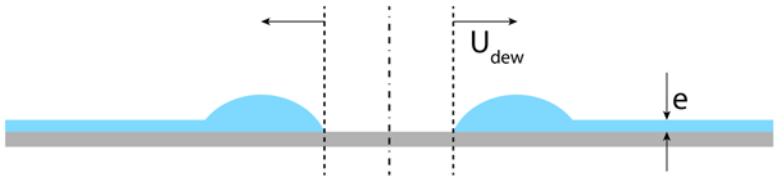

Figure 4: Dewetting velocity with which the dry patch opens up

The nucleation of a dry zone may start with a local surface defect or by a perturbation; the zone expands if its radius exceeds a critical value. For an air-water system with a receding contact angle as low as 1 degrees, the critical thickness becomes about $45\ \mu m$, much thicker than a possible liquid film around an elongated bubble in microchannels. As microfluidic systems are not usually free of surface defects the chances for dewetting of the thin films around bubbles are relatively high. The dewetting velocity with which the dry zone opens up is constant,

$$U_{dew} = \frac{k\sigma}{\mu}\theta_{rec}^3 \tag{3}$$

where k is an empirical coefficient that depends on the nature and molecular weight of the fluid and also the solid surface quality [23].

Experimental results of Cubaud and Ho [21] have shown that, in a partially wetting square channel, bubbles moving slower than the dewetting velocity are completely dry. For velocities between the dewetting velocity and a critical velocity, the rear of the bubble is dried out while the front of the bubble remains lubricated (hybrid bubbles). At velocities higher than the critical velocity, bubbles are lubricated. The critical velocity was estimated by

$$U_{crit} \approx U_{dew} l_b / h \tag{4}$$

where l_b is the length of the bubble and h is the width of the square microchannel [21]. Figure 5 presents images of dry, hybrid, and lubricated bubbles. The presence of droplets on the channel walls around a bubble is indicative of dewetting.

We reviewed the conditions leading to the presence of dry bubble in microchannels. Because of the contact angle hysteresis on a non-ideal surface, a dry moving bubble forms different dynamic contact angles at the front and back. The pinning forces applied on the contact lines and the possible capillary pressure induced by pinning resist the motion of a dry bubble. At low flow velocities, the pressure difference across the length of the bubble may not be enough to overcome these forces. In such a

situation, the bubble becomes stationary. If there is no bypass for the flow, the bubble eventually starts crawling due to the liquid accumulation and pressure buildup behind it. When a bypass (e.g. a parallel channel or corner flow) exists, the bubble may remain stationary indefinitely. Dry stationary bubbles present in our microchannel array device, as shown in Figure 6, further motivate this theoretical and experimental study of the pressure required to stimulate motion of dry bubbles and effectively clear the channel.

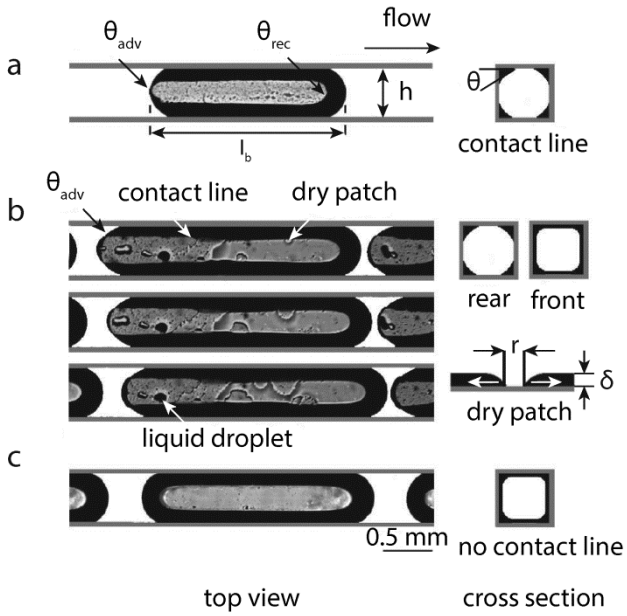

Figure 5: Bubbles with different wetting conditions: a) dry bubble, b) consecutive images of a hybrid bubble, and c) lubricated bubble, reproduced with permission from Cubaud and Ho [21]

Figure 6: Dry stationary bubbles in a microchannel array where clear channels act as a bypass for the flow. Upon stagnation, small droplets start to condense and enlarge on the channel walls inside the saturated bubbles; the picture was taken 17 minutes after stagnation.

2.2 THEORETICAL MODEL: THE ROLE OF CONTACT LINE FORCES ON BUBBLE BLOCKAGE

In this section a theoretical model that describes the roles of contact line forces on the bubble pinning phenomenon is proposed. de Gennes et al. [22] have presented the forces acting on a *dynamic* triple contact line on non-ideal surfaces. Herein, we develop the force balance equations for the situation where an external force on the contact line is not enough to initiate movement. Then we expand our model for a stationary bubble having two contact lines at its front and back.

Young's equation presents the balance of forces for a triple contact line at equilibrium shown in Figure 7.

$$\sigma_{lg} \cos\theta_{equ} = \sigma_{sg} - \sigma_{sl} \tag{5}$$

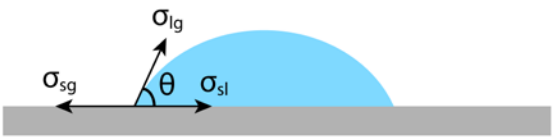

Figure 7: Surface tension forces acting on a triple contact line

When an external force is applied on a contact line, the contact angle varies from the local equilibrium contact angle. For the liquid segment in the circular tube described in Figure 8 the force equilibrium yields,

$$F = s(\sigma_{sg} - \sigma_{sl} - \sigma_{lg}\cos\theta) \tag{6}$$

where s refers to the arc length of the contact line. The magnitude of this force is equal to the magnitude of the pinning force which acts in the opposite direction and resists motion. Substituting the term $\sigma_{sg} - \sigma_{sl}$ from Young's equation we get

$$F = s\sigma_{lg}(\cos\theta_{equ} - \cos\theta) \tag{7}$$

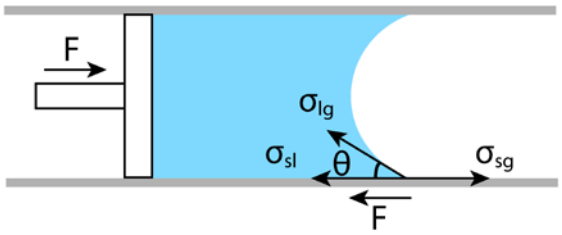

Figure 8: Pinning forces resisting motion under the action of a piston in a circular tube, adapted from de Gennes et al. [22]

Similar forces acts on the back and front (left and right) *triple* contact lines (s_L and s_R) of a stationary bubble in a rectangular channel as shown in Figure 9a.

$$F_L = s_L \sigma_{lg} (\cos\theta_{equ} - \cos\theta_L) \tag{8}$$

$$F_R = s_R \sigma_{lg} (\cos\theta_R - \cos\theta_{equ}) \tag{9}$$

Depending on the hydrophilicity and geometry of the channel liquid regions may or may not be present in the corners of the channel, as illustrated in Figure 9b and Figure 9c. Liquids with equilibrium contact angles below 45° most likely occupy the corner regions in rectangular channels [24].

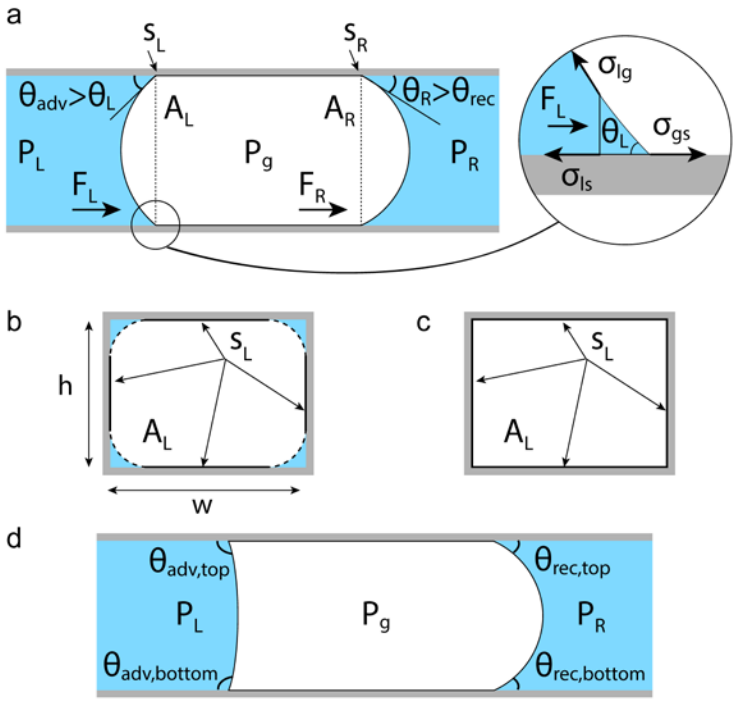

Figure 9: a) Side view of a stationary bubble and forces applied on it by the pressure field and the channel walls, b and c) channel cross section at the left contact line with and without liquid in the corner regions, respectively, note that the dotted border is not a part of the triple contact line but rather a gas liquid interface, d) a moving bubble with a convex back interface

The contact angle of the non-ideal surface varies between the receding and advancing contact angles. The maximum external force that can be compensated by pinning corresponds to the situation where the contact angle equals the advancing or the receding contact angle, depending on the direction of the force. By assuming slip boundary conditions on the liquid-gas bubble interface the roles of static friction and drag forces by the corner flow on the bubble become negligible. Therefore, for the continuous motion of the contact line the external forces must be larger than the maximum pinning forces.

$$F_L \geq s_L \sigma_{lg} (\cos\theta_{equ} - \cos\theta_{adv}) \tag{10}$$

$$F_R \geq s_R \sigma_{lg} (\cos\theta_{rec} - \cos\theta_{equ}) \tag{11}$$

The external forces on the bubble are the result of the pressure field maintained by the corner flows. These forces can be approximated by

$$F_L = A_L (P_L - P_g) \tag{12}$$

$$F_R = A_R (P_g - P_R) \tag{13}$$

where A_L and A_R are the bubble cross sectional areas at the back and front, respectively. These are slightly different from the microchannel cross sectional area when the bubbles do not occupy the corner regions [25].

In order for a bubble with a concave interface on the back $(\theta_{rec} < 90^\circ)$ to move Eq. (10) and (11) should both be satisfied. By substituting Eqs. (12) and (13) into Eq. (10) and (11) we get

$$P_L - P_g \geq \frac{s_L}{A_L}\sigma_{lg}(\cos\theta_{equ} - \cos\theta_{adv}) \tag{14}$$

$$P_g - P_R \geq \frac{s_R}{A_R}\sigma_{lg}(\cos\theta_{rec} - \cos\theta_{equ}) \tag{15}$$

Assuming that the bubble has equal cross sectional areas, contact line lengths, and equilibrium contact angles at the front and the back, adding Eq. (14) to Eq. (15) yields

$$P_L - P_R \geq \frac{s}{A}\sigma_{lg}(\cos\theta_{rec} - \cos\theta_{adv}) \tag{16}$$

For a square channel with a width of h, Eq. (16) simplifies to

$$P_L - P_R \geq 4\sigma_{lg}\frac{(\cos\theta_{rec} - \cos\theta_{adv})}{h} \tag{17}$$

Considering only the pinning forces, Eq. (17) provides the necessary condition for bubble motion for θ_{rec} and $\theta_{adv} < 90^\circ$. However, it is not a sufficient condition for movement as both Eqs. (14) and (15) should be simultaneously satisfied.

For a bubble with a convex interface on the back $(\theta_{adv} > 90^\circ)$, as shown in Figure 9d, the required condition for the motion of the back contact line might be different. If the pressure difference across the bulging back interface exceeds what interfacial forces can compensate for, surface tension cannot hold the interface and the interface will move forward [15, 26]. In this case, according to the Young-Laplace equation

$$P_L \geq P_g - 4\sigma\frac{\cos\theta_{adv}}{h} \tag{18}$$

Adding Eq. (18) to Eq. (15) written for a square microchannel results in the necessary condition for the motion of both the front and the back contact lines

$$P_L - P_R \geq 4\sigma_{lg} \frac{(\cos\theta_{rec} - \cos\theta_{equ} - \cos\theta_{adv})}{h} \tag{19}$$

If θ_{equ} and θ_{adv} are both larger than 90° and very close to each other, the pinning may be overcome before the back pressure reaches the limit predicted by the Young-Laplace equation. In such a case, Eq. (16) will be applicable. Furthermore, our experimental results suggest that for moving bubbles with a slightly bulged back interface $(90^\circ \leq \theta_{adv} \leq 92^\circ)$, Eq. (16) can predict the pressure difference across the bubble much better than Eq. (19). For slightly bulged interfaces, the pinning forces may be still able to assist the surface tension to withstand the pressure difference across the meniscus and the motion of the back contact line happens by overcoming the pinning forces.

It is important to note that the motion of the front contact line is always triggered by overcoming the pinning forces. Also for $\theta_{adv} < 90^\circ$ pressure differences up to $4\sigma\cos\theta_{equ}/h$ across the interface can be easily held by the surface tension. Therefore, the motion of the back contact line can only occur by overcoming the pinning forces.

In the absence of liquid regions in the corners of the channel, pinning forces are the only resistive forces acting on the bubbles. However, when liquid regions exist, capillary forces may act on the bubble as well [17, 27].

2.2.1 DIFFERENTIATION BETWEEN CAPILLARY AND PINNING FORCES

It is easy to confuse capillary and pinning forces because the mathematical form of the right hand of Eq. (11) looks similar to capillary pressure if we replace s and A with $2\,(w+h)$ and $w \times h$, respectively. It is important to distinguish between the concepts of capillary and pinning forces and to understand that both of these forces may act on a dry bubble. In our example, the capillary pressure gradient was caused by the difference in the back and front curvatures due to pinning and contact angle hysteresis. An integration of capillary pressure over the interface results in the capillary force [7].

It is also possible to have capillary forces in the absence of pinning; for example, lubricated bubbles passing through contractions or expansions experience capillary forces [7]. The capillary pressure gradient and subsequently the capillary force can also be produced by a surface tension gradient due to variations in the temperature, concentration, or electric field [24].

Unlike pinning forces which always resist the motion, capillary forces may stimulate it. An interesting example presented by Paust et al. [28] demonstrates a conflict between the capillary and pinning forces: A growing bubble in a tapered geometry is pinned at the back side. The bubble growth toward a bigger cross section reduces the front curvature and increases the capillary force which eventually overcomes the pinning force at the back and detaches the bubble from the pinning point.

2.2.2 CAPILLARY PRESSURE

In the presence of liquid regions in the corner of a channel, the capillary pressure gradient induces an interfacial liquid flow on the gas-liquid menisci (represented by dotted line in Figure 9b) from the back to front that wants to move the bubble backward [24, 28]. Indeed, the corner liquids act as a medium for implementing the capillary pressure. The maximum capillary pressure gradient occurs when both front and back contact angles hold their limiting values. For a rectangular channel with a width of w and depth of h the Young-Laplace equation yields

$$\Delta P_{cap} = 2\sigma_{lg}\left(\cos\theta_{rec} - \cos\theta_{adv}\right)\left(\frac{1}{w} + \frac{1}{h}\right) \tag{20}$$

Assuming the capillary pressure can be completely transferred through the small gas-liquid menisci, ΔP_{cap} should be added to the right hand side of Eq. (16) to result in the necessary condition for the onset of bubble motion

$$P_L - P_R \geq \sigma_{lg}(\cos\theta_{rec} - \cos\theta_{adv})\left[\frac{s}{A} + 2\left(\frac{1}{w} + \frac{1}{h}\right)\right] \tag{21}$$

The pressure drop along the length of the bubble is maintained by the bypassing corner flow. Treating the corner flow as Poiseuille flow Wong et al. [17] approximated the pressure drop along a stationary bubble by

$$P_L - P_R = \frac{128 Q \mu l_b}{\pi d_{eff}^4} \tag{22}$$

where Q is the flow rate and d_{eff} is the effective dynamic diameter of the liquid flow. Equation (22) suggests that for any bubble length there is a critical flow rate that provides a pressure drop sufficient for bubble motion. The dynamic contact angles of the front and back of the dry moving bubble vary between receding and advancing contact angles as the triple contact line still exists. If the velocity of a dry bubble becomes high enough a thin film around the bubble will start to form and eventually the bubble will become lubricated again [29], as shown in Figure 10. As the velocity increases the bubble caps deform asymmetrically resulting in the so-called "bullet-shaped" appearance [24, 30].

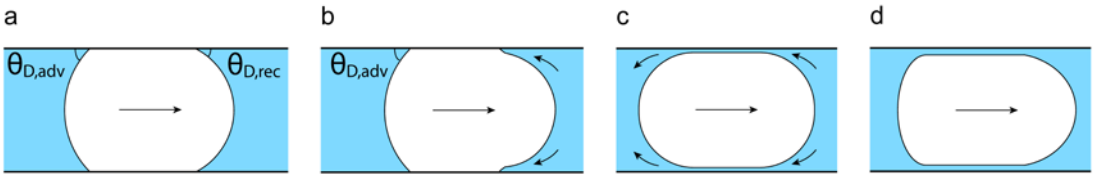

Figure 10: Progression of bubble shape with increasing velocity: a) dry dynamic bubble, b) thin film forming, c) lubricated bubble, and d) bullet-shaped lubricated bubble, adapted from Jensen [29]

2.3 THEORETICAL MODEL VALIDATION

The objective of the experiments is to measure the pressure required behind a dry bubble (with no corner flow and hence no resistive capillary pressure) to overcome the pinning forces and maintain its crawling motion. At low velocities $(\mathrm{Re} << 1)$, inertial forces are negligible and we can assume that the pinning forces are the only forces resisting the motion. Furthermore, at low velocities $(Ca < 10^{-3})$, dynamic contact

angles are independent of velocity and are equal to the static receding and advancing contact angles [31].

2.3.1 EXPERIMENTAL SETUP AND PROCEDURE

A schematic view of the experimental setup is presented in Figure 11. Square borosilicate glass channels (VitroCom P/N 8100) with a height and width of $976 \pm 8\ \mu m$ and a length of 10 cm have been used as the test channel. In order to decrease the hydrophilicity of the glass and have contact angle readings with high accuracy, four brand new channels were washed with "Rain X Original" glass treatment solution for 1–3 seconds and then rinsed with water and dried with compressed air. Depending on the duration of the treatment and the velocity of solution injection, each glass channel show different receding and advancing contact angles in the experiments. The fluid used in the experiments was deionized water. The treatment increased the equilibrium contact angle of water on the channel surface from below 10° to $60^{\circ} - 85^{\circ}$.

A syringe pump (Harvard Apparatus PHD 2000 Programmable stock no. 71-2019) was used for flow delivery. A 100-µl gastight syringe (Hamilton stock no. 81020) was used for bubble injection. The syringe was assembled on a reproduction adapter (Hamilton stock no. 14725) for better control.

A pressure transducer (Omega PX409-10WG5V) with a range of 0-2490 Pa and a 0.08% accuracy $(\pm 2\ Pa)$ was used for pressure acquisition. The pressure sensor has a

0.008% per degree Fahrenheit error associated with temperature change. The pressure signal was recorded with an NI-USB 6211 DAQ system and Labview.

a

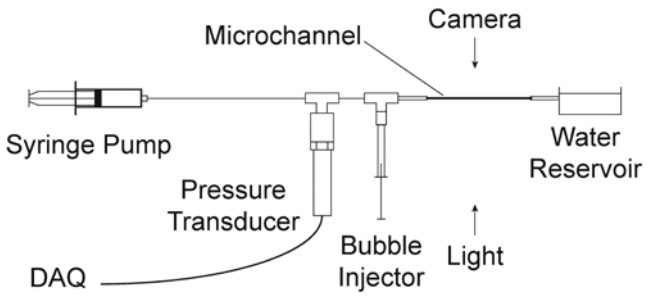

b

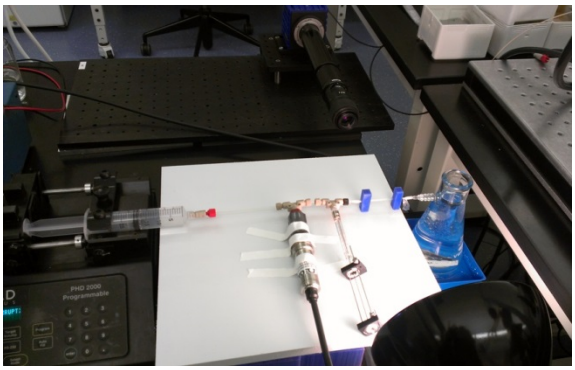

Figure 11: Experimental setup for pressure measurements

The bubble injecting syringe and the pressure transducer were connected to the main stream with two T-junctions (Idex stock no. P-714) using appropriate fittings (Idex stock nos. P-624 and U-501, and McMaster stock no. 4596K51). The syringe pump and the T-junctions were connected together by Radel tubing with a 0.03-inch inner diameter (Idex stock no. 1230). Tygon tubing with an inner diameter of 1/16" (McMaster stock no. 5155T12) was used to connect the glass microchannel inlet to the T-junction using a barbed to flat bottom adapter (Idex stock no. D-646). The same type of tubing was used to connect the microchannel outlet to a large water reservoir.

The imaging system consisted of a LaVision sCMOS camera coupled with a Navitar 12X Zoom lens (with a 0.5X lens attachment). An incandescent 100-Watt globe lamp was used for backlighting.

Several precautions were taken to reduce the pressure fluctuations in the room and test loop: The pressure transducer was connected to its fittings under water to avoid air trapping in the fittings and the transducer branch. The presence of a stratifying triple contact line in the path between the bubble and the sensor results in inaccurate pressure readings. The syringe pump was kept running for 30 minutes before the experiments for the system to become steady. Turning on or off the syringe the pump or changing the flow rate causes a temporary sharp increase in pressure readings. The lighting was kept on for one hour before the experiment to ensure that the temperature around the setup is steady. The laboratory doors were kept closed and the lab fume hoods were kept off before and during the experiments.

The flow rate was set at $2\ \mu l/min$ which corresponds to an average velocity of 2 mm/min in the channels $(Ca < 10^{-6})$. A single bubble with a volume between 5 to $10\ \mu l$ was injected into the flow stream for each experiment. To insure the repeatability, on two of the channels, two sets of experiments were performed.

The required pressure to maintain a flow rate of $2\ \mu l/min$ was measured prior to bubble injection. The change in the water reservoir level between this reading and the beginning of image and pressure acquisition is carefully calculated for each

experiment ($<120\ \mu m$) and accounted for. We are interested in the pressure difference across the bubble length; therefore, the pressure prior to bubble injection was subtracted from the measured pressure during the bubble motion. The change in the reservoir water level during image and pressure acquisition was about $29\ \mu m$ (0.28 Pa hydrostatic pressure) and was neglected.

Image and pressure data acquisition started almost simultaneously at rates of 5 fps and 1000 Hz respectively and continued for 12 minutes. The pressure data has been condensed to an average pressure value for every 0.2 s interval. By matching a pressure peak in the pressure signal to its corresponding closely-timed image with an apparent maximum pinning, the lag between the imaging and pressure measurements was revealed. Using this information, each image has been mapped to a single pressure reading.

2.3.2 RESULTS

In order to calculate the required pressure to keep the bubbles moving form Eq. (17) and Eq. (19) the contact angles must be measured from the images. Accurate measurement of the contact angles is only possible when the image of the bubble interface is a uniform line as shown in Figure 12a and 12c, in contrast to Figure 12b and 12d. For the selected images, accurate measurement of the contact angles was possible. Furthermore, within one second before and after the image was captured the motion of the bubble was steady and there was no observed rapid change in the shape of the front and back interfaces. For those cases, the variation in the measured pressure

during the two second period was always within and often much lower than ±2 Pa accuracy range of the transducer.

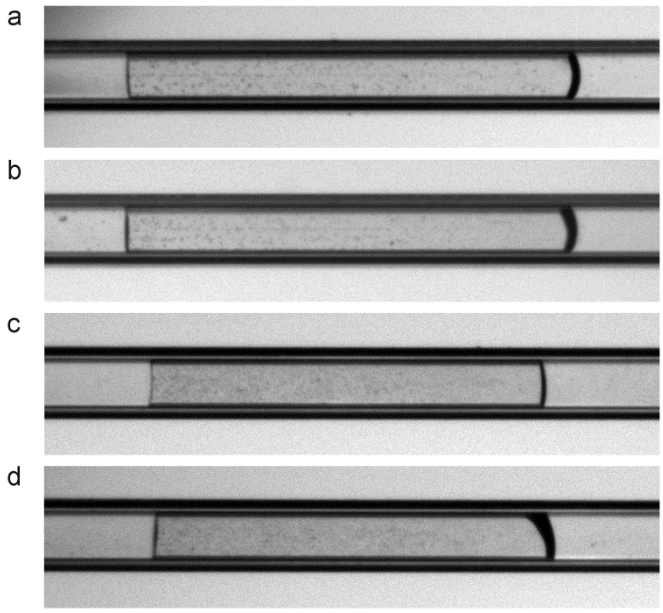

Figure 12: Variation in the contact angles during the motion, a and b are images of one bubble and c and d are images of another. a) concave back interface, c) convex back interface, b and d) nearly flat back interfaces and unequal front contact angles at the side walls

The top and bottom contact angles of an interface (see Figure 9d) are often different and the average of their cosine values should be used instead in the equations. To use Eq. (19) the equilibrium contact angle must be known. We have estimated the cosine of equilibrium contact angle by averaging the cosine of advancing and receding contact angles of all the selected occurrences in each dataset [32, 33].

Table 1 presents the length of the bubbles in each experiment and the range of the advancing and receding contact angles for the selected occurrences. Note that the top

and bottom contact angles are often different. It is possible to either have a concave or a convex back interface when one of the back contact angles (top or bottom contact angles) is below 90° and the other one is above 90°.

Table 1: Details of the six sets of experiments

Experiment No.	Channel No.	Length of the injected bubble (mm)	θ_{rec}(deg) of occurrences	θ_{adv}(deg) of occurrences
1	1	8.1	70 – 83	87 – 97
2	1	10.2	69 – 84	86 – 94
3	2	9.3	56 – 70	77 – 90
4	3	5.3	44 – 60	93 – 98
5	4	5.6	68 – 81	89 – 97
6	4	5.4	66 – 78	86 – 96

Figure 13 presents a sample measured pressure difference across the bubble length over time. The values of receding and advancing contact angles vary locally and the peak pressure values correspond to severe pinning cases.

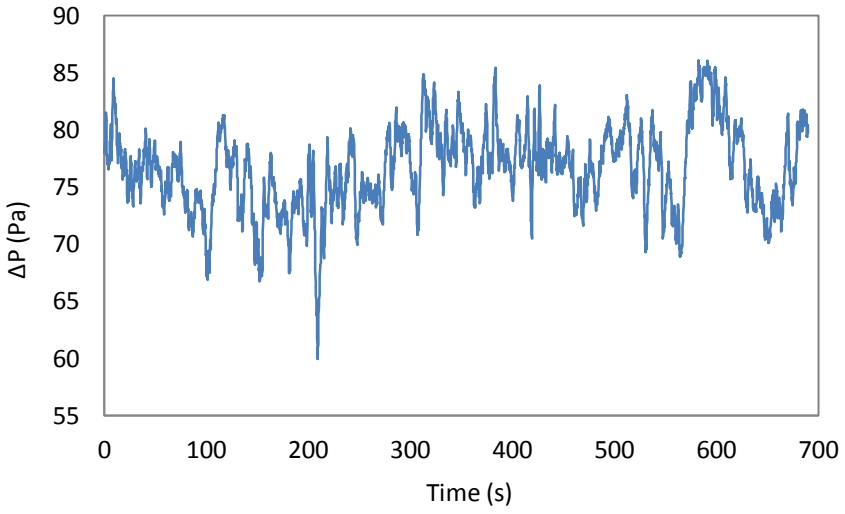

Figure 13: Pressure difference across the length of the crawling bubble

A sample pressure reading prior to bubble injection at a flow rate of $2\,\mu l/min$ is presented in Figure 14. Average pressure values for every 0.2 s interval have been shown in blue. The periodically averaged pressure values were fairly steady and the variations were within the $\pm 2\,Pa$ accuracy range. The summation of the average pressure and the change in the hydrostatic outlet pressure was subtracted from the pressure readings acquired during the motion of the injected bubble in each experiment.

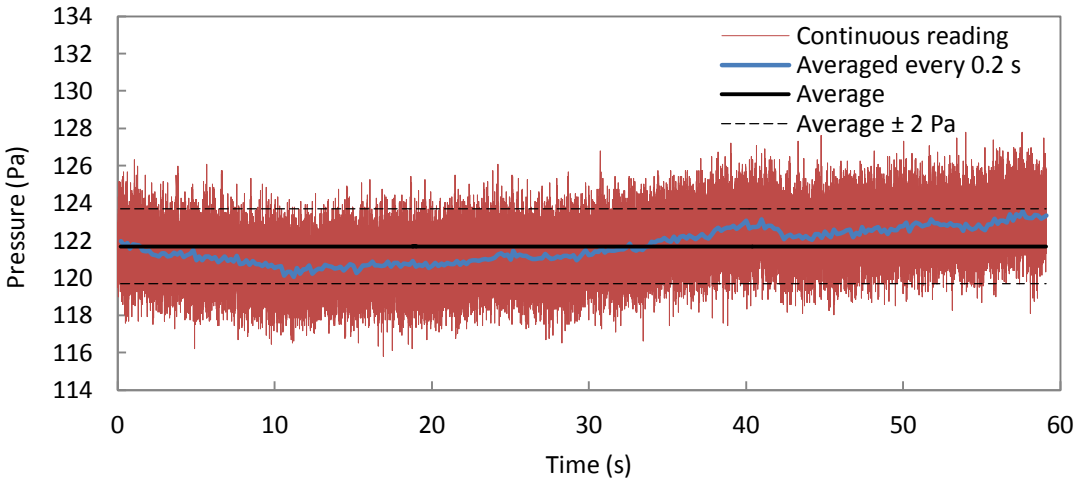

Figure 14: Pressure readings prior to bubble injection

Figure 15 presents an overview of the measured pressures in the six sets of experiments and the model's predictions. For bubbles with a concave back interface, the convex back model underestimates the required pressure to move the bubbles while for bubbles with a convex back interface, the concave back model overestimates the required pressure.

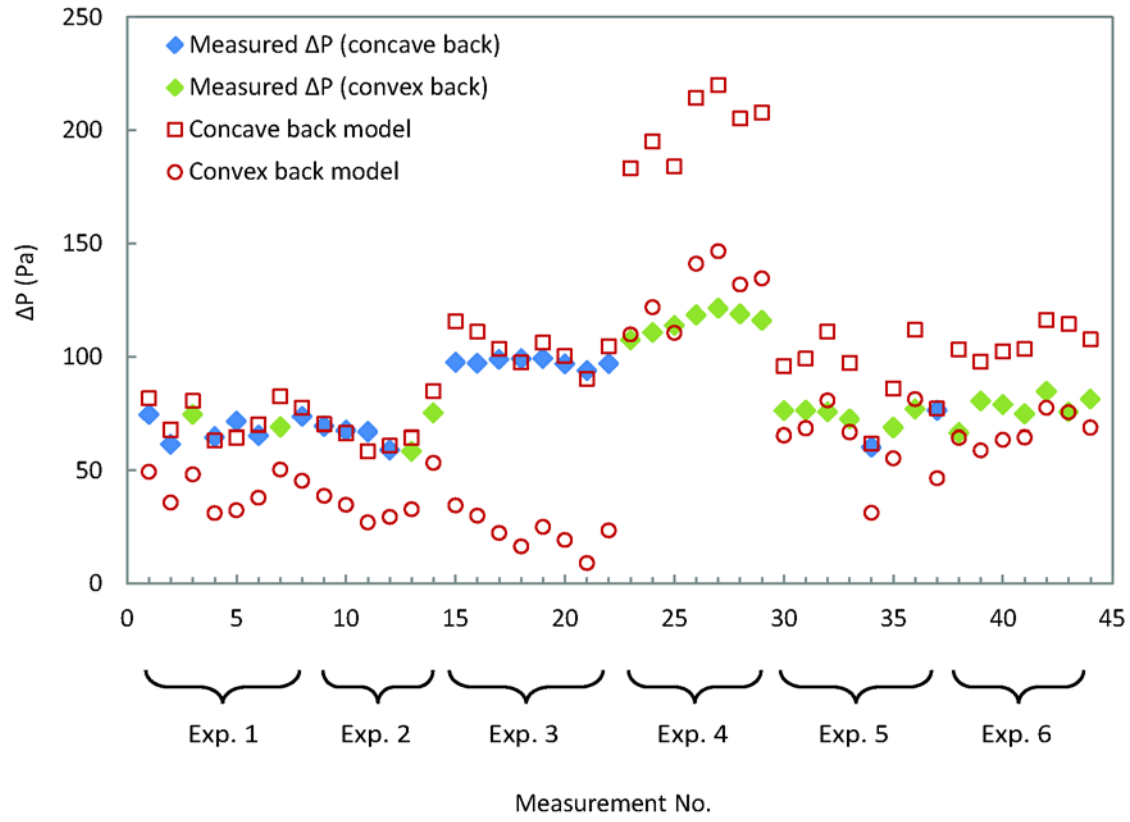

Figure 15: Comparison between the model's predictions and the measured pressures for the 6 sets of experiments. There could be a large difference between the concave and convex back model predictions.

The measured pressure is compared with the model's predictions for bubbles in the six sets of experiments in Figure 16. Four of the occurrences have advancing contact angles slightly larger than 90° ($90^\circ \le \theta_{adv} \le 93^\circ$) but they matched the concave back model's prediction better. We presume for those four consequences the motion of the back contact line was achieved by overcoming pinning forces and not by failure of the meniscus in withstanding the pressure difference across it.

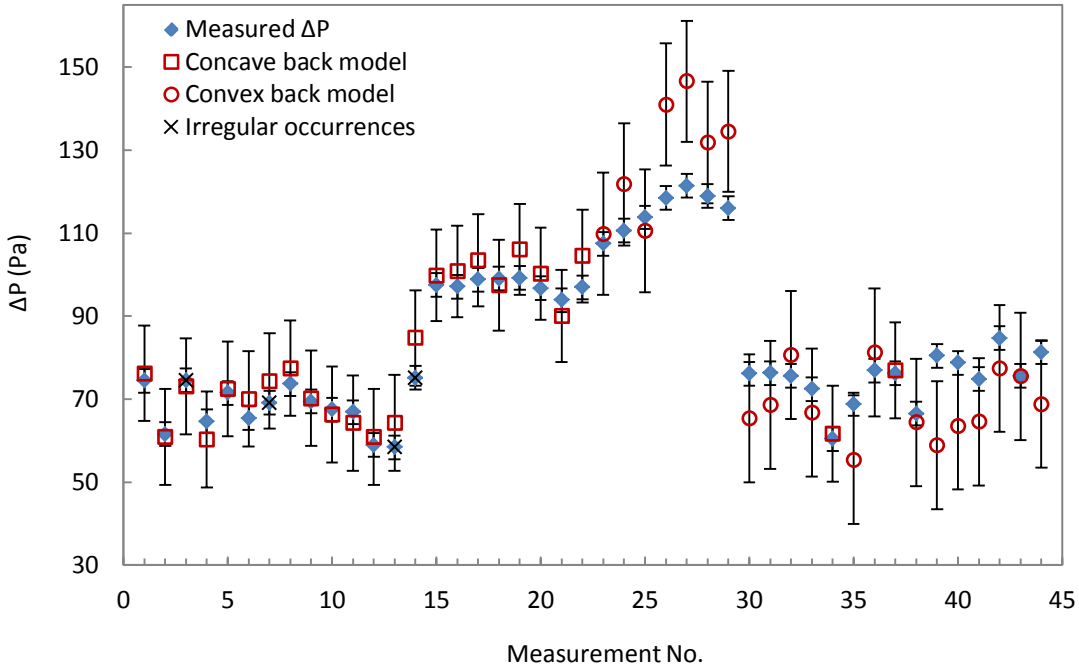

Figure 16: Comparison between the measured pressure and the matching models' prediction. There are four irregular occurrences that have a slightly convex back interface but match the concave back model's prediction better.

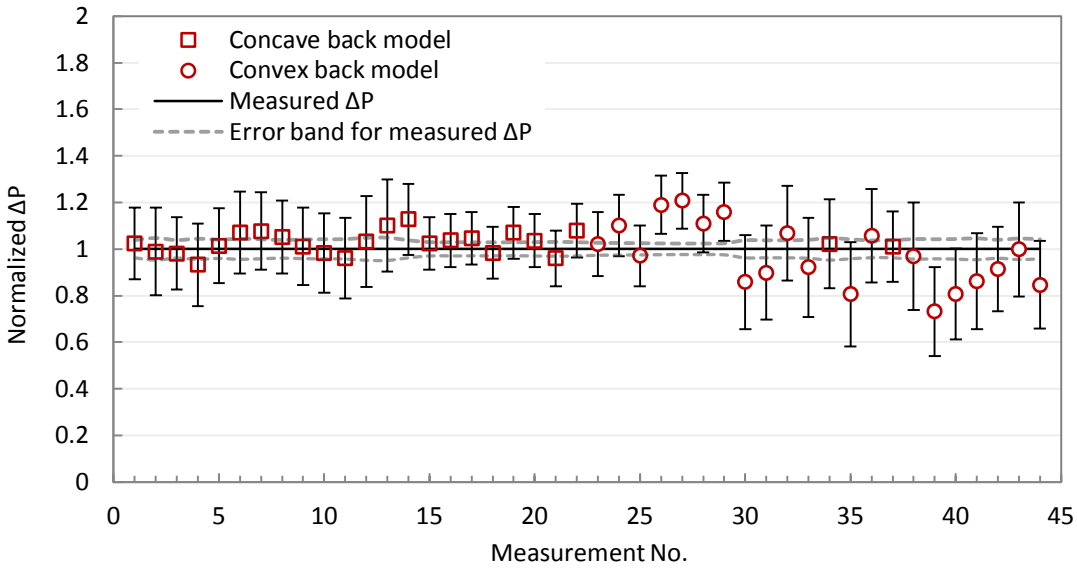

Figure 17: Normalized models' predictions based on the measured pressure

Figure 17 gives an overview of the normalized model's predictions with respect to measured pressures. The model successfully predicts the required pressure to maintain the crawling motion of the bubbles.

The quantified errors associated with pressure measurements are due to the accuracy of the transducer. The periodically averaged pressure values for every 0.2 s interval prior to bubble injection were relatively steady and the variations were within the ±2 Pa accuracy range of the transducer (see Figure 14). Therefore, pressure fluctuations sourced from the syringe pump or room pressure has been neglected in error estimations. A sudden pressure drop during the pressure reading in the absence of a bubble is observed, as shown in Figure 18, which was probably sourced from the syringe pump. These fluctuations have not been taken into account in error calculation because they occurred occasionally. However, they might have contributed to the differences observed between the measured pressure and the model prediction.

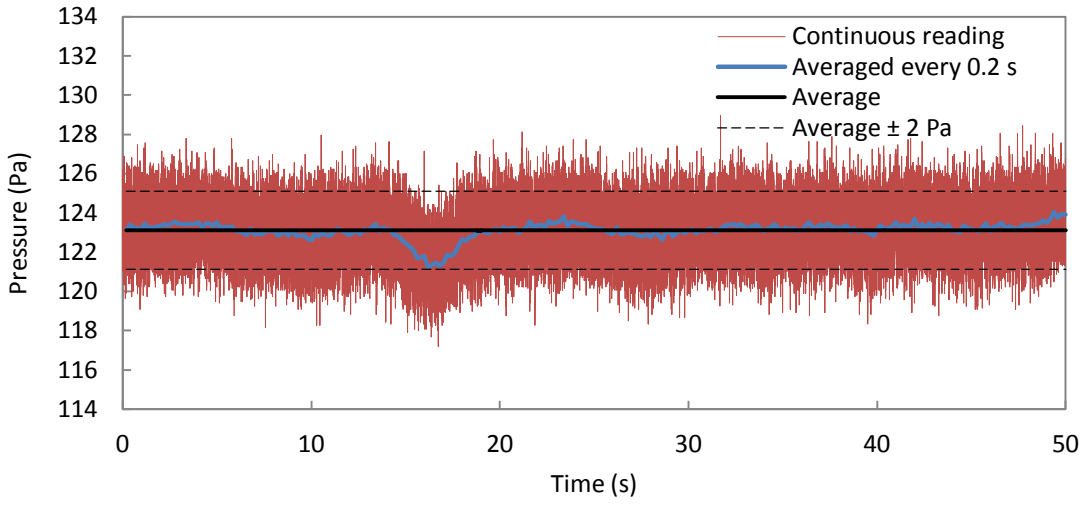

Figure 18: Pressure fluctuations that might be caused by the syringe pump

The errors associated with the model's prediction include uncertainty in the size of the channel and the measurement of the four contact angles for a bubble ($\pm 2.25^{\circ}$). An additional error is involved in the prediction of convex back model due to the estimation of the equilibrium contact angle which results in larger error bars for the convex back model's predictions. The cosine of equilibrium contact angle was estimated by averaging the cosine of advancing and receding contact angles of studied occurrences in each data set [32, 33]. A standard error of a $\pm 2.25^{\circ}$ was assigned to this estimation. In reality, equilibrium contact angle varies locally but we have assumed it is a single value in each dataset. The errors were calculated using the Kline and McClintock method [34] as described in Appendix A.

One of the most important factors contributing to the differences observed between the measured pressure and the model's predictions is the contact angle measurement. With a two dimensional image from the bubble caps it is not possible to measure the contact angles on all 4 sides of the channel. We only measure the contact angles on the top and bottom sides of the bubble caps (as shown in Figure 9d). We assume that the cosine of contact angles on the other two sides are an average of the cosine of contact angles on the top and bottom sides. For a uniform cap this assumption is reasonable but may not be accurate. Some assumptions were made in the development of our theoretical model such as assuming equal cross sectional areas, contact line lengths, and equilibrium contact angles at the front and the back of the bubbles. There is a definite deviation from these assumptions in the experiments which also contributes to the differences between the measured pressure and the model's predictions.

2.4 EFFECT OF PEO COATING ON BUBBLE MOVABILITY IN MICROCHANNELS

The triblock copolymer of polyethylene oxide-polybutadiene-polyethylene oxide (PEO-PB-PEO) has been developed primarily to prevent protein adsorption on polycarbonate for biomedical applications [1]. However, for our microchannel hemodialysis application, another function of the PEO coating is facilitating the bubble movement through the system. Experimental results of Matthew Coblyn have shown that bubbles are less prone to getting stuck in an array of coated microchannels compared to an uncoated one. In this section the reasons behind the positive influence of PEO coating on bubble movability are investigated.

The PEO brush layers mask the surface electrostatic charge and surface heterogeneities to some extent and make the polycarbonate surface more hydrophilic. Table 2 presents the contact angle characteristics of the coated and uncoated surfaces. The measurements were taken by placing 10-μl water droplets on planar embossed PEO-coated and uncoated polycarbonate sheets that mimic the surface characteristics of the two laminas in our experiments. There is no unique equilibrium contact angle for non-ideal surfaces [22]. Here, we report the range of observed equilibrium contact angles for several droplets. The limiting advancing and receding contact angles occur before the contact line shifts while varying the volume of droplets [22]. The maximum and minimum contact angles in a series of inflation and deflation experiments are reported as the advancing and receding contact angles, respectively.

The theoretical model has shown that resistant pinning and capillary forces are proportional to $\cos\theta_{rec} - \cos\theta_{adv}$. The use of PEO coating reduces the contact angles. Although the contact angle hysteresis $(\theta_{adv} - \theta_{rec})$ did not decrease with the coating, the influence of hysteresis on the pinning and capillary forces given by $\cos\theta_{rec} - \cos\theta_{adv}$ was significantly smaller. Thus bubbles experience less resistive forces in the coated system.

Table 2: Contact angles on uncoated and coated embossed polycarbonate sheets

	θ_{rec}	θ_{equ}	θ_{adv}	$\theta_{adv} - \theta_{rec}$	$\cos\theta_{rec} - \cos\theta_{adv}$
Uncoated	45°	$59^\circ - 65^\circ$	80°	35°	0.53
Coated	5°	$25^\circ - 35^\circ$	42°	42°	0.25

The accuracy of the angle measurements is $\pm 1^\circ$.

The dewetting velocities of the coated and uncoated surfaces were also measured. Following de Gennes et al. [22] circular thin films were produced by depositing water inside the wetting rings etched on the surfaces by sulfochromic acid. A small amount of liquid was removed from the center of the film with a pipette to nucleate a dry zone that expanded with the dewetting velocity, as shown in Figure 19. High speed images of the dewetting were captured with a Phantom V310 camera at a rate of 1000 fps.

Unfortunately the dry patches did not always grow as perfect circles, especially on the uncoated surface, which might be due to a non-uniform initial film thickness. Here we report the dewetting velocity of the cases that had the most uniform and circular growth of dry zones. The measured dewetting velocities for the coated and uncoated

surfaces were 1.47 ± 0.02 cm/s and 3.42 ± 0.03 cm/s, respectively (see Appendix B). As expected, the coating reduces the dewetting velocity; therefore, bubbles in the coated system have a better chance of remaining lubricated at low flow rates.

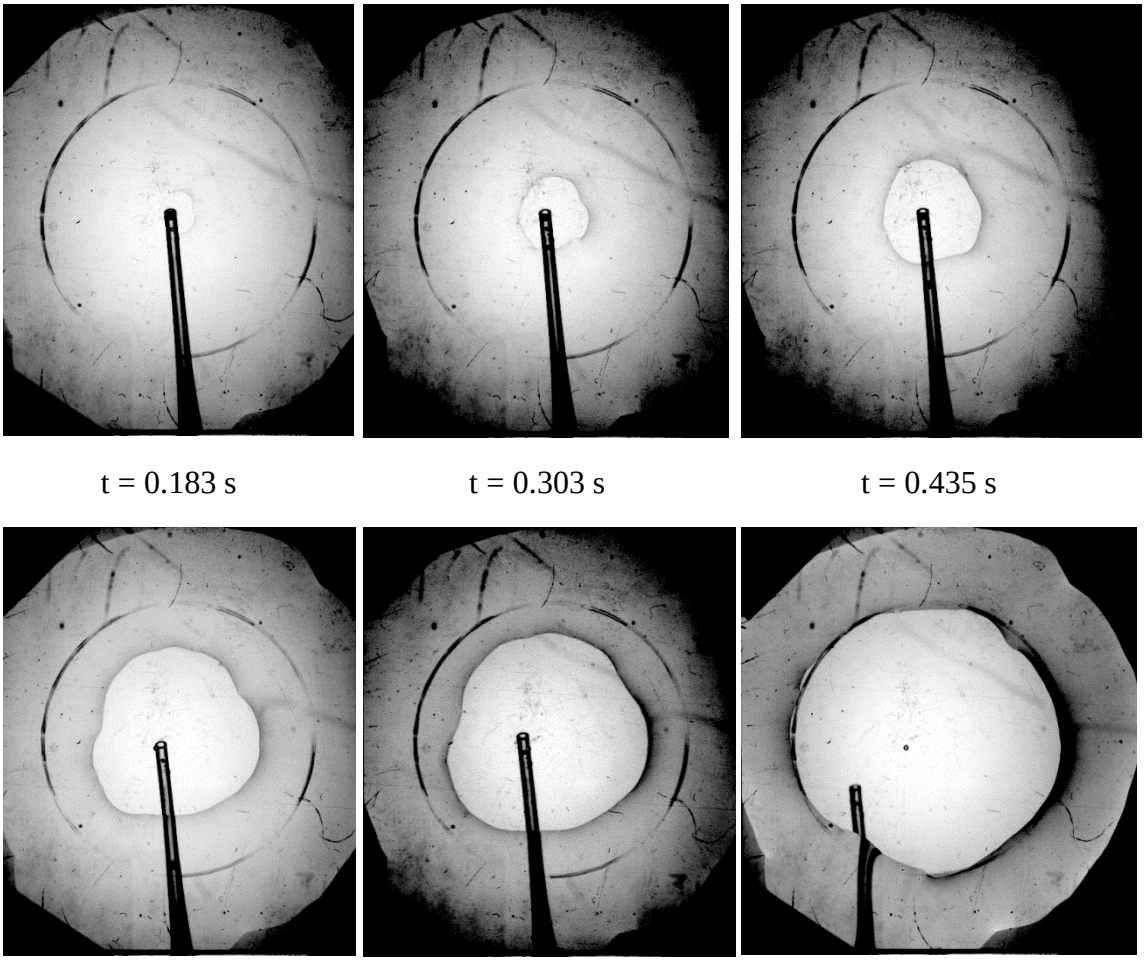

Figure 19: Consecutive images of dewetting on the coated surface

In general, our theoretical model and also the velocity conditions for the formation of lubricating thin films around the bubbles suggest that increasing the hydrophilicity of surfaces is a robust approach to reducing bubble clogging in microfluidic systems.

2.5 THE MERIT OF STUDYING AN AIR-WATER MODEL SYSTEM

In dialyzer devices, bubbles may appear in both the dialysis fluid and the blood side. The behavior of bubbles in the dialysis fluid side is expected to be quite similar to their behavior in water. The dialysis fluid is a water-based solution and does not contain large particles but it contains electrolytes. The presence of electrolytes is expected to hinder the coalescence of bubbles [35]. However, the mechanical properties of blood are different from water; blood contains large molecules and blood cells. For these reasons, we do not expect an air-water system to exactly replicate an air-blood system. Studying a model air-water system is a step toward learning about the behavior of bubbles in a microchannel geometry. However, the basic *principles* related to capillary pressure and contact line forces and also the influence of geometry on the motion of bubbles are expected to stand for an air-blood system as well. Herein, we identify some of the differences between blood and water that will influence bubble behavior. Most of these differences are expected to result in higher bubble movability in blood compared to water as explained below.

a) The viscosity of blood at shear rates higher than 100 (1/s) is nearly constant for each channel size and always larger than the viscosity of water (up to 3.48 times) [36, 37]. Therefore, with the same volumetric flow rate for water and blood through the same geometry, blood will experience larger pressure drop per unit length than water. Stagnant bubbles start to move when the pressure drop along their length can overcome the capillary and pinning forces. The larger pressure drop in blood results in higher bubble movability in the device.

In the laminar regime, we can assume a linear relationship between the pressure drop and the flow rate and also the channel length. Therefore, if a bubble starts to move at a certain volumetric water flow rate, it is estimated that the same bubble would move at a smaller blood flow rate.

b) At $22^{o}C$, the surface tension of blood is 56 mN/m while the surface tension of water is 72 mN/m [38]. The resistive capillary and pinning forces on bubbles are proportional to the surface tension; therefore, bubbles in blood experience less resistance compared to water and are more willing to move.

c) The lower the surface tension is, the more easily the bubbles break up [39]. This may lead to the presence of more small stagnant bubbles in blood compared to water since small bubbles are the most stubborn bubbles in the system. The author hypothesizes that due to the presence of large molecule and cells inside blood, the surface tension of blood varies locally at the micro scale level which may also lead to bubble break up.

d) In the absence of surfactants in water, a slip boundary condition (no shear stress) can be assumed at the bubble interface. With a slip boundary condition, bubbles do not experience a drag force by the liquid. On the other hand, for bubbles in blood, the boundary condition is no-slip due to the presence of blood proteins at the interface [40, 41]. Proteins are composed of amino acids that contain either hydrophilic or hydrophobic side chains (R-groups); they act like surfactants and stick to the bubble interface from the hydrophobic side

chains with the hydrophilic groups pointing toward the liquid phase. Bubbles in blood experience drag forces which promote bubble mobility.

e) Blood proteins at the gas-liquid interface create repulsive electrostatic forces that hinder the coalescence of bubbles. In the studied air-water system bubble coalescence was occasionally observed which contributed to the bubble movability since large bubbles are less prone to becoming stagnant. Moreover, both blood and dialysis fluid contain electrolytes. Electrolytes may form an electrical double layer at the interfaces between two bubbles and the draining liquid. The attraction force of the opposite charges causes retardation of the draining film [42]. This may prevent bubble coalescence as well.

2.6 A BLOCKAGE-FREE MULTICHANNEL ARRAY

In the presence of a flow bypass (either corner regions or parallel channels), those bubbles which become stationary due to resistive capillary and pinning forces may never start crawling. The contact angle of water on coated channels is less than 45°; therefore, it is expected that corner flows exist around the bubbles in the present multichannel array fabricated at Oregon State University [24]. The chances of small bubbles becoming stagnant is high since they experience approximately the same resistive forces as long bubbles do while the pressure drop along their length is small.

The desired situation for the microchannel dialyzer is having no blocked channels in the entire array of channels on each lamina. Bubbles with a length smaller than the

channel width are tolerable since they only partially block the channels. Also, such small bubbles are very stubborn in terms of removal.

In order to have no blocking bubbles, the pressure drop maintained by the corner flow along an elongated bubble with a length equal to channel width should be larger than the pressure required to overcome pinning and capillary forces.

Substituting Eq. (21) in the left hand side of Eq. (22) and replacing the bubble length (l_b) with channel width (w) we get

$$\frac{128Q\mu w}{\pi d_{eff}^4} \geq \sigma_{lg}(\cos\theta_{rec} - \cos\theta_{adv})\left[\frac{s}{A} + 2\left(\frac{1}{w} + \frac{1}{h}\right)\right] \tag{23}$$

In the above inequality, d_{eff} (the effective dynamic diameter of the liquid flow) and s (the length of the front or back contact line of the bubble) are unknown. These values depend on the channel dimensions and cross-sectional shape of the channel e.g. rectangular, trapezoidal, curved bottom, etc. Obtaining the exact values of d_{eff} and s for elongated bubbles would require an experimental method such as confocal scanning microscopy. These values can themselves be a function of channel width, depth, and velocity. Therefore, it is very difficult to use Eqs. (21) and (22) to estimate the required flow rate *Q* (or velocity in each channel) that assures no blockages as a function of channel width and depth.

The most feasible approach to estimate the required velocity as a function of channel width and depth is performing statistical studies on bubble blockage in laminas with

different channel dimensions. This is one of the recommended studies for future works. For each channel size, statistical studies can provide the required velocity that is able to remove all bubbles larger than the channel width and assure no blockages. We can use interpolation to estimate the required velocity for continuous ranges of channel width and channel depth.

3 SHEAR-INDUCED BLOOD DAMAGE IN MICROCHANNELS

Medical devices such as heart valves, artificial heart pumps, and hemodialyzers subject blood to much higher shear stress than experienced in the human body. Normal vascular flow is characterized by low shear stresses, between 0.1 and 1 Pa in venous flows, at about 5 Pa in arterial flows, and peaks at about 6 Pa in arterioles. In patients with a stenosed artery the shear stress may reach 38 Pa [43]. However, in blood handling devices shear stresses, often reach hundreds of Pascals [44]. High shear stress at a long enough exposure time may cause multiple complications arising from hemolysis (red blood cell rupture) and thrombosis (blood clotting) [45].

In this chapter, the characteristics of blood flow in microchannels and shear-induced blood damage are reviewed. Furthermore, an estimation of the maximum shear stress applied on blood flow in microchannels is provided. For our microchannel dialyzer device with a restricted channel length (< 20 cm), the residence time of blood is expected to be in the order of seconds. Based on the data available in literature on the subject of shear-induced blood damage, a velocity-dependent constraint is placed on the depth of the present microchannel dialyzer device to prevent shear-induced blood damage.

3.1 BLOOD COMPONENTS

Blood is a physiological fluid that consists of erythrocytes or red blood cells (RBCs), leukocytes or white blood cells (WBCs), thrombocytes or platelets, and plasma

containing various molecules and ions. RBCs constitute approximately 45% of the total blood volume, WBCs account for around 0.7%, and the rest is taken up by blood plasma and its substances including platelets. Figure 20 presents a scanning electron micrograph of blood cells. Due to the high volume fraction of RBCs, the rheological properties of blood are mainly determined by the RBC properties [46]. The volume fraction of red blood cells in blood or a diluted blood solution is called the hematocrit level (Hct).

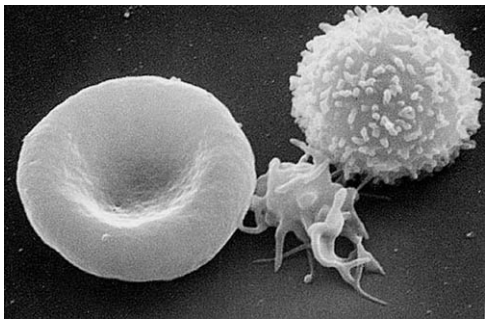

Figure 20: Scanning electron micrograph of blood cells. From left to right: human erythrocyte (RBC), thrombocyte (platelet), leukocyte (WBC), from Wikimedia Commons

Red blood cells carry oxygen to the body tissues and collect carbon dioxide. Hemoglobin, the iron-containing respiratory protein in RBCs, is responsible for the oxygen and carbon dioxide transportation. Under healthy conditions human RBCs have a biconcave shape with a diameter of approximately $6-8\,\mu m$. RBCs are highly deformable mainly due to the viscoelastic properties of the cell membrane. The average life span of RBCs is about 4 months. The high deformability allows them to pass through narrow capillaries smaller than the RBC size, the diameter of blood

capillaries in the human body varies between $2-3.5\ \mu m$ in the conjunctiva to $12\ \mu m$ in the diaphragm [47].

White blood cells are the cells of the immune system that defends the body against both infectious diseases and foreign materials. Five different and diverse types of WBCs exist, but they are all produced and derived from a multipotent cell in the bone marrow. The diameter of the WBCs varies between $7-15\ \mu m$ [48]. They live for about a few hours to a few days in an average human body [49].

Platelets are small disk-shaped clear cell fragments $1-3\ \mu m$ in diameter [48]. They are involved in hemostasis: a process which causes bleeding to stop and leads to the formation of blood clots. A low number of platelets in blood results in excessive bleeding at the time of injury. The average lifespan of a platelet in the human body is 8 – 10 days [48].

Blood plasma is about 90% water by volume. It contains dissolved proteins (e.g. albumins, globulins, and fibrinogen), clotting factors, glucose, lipids, enzymes, hormones, antibodies, vitamins, electrolytes (Na^+, K^+, Ca^{2+}, Mg^{2+}, HCO^{3-}, Cl^-, etc.) and carbon dioxide [48].

3.2 BLOOD FLOW IN MICROCHANNELS

A single phase pressure-driven Newtonian laminar flow in a channel results in a parabolic Poiseuille velocity profile. The velocity profile can be obtained by solving the Navier-Stokes equation with a constant pressure gradient along the flow direction

and with no-slip boundary conditions at the walls. The velocity profile for whole blood in a microchannel has some distinctive characteristics which differ from the Poiseuille velocity profile. Blood is a suspension of deformable red blood cells. The migration of red blood cells from the channel center forms a blunt velocity profile and the deformability of red blood cells may results in a non-Newtonian behavior [46, 50]. In the following sections, the important characteristics of blood flow in microchannels most relevant to the present work will be reviewed.

3.2.1 CELL-FREE LAYER

The cell-free layer (CFL) is a near-wall layer of blood plasma lacking RBCs. The blood cells are subject to migration from the wall to the tube center in Poiseuille flow; as a result of the cell to wall interactions [46]. The fluid viscosity of the CFL region is much smaller than that of the tube core populated with RBCs providing effective lubrication for the core to flow. The thickness of the CFL changes with the hematocrit level [51] and flow rate [46].

3.2.2 FAHRAEUS-LINDQVIST EFFECT

The Fahraeus-Lindqvist effect explains an decrease in the apparent blood viscosity with decreasing tube diameter and hematocrit level [37]. The apparent viscosity in a tube is defined as [46]

$$\mu_{app} = \frac{\pi \Delta P d^4}{128 Q L} = \frac{\Delta P d^2}{32 U L} \tag{24}$$

It is more convenient to define a relative apparent viscosity as

$$\mu_{rel} = \frac{\mu_{app}}{\mu_{plasma}} \tag{25}$$

Increasing the hematocrit level increases the apparent viscosity since cell crowding results in larger flow resistance. At small tube diameters (< 500 μm), the thickness of the cell-free layer is comparable to the central core which significantly reduces the apparent viscosity of flow through the tube. As the tube diameter increases, the cell-free layer thickness becomes negligible with respect to the tube diameter and the viscosity coefficient approaches the asymptotic value, as shown in Figure 21. The lowest viscosity values are at diameters around $5-7\,\mu m$ when the RBCs align themselves with the capillary tube (single-file flow) [52]. Figure 21 presents the relative apparent viscosity of blood at different tube diameters for the natural hematocrit level of human blood (*Hct* = 0.45).

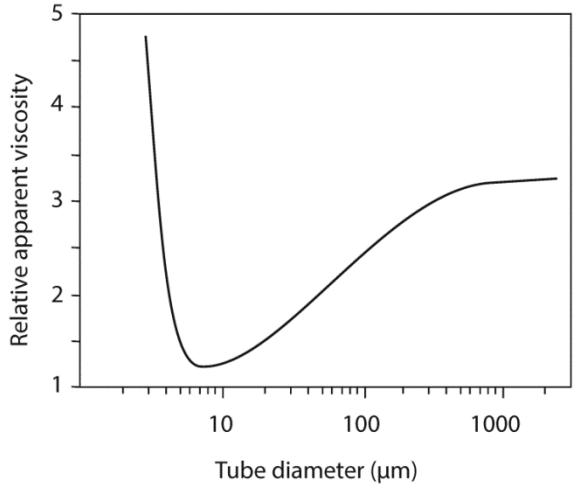

Figure 21: An estimation of the relative viscosity of red cell suspensions perfused through tubes of different diameters for *Hct*= 0.45, adapted from Pries et al. [37]

3.2.3 NON-NEWTONIAN BEHAVIOR

Blood is often referred to as a non-Newtonian fluid with shear-thinning characteristic meaning its viscosity decreases when shear stress increases. This property is considered to be a result of microscale structural rearrangements within the blood and red blood cell deformability. However, blood does not always exhibit non-Newtonian behavior. The Newtonian behavior of blood at high shear rates is widely agreed upon; the reported shear rates for transition from non-Newtonian to Newtonian vary from 100 to 1000 1/s [36, 53]. The variation in viscosity values at shear rate above 100 1/s is very small. Figure 22 and Figure 23 present shear rate dependent Newtonian and non-Newtonian behavior of blood.

The viscosity asymptotically approaches 0.00348 Pa.s in scales larger than 1 mm [54]. However, blood shows a viscosity lower than 0.000348 Pa.s in smaller scales due to the Fahraeus-Lindqvist effect. Beissinger and Laugel [55] reported a constant viscosity of 0.0027 Pa.s for a $500\ \mu m$ capillary for shear rates larger than 2500 1/s.

It has also been confirmed that dilute blood suspensions behave like Newtonian fluids [56]. Confocal micro PIV results by Lima et al. [57] showed that for 20% Hct there is a good agreement between the analytical velocity solution for a Newtonian fluid with the plasma viscosity and the experimental velocity profile. Such studies suggest that red blood cells are responsible for the high viscosity of blood and the blunt velocity profile of blood (45% Hct) in microchannels.

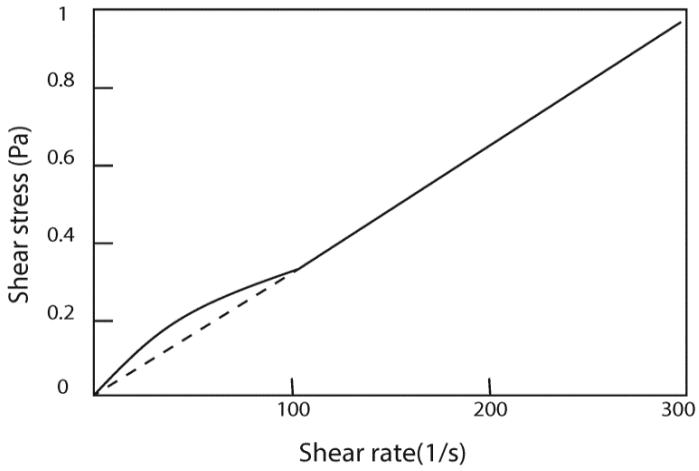

Figure 22: Shear-thinning behavior of blood at low shear rates, adapted from Merrill [36]

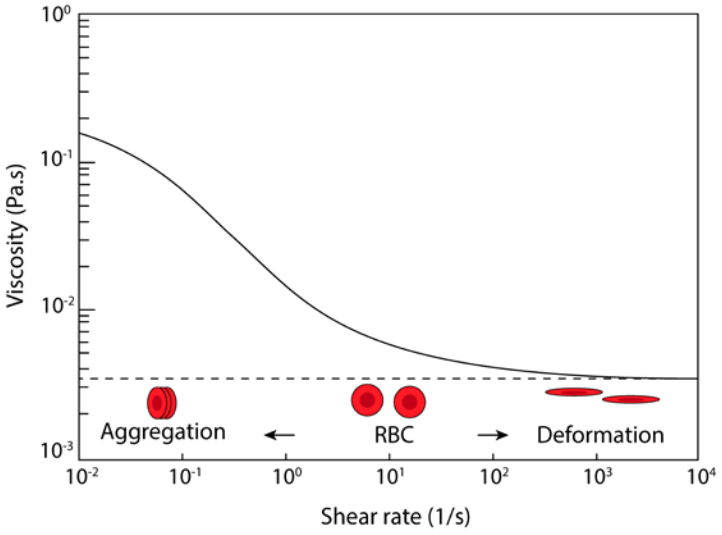

Figure 23: Dependence of the viscosity of blood on shear rate, adapted from Kwak and Kiris [54]

3.3 SHEAR EFFECTS ON RED BLOOD CELLS

Red blood cells are the most extensively studied blood component in terms of shear-induced damage. Depending on the magnitude of the shear stress and the duration of the time that blood is exposed to shear stress, red blood cells may be

damaged [58]. Mechanical damage of red blood cells often refers to hemolysis: the rupture of red blood cell membrane releasing its contents (cytoplasm) into the blood plasma. Less severe types of mechanical damage can result in a reduction in the cell deformability and membrane elasticity.

3.3.1 SHEAR EFFECTS ON RED BLOOD CELL DEFORMABILITY

Most of the studies on shear-induced RBC damage have focused on hemolysis. However, today it is also known that without hemolysis occurring, the membrane of RBCs can get damaged which affects the RBC metabolism [58, 59]. It is important to remember that a normal RBC demonstrates extraordinary ability to undergo reversible large deformations and fluidity [60]. RBCs pass through the blood capillaries as small as $2\ \mu m$ in a human body. In in vitro experiments, RBCs could deform and pass a $4\ \mu m \times 4\ \mu m$ PDMS channel and recover afterwards [60].

One way to investigate the effect of shear stress on deformability of the RBCs is by investigating the ratio of length over width of RBCs (L_{RBC} / W_{RBC}) during exposure. In the absence of shear stress this ratio is equal to 4. Experimental results of Watanabe et al. [58] suggested that under the constant shear stress of 64 Pa in a cone-cup viscometer, an exposure time larger than 10 minutes is required to affect the mean L_{RBC} / W_{RBC}.

Another way to explore the effect of shear stress on deformability is by considering the elongation index (EI) which is defined as $(A-B)/(A+B)$ where A and B are

the length of the major and minor axes of the RBC eclipse. Pre-sheared RBCs may exhibit different EI than unsheared RBCs. Experimental results of Lee et al. [59] with a Couette viscometer showed that RBCs that were exposed to a constant pre-shear stress of 54.9 Pa for 30 s exhibited slightly different elongation indices ($\simeq 3\%$) than unsheared control RBCs. An exposure to a pre-shear stress as large as 112.8 Pa for 30 s reduced the elongation index of RBCs by 15% [59].

3.3.2 HEMOLYSIS

The concentration of free hemoglobin in the blood plasma (mg/dL) yields the hemolysis index (HI) which determines the severity of the damage. The hemolysis index can also be defined as the number of grams free hemoglobin released per 100 L of pumped blood. The percentage of released hemoglobin (normalized by hematocrit) is reported as the normalized hemolysis index [61]. Extreme cases of hemolysis can result in the activation of clotting factors through hemoglobin release into the blood stream [62, 63]. Increased viscosity and hematocrit were found to cause increased levels of hemolysis, suggesting that patients with a naturally lower hematocrit, such as females, may be at lower risk for hemolysis [64].

The U.S. Food and Drug Administration (FDA) requires medical devices to undergo in vitro and in vivo hemolysis tests (following ISO 10993-4 or ASTM F756-08 standards) prior to clinical studies. According to ISO 10993-4:2009, “it is not possible to define a universal level for acceptable and unacceptable amounts of hemolysis for all medical devices and applications…. In practice, many devices cause hemolysis, but

their clinical benefit outweighs the risk associated with the hemolysis. Therefore when a device causes hemolysis, it is important to confirm that the device provides a clinical benefit and that the hemolysis is within acceptable limits clinically. Acceptance criteria should be justified based on some form of risk and benefit assessment." In general, devices with a hemolysis index less than 5% are considered non-hemolytic [65].

The hemolysis level typically depends on the magnitude of shear stress and the exposure time. The larger the shear stress, the smaller the minimum exposure time prior to damaging RBCs. Threshold values of shear stress for long exposure times (from seconds to minutes) were reported by a few studies [55, 66]. Several studies have investigated the high shear stress regime with short exposure times (less than one second) [45, 53, 67, 68]. However, there are some discrepancies between the results of different studies which have been discussed by Paul et al. [53]. One important reason for such discrepancies is the different bloods used in these studies. The type of the blood (human/animal), sex, blood composition, and the duration of storage before experiments appear to affect the behavior of the blood exposed to shear [69]. To the best of the author's knowledge, so far no explicit correlation for blood damage for a wide range of shear stresses and exposure times has been reported.

For short exposure times (< 1 s), Giersiepen et al. [68] provided a comprehensive study. For a shear stress up to 255 Pa (applied by a Couette viscometer) and exposure

times up to 700 ms, Giersiepen et al. [68] suggested a model that was in agreement with their experimental data by a deviation below 12%:

$$HI\% = 3.62 \times 10^{-5} \tau^{2.416} t^{0.785} \tag{26}$$

where τ and t have the dimensions of Pa and seconds, respectively. This model is widely used for predicting hemolysis rates in heart valves and artificial hearts [70]. The exposure time to high shear in heart valves is less than one second.

Leverett et al. [66] constructed a graph that estimates the threshold shear stress for a given exposure time by summarizing the results of several studies. Based on experimental results obtained by a Couette viscometer, they suggested that at shear stress larger than 150 Pa and exposure times larger than 100 s hemolysis is mainly due to shear stress and not due to surface effects and cell-cell interactions. For exposure times up to 10 s, the range of the exposure time expected for the microchannel dialyzer, the threshold shear stress is estimated to be about 200 Pa. The device should be designed in a way that keeps the shear stress in the channels below this threshold.

3.4 SHEAR EFFECTS ON PLATELETS

High shear stress stimulates platelet aggregation in blood [43]. Platelet aggregation and interactions with plasma proteins leads to the entrapment of red cells and clot formation. Blood clots may obstruct blood vessels and result in such events as a stroke, myocardial infarction (heart attack), pulmonary embolism (blockage of the main artery of the lung), or the blockage of blood vessels serving other parts of the

body, such as the extremities of the arms or legs. Therefore, it is very important that the biomedical devices be designed such that extreme shear stresses are not applied on the blood resulting in platelet aggregation.

The platelet response to shear stress depends on two main factors: a) solid surface interactions and b) the exposure time and the magnitude of the shear stress [43]. Platelet reactions with the solid surface of damaged blood vessels are essential for hemostasis. However, in biomedical devices the platelet-solid surface interactions should be minimized or eliminated to avoid thrombosis [43]. Studies which investigate the shear-induced platelet aggregation must coat the viscometers with silicone or another nonthrombogenic material to minimize the surface interactions. Surface-induced platelet aggregation and clot formation is not the focus of this context. It is assumed that the coating applied on the surface of our device prevents protein absorption and subsequent platelet activation.

The process of platelet activation in high shear rate flows is different from in low shear environments and hemostasis in the human body upon bleeding [44]. At high shear stresses the Von Willebrand factor (vWF) blood protein binds to platelet membrane glycoprotein receptors which substantially contributes to the aggregation. A detailed description of the shear-induced aggregate formation is provided by Kroll et al. [43]. By changing the viscosity of blood but applying the same shear rate, Jesty et al. [71] showed that most likely shear stress directly induces aggregation not the shear rate.

Similar to RBCs, the extent of platelet activation under shear stress is related to both the magnitude and the duration of exposure [72]. The critical stress level for platelet activation at a given exposure time of 10 s is about 11 Pa [44]. This estimation was based on the data for which constant shear stress was applied on blood through a viscometer. Maxwell et al. [73] applied shear stress on the blood by passing it through micro-capillaries. Therefore, the applied shear stress on the platelets was position dependent and not constant. At a maximum shear rate of 5000 1/s occurring at capillary wall (corresponding to 17.4 Pa if we assume the viscosity is 0.00348 Pa.s), an exposure time of 15 s did not result in platelet aggregation. This implies that either the actual threshold shear stress in the capillaries is less than the threshold values obtained by applying a constant shear rate in viscometers, or the apparent blood viscosity in their experiment was less than 0.00348 Pa.s.

The results of several studies on platelet aggregation and hemolysis have been summarized in Figure 24. The change in the deformability of red blood cells was not the subject of those studies. Results were obtained under constant shear stress conditions on the bulk of the fluid. However, when blood passes through microchannels, cells in different cross sectional positions experience different shear stresses. Most of the blood cells experience a lower shear stress than the maximum shear stress on the walls. Therefore, it is expected that the limit for the maximum shear stress in microchannels be larger than the estimated threshold values in Figure 24.

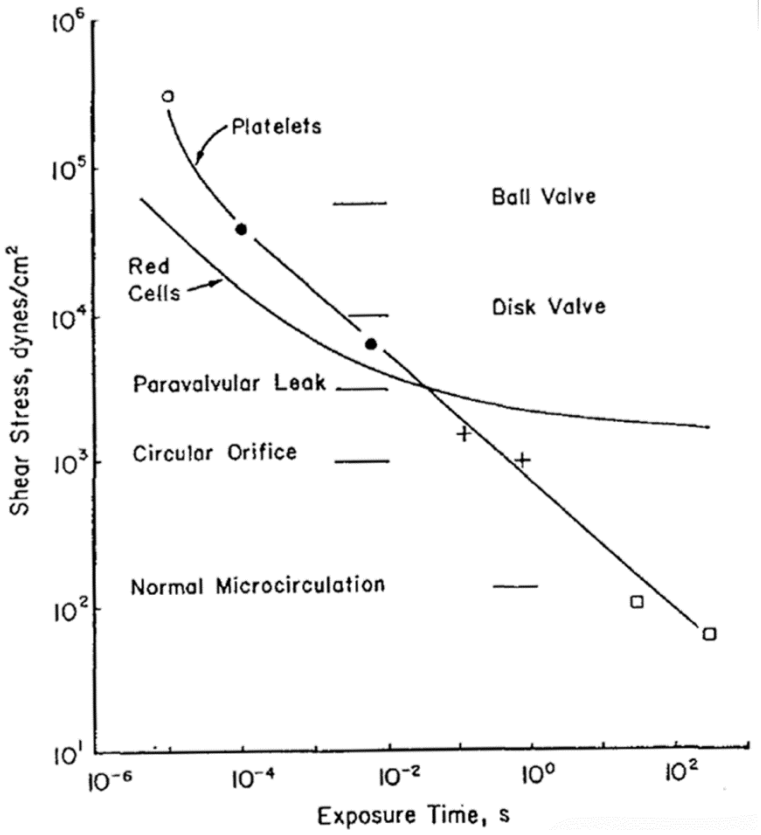

Figure 24: The locus of onset of hemolysis and onset of serotonin release from platelet upon aggregation. Estimates of stress levels in cardiac valves and the normal blood circulation system are also shown (dyne/cm^2 = 0.1 Pa), reproduced with permission from Hellums [44]

3.5 SHEAR EFFECTS ON WHITE BLOOD CELLS

White blood cells are the least studied blood components in terms of shear-induced blood damage. Some of the reasons for the lack of studies in this area might be that WBCs compose less than 1% of blood and naturally have a short 4-day life span. Similar to RBCs and platelets, they show the shear stress and time dependence effect. Measures of white cell damage have included white cell count, cell membrane integrity, cell adhesiveness, etc. [69]. Dewitz et al. [74] reported that at an exposure time of 2 min, at shear stresses above 15 Pa, the membrane permeability of leukocytes

started to change. For the same exposure time, at shear rates above 30 Pa, significant increase in the ruptured cell and significant reduction in the cell count were observed. Carter et al. [69] investigated the effect of shear for exposure times up to 125 ms. Unfortunately, the author could not find sufficient information on WBC shear-induced damage for exposure times in the order of a few seconds which is of interest for our application.

3.6 SHEAR STRESS IN RECTANGULAR MICROCHANNELS

The shear rate on the fluid passing through a channel is a function of the velocity profile. Shear stress depends on the shear rate and the viscosity of the fluid. For a fully-developed incompressible Newtonian flow in a rectangular duct it is possible to solve the Navier-Stokes equations with no-slip boundary conditions at the walls. Shah and London [75] provided the analytical solution for the velocity with the flow direction along the x axis for the rectangular duct described in Figure 25 as

$$u = -\frac{16c_1a^2}{\pi^3}\sum_{n=1,3,\ldots}^{\infty}\frac{1}{n^3}(-1)^{(n-1)/2}\left[1-\frac{\cosh(n\pi y/2a)}{\cosh(n\pi b/2a)}\right]\cos\left(\frac{n\pi z}{2a}\right) \qquad (27)$$

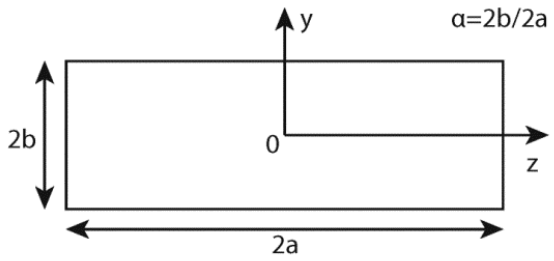

Figure 25: Aspect ratio of a rectangular microchannel

The following approximation for the velocity has been proposed which is in good agreement with experimental measurements (y and $z > 0$) [75]

$$\frac{u}{u_{mean}} = \left(\frac{m+1}{m}\right)\left(\frac{n+1}{n}\right)\left[1-\left(\frac{y}{b}\right)^{n}\right]\left[1-\left(\frac{z}{a}\right)^{m}\right] \tag{28}$$

where m and n are given by

$$m = 1.7 + 0.5(\alpha)^{-1.4} \tag{29}$$

$$n = \begin{cases} 2 & \text{for } \alpha \le 1/3 \\ 2 + 0.3(\alpha - 1/3) & \text{for } \alpha \ge 1/3 \end{cases} \tag{30}$$

The largest shear rates occur at the centerline of the walls, where the velocity gradient is at its maximum, as shown in Figure 26. The velocity gradient is always larger along the smaller dimension of the channel. Therefore, for the rectangular channel depicted in Figure 25 the maximum shear rate occurs at the centerline of the horizontal walls $(y = b, z = 0)$.

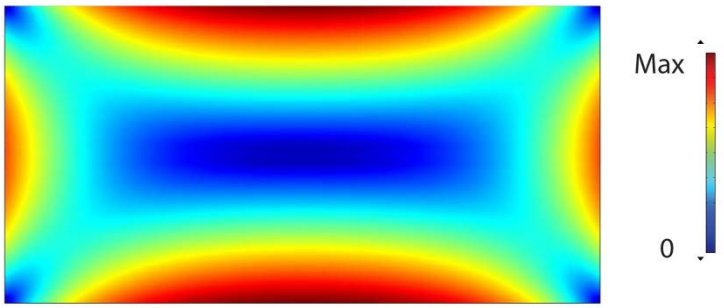

Figure 26: A sample shear rate profile in a $200\ \mu m \times 100\ \mu m$ channel

The stress tensor is composed of normal and shear stresses

$$\sigma_{ij} = -P\delta_{ij} + 2\mu e_{ij} \tag{31}$$

where P is thermodynamic pressure, δ_{ij} is the Kronecker Delta operator, and e_{ij} is the strain rate tensor given by

$$\begin{aligned} e_{ij} &= \frac{1}{2}\left(\frac{\partial u_i}{\partial x_j} + \frac{\partial u_j}{\partial x_i}\right) \\ &= \begin{pmatrix} \frac{\partial u}{\partial x} & \frac{1}{2}\left(\frac{\partial u}{\partial y} + \frac{\partial v}{\partial x}\right) & \frac{1}{2}\left(\frac{\partial u}{\partial z} + \frac{\partial w}{\partial x}\right) \\ \frac{1}{2}\left(\frac{\partial u}{\partial y} + \frac{\partial v}{\partial x}\right) & \frac{\partial v}{\partial y} & \frac{1}{2}\left(\frac{\partial v}{\partial z} + \frac{\partial w}{\partial y}\right) \\ \frac{1}{2}\left(\frac{\partial u}{\partial z} + \frac{\partial w}{\partial x}\right) & \frac{1}{2}\left(\frac{\partial v}{\partial z} + \frac{\partial w}{\partial y}\right) & \frac{\partial w}{\partial z} \end{pmatrix} \end{aligned} \tag{32}$$

To investigate the effects of shear stresses we have to isolate the shear components from the normal components in the strain rate tensor. Therefore, the diagonal components must be neglected. For a Newtonian fluid, the shear rate magnitude is given by [54]

$$\begin{aligned} \left|\dot{\gamma}\right| &= \sqrt{2(e_{ij}e_{ij} - e_{ii}^2)} \\ &= \sqrt{\left(\frac{\partial u}{\partial y} + \frac{\partial v}{\partial x}\right)^2 + \left(\frac{\partial u}{\partial z} + \frac{\partial w}{\partial x}\right)^2 + \left(\frac{\partial v}{\partial z} + \frac{\partial w}{\partial y}\right)^2} \end{aligned} \tag{33}$$

Multiplying the shear rate magnitude by the viscosity yields the magnitude of the shear stress

$$\left|\tau\right| = \mu\left|\dot{\gamma}\right| \tag{34}$$

For the rectangular channel it is possible to calculate the velocity derivatives using Eq. (28). Following are the only non-zero velocity derivatives terms for a channel geometry

$$\frac{\partial u}{\partial y} = -u_{mean}\left(\frac{m+1}{m}\right)\left(\frac{n+1}{n}\right)\left(\frac{n}{b}\right)\left(\frac{y}{b}\right)^{n-1}\left[1-\left(\frac{z}{a}\right)^{m}\right] \tag{35}$$

$$\frac{\partial u}{\partial z} = -u_{mean}\left(\frac{m+1}{m}\right)\left(\frac{n+1}{n}\right)\left(\frac{m}{a}\right)\left(\frac{z}{a}\right)^{m-1}\left[1-\left(\frac{y}{b}\right)^{n}\right] \tag{36}$$

At $z = 0$ and $y = b$ (the location of maximum shear rate)

$$\begin{aligned}\left.\frac{\partial u}{\partial y}\right|_{y=b,z=0} &= -u_{mean}\left(\frac{m+1}{m}\right)\left(\frac{n+1}{n}\right)\left(\frac{n}{b}\right)\\ \left.\frac{\partial u}{\partial z}\right|_{y=b,z=0} &= 0\end{aligned} \tag{37}$$

Therefore, from Eq (33) we get

$$\left|\dot{\gamma}_{\max}\right| = u_{mean}\left(\frac{m+1}{m}\right)\left(\frac{n+1}{b}\right) \tag{38}$$

For parallel plates $(\alpha = 0)$ the velocity profile is given by

$$\frac{u}{u_{mean}} = \frac{3}{2}\left[1-\left(\frac{y}{b}\right)^{2}\right] \tag{39}$$

The only non-zero velocity derivative term is

$$\frac{du}{dy} = -3u_{mean}\left(\frac{y}{b^{2}}\right) \tag{40}$$

At $y = b$, the location of maximum shear rate

$$\left.\frac{du}{dy}\right|_{y=b} = -3u_{mean}\left(\frac{1}{b}\right) \tag{41}$$

Therefore,

$$\left|\dot{\gamma}_{\max}\right| = 3u_{mean}\left(\frac{1}{b}\right) \tag{42}$$

$$\left|\tau_{\max}\right| = 3\mu u_{mean}\left(\frac{1}{b}\right) \tag{43}$$

3.6.1 ESTIMATION OF THE MAXIMUM SHEAR STRESS FOR BLOOD FLOW IN MICROCHANNELS

In order to use Eq. (43) to estimate the maximum shear stress, the blood viscosity needs to be known. Using Eq. (42) a preliminary estimation for the minimum shear rate ($u_{mean} = 1$ cm/s and $b = 50$ μm) yields a shear rate of 600 1/s. At such high shear rates, blood exhibits a Newtonian behavior and the viscosity is approximately 0.0038 Pa.s (see Figure 22). Due to the Fahraeus-Lindqvist effect sourced by the formation of the cell free layer, the apparent viscosity of blood in tubes with a diameter smaller than $500\,\mu$m is less than 0.00348 Pa.s. Herein, for simplicity we neglect variations in viscosity and assume that the viscosity is equal to 0.00348 Pa.s for all channel dimensions. By this assumption the magnitude of shear stress will be overestimated. In the next section, we will see that the influence of this overestimation on the final limitations for channel depth is unimportant.

Figure 27 presents the dependence of maximum shear stress on the aspect ratio and depth of the channels, obtained by Eq. (38). The magnitude of the maximum shear stress has a linear relationship with the mean velocity of the flow in the channels and an inverse relationship with the depth of the device. By increasing the depth the maximum shear stress asymptotically approaches zero.

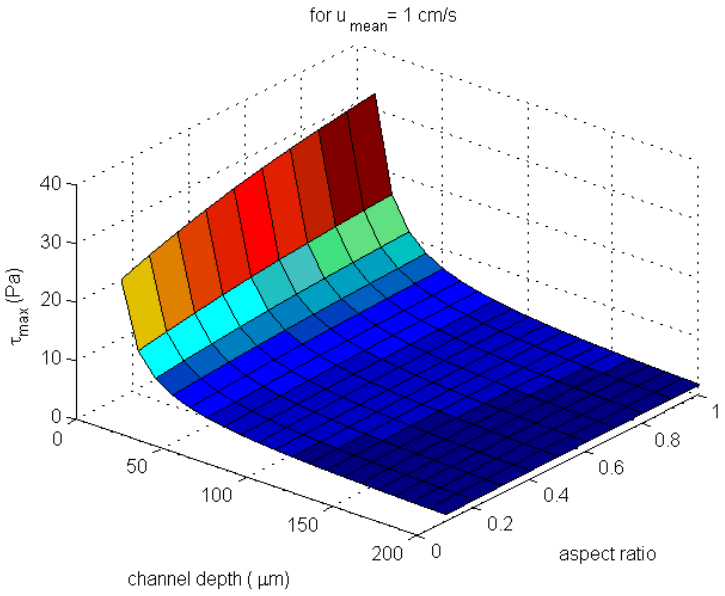

Figure 27: An illustration of the dependence of maximum shear stress on aspect ratio and depth of channels

At a fixed depth, *2b*, for the channels with any aspect ratio, the maximum shear stress varies between two limiting values, the maximum shear rate for a square channel of size *2b* and that of two parallel plates with a distance of *2b*, corresponding to the upper and the lower limits respectively. Figure 28 presents the maximum shear stress in the square channel and parallel plates geometry with depths varying between $5\ \mu m$ to $200\ \mu m$ for velocities of 1, 4, and 10 cm/s and 1 m/s. Note that no constraint has been

placed on the depth of the device and the flow velocity yet; the goal is to find the minimum allowable depth for various flow velocities.

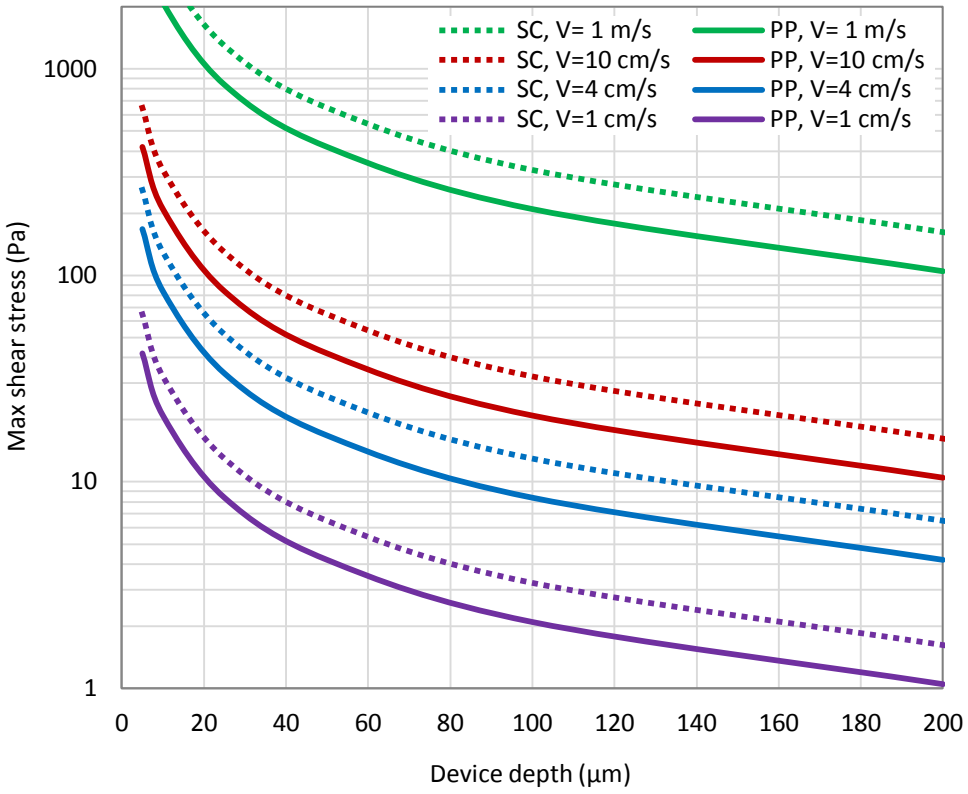

Figure 28: Maximum shear stress in the square channel (SC) and parallel plate (PP) geometry for a wide range of velocities and device depths. Dashed lines represent square channels and continuous lines represent parallel plates.

3.7 LIMITATION ON DEVICE DEPTH BASED ON CONSIDERATION OF BLOOD DAMAGE

The microchannel dialyzer is envisioned to be a portable device with channels smaller than 20 cm in length. The velocity of the blood in channels is expected to be in the order of few centimeters per second. Higher velocities will results in a large pressure

drop in the system and a huge amount of dialysate consumption per treatment. Therefore, the residence time of the blood inside the microchannels is expected to be of the order of seconds. For such an exposure time, hemolysis and platelet aggregation yield different limiting values on shear stress, according to Figure 24.

In conventional dialysis practice, platelet aggregation is prevented by injection of anticoagulants, most commonly heparins, into blood. Such an action will be taken for the microchannel dialyzer as well; therefore, we must focus solely on the hemolysis part of blood damage.

According to Leverett et al. [66] and Figure 24, for an exposure time of 1 to 10 s the threshold shear stress for hemolysis is estimated to be about 200 Pa. For a wide range of velocities and all channel aspect ratios, the minimum depths that will result in a maximum shear stress below 200 Pa, are summarized in Table 3. As having velocities larger than 10 cm/s is highly unlikely, we can assume that the use of any channel with any aspect ratio with a depth larger than $16\ \mu m$ will not result in hemolysis.

Table 3: Estimation of the minimum allowable channel depth for various flow velocities

Velocity	1 cm/s	4 cm/s	10 cm/s	1 m/s
Minimum allowed depth to avoid hemolysis	$< 5\ \mu m$	$7\ \mu m$	$16\ \mu m$	$166\ \mu m$
Minimum allowed depth to avoid platelet aggregation with no anticoagulants	$18\ \mu m$	$64\ \mu m$	$164\ \mu m$	$200\ \mu m <$

Knowing that white blood cells can be as large as $15\,\mu m$, the use of channels shallower than $15\,\mu m$ was not a smart choice since it could result in complications for white blood cells. Therefore, the minimum allowed depth to avoid hemolysis $(16\,\mu m)$ does not really put an extra limitation on the depth of device. Thus, assuming a constant blood viscosity of 0.0038 Pa.s for all channel dimensions and the subsequent overestimation in the magnitude of shear stress applied on the blood in our calculation is justified.

In the absence of anticoagulant agents, the minimum allowed depth will significantly increase. According to Hellums [44] and Figure 24, for the exposure time of 10 s the threshold shear stress for platelet activation and aggregation is estimated to be about 20 Pa. The minimum depths that result in a maximum shear stress below 20 Pa are also summarized in Table 3. These values are only provided to show that without anticoagulant agents, the minimum allowed depth would be significantly larger.

4 SELECTION OF GEOMETRICAL PARAMETERS FOR MICROCHANNELS

Both the structural parameters of the microchannels and flow velocity affect mass transfer characteristics, pressure drop through each layer, shear stress on blood, bubble movability, and the flow uniformity among channels. In this chapter, a general guideline that describes the effect of channel structural parameters and flow velocity in each channel on mass transfer, pressure drop, and bubble movability is provided. In the end, potential objective and constraint functions for a design optimization have been suggested. Only an optimization approach is able to determine the optimum values of the design parameters in such a complicated nonlinear design problem with several constraints.

4.1 MASS TARANSFER

The influence of channel structural parameters including depth, width and length on the mass transfer performance of the dialyzer is described in this section. A simple model of the dialyzer consisting of two channels and a membrane in between has been developed in COMSOL Multiphysics 4.3. The model is not expected to replicate the performance of an actual microchannel dialyzer; however, it can show the effect of geometrical parameters on the mass transfer characteristics of a microchannel dialyzer. In other words, we expect the observed *trends* in the studies to hold for an actual blood dialyzer.

4.1.1 MASS TRANSFER MODEL

The mass transfer unit of a multilayer microchannel dialyzer consists of an array of microchannels for blood (carrying toxins e.g. urea), an array of microchannels for dialysate, and a membrane in between (see Figure 2). Each pair of microchannels operates in a manner similar to the other parallel channel pairs; therefore, only one pair needs to be simulated. Two and three dimensional models of the microchannel pair with a membrane in between have been developed in COMSOL Multiphysics 4.3. Since the three-dimensional model had a high computational cost, it was only used to study the effect of channel width (the third dimension of the channels) on mass transfer. Steady state Navier-Stokes equations coupled with the incompressible continuity equation and mass conservation equations have been solved within the laminar flow and transport of diluted species modules of COMSOL.

A diluted solution of urea in water was used as the carrier fluid in the side representing the blood side in an actual dialyzer. Water was used as the carrier fluid in the dialysate side. As the concentration of the solute (urea) is small (1 gr/L at its maximum) and has no impact on the flow field, a dilute solution assumption is appropriate. The viscosity and density of water at 20°C were used in the simulations. All the studies were done at a 1:1 urea solution to dialysate flow rate ratio; both channels had the same inlet velocity.

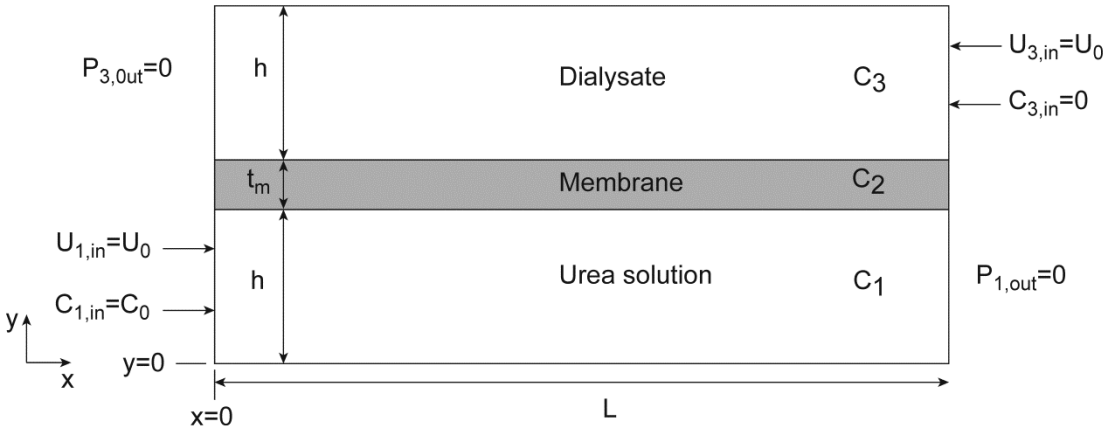

Figure 29: Two-dimensional computational domain, in a three-dimensional domain the width of the channel would be normal to the page

The two-dimensional computational domain is presented in Figure 29. The Navier-Stokes equations, Eq. (44) in its steady state form, and the continuity equation, Eq. (45) in its incompressible form, were solved in the channel domains to calculate the velocity fields. The boundary conditions are provided in Table 4.

$$\rho\left(\frac{\partial \vec{U}}{\partial t} + \vec{U}\cdot\nabla\vec{U}\right) = -\nabla P + \mu\nabla^2\vec{U} \tag{44}$$

$$\frac{\partial \rho}{\partial t} + \nabla\cdot\left(\rho\vec{U}\right) = 0 \tag{45}$$

COMSOL uses the GMRES (Generalized Minimal Residual) method to solve the linearized equations. The discretization of pressure, concentration, and velocity components was of the first order (linear), which is the default setting for the laminar flow interface in COMSOL.

Table 4: Boundary conditions for Navier-Stokes equations

Inlets	$\vec{U}_{1,in} = -U_0\,\hat{n}$ and $\vec{U}_{3,in} = -U_0\,\hat{n}$ where $\hat{n}$ is the boundary normal unit vector pointing out of plane
Outlets	$P_{1,out} = P_{3,out} = 0$ and on both outlets $\mu(\nabla\vec{U} + (\nabla\vec{U})^T)\cdot\hat{n} = 0$ (zero pressure with no viscous stress)
Walls	$\vec{U}\big\|_{x=0} = \vec{U}\big\|_{x=h} = \vec{U}\big\|_{x=h+t_m} = \vec{U}\big\|_{x=2h+t_m} = 0$

In actual dialyzers, convective transport or ultrafiltration is necessary for water removal from the blood and also important in solute removal. Ultrafiltration occurs due to the hydrostatic pressure difference between the two sides of the membrane. Herein, no hydrostatic pressure difference between the sides of the membrane is imposed. We defined the diffusion as the only mass transport mechanism in the membrane and neglected the convective mass transfer across the membrane.

The mass conservation equation, Eq. (46), in its steady state form, should be solved for all the three sub-domains.

$$\rho\left(\frac{\partial C}{\partial t} + \vec{U}\cdot\nabla C\right) = D\nabla^2 C \tag{46}$$

The diffusivity of urea in water of 1.38×10^{-9} m^2/s and effective diffusivity of urea in water in the membrane of 5.5×10^{-10} m^2/s [5, 76] are used as diffusion coefficients in the channel domains and the membrane domain, respectively. In the membrane

domain, where velocity is equal to zero, Eq. (46) will be simplified to a diffusion equation

$$\nabla^2 C = 0 \tag{47}$$

The mass transfer flux at the membrane surface is given by

$$\vec{N}_y = -D\frac{K}{t_m}\Delta C \tag{48}$$

where D is the diffusion coefficient of solute in the membrane, K is the partition coefficient, t_m is the membrane thickness, and ΔC is the difference between the concentration of the solute right outside the membrane surface [77]. The partition coefficient depends on the permeability of the solute in the membrane. K=1 indicates continuity of concentration at the walls while K<1 indicates a discontinuity, as shown in Figure 30. The partition coefficient describes the interface concentrations in the liquid and membrane phases as

$$K = \frac{C_{2,x}}{C_{1,x}} = \frac{C_{2,x+t_m}}{C_{3,x+t_m}} \tag{49}$$

Herein we assumed K=1 for simplicity. Therefore, the boundary condition on each side of the membrane becomes equal to the concentration of the fluid at the same side (Dirichlet boundary condition).

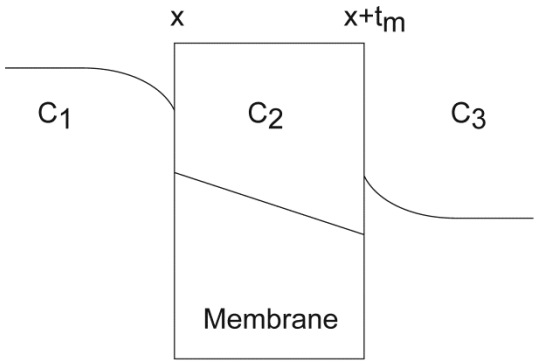

Figure 30: Concentration profile around a membrane (K<1)

Table 5: Boundary conditions for mass transfer equations

Inlets	$C_{1,in}$=1 gr/L=16.65 mol/m^3 $C_{3,in} = 0$
Outlets	$-\hat{n}.D\nabla C = 0$ (no diffusion normal to the outlets)
Walls	$C_1\big\|_{y=h} = C_2\big\|_{y=h}$ $C_2\big\|_{y=h+t_m} = C_3\big\|_{y=h+t_m}$ $-\hat{n}.\overrightarrow{N}\big\|_{y=0 \text{ and } y=2h+t_m} = 0$

4.1.2 INFLUENCE OF CHANNEL LENGTH ON MASS TRANSFER

Diffusion length, the characteristic length scale for diffusion in one dimension is defined as

$$L_D = \sqrt{2Dt} \tag{50}$$

The relevant time to define the diffusion length is the residence time of the species in the reactor $(t = L/U)$. If the diffusion length is much longer than the system size,

diffusion dominates the mass transfer and velocity is not important. Changing the length of the reactor may result in linear concentration variations. On the other hand, when the diffusion length is much shorter than the system size convection dominates the mass transfer. Changing the length of the reactor may result in an exponential concentration variation.

The dimensionless Peclet number (Pe) which compares the diffusion length to the system length is defined as

$$\mathrm{Pe} = \frac{LU}{D} = 2\left(\frac{L}{L_D}\right)^2 \tag{51}$$

For Pe << 1 diffusion dominates the mass transfer and for Pe >> 1 convection dominates the mass transfer. The diffusion coefficient of urea in water and the membrane are 1.38×10^{-9} and 5.5×10^{-10} m^2/s, respectively [5, 76]. Knowing the desired size of the device is less than 20 cm and the velocity required to generate enough pressure drop to keep the bubbles moving is in the order of several centimeters per second, our Pe number will be much larger than 1 and convection will dominate the mass transfer.

The 2D mass transfer model has been used to compare the fractional removal of urea at the end of channels with 1, 2.5, 5, 10, and 20 cm lengths. The depth of the channels was $50\,\mu\mathrm{m}$ and the velocity of the urea solution and dialysate was 2 cm/s. The fractional removal of urea that can be calculated from Eq. (52) has been chosen as the

performance metric. Figure 31 presents the dependence of urea fractional removal on the channel length.

$$FR = 1 - \frac{C_{1,out}}{C_{1,in}} \tag{52}$$

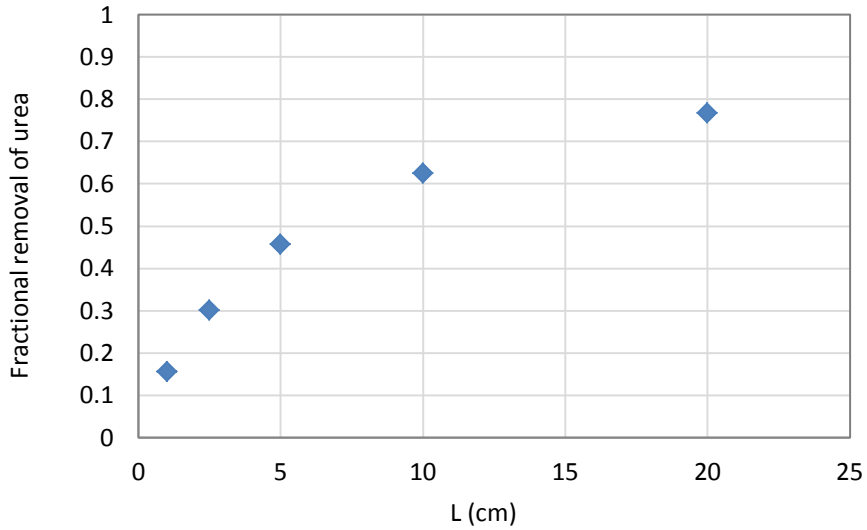

Figure 31: Urea fractional removal in channels with different lengths

Due to the counter flow arrangement, the concentration difference along the membrane remains constant which results in a linear urea concentration profile along the length, as shown in Figure 32.

If the concentration of urea at the dialysate side were to be relatively constant along the length and to remain small everywhere, e.g. because of a very high dialysate flow rate compared to the urea solution, the profile of urea concentration along the length would become exponential: a larger gradient at the beginning of the channel and a smaller gradient near the end of the channel.

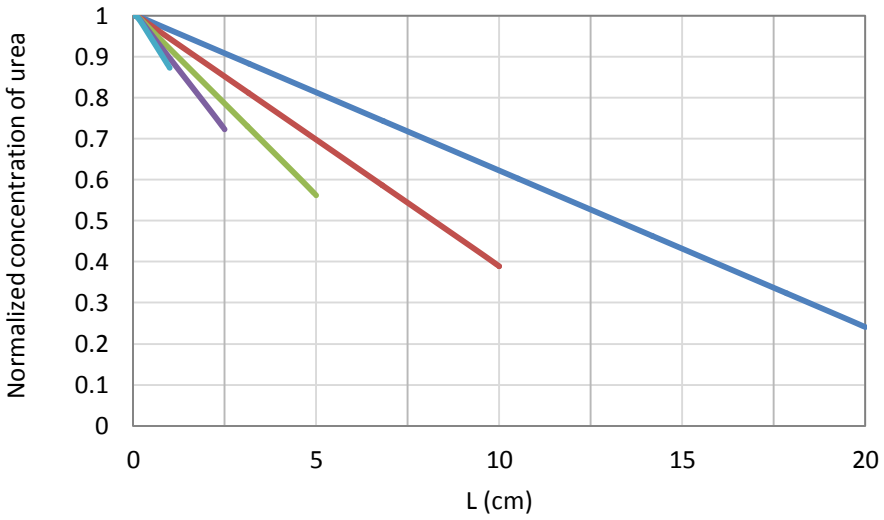

Figure 32: Normalized concentration of urea along the centerlines of channels with different lengths

4.1.3 INFLUENCE OF CHANNEL DEPTH ON MASS TRANSFER

For the one-dimensional diffusion, the diffusion coefficient is the mean squared particle displacement (x) divided by two times the time of the movement [76].

$$D = \frac{x^2}{2t} \tag{53}$$

In our problem, the length scale for the particles traveling from the bottom of the channels to the membrane at the top is equal to the depth of the channel (h). Therefore, the diffusion time scale will be

$$t_D = \frac{h^2}{2D} \tag{54}$$

Reducing the depth of the channel by half reduces the required time for the diffusion of toxins from the bottom of the channels to the top by a factor of 4. However, the mass transfer in the dialyzer is not diffusion-dominated as explained in the last section. Therefore, a fourfold diffusion time scale does not result in a fourfold fractional removal. The diffusion coefficients and the depth of the channels are still important though since the convection occurs only in the direction of the flow and the mass transfer at the membrane occurs due to molecular diffusion. Moreover, the diffusion coefficient for the transport of urea in the membrane is smaller than that of urea in the channel, and changing the depth of the channel does not affect the diffusion time scale in the membrane.

The urea fractional removal for four channel depths of $25\ \mu m$, $50\ \mu m$, $100\ \mu m$, and $200\ \mu m$ have been compared for the 2D dialyzer model. The length of the channels was 5 cm and the velocity of both fluids at the different sides of the membrane was 2 cm/s. Figure 33 illustrates that the fractional removal has almost an inverse relationship with the depth of the channels to the power of 0.8. Reducing the channel depth to half increases the fractional removal by 74%.

It is important to note that decreasing the depth reduces the cross sectional area and subsequently the flow rate. The mass transfer rate has a linear relationship with the volumetric flow rate given by

$$\dot{m} = Q(C_{in} - C_{out}) = whUC_{in}FR \tag{55}$$

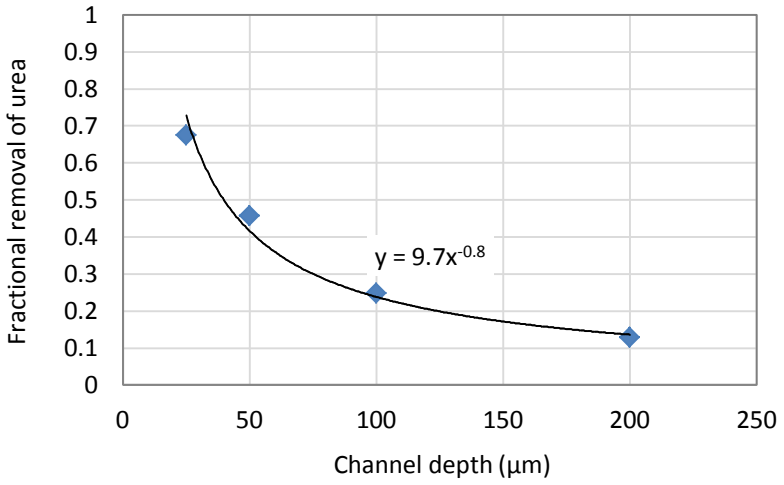

Figure 33: Urea fractional removal at varying channel depths

As all the variables except for channel depth and fractional removal are constant, $hFR = \dot{m} / wUC_{in}$ presents the trend of the mass transfer rate, as shown in Figure 34. Although reducing the channel depth increases the fractional removal, it decreases the mass transfer rate of a single channel because of the reduction in flow rate.

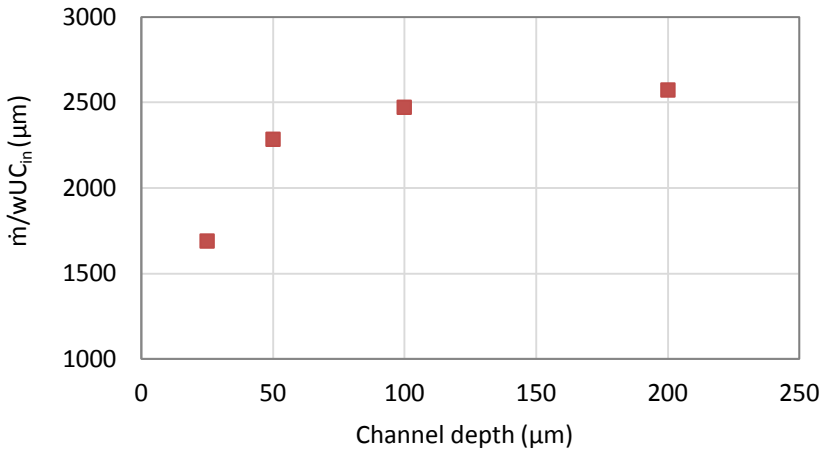

Figure 34: Effect of channel depth on mass transfer rate

Overall, in terms of mass transfer rate, one channel with a depth of *h* may be better than a single channel with a depth of *h/2*, but two channels with a depth of *h/2* will *definitely* be better than both. Because adding more channels to the device causes additional cost, selection of the channel depth requires an optimization approach.

4.1.4 INFLUENCE OF CHANNEL WIDTH ON MASS TRANSFER

Keeping the inlet flow velocity constant, reducing the width of the channels increases the velocity magnitudes at the centerline but reduces the velocity magnitudes around the side walls. To understand the effect of channel width on mass transfer, a 2D model of the dialyzer with $100\ \mu m$ deep channels is compared with a 3D model of the dialyzer with a channel width of $200\ \mu m$. The inlet velocity of both liquids was 2 cm/s and the length of the channels was only 2 cm to reduce the high computational cost of the 3D model. The models resulted in fractional removals of 90.3% and 86.6% for the 2D parallel plate model and 3D channel, respectively. The higher flow velocity near the membrane for parallel plates increases the convective mass transfer but since our problem is convection-dominated, the difference in the fractional removal is relatively small. We can think of the parallel plate model as a channel with an infinite width. The results suggest that changing the distance of the side walls from infinity to a dimension comparable to the depth of channels slightly reduces the fractional removal. Reducing the width also reduces the channel cross sectional area and the mass transfer rate of a single channel. We can add more channels to the design to compensate for the reduced width but more channels means more channel spacers and

more membrane waste. In brief, the wider the channels, the higher the mass transfer rate.

4.1.5 INFLUENCE OF VELOCITY ON MASS TRANSFER

Increasing the velocity reduces the residence time of solutes in the dialyzer which lowers the fractional removal. On the other hand, the mass transfer rate has a linear relationship with the volumetric flow rate and subsequently the velocity.

$$\dot{m} = Q(C_{in} - C_{out}) = AUC_{in}FR \tag{56}$$

Figure 35 presents the effect of velocity on urea fractional removal and mass transfer for a $50\ \mu m$ deep and 5 cm long 2D parallel plate geometry. Although the fractional removal decreases at higher velocities the overall influence of increasing velocity on mass transfer is positive.

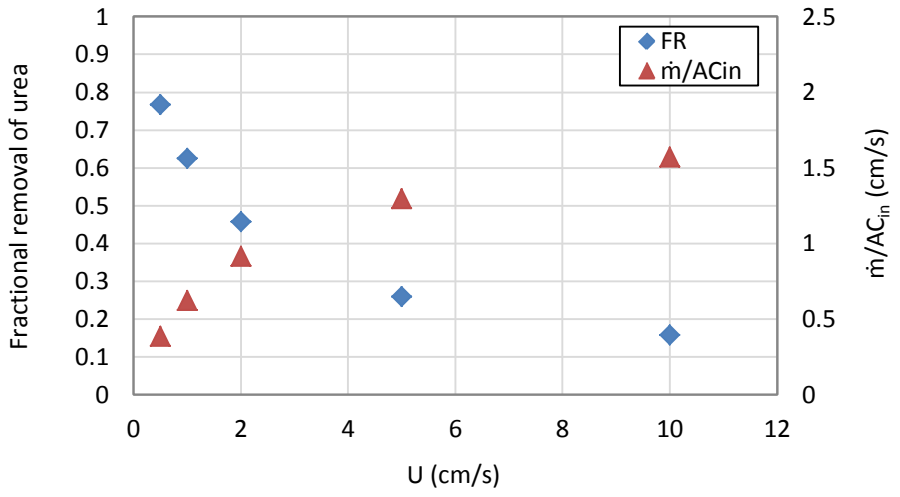

Figure 35: Effect of velocity on fractional removal and mass transfer rate

4.2 PRESSURE DROP

The pressure drop in each layer of the microchannel dialyzer is the sum of the pressure drop through the manifolds and the microchannels. The microchannels are parallel to each other and have equal pressure drop. The flow paths in the manifold areas are much shorter than the channels; therefore, the pressure drop through the device is almost equal to the pressure drop of one channel. The allowable pressure for pumping the fluids through the device has to be smaller than the maximum sealing pressure of the device considering a safety factor. The maximum sealing pressure is expected to be 2–3 psi [78]. Herein, we investigate the effect of the structural parameters of a single channel on pressure drop.

Using the analytical solution for velocity in rectangular ducts, the Fanning friction factor for the fully developed laminar flow in a rectangular channel is approximated by [75]

$$f\,\mathrm{Re} = 24\left[1 - 1.3553\alpha + 1.9467\alpha^2 - 1.7012\alpha^3 + 0.9564\alpha^4 - 0.2537\alpha^5\right] \quad (57)$$

The pressure drop in the fully developed region of a channel can be calculated by

$$\Delta P = 2 f \rho \frac{L}{d_h} U^2 \quad (58)$$

Substituting the friction factor from Eq. (57) in Eq. (58) yields

$$\frac{\Delta P}{L} = 48\mu \frac{U}{d_h^{\,2}}\left[1 - 1.3553\alpha + 1.9467\alpha^2 - 1.7012\alpha^3 + 0.9564\alpha^4 - 0.2537\alpha^5\right] \quad (59)$$

For aspect ratios of 0 (parallel plates) and 1 (square channel) pressure drop per unit length can be simplified to

$$\frac{\Delta P}{L} = \begin{cases} 48\mu\frac{U}{d_h^{\,2}} = 12\mu\frac{U}{h^2} & \text{parallel plates } (\alpha=0) \\ 28.46\mu\frac{U}{d_h^{\,2}} & \text{square channel } (\alpha=1) \end{cases} \tag{60}$$

Figure 36 presents the pressure drop per unit length predicted by Eq. (59) for a velocity of 1 cm/s while the channel depth was changed and the channel width was kept constant $(0 < \alpha \leq 1)$. At channel depths smaller than $100\ \mu\text{m}$, pressure drop has an almost inverse relationship with the square of the depth. Eq. (60) also verifies that at small depths, where the hydraulic diameter approaches the depth magnitude, this relationship holds.

At a constant channel width and velocity, reducing the depth of the channels by half increases the pressure drop per unit length of a channel by at least a factor of two (up to a factor of four). We can roughly estimate that the pressure drop in the whole device increases by at least a factor of two as well since the channels form the majority of the device and the flow paths in the manifolds with microposts are short.

Because of the mass transfer application envisioned for the device and the fact that channel spacers waste the membrane area, the channels are larger in width than depth. Looking at Figure 36 derived from Eq. (59), it is clear that at channel depths smaller than $100\ \mu\text{m}$ the pressure drop does not vary much with width variations. Therefore, it is possible to assume that at small channel depths pressure drop is independent of

channel width. According to Eq. (58) the length of the channels has a linear relationship with the pressure drop. Increasing the length of the channel increases the pressure drops.

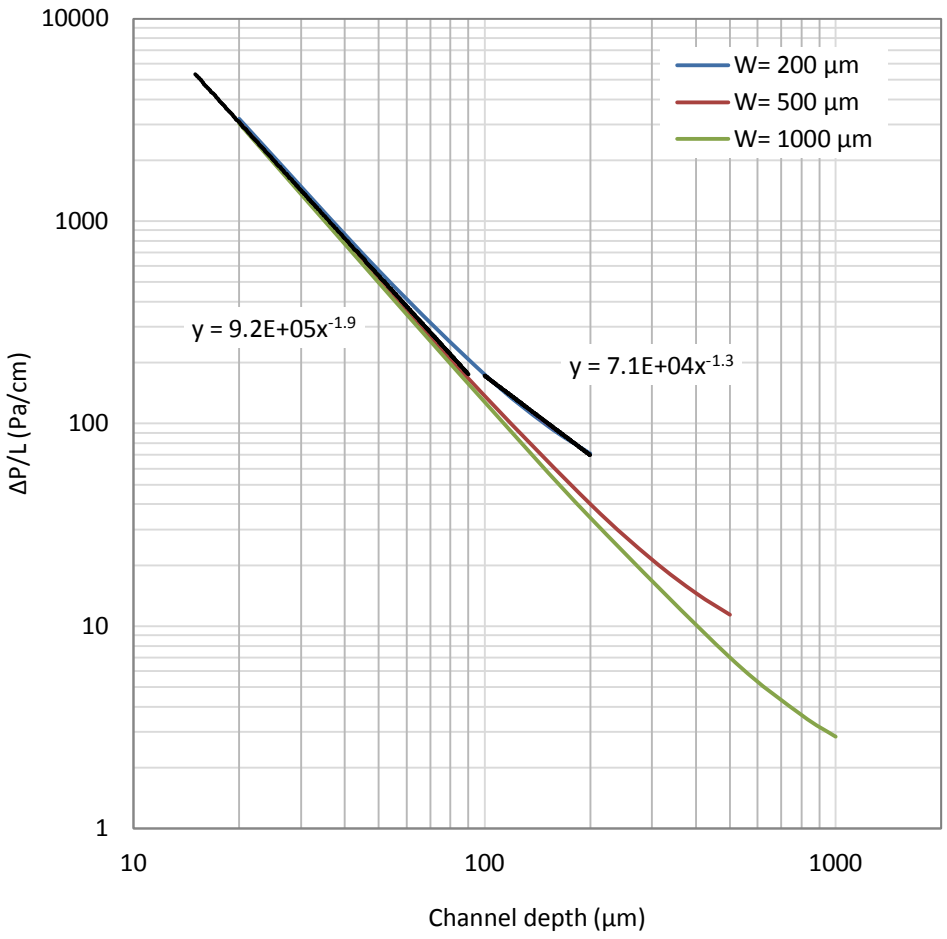

Figure 36: Influence of channel depth on the pressure drop per unit length of channel for a velocity of 1 cm/s

4.3 BUBBLE MOVABILITY

Dimensions of the microchannels affect the bubble movability. According to Eq. (21) the magnitude of the capillary and pinning forces applied on the bubble depends on the channel cross section and the length of the contact line.

$$F_{cap} + F_{pin} \propto 2wh\left(\frac{1}{w} + \frac{1}{h}\right) + s \tag{61}$$

The length of the contact lines can be roughly estimated by the perimeter of the channel

$$s \approx 2\left(w + h\right) \tag{62}$$

By simplifying Eq. (61) we get

$$F_{cap} + F_{pin} \propto \left(w + h\right) \tag{63}$$

Keeping the channel width and length constant, reducing the depth to half, reduces the magnitude of resistive forces by less than half. Halving the depth increases the pressure drop per unit length by a factor of at least two and up to four. Therefore, we can roughly estimate that the pressure drop along a bubble with a certain length (but half volume) will also increase at least by a factor of two. On the other hand, the cross sectional area of the bubble will be reduced by half. The force on the bubble applied by the pressure field (pressure drop multiplied by cross sectional area) becomes larger and up to twice as large as that of the device with a full depth. Earlier we showed that the resistive forces are reduced by less than half. Therefore the overall influence of

reducing the depth of the device on bubble movability is positive. If we look at equal bubble volumes, reducing the depth has an even more positive effect since the elongated bubble will experience more pressure drop along its length.

Keeping the channel depth and length constant, changing the width has an effect similar to changing depth on the resistive forces on stagnant bubbles. However, as discussed previously, at small channel depths pressure drop is independent of channel width. Therefore, reducing the width of the channels has a positive effect on bubble movability.

Keeping the channel depth and width constant, changing the length of the channels does not have an effect on the capillary and pinning forces applied on the bubbles. However, it changes the flow rate in channels with stagnant bubbles. Assuming a stagnant bubble applies a certain flow resistance proportional to its own size, the flow rate in a longer channel remains larger facing the same exact bubble. Therefore, the pressure drop along the bubble will be larger and the bubble will have a higher chance of movability.

4.4 SUMMARY

Table 6 summarizes the effect of increasing the channel structural parameters and flow velocity on some important factors for design. For studying the effect of each parameter other parameters were held constant. Plus and minus signs indicate positive and negative effects, respectively.

Table 6: Effect of channel structural parameters and velocity on the studied design elements

Increasing	Width (w)	Depth (h)	Length (L)	Velocity (U)
Fractional removal	Increase	Decrease	Increase	Decrease
Mass transfer rate (single channel)	Increase (+)	Increase (complicated)	Increase (+)	Increase (+)
Pressure drop (single channel)	Not significant Slight decrease (+)	Decrease (+)	Increase (-)	Increase (-)
Bubble movability	Decrease (-)	Decrease (-)	Not significant Slight increase (+)	Increase (+)

4.5 MAXIMUM CHANNEL WIDTH TO PREVENT MEMBRANE SAGGING

The channel spacings and the microposts in the manifolds are responsible for supporting the membrane and prevent membrane sagging. The worst scenario for sagging can occur during ultrafiltration when the hydrostatic pressure of dialysis fluid is decreased to assist water removal. The membrane is sandwiched between the laminas. The pressure on the blood side of the microchannel dialyzer can push the membrane into the dialysate side and causes variation in depth on both sides. We require the depth variation to be less than $5\ \mu m$. To insure that we must calculate the maximum channel width that prevents the membrane deflections from exceeding $5\ \mu m$. The membrane is an elasto viscoplastic material and correlating its maximum

deflection to the width of the channel is a complicated subject. Herein, we assume a linear elastic behavior for the membrane and model it as a plate with pinned ends. Our estimation is preliminary and could be described as an absolute upper limit for the channel width. Figure 37 shows a schematic of the membrane deflection due to the pressure.

The maximum pressure difference across the membrane is equal to the sum of the ultrafiltration pressure and the pressure drop in the device. The pressure drop in the device has to be smaller than the sealing pressure, expected to be around 2 psi [78]. To proceed we assume a constant pressure difference of 2 psi across the membrane.

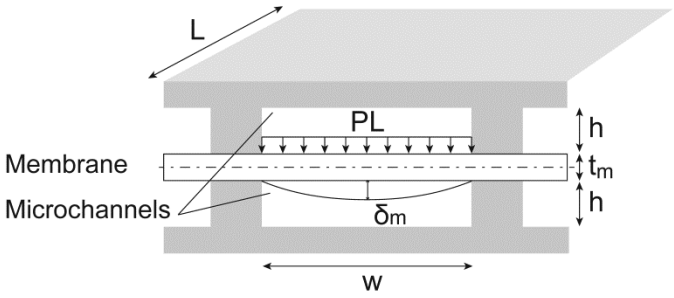

Figure 37: Membrane deflection due to the ultrafiltration pressure

The maximum deflection is given by

$$\delta_{\max} = \frac{5PLw^3}{384EI} \tag{64}$$

where E is the tensile module (also referred to as Young's module) and I is the moment of inertia along centerline [79]. The moment of inertia for a plate with a thickness of t_m and length of L is $Lt_m^{\,3}/12$; therefore Eq. (64) will be simplified to

$$\delta_{\max} = \frac{5Pw^3}{32Et_m{}^3} \tag{65}$$

The membrane has a lower tensile module in its rolling direction than the other, 90 MPa and 426 MPa, respectively [78]. These properties are related to the wet gamma-irradiated membrane (data provided by Padma Chandran, personal communication); the device will become irradiated with gamma rays in the coating process. Herein, we use the lower value of the tensile module. For P equal to 2 psi (13788 Pa) and t_m equal to $20\ \mu m$, channel widths smaller than $284\ \mu m$ result in maximum deflections less than $5\ \mu m$.

4.6 DECISION MAKING AND OPTIMIZATION

Several aspects should be considered in the design of a microchannel dialyzer: cost, toxin removal, pressure, bubble movability in channels, dialysate fluid consumption, and the desired duration of treatment. Each of these factors can be considered as a constraint or an objective for an optimization that reveals the optimum values for the design parameters. These parameters include channel width, channel depth, channel length, flow velocity in each channel, number of channels per layer, and number of layers.

Defining the objective and constraint functions is an important part of any optimization problem and depends on the priorities of the project. Herein, we assume that the objective is minimizing the cost of the device. The other functions are considered to be the constraints of the optimization, meaning that their values should

be larger or smaller than a certain value. Note that there are some limitations on channel width and depth as described in sections 4.5 and 3.7.

As presented in Table 6, a larger channel width is advantageous for mass transfer and pressure drop while disadvantageous for bubble movability. Most importantly, a larger channel width reduces the cost of the device by lowering the number of channel spacings that waste the membrane area. It is expected that the maximum allowed channel width be the optimum channel width in spite of its adverse effect on bubble movability.

4.6.1 OBJECTIVE

If the microchannel dialyzer is to be a commercial success it must work properly and it must be inexpensive. The most important factor affecting the cost of the device is membrane usage which is proportional to the area of each layer and the number of layers. The material and fabrication cost of the layers also depends on the area of each layer. The area of each layer itself is a function of channel width, channel spacing, number of channels, channel length, and manifold shape (a function of channel width, channel spacing, and number of channels). The objective of the optimization problem can be minimizing the cost function.

4.6.2 CONSTRAINTS

The dialyzer device should be able to remove a certain amount of toxins (e.g. *x* grams of urea) from patient's blood during each session of treatment. The removal capability

is a function of the duration of the treatment, mass transfer rate of each layer, and the number of layers. The mass transfer rate of each layer is itself a function of the mass transfer rate of a channel and the number of channels on each layer. The mass transfer rate of a single channel is also a function of channel width, channel depth, channel length, and velocity.

The maximum fluid pressure in each layer is related to the pressure drop on each layer and should be less than the sealing pressure. Pressure drop can be estimated by the pressure drop of a single channel. The effect of structural parameters and velocity on pressure drop is clear, as shown in Table 6.

Bubble movability in channels depends on the channel width and depth, flow velocity, number of the bubbles in the same channels, and most importantly the length of the bubble. Surface quality (contact angle hysteresis) also plays an important role on bubble movability but it is established by the PEO coating which is not a design parameter. As presented in section 2.6, statistical studies can result in a criterion between channel width and depth, and flow velocity which if satisfied, no channel becomes blocked. That criterion puts a constraint on the optimization problem assuring no complete blockage in channels.

Dialysate fluid consumption is one of the factors that might be a constraint for the design. The microchannel dialyzer is aimed for home operation and storage of a large volume of dialysate at patients' homes is not convenient. Therefore, designers may want to put a constraint on the dialysate consumption for each treatment. The dialysate

consumption is a function of flow rate and duration of treatment. The flow rate itself is a function of the number of layers, number of channels per layer, channel width, channel depth, and the flow velocity in each layer.

The microchannel dialyzer is envisioned to be a long-duration everyday treatment for patients during sleeping hours. The designers may want to limit the duration of the treatment to be less than for example 8 hours.

4.6.3 METHODS

Genetic algorithm (GA) and particle swarm optimization (PSO) are both suitable metaheuristic methods for solving this optimization problem. Metaheuristic algorithms iteratively try to improve a group of candidate solutions with regard to a given objective function. Such algorithms only use function values in their search process and do not require the problem functions to be differentiable or continuous [80]. Moreover, they tend to converge to the global minimum point for the cost function, in contrast to a local minimum point as with gradient-based methods.

GA and PSO methods are valid for unconstrained optimization problems. The constrained problem can be modified to an unconstrained problem by using the penalty method. A term consisting of a penalty parameter multiplied by the violation of the constraint (if any) is added to the objective function. The solution of the new unconstrained problem ideally converges to the original constrained one.

For our mixed-variable problem (integer and continuous design variables), a discrete or a hybrid version of the algorithms should be used. The continuous variables including channel depth, channel length, channel width, and velocity are varied in small allowable ranges; thus, fine discretization of them inside their allowable range is feasible and does not disturb the problem. The integer variables including number of layers and number of channels per layer are already discrete. Binary encoding can be used to generate a string representing the design of the system. The optimum design point will result in minimum cost while satisfying the other constraints of the problem. It is important to remember that the design optimization cannot be pursued until all the constraints of the problem become defined as functions of the design parameters in the next stages of the project.

5 EXPERIMENTAL FACILITY AND METHODS

This chapter describes the experimental facility including the imaging system for bubble retention studies in microchannels of a single lamina along with the fabrication and assembly of the lamina. The key considerations of this setup were to provide visual accessibility for double magnification imaging while keep the microchannel test section sealed.

5.1 TEST SECTION

An exploded view of the test section is presented in Figure 38. The lamina featuring the microchannels and hemodialysis membrane (Gambro AN69 ST) are pressed together by two thick polycarbonate plates. A compressible gasket with a thickness of 0.5 inch (Bisco foam, Rogers Corp. stock no. HT-800) uniformly transfers the pressure of the aluminum plate to the top polycarbonate plate. The inlet and outlet ports are embedded in the top polycarbonate plate. Using flat bottom fittings (Idex stock nos. P-200 and P-201), PEEK tubing (Idex stock no. 1538) has been connected to the inlet and outlet ports of the device to carry fluid. The drawings of the machined parts are provided in Appendix D.

Originally, one infusion and one withdrawal syringe pump were used for fluid circulation. The use of only an infusion pump resulted in leakage from the test section. The use of only a withdrawal pump resulted in a negative gauge pressure (up to -1 psig) in the outlet and degasification of the dissolved gases in the system. The

suction might deplete the thin liquid films around the bubbles in the outlet manifold and impede bubble movement as well.

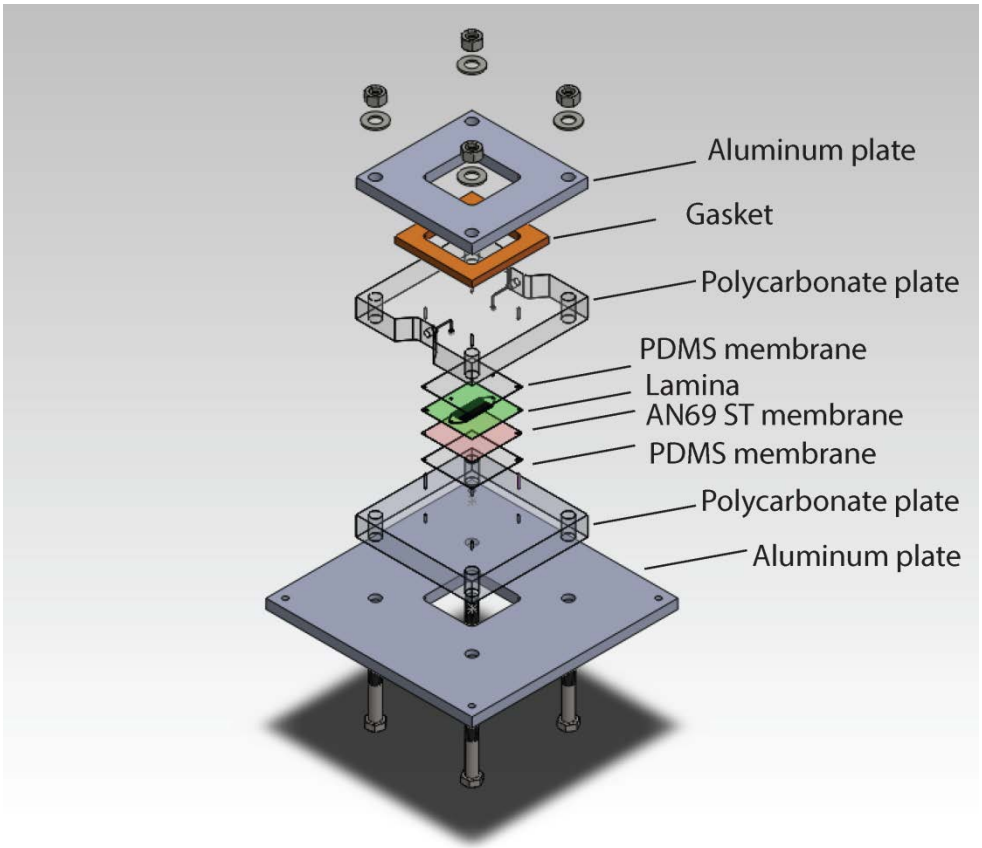

Figure 38: Exploded view of the test section

Two Polydimethylsiloxane (PDMS) membranes with thicknesses of 355 μm (SSP stock no M823-0.014) were added on the top and bottom of the test section. The details are presented in Figure 39 and Figure 40. The use of this novel method enabled the progress of experiments without leakage. Moreover, it allowed for the removal of the suction pump from the test loop which could have adverse effects on bubble movability.

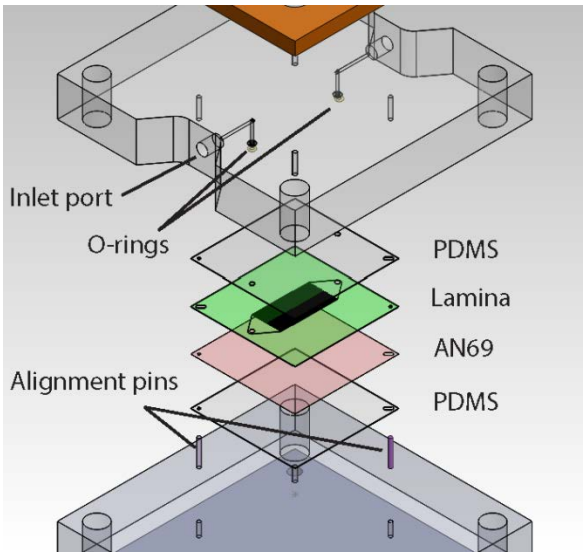

Figure 39: A close-up view of the exploded test section

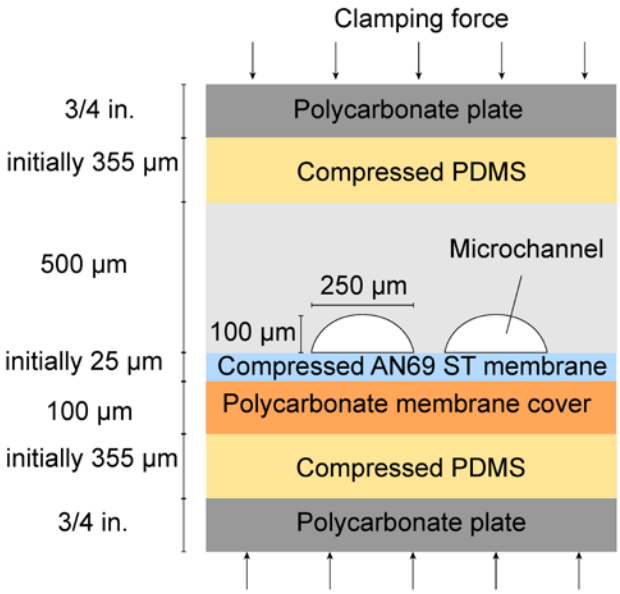

Figure 40: A close-up view of the compressed test section

The bottom PDMS membrane supports the 20-µm hemodialysis membrane with its 100-µm polycarbonate cover on the bottom. The top PDMS membrane fills the micro gaps between the thick polycarbonate plate and the lamina and prevents the occasional

leakage from the inlet O-ring. Adding a PDMS membrane to the back of the AN69 ST membrane disables the latter's mass transfer capability; however, for studying bubble behavior in an array of microchannels the membrane is only needed to prevent leakage. The membrane is crucial for compression sealing to fill the micro-scale surface irregularities of the polycarbonate laminas.

The infusion syringe was mounted on a syringe pump (Harvard Apparatus PHD 2000 Programmable stock no. 71-2019). Bubbles were injected into the device through the perpendicular arm of a T-junction (Idex stock no. P-714) upstream of the inlet as shown in Figure 41. The arm was featured with a check-valve (Idex stock no. CV-3330) that did not allow the main flow stream to enter the bubble injection line. The T-junction was connected to a 1-ml syringe filled with air. The cracking pressure of the check valve is 1 psi.

A 10-ml syringe connected to a check valve (Idex stock no. CV-3315) with a cracking pressure of 3 psi was used for water injection to wash the remaining bubbles in the test section if necessary. A miniature gauge pressure sensor (Omega stock no. PX26-005GV) with a range of 0 to 5 psi and accuracy of ± 0.05 psi was occasionally used to measure the inlet pressure upstream of the bubble injector. The pressure signal was captured by an NI-USB 6211 DAQ system and recorded by a Labview program.

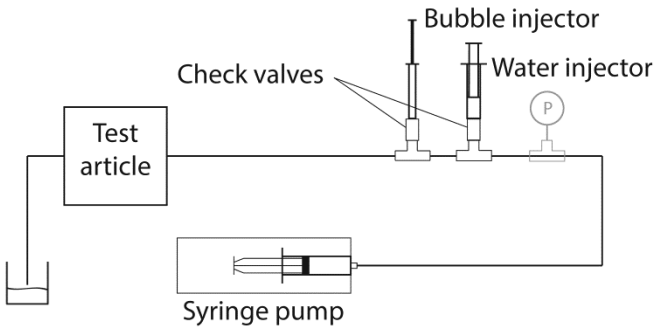

Figure 41: Experimental setup

5.2 LAMINA FABRICATION

Two methods have been used for lamina fabrication. Method A uses chemically etched masters fabricated by a commercial entity and method B uses masters manufactured in-house.

5.2.1 METHOD A

Part drawings for the stainless steel positive masters made in SolidWorks were sent to the Great Lakes Company where they were manufactured using acid etching techniques. There is always a large deviation between the size of the features in the drawings and the masters delivered by the company (up to 150 μm depending on the size and the shape of the features). The stainless steel masters were placed into a Camco vacuum furnace and kept at $1050^{o}C$ for one hour. This process cleans residues from the masters and also flattens them. The stainless steel master is embossed into a polyethylenimine (PEI) plate with a thickness of 1 mm using the Jenoptik Nanoimprinter (vacuum hot embosser) equipment at Microproducts

Breakthrough Institute (MBI). The negative PEI masters were registered and trimmed with the ESI 5330 UV Laser uVia Drill. Placing the masters in a sonic bath for 5 minutes removes the machining residues and cleans the pieces.

The fabrication steps are summarized in Figure 42. The PEI master is embossed onto 500-µm polycarbonate plates. Each PEI master can be used many times. Registration, trimming, and cutting the alignment holes in the polycarbonate lamina are done with the laser drill as well. The inlet and outlet holes which are smaller than the alignment holes are cut with a press drill tool. Figure 43 presents the microscope images of the channels and microposts fabricated by method A.

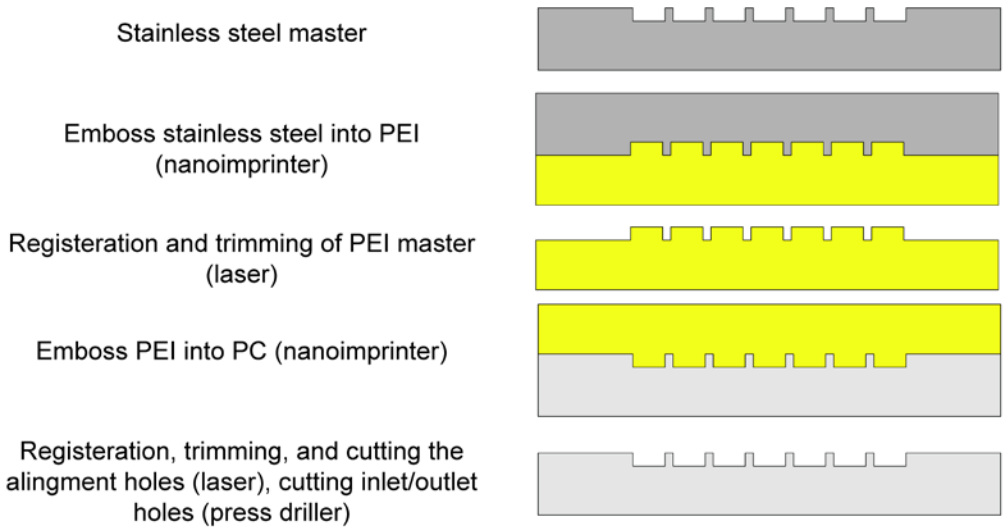

Figure 42: Lamina fabrication steps, method A

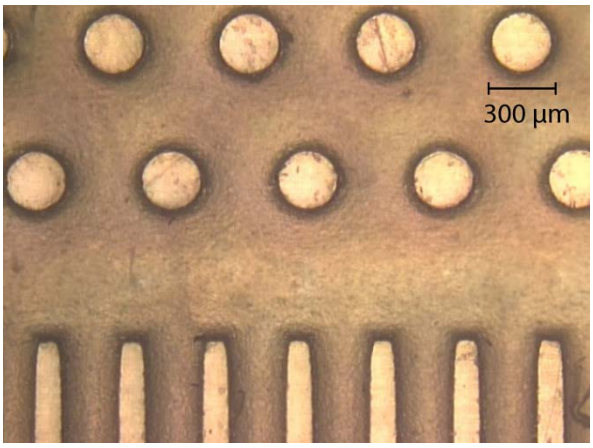

Figure 43: Image of microchannels and microposts fabricated by method A

5.2.2 METHOD B

Part drawings for the geometries were made in SolidWorks and used to generate G-codes. The G-codes were fed to the ESI 5330 UV Laser uVia Drill at MBI to fabricate the positive PEI masters. The remainder of the procedure is similar to method A. The fabrication steps are summarized in Figure 44. Pieces made using this method are not able to be sealed completely due to small variation in the height of the sealing boss. However, the fabrication procedure is fast and completely in-house. The bottom of the microchannels is also completely flat. Figure 45 presents the microscope images of the microposts fabricated by method B. Each post's center is slightly shallower than its edge since the drilling of a post on the PEI master starts from the edge and ends at the center.

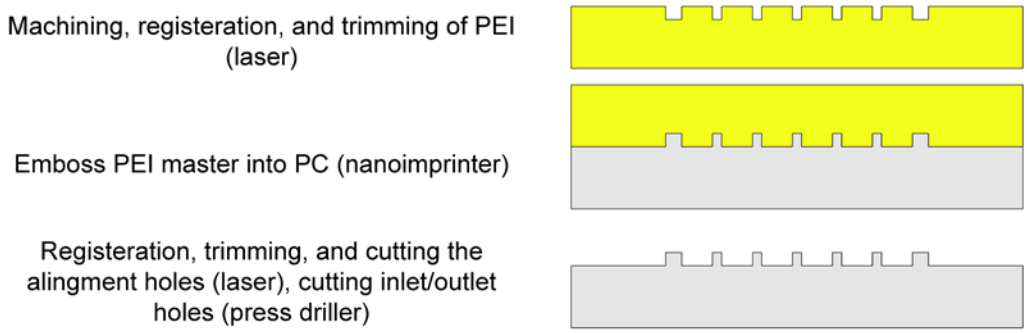

Figure 44: Lamina fabrication steps, method B

a b

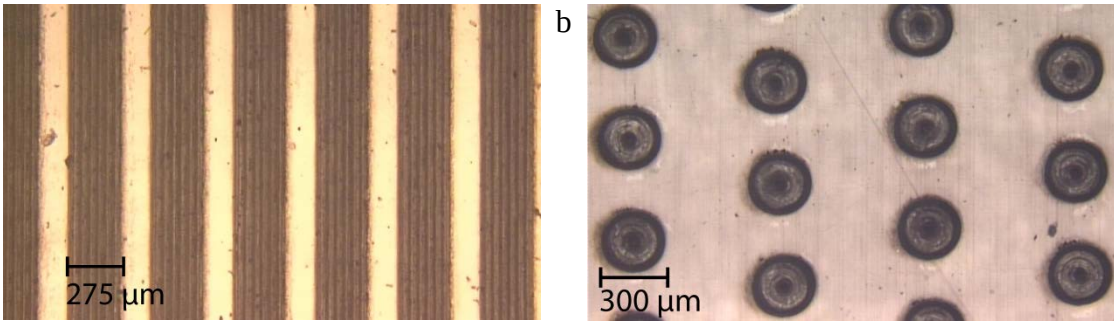

Figure 45: Images of a) microchannels (in the darker color) and b) microposts fabricated by method B

5.3 MEMBRANE PREPARATION

Handling of the AN69 ST hemodialysis membrane is a delicate matter because the 20-µm thick membrane is extremely fragile. The AN69 ST sheets are sandwiched between two 100-µm polycarbonate sheets for ease of handling. The sheet is cut into square pieces and registration holes are then drilled using the ESI 5330 UV Laser uVia Drill. The top polycarbonate cover of the membrane is removed before being placed in the assembly. The membrane roll and the small pieces should be kept refrigerated before use.

5.4 IMAGING SYSTEM

A shadowgraphy technique is used for capturing images of the test section. The imaging system is shown in Figure 46. The light source (60 Watt globe incandescent bulb) is positioned above the test section and the opening underneath the test section allows for light transmission. A right-angle prism is placed beneath the test section which deviates the light path by 90 degrees and changes its orientation from vertical to horizontal. When the input light is incident on one of the prism's legs, it undergoes total internal reflection at the glass/air boundary of the hypotenuse and exits via the other prism leg. Compared to a mirror, the prism is more efficient and easier to align.

A beam splitter plate (Edmund optics stock no. 62-882) is positioned at a 45 degree angle of incidence in front of the prism to enable dual magnification imaging. About fifty percent of the visible light striking the beam splitter is transmitted and the rest is reflected. A LaVision system consisting of two sCMOS cameras operated by Davis 8.1.4 is used for image acquisition. The maximum frame rate of each sCMOS camera is 50 frames per second; the sensor resolution is 2560×2160 pixels; and the minimum exposure time is $15\ \mu m$.

The first camera is equipped with a micro-Nikkor 60 mm f/2.8D lens with 1X magnification. The working distance that yields the required field-of-view (FOV) of $45\ mm \times 38\ mm$ is about 15 cm. The minimum resolvable feature in an imaging system overlaps with at least 2 pixels. Therefore, the spatial resolution of this system is $35\ \mu m$.

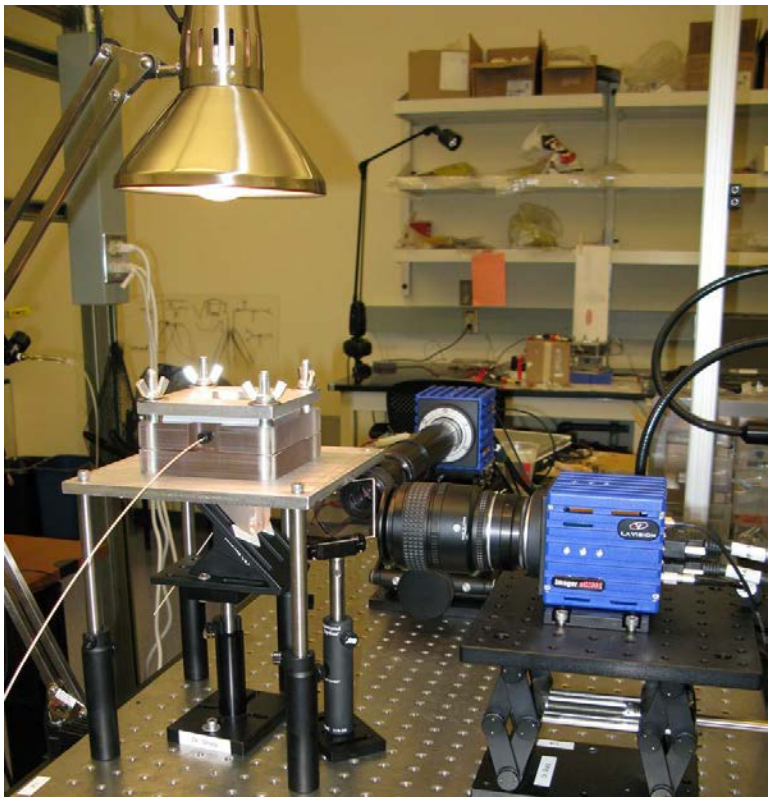

Figure 46: Imaging system

The second camera equipped with a Navitar 12X Zoom lens (+ 0.5X lens attachment) is able to look at much smaller FOVs. The 12X zoom lens has variable magnification ranging from 1.16X to 14X with a working distance of 86 mm. This working distance was too small for a dual imaging system and did not allow for the use of the beam splitter between the prism and camera lenses. Adding a 0.5X lens attachment increased the working distance to 165 mm but reduced the magnification range to 0.58X–7X. Table 7 presents the detailed specifications of the Navitar lens and the FOV of the imaging system. The resolvable limits are given by the lens manufacturer. Matching pixel size is defined as the resolvable limit multiplied by the magnification divided by 2 since the resolvable limit needs to overlap with at least 2 of the sensor

pixels. As the camera pixel size of $6.5\ \mu m$ is smaller than the matching pixel size, the system is lens limited and the imaging spatial resolution is equal to the lens resolvable limit [81].

Table 7: Specifications of the Navitar lens and the FOV of the imaging system

Working distance (mm)	System magnification		Resolvable limit (μm)		Matching pixel size (μm)		Depth of field (mm)		FOV (mm^2)	
165	Low Mag.	High Mag.	Low Mag.	High Mag.	Low Mag.	High Mag.	Low Mag.	High Mag.	Low Mag.	High Mag.
	0.58	7	18.52	3.33	22.89	10.74	6.17	0.19	9.7x8.2	2.4x2.0

5.5 IMAGE PROCESSING

The methodology involved in image processing varies depending on lighting conditions and the clarity of the acquired images. The desired result of image processing is a binary image separating the bubbles from the background. All background data including the microchannel device, shadows due to non-uniform illumination or impurities in the layers above the channels should be removed. The challenge is in maintaining the original shape of the bubbles while removing the background.

The bubbles flowing through the channels differ in shape and the produced shadow from those present in the header sections. Due to this difference, the bubbles in each section should be processed separately.

For each set of experiments where either the camera, microchannel device, or light source have been moved or altered an image of the device filled with water without any bubbles should be captured. This image will be used as a background image and each frame of the recorded video will be subtracted from it. The subtraction would result in an image containing clear representations of the bubbles with some left over pixels and shades resulting from differences between the two images. Appropriate thresholding followed by morphological operations can result in a binary image accurately representing the bubbles.

There are a number of uncertainties in the imaging process that can affect the final bubble size and velocity calculations. The quantifiable uncertainties in this system are image distortion due to the optics, uncertainty in the scale of the reference length, the uncertainty of the measurement of that reference length, and the thresholding uncertainty. The combination of the first three types of uncertainties is referred to as calibration uncertainty. The total uncertainty is the root sum square (RSS) of calibration and thresholding uncertainties as they are independent of each other.

5.5.1 CALIBRATION UNCERTAINTY

The measured length between any two points in the images is the product of the distance between the two points in pixels (Δx) and the pixel correspondence. The pixel correspondence is defined by dividing the length of the reference geometry (span) by the number of pixels in the image of the reference geometry.

$$L(\mu m) = \Delta x(px)\frac{span(\mu m)}{pixel\ count(px)} \tag{66}$$

Since the errors in the three parameters are independent of each other, the Kline & McClintock method [34] can be used to estimate the calibration uncertainty

$$\varepsilon_L = \sqrt{\left(\frac{\partial L}{\partial \Delta x}\varepsilon_{\Delta x}\right)^2 + \left(\frac{\partial L}{\partial\ span}\varepsilon_{span}\right)^2 + \left(\frac{\partial L}{\partial\ pixel\ count}\varepsilon_{pixel\ count}\right)^2} \tag{67}$$

Equation (67) can be simplified to

$$\frac{\varepsilon_L}{L} = \sqrt{\left(\frac{\varepsilon_{\Delta x}}{\Delta x}\right)^2 + \left(\frac{\varepsilon_{span}}{span}\right)^2 + \left(\frac{\varepsilon_{pixel\ count}}{pixel\ count}\right)^2} \tag{68}$$

The uncertainty in the distance ($\varepsilon_{\Delta x}$) is due to lens distortion. To quantify the uncertainty due to optics, a distortion error gradient was calculated for each lens by first creating a distortion map for each lens. To create the distortion map a fixed frequency grid distortion target was placed in front of the camera at a distance at which the microchannel device would be placed during experiments.

The 25 mm $\times$ 25 mm grid consists of 0.0625 mm diameter dots with 0.125 mm dot spacing (Edmund optics stock no NT58-509), as shown in Figure 47a. The acquired images were analyzed to locate the dot centroids by intensity weighing the region of each dot, as shown in Figure 47b. The resolved grid was then compared to an ideal grid generated in Matlab with vertical and horizontal dots spaced at a distance equal to the average of the horizontal and vertical spacing of the centroids in the resolved image. The distortion map was generated by aligning the ideal grid at the center of the

resolved grid and computing the centroid displacements, as shown in Figure 47c. The optical distortion rate $(\varepsilon_{\Delta x} / \Delta x)$ was calculated by measuring the difference in the distance between each two consecutive dots in the acquired image and in the ideal gird, and dividing it by the distance in the ideal grid. Figure 47d displays the distortion rate due to optics calculated for the micro-Nikkor lens. It is evident that the majority of the area of the image has a relatively low distortion error. The displayed quantity is unitless (pixel/pixel).

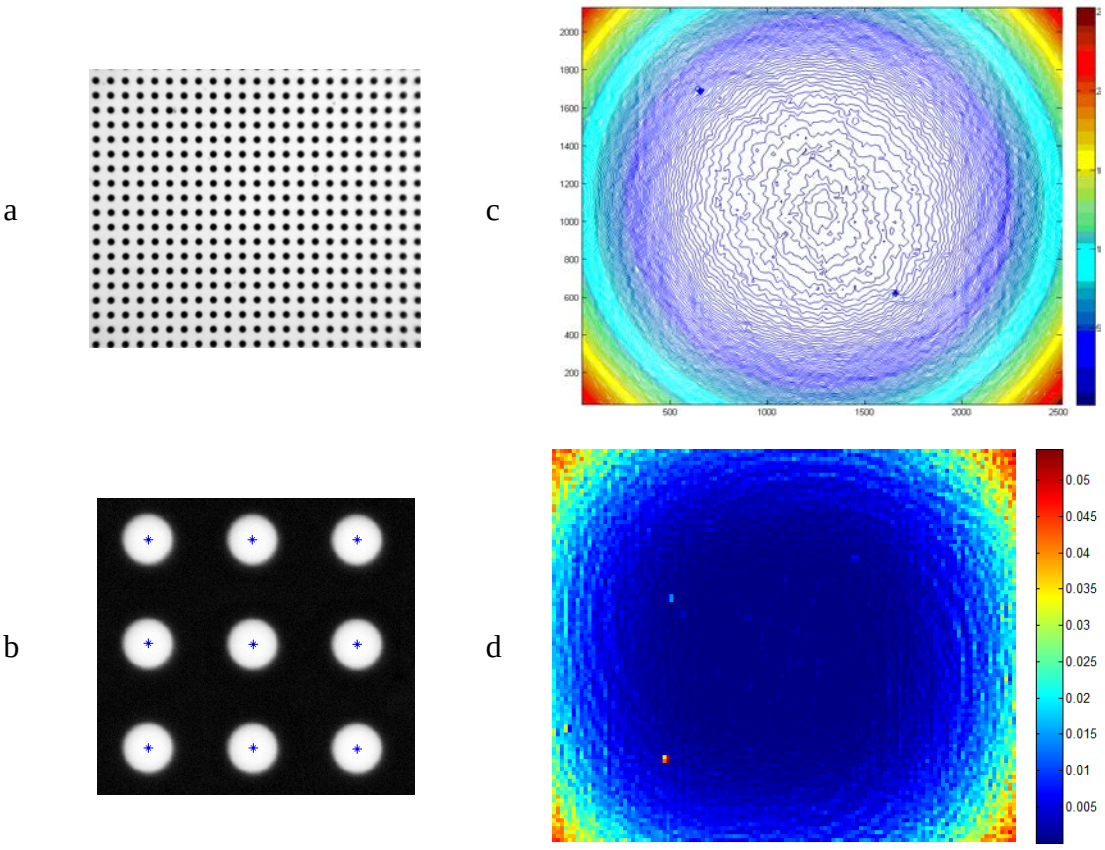

Figure 47: Uncertainty across the image for the micro-Nikkor lens a) an image of the resolved grid, b) the centroid locations of a small section of the grid, c) contour of lens distortion across the image, and d) image distortion rate due to optical aberration

The maximum uncertainty value was 0.0543 occurring at the bottom right corner of the image. The root mean square (RMS) of the distortion rate across the image was calculated to be 0.0172, much lower than the maximum value. The same procedure was repeated for the Navitar lens which yielded a maximum distortion rate of 0.0178 and an RMS of 0.0057. The RMS and the maximum uncertainty values are very small and can be neglected in the total uncertainty calculation.

The uncertainty in the span is the error in the size of a reference geometry which is measured by an optical microscope and it is equal to 1 μm. The references are the width of the channels or the diameter of the microposts. The uncertainty divided by the size of the reference geometries (> 200 μm) is negligible. The uncertainty in the pixel count is a function of human error and resolution. The human error is believed to be much smaller than the resolution, and the resolution (1 px) is taken as the total uncertainty in the pixel count. This uncertainty divided by the size of the span in pixels is negligible as well.

5.5.2 THRESHOLDING UNCERTAINTY

In general, thresholding uncertainty includes errors due to defocus and unparalleled lightening which both can cause blurry edges in the bubbles in images. In our experiment, defocus error is completely negligible since the depth of field of the imaging system is larger than the depth of the device. At large angles of incident light, the reflected rays can cause the size of the bubble to be underestimated as shown in

Figure 48. It is important to note that refracted and reflected light beams have lower energy than the unaffected light beams.

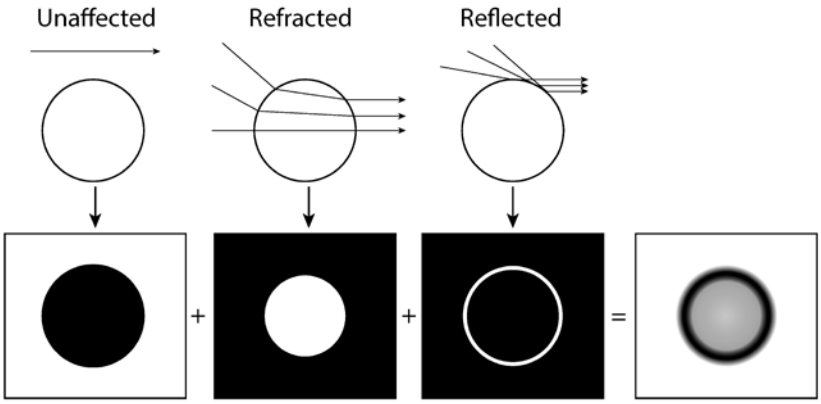

Figure 48: The final image of a spherical bubble as the outcome of the various paths light takes when interacting with the bubble.

The sizing error is related to the largest angle of incidence of the light into the object. Bongiovanni et al. [4] suggested that the sizing error of a spherical bubble to be $(1-\cos\beta/2)$ multiplied by the bubble diameter, where β is the maximum angle of incident of the backlight. The angle of incident can be calculated as illustrated in Figure 49 (in our system L1= 15 cm, L2= 4 cm, and L3= 2 cm). For flattened bubbles between two parallel plates it is possible to assume that the maximum diameter of curvature is equal to the distance between the plates. Using the same approach the maximum sizing error for those bubbles becomes $(1-\cos\beta/2)$ multiplied by the depth of the device. In our system the maximum angle of incident is 21° therefore the thresholding uncertainty becomes $(1-\cos 10.5^{\circ})\times 100\ \mu m = 1.67\ \mu m$. This amount is

negligible considering it would be much smaller than the size of one pixel in our resulting images.

The thresholding uncertainty in image processing will only be due to the thresholding resolution (1 px) if we choose the right thresholding value that results in the best match between the actual and binarized images.

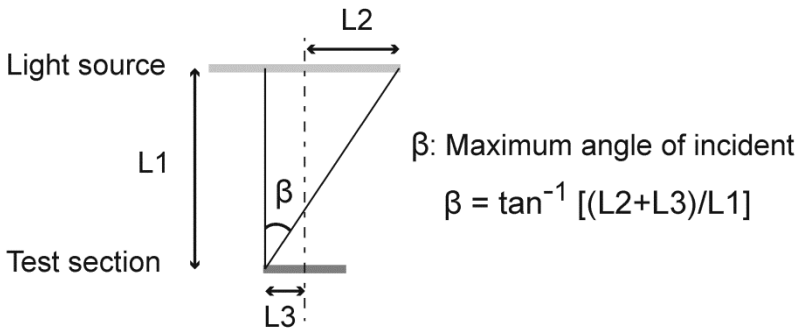

Figure 49: Maximum angle of incident light

6 MANIFOLD DESIGN: FLOW UNIFORMITY

Flow uniformity among individual channels within a microchannel array can be a significant factor affecting the performance of laminated structured micro-devices. In our biomedical application, it is important to have low dead volume and residence time in the manifolds. In this chapter, numerical modeling is used to quantitatively investigate the impact of the geometry of the right triangular manifold and the dimensions of microchannels on desired uniformity and pressure drop. A methodical approach is introduced to identify a design that balances low manifold volume and maintenance of flow uniformity. It has been shown that including a short vertical spacing at the corner of manifolds is critical to achieving a high level of flow uniformity. Careful analysis and physical interpretation of trends herein enables a more intuitive approach to array design.

The studies in this chapter, also presented in Ref. [82], are quite general and applicable to a wide range of devices. The focus is on the overall manifold geometry; no micropost arrays are embedded inside the manifolds. Investigating the level of flow uniformity in right triangular manifolds featuring micropost arrays can be a topic for future studies.

6.1 INTRODUCTION

Uniform flow distribution is desirable in numerous engineering devices such as fuel cells, chemical reactors, piping systems, solar thermal collectors, plate-type heat exchangers, heat sinks for cooling electronic devices, and more [83]. Over the past

few decades, advances in microfabrication techniques have made microchannel reactor and heat exchanger studies a popular area of research, and the issue of flow uniformity remains one of the challenges in this area. Microfluidic devices have several advantages over traditional larger-scale systems. In general, the most important feature of microfluidic systems is the large surface-to-volume ratio that results in high heat and mass transfer efficiencies. The small dimensions of microchannel devices also provide safe operation with highly reactive or hazardous products. Moreover, the rapid response time inherent in small-scale devices is advantageous for process control, in particular for heterogeneous reactions which are mostly limited to the catalyst-coated walls [84].

Flow distribution among individual microchannels plays an important role in the performance of microchannel reactors and heat exchangers. In microchannel heat sinks used for cooling electronic chips, a nonuniform flow distribution can cause nonuniform heat transfer conditions and produce undesirable transverse temperature gradients which lead to lower performance [85].

In chemical reactors, the residence time of the reactants varies with flow rate; thus, the conversion may vary among individual microchannels as a function of flow nonuniformity. Using a stochastic model, Anderson [86] showed that an increase in the magnitude of the velocity variance in a microreactor with a large number of parallel microchannels results in a decrease in the fractional removal. In addition, he

found that the influence of a nonuniform velocity distribution can be critical for microreactor performance in the vicinity of the design point.

In temperature-controlled microreactors, similar to heat sinks, nonuniform flow distribution causes nonuniform heat transfer coefficients which result in temperature variation among microchannels. The reaction rate coefficient in individual channels may vary considerably with temperature leading to unequal conversion among channels and consequent degradation in performance of the microreactors. In contrast, in catalytic chemical reactors, the influence of flow nonuniformity on the overall reactant conversion is relatively small, but the influences of variations in channel dimensions due to fabrication tolerances and the amount of catalyst coating on the channel walls are more pronounced [87].

Flow distribution among microchannels strongly depends on the geometrical structure of a given micro device. A laminated-sheet structure is one of the fundamental architectural approaches in which multiple microstructured laminas that feature parallel microchannels and inlet and outlet manifold structures are stacked together to form a unit [88] as shown in Figure 50a.

In such structures, the inlet stream is divided into substreams between laminas, and each substream is distributed among the channels of a single lamina. Incorporating parallel microchannel arrays into microreactors can enable integration of a complicated system with multiple reactions, as well as the coupling of endothermic and exothermic reactions, which improves energy recovery [89]. The other

fundamental structure is the monolithic construction in which microchannels or microstructures are incorporated into a single metal or silicon block [90].

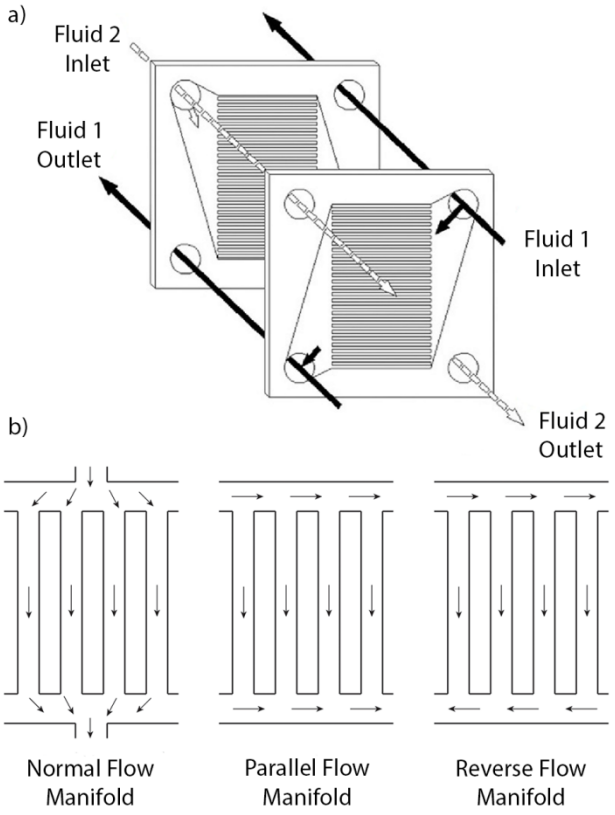

Figure 50: a) Laminated-sheet structure, reproduced with permission from Pan et al. [89] and b) manifold categorization based on the flow direction, adapted from Webb [91]

Although the fabrication of the monolithic construction is relatively simple, it has limited application [92]. For example, the coupling of endothermic and exothermic reactions is not possible in this design. Furthermore, stationary vortices often appear in the distribution chamber in the monolithic structures, precluding the establishment of a relatively uniform flow distribution [84]. The focus of this study is on the flow

distribution among the microchannels of one single lamina that can be incorporated into a laminated-sheet structure. Flow distribution among the stacked laminas of laminated-sheet structure is not covered herein; extensive discussion on this topic is available in several papers [93, 94].

Manifold geometries for a laminated-sheet structure can be categorized into normal, parallel, and reversed flow manifolds [95, 96]. Essentially, as shown in Figure 50b, flow direction in the inlet and the outlet manifolds is the same in parallel flow manifolds while it is opposite in reverse flow manifolds. The more frequently-used terms “Z-shape” and “U-shape” manifolds refer to parallel and reverse flow types, respectively [91, 97]. The term “slanted Z-shape” manifold refers specifically to an oblique (triangular or trapezoidal) manifold, as distinct from a rectangular one. Numerous researchers have studied the effect of the geometrical structure of a microchannel device on flow distribution among microchannels. Both theoretical and numerical studies have been performed in this area, as summarized in Table 8.

A theoretical modeling approach in the form of an electrical resistance network was proposed by Commenge et al. [84] to optimize the trapezoidal manifold geometry and obtain a uniform velocity distribution among microchannels. The calculation results were validated against CFD simulations. This approximate model establishes a relationship similar to Ohm’s law between pressure drop, flow rate, and flow resistance. Singular losses in the manifolds (pressure losses due to merging and branching effects) are neglected, and only wall friction is considered. Therefore, the

relationship established between pressure drop and flow rate is linear, and flow distribution is independent of the flow rate. Since the model by Commenge et al. [84] neglects inertial forces, it is only valid for low Reynolds number flows.

Table 8: Reviewed studies on manifold and microchannel structures

Ref.	Year	Study type	Fluid	Manifold shape	W_c	Channel depth	N	Re
[85]	1995	2D CFD	water	R, T (right), Tr	5 mm	NA	8	50-300
[84]	2002	Theoretical and 3D CFD	Nitrogen	Tr	300,500 µm	100,500 µm	13-34	NA
[98]	2004	3D CFD	water	R, Tr	100 µm	100 µm	5	10-100
[99]	2007	2D and 3D CFD	isopropanol	T (obtuse)	7.1 mm	410 µm	12	0.006-45
[100]	2007	Theoretical	NA	Tr	500 µm	200 µm	20	NA
[89]	2008	Theoretical	NA	Tr	200-500 µm	100-490 µm	9-15	NA
[92]	2009	Theoretical and 3D CFD	water and gaseous water	T (right, obtuse)	500 µm	500 µm	20	0.6-3000
[101]	2009	3D CFD	water	T (obtuse)	100-500 µm	100-500 µm	20	1.25-2.1
[102]	2009	3D CFD	water	R	50-200 µm	50-200 µm	10	8.3-2000
[88]	2010	Theoretical	NA	T (obtuse)	100-500 µm	100-500 µm	20	NA
[103]	2011	Theoretical and 3D CFD	water	Tr (segmented)	300 µm	300 µm	5,10	5-500
[104]	2012	3D CFD and Experiment	methanol	T (right, obtuse)	270 µm	1000 µm	50	NA

R=Rectangular, T=Triangular, Tr=Trapezoidal, NA= Not Applicable/ Not Available (not mentioned)

Using the electrical resistance network method, several studies have been conducted on microchannel structures with triangular and trapezoidal manifolds to investigate the effect of geometrical parameters on flow distribution uniformity [88, 89, 92, 100, 101]. A similar theoretical method was used by Solovitz and Mainka [103] to design multi-segmented manifold geometries for uniform flow distribution. They proposed a

power law relationship to calculate the width of each segment. The outcome of such a segmented geometry resembles a trapezoidal manifold.

Numerical simulations have also been used to study the influence of geometrical parameters of a microstructure on flow uniformity. Kim et al. [85] compared the flow distribution of three different Z-shape manifold geometries: rectangular, triangular, and trapezoidal. In their study case, 2D CFD simulations showed that a triangular manifold design provided the most uniform flow distribution irrespective of the Reynolds number. Tonomura et al. [98] performed a 3D CFD study on a Z-shape rectangular manifold and tried to optimize the manifold area by trimming the crosswise edges of the rectangles. The results of 2D and 3D CFD simulations on the flow distribution in microchannel structures with an obtuse triangular manifold has been compared by Griffini and Gavriilidis [99]. They concluded that for their study cases 2D simulations were misleading because they gave an overestimate of flow maldistribution, and in order to accurately describe the correct velocity distribution 3D simulations are required. Pan, Zeng, et al. [101] performed a 3D numerical study to investigate the effect of the structural parameters of microchannels and obtuse triangular manifolds on flow uniformity. The effect of channel width and channel spacing on flow distribution among microchannels with U-shape rectangular manifolds has been investigated by Mathew et al. [102].

Zeng et al. [104] performed a 3D CFD study on a triangular manifold structure in a methanol steam reformer for hydrogen production. It was found that, as compared to

the obtuse-angled manifold, the right-angled manifold resulted in a more uniform flow distribution for all inlet velocities. The study also showed that the methanol conversion rate and the selectivity of the process were higher with the use of right-angled manifolds, which can be attributed to the more uniform flow distribution of this design. A similar performance improvement with a more uniform flow distribution in methanol steam reformers was reported by Jang et al. [105]. Such findings affirm the influence of flow distribution uniformity on the performance of microreactor devices and reflect the importance of efficient manifold design.

The most unanimous conclusion made by the studies reviewed herein is related to the effect of microchannel length on flow distribution. It was indicated by several researchers that increasing the channel length results in a more uniform flow distribution among microchannels [98, 99, 101, 102]. The degree of flow uniformity that can be achieved depends on how small the pressure drop in the manifold is in comparison with the pressure drop in the channels [102]. Increasing the channel length makes the pressure drop in the microchannel relatively larger than that in the manifolds which improves the flow uniformity. Moreover, several studies have investigated the effect of Reynolds number on flow distribution [85, 92, 98, 99, 102, 103]. It has been shown that above a critical Reynolds number (where the critical Re number depends on the geometry of the device), increasing the Reynolds number degrades the flow uniformity due to the significance of the singular losses.

Right triangular manifolds can distribute flow more uniformly than obtuse ones [92, 104]. To the best of the authors' knowledge, no parametric study has yet been performed on this particular geometry. In the present study, the CFD tool COMSOL is used to perform 3D simulations on microchannel structures with right triangular manifolds. The effects of the structural parameters of microchannels and manifolds on velocity distribution and pressure drop have been studied within a low Reynolds number system $(5 \le \mathrm{Re} \le 25)$. One of the objectives was to achieve a broad perspective on the influence of structural parameters on flow uniformity and pressure drop. As a contribution, the observed trends have been carefully interpreted to provide a logical framework not limited to the studied cases. The direct relationship between the channel dimensions, degree of flow uniformity, and pressure drop through the manifold and microchannels has been presented. For the first time, the concept and procedure for minimizing the manifold area while maintaining a required level of flow uniformity has been introduced, which is very significant for reducing dead volume and residence time in the manifolds.

In all of the aforementioned CFD studies or theoretical studies in which the results were compared to CFD simulations (listed in Table 8), the lack of information about the grid convergence study is noticeable. Pan et al. [101] provided a picture from the meshed model with very large elements, which may introduce large computational errors into CFD simulations. To firmly establish the reliability of our CFD results, the grid convergence and meshing information have been included alongside the results.

Validation assessment on a single microchannel has been performed to ensure that the embedded numerical errors are small.

6.2 CFD MODELING

In the present study, microstructures containing an array of 20 microchannels with right triangular manifolds have been studied numerically. The influence of structural parameters of the microchannel and manifolds, including the width and the depth of microchannels, channel spacing, corner angle and vertical short spacing in the corner of the triangular manifolds on flow distribution and pressure drop have been investigated via parametrical study. A schematic view of the microstructure is shown in Figure 51.

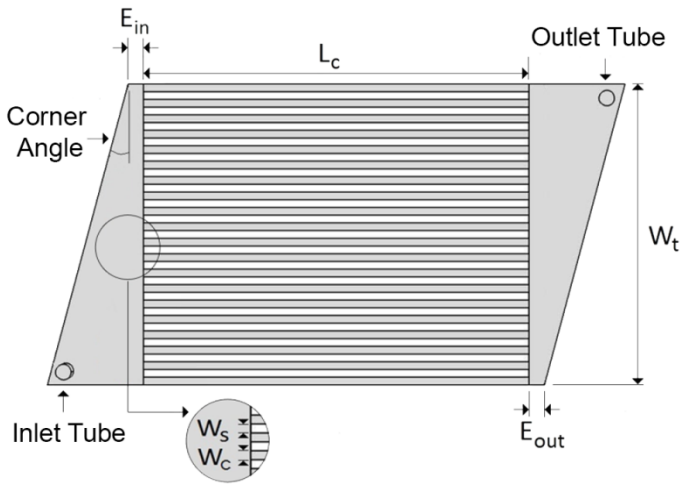

Figure 51: Schematic view of the microstructure including geometrical parameters

The single-phase steady-state laminar flow module in COMSOL Multiphysics 4.2 was used to perform the CFD simulations. COMSOL implements finite element methods

for solving partial differential equations. The Navier-Stokes equations with negligible gravity term, Eq. (69), coupled with the continuity equation in incompressible mode, Eq. (70) were solved. COMSOL uses the GMRES (Generalized Minimal Residual) method to solve the linearized equations. The discretization of both pressure and velocity components was of the first order, which is the default setting for the laminar flow interface in COMSOL. The working fluid was taken to be water at 20 °C.

$$\rho\left(\frac{\partial \vec{U}}{\partial t} + \vec{U} \cdot \nabla \vec{U}\right) = -\nabla P + \mu \nabla^2 \vec{U} \tag{69}$$

$$\nabla \cdot \vec{U} = 0 \tag{70}$$

The inlet boundary condition was normal inflow velocity; the velocity magnitude was adjusted to maintain a constant total inlet flow rate of 3 ml/min regardless of inlet tube diameter. At the outlet, the imposed boundary condition was zero pressure with no viscous stress. No-slip boundary conditions were applied at the walls of the microstructure. The mathematical forms of the boundary conditions are shown in the following equations where $\hat{n}$ is the boundary normal unit vector pointing out of the domain.

$$\vec{U}_{in} = -\, U_0\, \hat{n} \tag{71}$$

$$P_{out} = 0, \;\; \mu(\nabla \vec{U} + (\nabla \vec{U})^T) \cdot \hat{n} = 0 \tag{72}$$

$$\vec{U}_{wall} = 0 \tag{73}$$

In the microchannel section of the structure, a rectangular structured mesh was generated and swept through the depth of the channels to generate 10 layers of hexahedral elements. The number of grids in the width of the channels was chosen with regard to the dimensions of the channels in such a way that the quality of the elements was preserved. In the manifold sections of the structure, an unstructured triangular mesh was generated and swept to generate 10 layers of prism elements. In Figure 52, different angles of view of the generated mesh are presented for one of the studied cases.

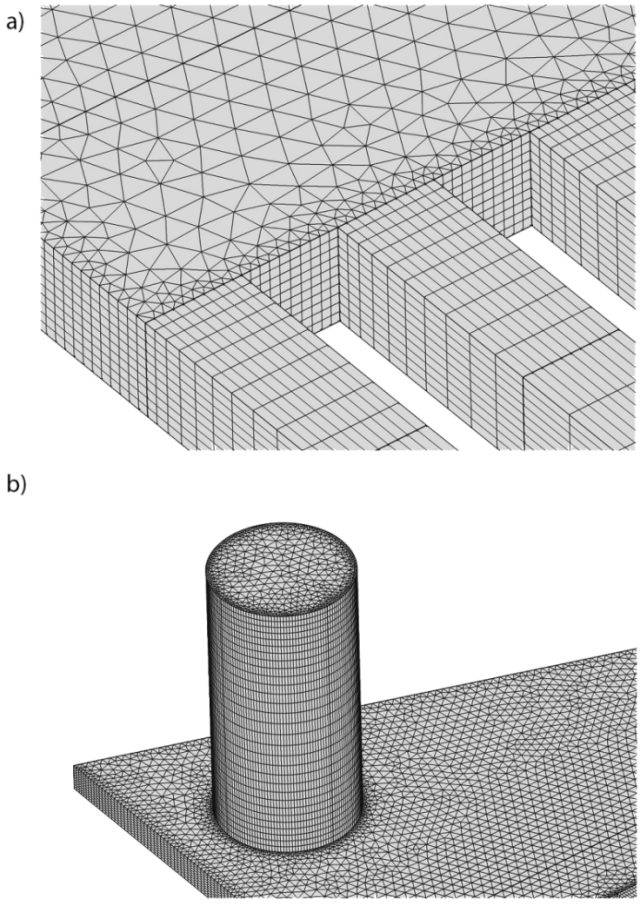

Figure 52: a) The mesh near the entrance of the channel and b) The mesh of the inlet tube

The general size of elements in the manifolds was defined as “extremely fine,” the smallest element size predefined by COMSOL for fluid dynamics. This size has been changed manually to study grid convergence. The average number of degrees of freedom in the studied cases was between 1,200,000 and 2,400,000. COMSOL utilized an iterative scheme to solve the governing partial differential equations. The prescribed converging tolerance was 0.0001.

6.2.1 SELECTION OF STRUCTURAL PARAMETERS

The primary focus of this study is on a microchannel hemodialysis device with mass transfer through a membrane on the top and bottom walls of the channels; appropriate structural parameters were selected to encompass a range relevant to this biomedical device. However, the selected structural parameters lie in a geometrical range relevant to many microchannel reactors and heat exchangers, and our Reynolds number range overlaps with all but one of the previous studies summarized in Table 8. A baseline channel depth of 200 μm was selected for our studies. All of the studies except for the “channel size study” are performed using this channel depth. In the channel size study, the width and depth of the channels were defined to vary between 100 μm and 500 μm to determine the effect of channel dimensions on the flow uniformity and to gain an understanding of the possible range of variations in flow uniformity achievable by varying channel dimensions. The depth of the manifold has been maintained equal to the depth of channel to ensure that our device can be easily fabricated by our group.

For our particular device, the channel width must be smaller than 300 μm in order to support the membrane. Channel spacing is typically chosen to be on the order of the channel width. Devices with small channel spacings (<100 μm) are difficult to fabricate in polycarbonate, and the use of larger channel spacing increases the total width of the device. In addition, to reduce the manifold volume and total residence time, as desirable for our application (among others), neither channel spacing nor corner angle should be selected to be unnecessarily large. The corner angle must be large enough to let the inlet/outlet holes fit in the manifolds.

It is known that increasing the channel length improves flow distribution uniformity. In the present investigation, the channel length was chosen 2 cm, which lies in the range relevant to many arrayed microchannel devices. In an operational microchannel dialyzer device, the channel length might be several times larger.

Flow rate is one of the factors affecting flow distribution uniformity. For all of the studies discussed herein except for the last one, the flow rate was kept constant at 3 ml/min to eliminate the effect of flow rate and to focus on the effect of the selected geometrical parameters. This flow rate provides velocities close or within the appropriate velocity range (4 – 6 cm/s) for the 200-μm deep and 200-μm to 500-μm wide channels. In the last study (section 6.4.5), the flow rate has been modified to ensure broader applicability of our results; in other words, the study in section 6.4.5 is designed to ensure that a slight adjustment of flow rate does not have a significant effect on flow distribution uniformity.

6.3 VERIFICATION AND VALIDATION

In the following sections the verification and validation of the simulation results are discussed. Pressure and flow velocity (including flow distribution across a single-layer channel array) are the primary parameters of interest for this study; thus, the verification and validation assessments were performed on these parameters.

6.3.1 VERIFICATION STUDY

The grid convergence study was performed on a single isolated microchannel and the inlet manifold. The investigated parameters were pressure drop and maximum velocity for the single channel and total pressure drop and flow distribution among the microchannels for the inlet manifold. For the single microchannel, simulations were done on a 2-cm long and 200-μm wide square microchannel with 0.04 m/s uniform inlet velocity and zero pressure outlet boundary conditions. The corresponding Reynolds number was 8. The results of grid refinement, summarized in Table 9, showed consistent convergence. By applying grid E (40×40) to the 20 microchannels of the complete model, about 12,800,000 hexahedral elements are generated in the microchannel portion of the model. The application of grid B (10×10) results in the generation of about 400,000 elements. In addition, using grid E in microchannels forces the use of 40 layers of prisms in the manifold parts, which is four times the required layers of mesh when the grid B is implemented. Given (i) the significant computational cost and (ii) the small difference between the results of grid B and E,

grid B or finer versions of it were used for the arrays of microchannels in the complete models.

Table 9: Grid convergence study on a single $200\text{-}\mu m$ square channel with Re=8

Case	A	B	C	D	E	Difference between A and E	Difference between B and E	Difference between C and E
$N_x \times N_y$	5×5	10×10	20×20	40×40	40×40			
N_z per cm	100	100	100	100	200			
$\Delta P_{fd}(Pa/cm)$	259.29	271.58	279.55	283.34	283.14	8.4%	4.1%	1.3%
$U_{\max}(m/s)$	0.0642	0.0804	0.0819	0.0828	0.0828	22.5%	2.9%	0.7%

To investigate the effect of element size in the manifolds, the element size in the inlet manifold was successively reduced. Based on the previous grid convergence study on the single microchannel, a 10×10 grid was used in the microchannel portion of the structure. The influence of the manifold mesh size on the total pressure drop and velocity distribution among the microchannels has been investigated. The triangular manifold had a 20 degree corner angle and a $500\text{-}\mu m$ vertical corner spacing. The microchannel array consisted of twenty $200\text{-}\mu m$ square channels. Three element sizes -A, B, and C- were generated in the inlet manifold. Element size B is used for the outlet manifold mesh in all three cases. Element sizes A and B correspond to the "extra fine" and "extremely fine" default mesh sizes of COMSOL, respectively. The maximum element size in case C was set manually. In addition to the comparisons made for pressure drop in Table 10, velocity distributions among microchannels for the three cases are compared in Figure 53. The velocity distribution is notably nearly equivalent for all cases. As the difference in the pressure drop for cases B and C is less

than 1% (Table 10), the use of element size B in the manifolds is considered the most reasonable for ensuring the accuracy of the results in the present study.

Table 10: Grid convergence study on the inlet manifold

Case	A	B	C	Difference in pressure drop between cases		
Max element size (μm)	132	74.4	37.2	A and B	A and C	B and C
Min element size (μm)	8.59	1.14	1.14			
Total pressure drop (Pa)	1084.6	1091.0	1100.6	0.59%	1.45%	0.87%

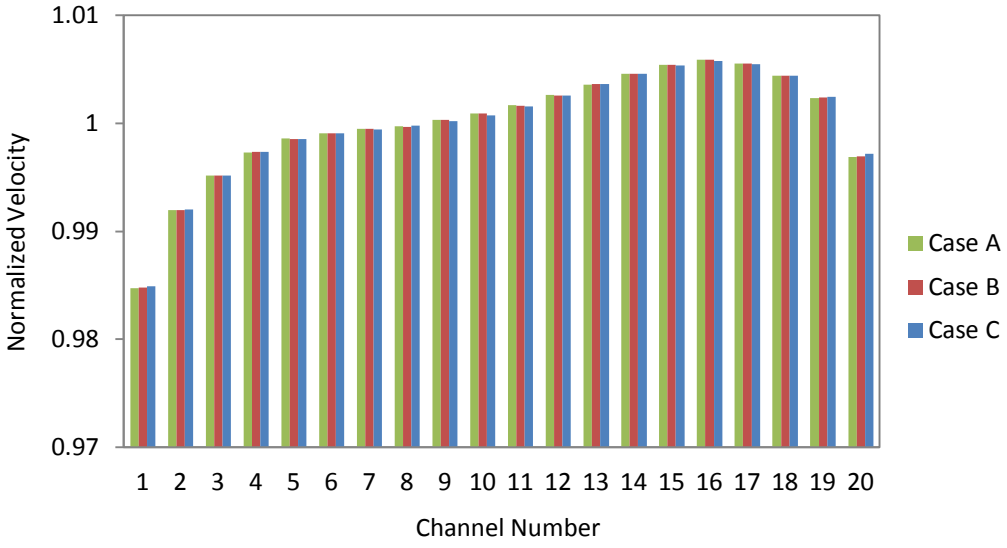

Figure 53: Effect of grid size in the inlet manifold on flow distribution

6.3.2 VALIDATION STUDY

A validation assessment was performed for a single microchannel geometry. The simulation results for pressure drop and maximum flow velocity in the fully developed region have been compared to the analytical solution for flow in rectangular channels. The hydrodynamic entrance length was also compared with analytical and experimental correlations for developing laminar flow in rectangular ducts. The

assessment was performed to verify that the errors embedded in the numerical method are sufficiently small and to confirm that the model accurately represents the phenomenon. A comprehensive validation study on the subject of flow distribution uniformity would include a comparison of the simulation results with experimentally obtained velocity data. However, no high-quality data are available in the literature at the current time, so such a validation could not be presently performed.

6.3.3 CORRELATIONS USED IN VALIDATION STUDY

According to Shah and London [75], Eq. (74) can be used as an approximation for U_{max} in rectangular channels.

$$\frac{U_{max}}{U_{mean}} = \left(\frac{m+1}{m}\right)\left(\frac{n+1}{n}\right) \tag{74}$$

The values of *m* and *n* are given by

$$m = 1.7 + 0.5(\alpha)^{-1.4} \tag{75}$$

$$n = \begin{cases} 2 \text{ for } \alpha \le 1/3 \\ 2 + 0.3\left(\alpha - \dfrac{1}{3}\right) \text{ for } \alpha \ge 1/3 \end{cases} \tag{76}$$

in which α (≤ 1) is the aspect ratio. Equation (74) is obtained from the Fourier series analytical solution of the velocity in rectangular ducts. Equations (75) and (76) are obtained by solving the momentum equation with a finite difference method and matching the velocity profile to the approximation of the Fourier series analytical

solution. Using the analytical solution for velocity in rectangular ducts, the Fanning friction factor for the fully developed flow in a rectangular channel is approximated by [75]

$$f\ \mathrm{Re} = 24\left[1 - 1.3553\alpha + 1.9467\alpha^2 - 1.7012\alpha^3 + 0.9564\alpha^4 - 0.2537\alpha^5\right] \quad (77)$$

The pressure drop in the fully developed region can be calculated by

$$\Delta P = 2 f \rho \frac{L}{D_h} U^2 \quad (78)$$

The hydrodynamic entrance length is defined as the length required to achieve 0.99 of the corresponding fully developed velocity magnitude [75]. The fully developed region begins at the point where the hydrodynamic boundary layers on the sides of the channel merge at the centerline. Downstream of this point, the velocity profile no longer changes along the length of channel. Shah and London [75] compared the obtained entrance length data of various investigators in a tabular format and acknowledged that the analytical data provided by Wiginton and Dalton [106] were the most accurate. For a rectangular channel, the data can be approximated by

$$L_e = \left(0.06 - 0.07\alpha + 0.04\alpha^2\right) \mathrm{Re}\ d_h \quad (79)$$

For a square channel Eq. (79) yields

$$L_e = 0.09\ \mathrm{Re}\ d_h \quad (80)$$

According to Ahmad et al. [107], the tabulated data of Shah and London [75] are not accurate for low Reynolds number flows (Re < 10) in microchannels. They proposed

the following correlation for the entrance length of low Reynolds number flows based on Micro Particle Image Velocimetry (μPIV) experimental results.

$$\frac{L_e}{d_h} = \frac{0.63}{0.035\ \mathrm{Re} + 1} + 0.0752\ \mathrm{Re} \tag{81}$$

6.3.4 *COMPARISON BETWEEN THE SIMULATION RESULTS AND ANALYTICAL/EXPERIMENTAL CORRELATIONS*

To estimate the entrance length of the channel, velocity profiles at different distances from the beginning of the channel are plotted as shown in Figure 54. The entrance length is estimated by finding the point at which U_{max} at the centerline of the channel becomes equal to 0.99 U_{fd}.

The results are compared with the entrance length calculations gained from Eq. (80) proposed by Shah and London [75] and Eq. (81) proposed by Ahmad et al. [107] in Table 11. There is better agreement between the simulation result and the Ahmad et al. correlation than with the Shah and London correlation; the Reynolds number of the simulated flow (Re ~ 8) and Ahmad et al. experiment (Re < 10) are well matched. The difference between the entrance length as defined by Ahmad et al. correlation and the numerical simulation may be due to the fact that the maximum velocity in the numerical simulations was 2.1% less than the maximum velocity calculated theoretically for the same flow rate. Subsequently, the flow reached fully developed conditions slightly earlier in the simulations.

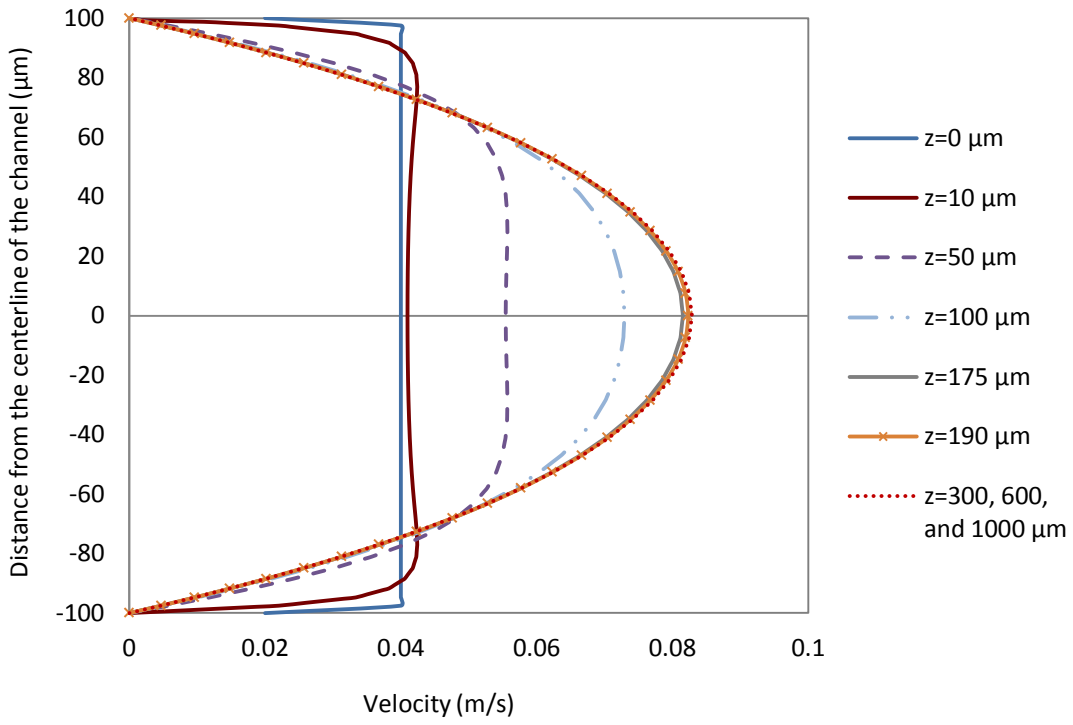

Figure 54: Velocity profiles along the length of the microchannel

Table 11: Comparison between the numerical results and theoretical estimations

	$U_{max}(m/s)$	f	$\Delta P_{fd}\ (Pa/cm)$	$L_e\ (\mu m)$	
Simulation (40×40 grid)	0.0828	1.771	283.34	190	
Theoretical estimations	0.0846 Eq. (74)	1.778 Eq. (77)	284.48 Eq. (78)	144 Eq. (80)	220 Eq. (81)
Difference	2.1%	0.4%	0.4%	24.2%	13.6%

6.4 CFD SIMULATION RESULTS

In this section, different studies performed on the microstructure geometry (manifold and channels) are presented. The structural parameters of the microchannels and the

manifolds in different studies are summarized in Table 12, where the study number refers to the related paper section. To discuss the concept of uniform flow distribution among the microchannels, a criterion on flow uniformity is defined as the standard deviation of the normalized velocities of the microchannels, $\sigma_U\%$. For an array of N channels this parameter is given by

$$\sigma_U\% = 100 \times \sqrt{\frac{1}{N}\sum_{j=1}^{N}\left(\frac{U_j}{U_{mean}} - 1\right)^2} \quad (j = 1, 2, \ldots, \mathrm{N}) \tag{82}$$

in which the mean velocity of the flow in the channels is

$$U_{mean} = \frac{1}{N}\sum_{j=1}^{N} U_j \quad (j = 1, 2, \ldots, \mathrm{N}) \tag{83}$$

The standard deviation of the normalized velocities will be used herein to compare different geometries of microchannels and manifolds from the point of flow distribution uniformity. The smaller the $\sigma_U\%$, the more uniform the flow distribution is among the microchannels.

Table 12: Structural parameters of the microchannels and manifolds in different studies, number of channels = 20, channel length = 2 cm

Study No.	Flow rate (ml/min)	Re	Inlet/outlet diameter (mm)	Depth (μm)	W_c (μm)	W_s (μm)	W_t (mm)	Corner Angle(deg)	E_{in} (μm)	E_{out} (μm)
1	3	4.98-24.9	2	100-500	100-500	105.3-526.3	12	30	500	500
2	3	12.45	1	200	200	200	7.8	30	500-5000	500-5000
3	3	12.45	0.756-1.730 0.634-1.730	200	200	100-500 50-500	5.9-13.5 4.95-13.5	20 30	500	500
4 (a)	3	12.45	1	200	200	200	7.8	15-40	0-1000	0-1000
4 (b)	3	7.11	1	200	500	500	19.5	5-40	0-1000	0-1000
5 (a)	6	24.9	1	200	200	200	7.8	15-40	0-1000	0-1000
5 (b)	1.5	6.22	1	200	200	200	7.8	15-40	0-1000	0-1000

6.4.1 *EFFECT OF MICROCHANNEL DIMENSIONS ON FLOW UNIFORMITY AND PRESSURE DROP*

This comparative study is designed to isolate and investigate the influence of channel depth and width on velocity distribution among the microchannels and pressure drop. The manifold geometry was fixed in this study to eliminate its effect on the aforementioned parameters. The only change in manifold dimensions occurred when the microchannel depth was changed which subsequently resulted in a change in manifold depth. By altering the channel spacing, the total width of the manifold remained constant even when the channel width was reduced or enlarged. The microchannel dimensions were varied from $100\ \mu m$ to $500\ \mu m$ in both width and depth at 100-μm intervals. The corresponding channel Reynolds numbers varied from 4.98 to 24.9. The corner angle of the manifold was held constant at 30 degrees, and the length of the short vertical spacing next to the corner angle was held constant at $500\ \mu m$. In general, the use of shallow channels is important for achieving effective diffusion in microreactors while the use of tall and narrow channels typically improves heat transfer in micro heat exchangers.

Figure 55 shows the effect of channel dimensions on flow uniformity among the microchannels. Reducing the channel width at a constant depth improved the flow distribution from a 2% standard deviation of normalized velocity to 0.5%, while reducing the channel depth had the opposite effect. In other words, for a given depth, the use of high aspect ratio (tall and narrow) microchannels improved the flow uniformity, a result that is in agreement with those obtained by Pan et al. [101].

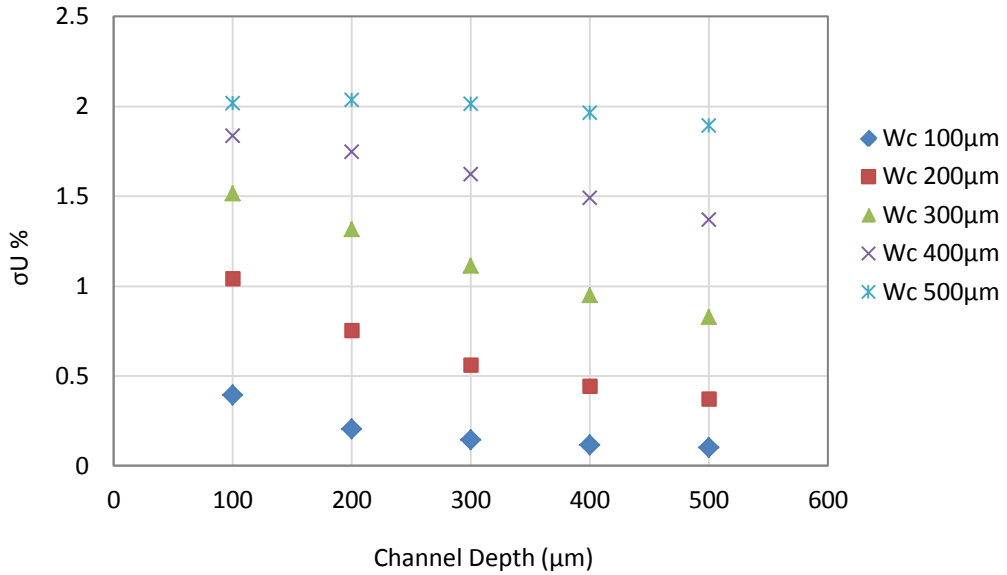

Figure 55: Effect of channel dimension on flow uniformity. For parameter definition, refer to Table 12 comparative study 1.

For explanation, one should refer to the primary factor contributing to the ability to achieve a uniform flow distribution using triangular manifolds. The lengths of the flow paths inside the triangular manifolds are much smaller than the channel lengths. Therefore, regardless of inertial forces at low Reynolds numbers, the pressure loss along the manifold flow paths is much smaller than the pressure loss occurring in the channels. This is the fundamental principle allowing the flow to uniformly distribute among the channels even though the flow paths in the manifold corresponding to individual channels are not the same.

In general, increasing the ratio of the pressure drop in the microchannels to the pressure drop of the manifold (for example, by elongating the channels) enhances flow uniformity. Similarly, reducing the width of channels increases the resistance and the

pressure drop through channels and improves flow uniformity. However, reducing the depth of the microchannels and subsequently the manifolds increases the pressure loss in both. The simulation results suggest that the effect of depth reduction on the pressure drop of the manifold flow paths was more than the pressure drop of the microchannels and the ultimate effect of depth reduction on the flow distribution was negative.

Figure 56a presents the effect of channel dimensions on the pressure drop through the whole device. As expected, the depth of the microstructure has the most impact on the total pressure drop; and at a constant depth, narrower channels introduce more pressure drop into the system. The effect of channel dimensions on the average pressure loss in the inlet manifold is shown in Figure 56b. The amount of pressure loss through the inlet manifold is almost independent of the channel width and only varies with changes in depth. As explained before, in low Reynolds number flows, inertial forces in the manifolds are negligible, and pressure loss is nearly entirely due to wall friction. As a result, for a fixed manifold geometry and a constant depth, we should not expect the pressure loss to be a function of channel width. This explanation is in agreement with the simulation results.

a

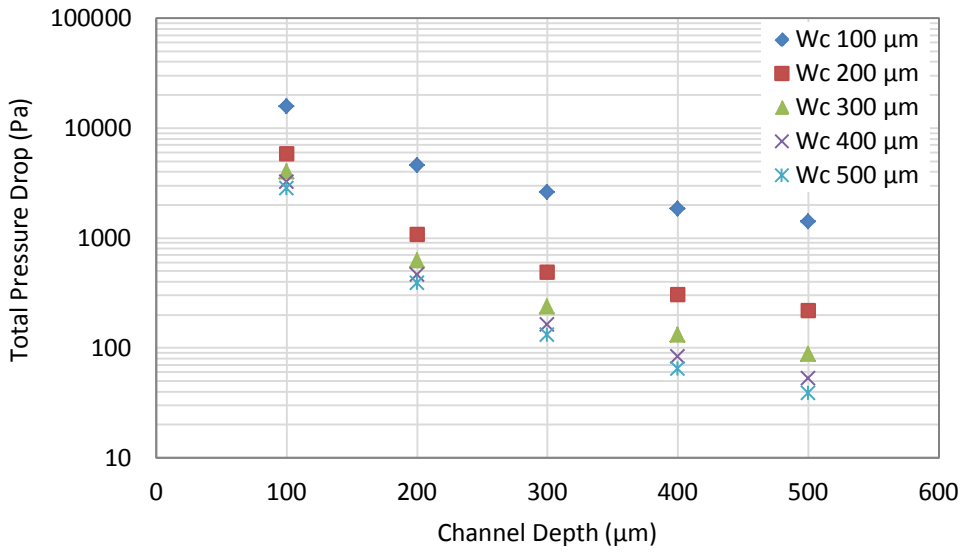

b

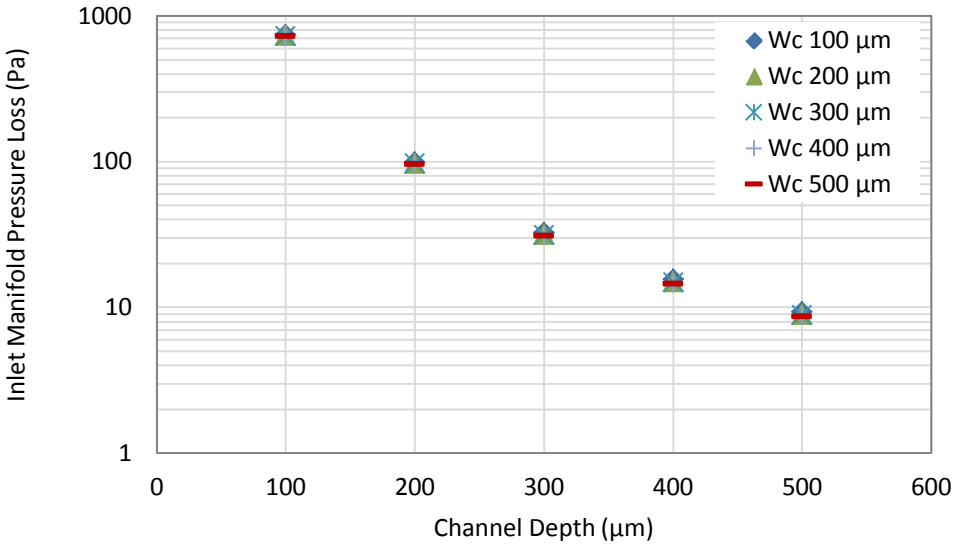

Figure 56: a) Effect of channel dimensions on total pressure drop and b) effect of channel dimensions on average pressure loss in the inlet manifold. For parameter definition, refer to Table 12, comparative study number 1.

Figure 57 presents the influence of channel dimensions on the ratio of pressure loss in the microchannels to the total pressure loss in the whole structure. The results suggest when taller and narrower channels are used a larger portion of the total pressure drop

occurs in the channels; the use of shorter and wider channels results in a smaller ratio of pressure drop in the channels to the total pressure drop, primarily because the manifold depth is held equal to the channel depth. The pressure loss in the manifold is different in these two cases. These results support the previously-stated argument about the influence of channel dimensions on flow uniformity.

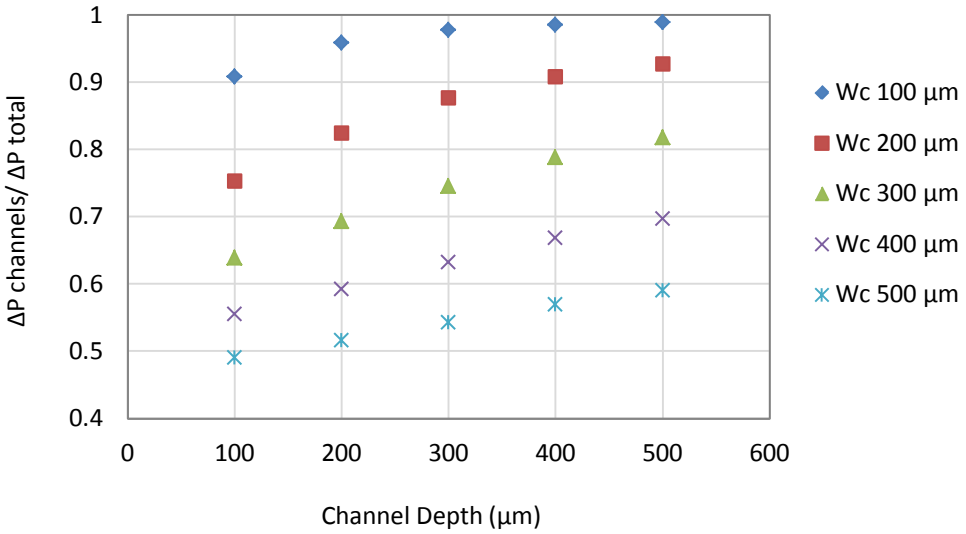

Figure 57: Effect of channel dimension on the ratio of the pressure loss in the microchannels to the total pressure drop. For parameter definition, refer to Table 12, comparative study 1

6.4.2 EFFECT OF MANIFOLD ASYMMETRY ON FLOW DISTRIBUTION

This comparative study investigates the effect of asymmetric manifolds on flow distribution among microchannels. The inlet and outlet manifolds were modified by increasing the vertical corner spacing (E_{in} and E_{out}). The dimensions of the microchannels were $200\ \mu m \times 200\ \mu m$, and the corner angle of the manifold was 30

degrees. The corresponding average channel Reynolds number was 12.45. When focusing on the inlet manifold, E_{in} was changed from $500\ \mu m$ to 5 mm while E_{out} was held constant at $500\ \mu m$. A similar modification was performed for the magnification of the outlet manifold. The effect of the use of an asymmetric manifold on the flow distribution is presented in Figure 58a and Figure 58b.

The results indicate that use of a bigger inlet manifold increases the flow rate of microchannels far from the inlet tube; the use of a bigger outlet manifold results in the opposite. Furthermore, symmetrical manifolds yield a more uniform flow distribution than asymmetrical ones. Such findings are in agreement with the results obtained by Pan et al. [100] and Pan, Zeng, et al. [101]. The results suggest that by increasing the vertical corner spacing, the influence of hypotenuse wall friction on the flow moving toward the corner channels becomes smaller, and the flow experiences lower resistance. As a consequence the corner channels will have higher flow rates than the other ones.

a

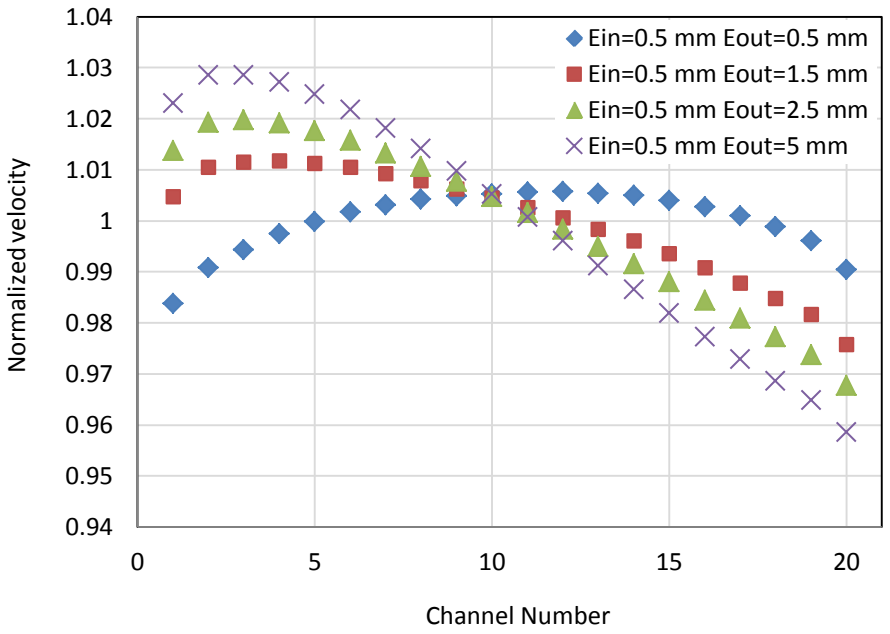

b

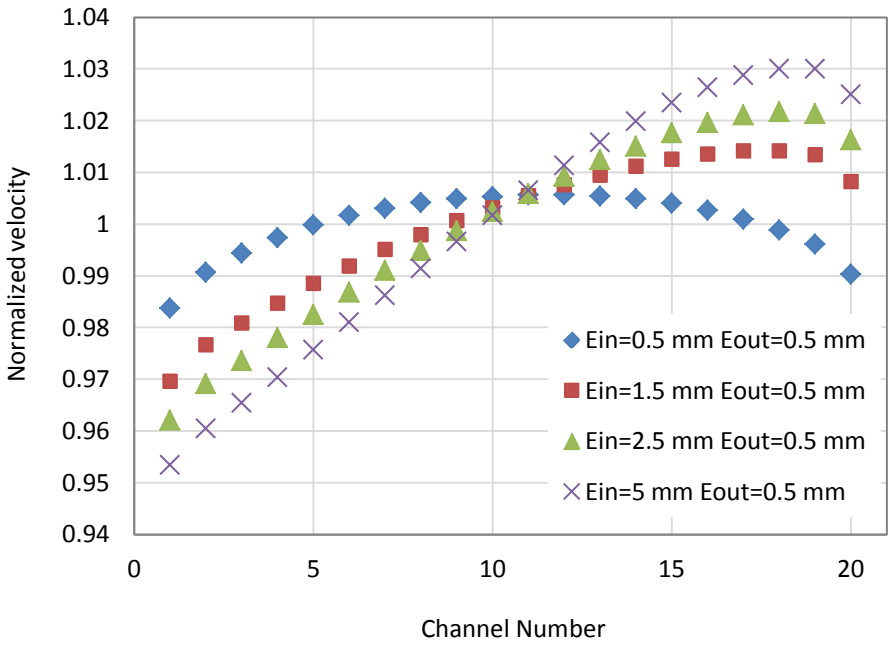

Figure 58: a) Effect of inlet manifold magnification on flow distribution and b) effect of outlet manifold magnification on flow distribution. For parameter definition, refer to Table 12, comparative study 2

6.4.3 *EFFECT OF CHANNEL SPACING ON FLOW UNIFORMITY*

The effect of channel spacing on flow distribution uniformity in structures with corner angles of 20 degrees and 30 degrees and vertical corner spacing of $500\ \mu m$ is addressed in this comparative study. The dimensions of the microchannels were $200\ \mu m \times 200\ \mu m$, and the corresponding average channel Reynolds number was 12.45. Along with increasing the channel spacing, the inlet/outlet tube diameters were increased to keep the triangle geometry analogous in different cases. The results, shown in Figure 59, indicate that flow uniformity changes only very slightly (~ 0.2%) with the channel spacing variation for the range of parameters considered here.

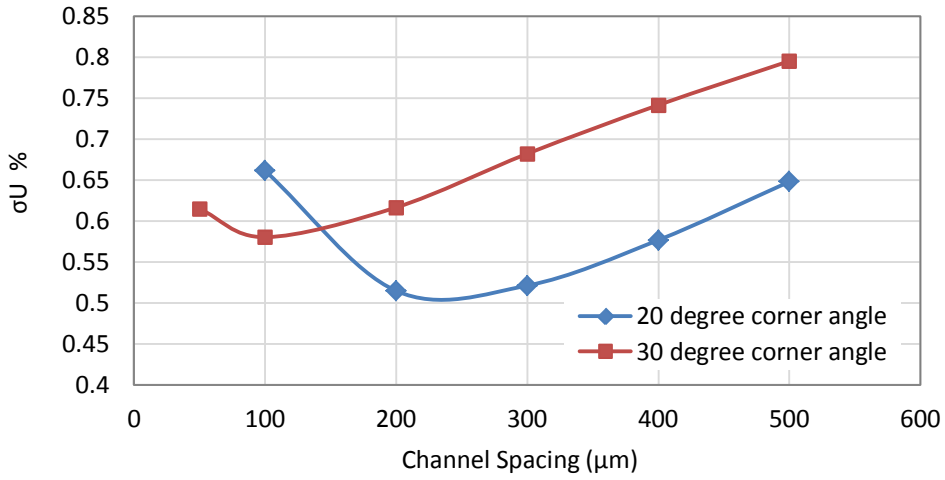

Figure 59: Effect of channel spacing on flow uniformity. For parameter definition, refer to Table 12, comparative study 3

The findings suggest that the optimum channel spacing in manifolds with larger corner angles is smaller than the one with smaller corner angles. From a design point of view, the difference in the flow distribution caused by channel spacing in the range

considered here is so small that one can ignore channel spacing as a parameter affecting flow distribution uniformity and choose the channel spacing based on other design considerations.

6.4.4 *EFFECT OF CORNER ANGLE AND VERTICAL CORNER SPACING ON FLOW UNIFORMITY AND PRESSURE DROP*

The influence of the corner angle and vertical corner spacing of the manifolds on the flow uniformity and pressure drop is investigated in this comparative study. To be able to compare the flow distribution trends in different manifold volumes, simulations were performed on two channel widths and channel spacings. In the first case (a), both channel width and channel spacing were $200\ \mu m$. In the second case (b), both channel width and channel spacing were $500\ \mu m$. As a result, in the second case the manifold was much larger. The depth of the microstructure was held constant at $200\ \mu m$ in both cases. The corresponding average channel Reynolds number was 12.45 for case (a) and 7.11 for case (b). The influence of corner angle and corner spacing on flow distribution uniformity for cases (a) and (b) is presented in Figure 60a and Figure 60b, respectively. A channel width of $500\ \mu m$ is not applicable to our specific application for a microchannel dialyzer device; however, case (b) has been studied here as a wide geometry in comparison to case (a). It is shown that the trends seen in Figure 60a are not limited to a single case and can be numerically obtained for geometries with different structural parameters.

a

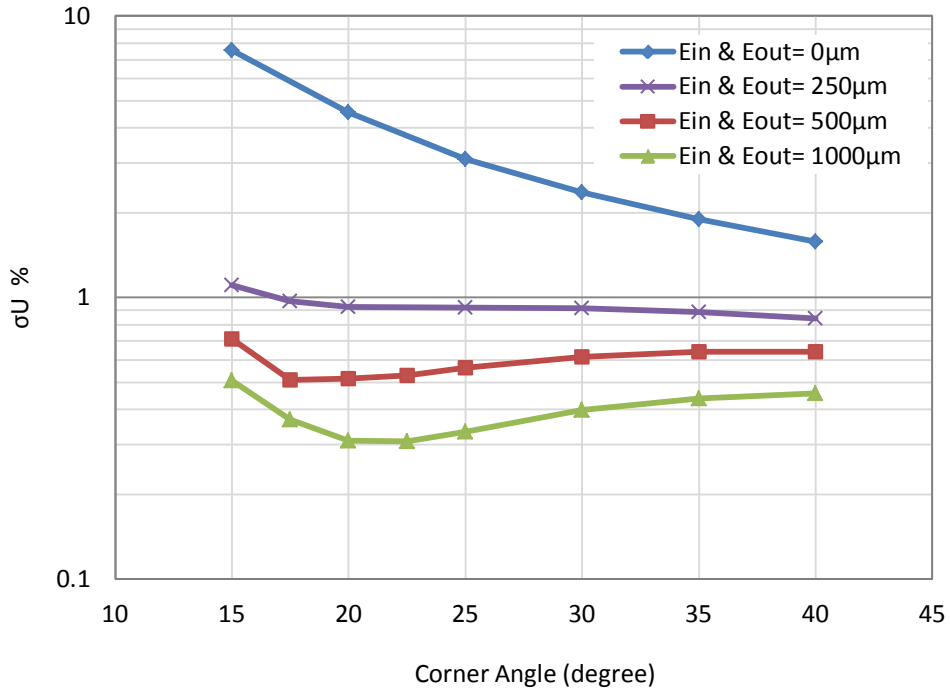

b

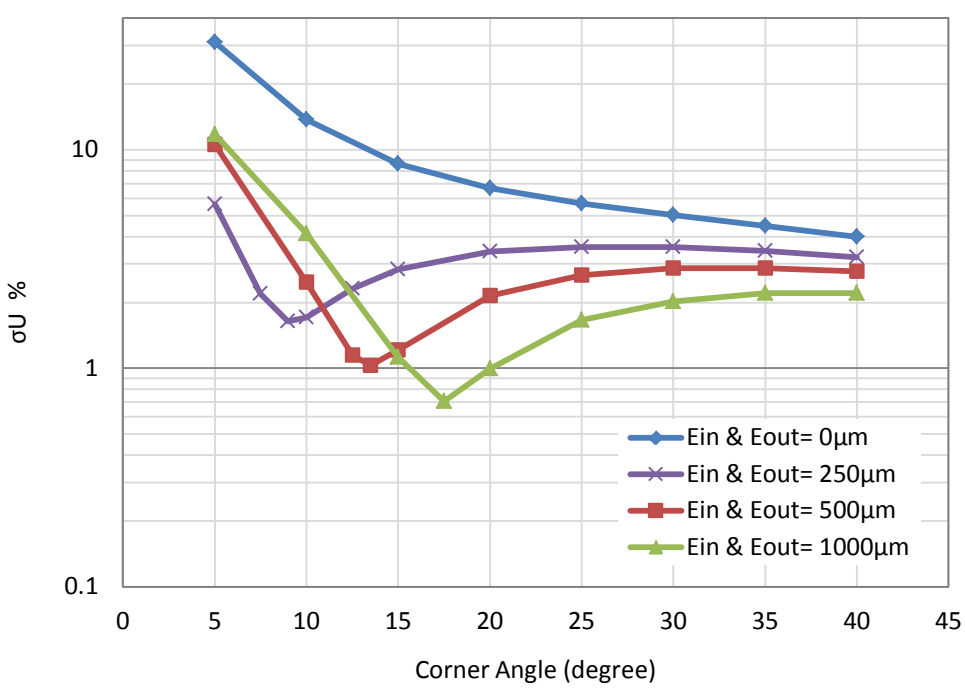

Figure 60: Effect of manifold corner angle and vertical corner spacing on flow uniformity, a) case (a) and b) case (b). For parameter definition, refer to Table 12, comparative study 4 (a) and 4 (b)

The results indicate that adding a vertical spacing to the corner of the manifolds improves flow uniformity significantly. The flow entering/existing the last/first few channels of the array experiences the shear forces generated on the triangle hypotenuse. The presence of this short space reduces the shear force sensed by the flow and lets the flow distribute more evenly. On the other hand, the results suggest that for achieving maximum flow uniformity, an optimum corner angle exists, and this angle varies for different amounts of vertical corner spacing. Generally, for structures with shorter vertical corner spacing, the optimum corner angle is smaller. In the case where the manifold width is relatively large, the optimum corner angle for a 250-μm vertical corner spacing is around 10 degrees, which is surprisingly small. Changing the corner angle when the other structural parameters and the flow rate are kept constant alters the flow uniformity because the flow distribution uniformity is determined by pressure loss variations in the different flow paths in the inlet and outlet manifolds. At the optimum corner angle, the variation between the pressure losses in different flow paths is the least.

Figure 61 presents the combined influence of the manifold corner angle and vertical corner spacing on the pressure drop throughout the whole device. While not visible in Figure 61, the simulation results also indicated that the pressure loss in the microchannel section of the device is almost independent of the corner angle and corner spacing, and pressure loss through the manifold showed a trend similar to the apparent trend in Figure 61.

The results suggest that adding the vertical corner spacing to the geometry is also beneficial for reducing pressure drop in the device. The use of large corner angles increases pressure drop through the manifolds in that it increases the manifold area and the flow path lengths inside the manifolds.

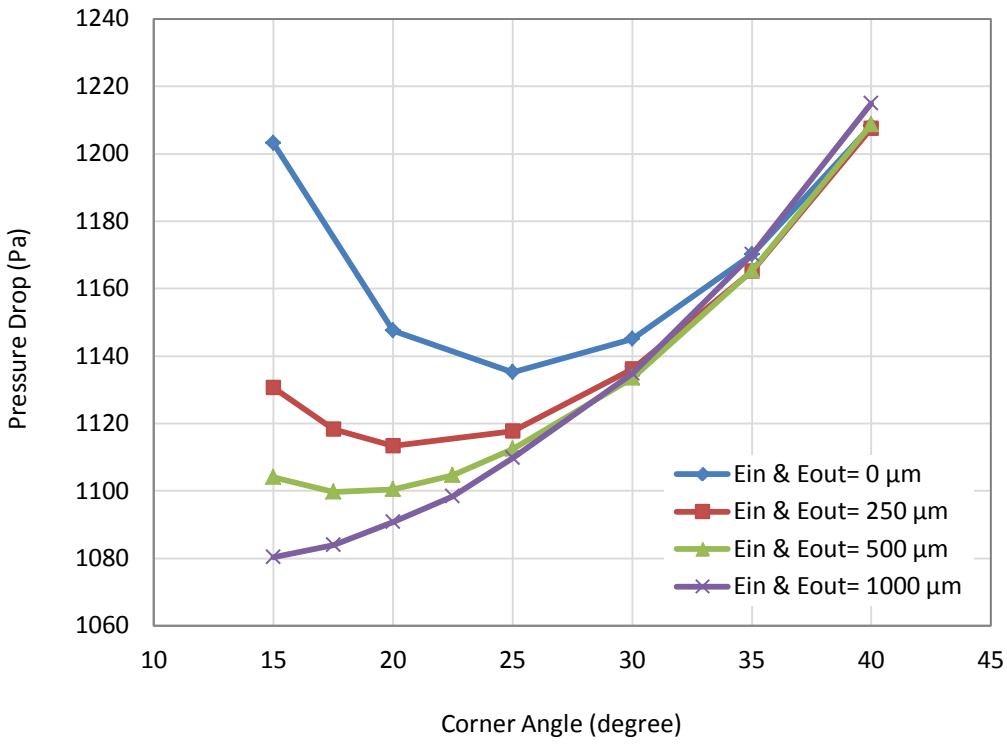

Figure 61: Effect of manifold corner angle and vertical corner spacing on pressure drop throughout the device related to case (a). For parameter definition, refer to Table 12 comparative study 4 (a)

The existence of the apparent relationships between corner angle, vertical corner spacing, and flow uniformity lets a designer reduce the manifold area while maintaining the flow uniformity. Knowing microchannel dimensions, channel spacing, inlet/outlet hole positions, and flow rate, it is possible to generate trends similar to

Figure 60a and Figure 60b. Those combinations of corner angle and corner spacing which satisfy the required level of flow uniformity should be compared with respect to the manifold size. The lowest manifold size can then be chosen to reduce dead volume and residence time in the manifolds.

6.4.5 *INFLUENCE OF FLOW RATE ON THE OBSERVED FLOW UNIFORMITY TRENDS*

Changing the flow rate and subsequently the Reynolds number affects the flow distribution uniformity. At low Reynolds numbers, where inertial forces and singular pressure losses are negligible, the impact of changes in the flow rate on flow uniformity is expected to be relatively small and is studied in this section. The dependency of flow uniformity on corner spacing and the corner angle is investigated at different flow rates for the case (a) geometry previously studied in section 6.4.4. Flow rates of 1.5 and 6 ml/min were studied in addition to the previously-studied flow rate of 3 ml/min. The influence of the corner angle and vertical corner spacing of the manifolds on the flow uniformity for the doubled and halved flow rates are presented in Figure 62a and Figure 62b, respectively. The corresponding average channel Reynolds numbers are 24.9 and 6.22.

Comparing with Figure 60a, the results indicate that increasing the flow rate and Re number slightly reduces the flow distribution uniformity, an effect that is due to the increase in singular pressure losses in the manifolds.

a

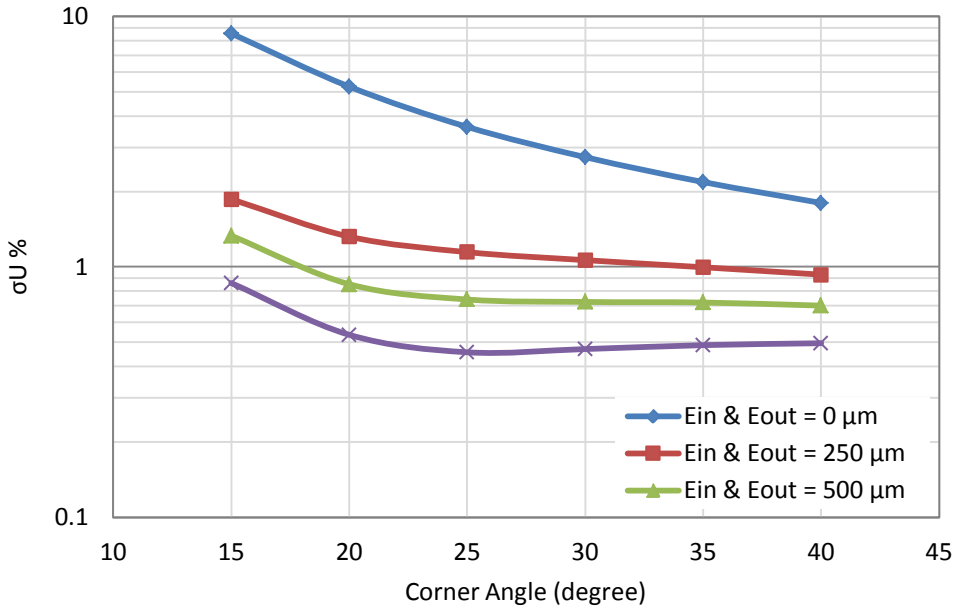

b

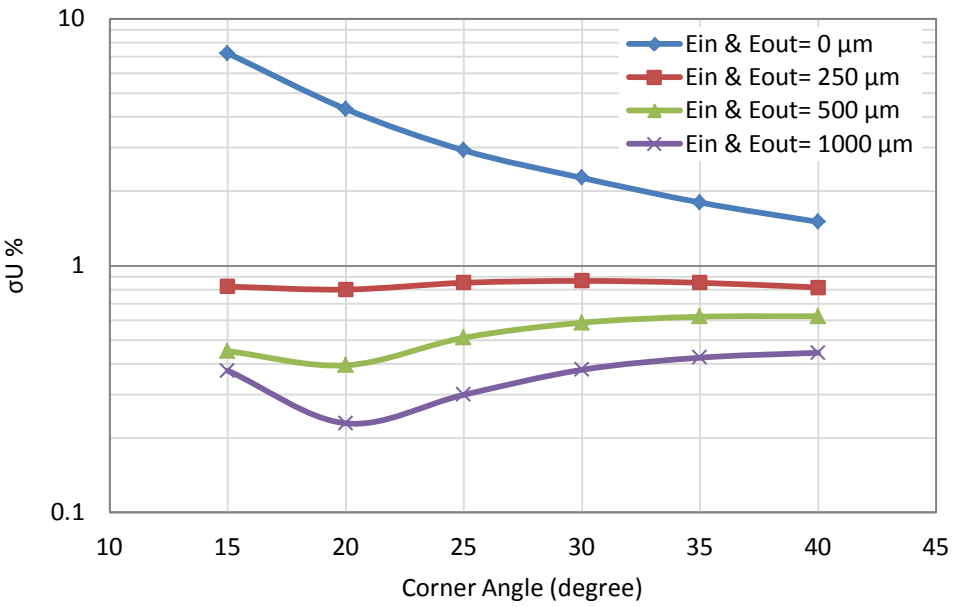

Figure 62: Effect of manifold corner angle and vertical corner spacing on flow uniformity for case (a) geometry, a) at the flow rate of 6 ml/min and b) at the flow rate of 1.5 ml/min. For parameter definition, refer to Table 12, comparative study 5 (a) and 5 (b)

As shown in Figure 62a, by doubling the flow rate, the prominence of the optimum corner angle decreases. By decreasing the flow rate though, the optimum corner angle becomes more noticeable, as shown in Figure 62b. This finding suggests that minimizing the manifold size by using the approach presented in section 6.4.4 is more beneficial for lower flow rates.

This study suggests that the effect of small deviations from a flow rate of 3ml/min on flow distribution uniformity is insignificant since doubling and halving the flow rate changed the degree of flow uniformity by a maximum of only about 1%.

6.5 CONCLUSIONS

A relatively uniform velocity distribution in a microchannel array offers the advantage of having near equal mass and heat transfer coefficients and residence time distribution among individual channels, which is required for reliable scale-up of microchannel structures.

Right triangular manifolds can distribute the flow remarkably uniformly into a number of parallel channels. In this chapter, the effects of the structural parameters of microchannels and the right triangular manifolds on velocity distribution among microchannels and pressure drop were investigated within a low Reynolds number system. Compared to the microchannel dimensions, manifold structural parameters including the corner angle and short vertical corner spacing of the manifold showed more influence on velocity distribution. Including a short vertical spacing at the corner of the manifold was critical to achieving a high level of flow uniformity. The results

imply that depending on the size of vertical corner spacing, an optimum corner angle exists which results in the most uniform flow distribution achievable for the particular structure. For a reduced Reynolds number, the existence of the optimum corner angle becomes more noticeable. The use of tall and narrow microchannels could improve the flow uniformity to some extent. The results also indicated that for the range of considered parameters, the variation of channel spacing had only a slight influence on flow distribution uniformity. Furthermore, magnification of the inlet manifold increased the flow rate of channels far from the inlet tube while magnification of the outlet manifold resulted in the opposite.

From a design point of view, no universal threshold value for velocity deviations among microchannels exists, and designers must define an acceptable degree of flow nonuniformity based on the application of the device. In an actual design process, the width and the depth of the channels must be selected in an appropriate range depending on the mass transfer or heat transfer considerations of the device. If feasible, the use of tall and narrow channels is encouraged to improve the flow uniformity. Channel length, average fluid velocity, and the number of channels on each plate should be chosen based on the required residence time and an acceptable maximum pressure drop throughout each plate. The channel spacing may be limited by the total width of the device or the fabrication restrictions. The designer may come up with groups of manifold structural parameters that result in a satisfactory velocity distribution. For a design process aimed at reducing the manifold volume, channel spacing and the structural parameters of the manifold, including corner angle and

vertical corner spacing, should be optimized together to minimize the manifold area while maintaining the required flow uniformity.

7 MANIFOLD DESIGN: MICROPOST ARRANGEMENT

The manifold regions have to be filled with microposts to support the membrane and prevent membrane sagging in our multichannel biomedical device. Bubble mitigation in the manifold areas requires an effective design of a micropost arrangement that exhibits low bubble retention characteristic while simultaneously supporting the membrane. In this chapter, we first study the issue of bubble clogging in micropost arrays. Next, we investigate preferential bubble paths in different staggered arrangements of microposts and identify arrangements in which bubbles are less likely to get stuck. Based on the results of the aforementioned studies, we identified four candidate manifold geometries with embedded post arrangements. Finally, the percentage of the manifold area that was blocked by bubbles has been compared between three of these candidate manifold geometries.

As discussed in section 4.5, the scenario under which there is the most membrane sagging in the microchannel dialyzer occurs during the ultrafiltration phase of the hemodialysis. The maximum open distance between the microposts to prevent significant membrane deflections is equal to the maximum allowable channel width, roughly estimated to be around $284\ \mu m$ (see section 4.5).

7.1 CLOGGING PRESSURE OF BUBBLES MOVING THROUGH CONTRACTIONS

Bubbles moving along a path with various cross sectional areas are prone to get stuck in contractions that are smaller than their size. These bubbles can block the flow and

disturb the flow distribution or functionality of the system. To clear the clogged contraction, an external pressure called clogging pressure has to be applied to push the bubbles out of the contractions.

As discussed in section 2.1, stationary bubbles or bubbles moving at a very slow rate are generally dry. The only situation in which stationary or slow bubbles remain lubricated is when the surface is totally wetting $(\theta_{equ} \approx 0)$. In reality, stationary bubbles in microfluidic systems are generally dry since the surfaces are rarely totally wetting. On non-ideal surfaces which exhibit contact angle hysteresis, dry bubbles experience pinning forces due to the contact angle hysteresis. They may also experience capillary forces if a liquid region exists around them (see section 2.2.2). In contractions between posts, even when a bubble is dry, the corner regions occupied by liquid provide gas-liquid interfaces and capillary pressure acts on the bubble; under such conditions, this same bubble also experiences an additional capillary pressure due to the change in the cross-sectional area.

Bubbles that have difficulty passing through contractions are herein referred to as clogging bubbles. We assume the velocity of the bubble is almost zero along the contraction and the rest of the system remains at equilibrium. This situation is called quasi-static. This assumption allows us to neglect all the dynamic aspects of the motion of the bubble through the contraction and focus on the effect of geometry on the clogging pressure [27].

For a circular channel contracting from a radius r_L to a radius r_R depicted in Figure 63, Jensen et al. [27] calculated the clogging pressure employing the quasi-static assumption. They neglected contact angle hysteresis and assumed that on both sides of the bubble the contact angle is constant; in other words, they assumed the surface is ideal. The clogging pressure is the maximum of the position-dependent pressure drop across the bubble, i.e. the minimal external pressure that must be supplied to avoid clogging. On ideal surfaces, where contact angle hysteresis and pinning forces do not exist, the clogging pressure is equal to the largest negative capillary pressure exerted on the bubble:

$$P_{clog} = P_L - P_R = \max\{-\Delta P_{cap}(x_C)\} \tag{84}$$

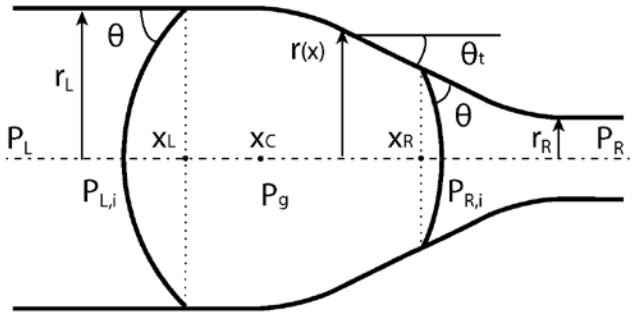

Figure 63: Bubble moving through a tapered contraction, adapted from Jensen et al. [27]

For dry bubbles on non-ideal surfaces with contact angle hysteresis, the clogging pressure will be larger than the largest negative capillary pressure since pinning forces are also acting on the bubble.

The capillary pressure difference between the left and right interfaces of the bubble can be calculated according to the Young-Laplace equation as shown in Eqs. (85) and (86). Note that $P_{L,i}$ and $P_{R,i}$ are the pressure of the liquid at the interfaces and are different from liquid bulk pressure, P_L and P_R.

$$\Delta P_{cap}(x_L) = P_g - P_{L,i} = 2\sigma \frac{\cos[\theta - \theta_t(x_L)]}{r(x_L)} \tag{85}$$

$$\Delta P_{cap}(x_R) = P_g - P_{R,i} = 2\sigma \frac{\cos[\theta + \theta_t(x_R)]}{r(x_R)} \tag{86}$$

The overall capillary pressure applied on the bubble can be calculated by subtracting the outside pressure at the right interface from that of the left interface. The direction of the net force applied by this pressure is from right to left.

$$\Delta P_{cap}(x_c) = P_{R,i} - P_{L,i} = \Delta P_{cap}(x_L) - \Delta P_{cap}(x_R) \tag{87}$$

Substituting Eq. (85) and Eq. (86) into Eq. (87) yields

$$\Delta P_{cap}(x_c) = 2\sigma \left(\frac{\cos[\theta - \theta_t(x_L)]}{r(x_L)} - \frac{\cos[\theta + \theta_t(x_R)]}{r(x_R)} \right) \tag{88}$$

Jensen et al. [27] found that the highest clogging pressure was associated with those bubbles which spanned the entire contraction. Smaller bubbles which can fit inside the contractions experience less capillary pressure.

The beginning of any contraction can be approximated by a circle tangent to the tapered walls with radius of r_L and the capillary pressure becomes an always positive value as shown in Eq. (89)

$$\Delta P_{cap}(x_c) = 2\sigma\left(\frac{\cos\theta}{r_L} - \frac{\cos(\theta + \theta_t(x_R))}{r_L}\right) > 0 \tag{89}$$

When $\Delta P_{cap}(x_c)$ is positive, it acts in favor of movement and no clogging pressure would exist. Therefore, bubbles tend to spontaneously enter a contraction. As the bubbles moves forward in the contraction, the capillary pressure becomes negative. This transformation is presented through a case study in Appendix E.

In the microchannel dialyzer, we are interested in using microposts in the manifold areas both to provide adequate support for the membrane and to mitigate bubble blockage. Therefore, the bubbles will have to pass through the contractions between the posts. We need to have an estimation of the pressure drop along a row of posts to understand whether that pressure drop can overcome the clogging pressure of the contractions.

7.2 LITERATURE REVIEW: PRESSURE DROP IN A MICROPOST ARRAY

Over the past century, numerous studies have investigated flow characteristics across conventional-sized circular and rectangular tube banks in staggered and in-line arrangements. Through experimental studies, pressure drop data have been used to

develop friction factor correlations in different flow regimes, i.e. laminar, transitional and turbulent flows [108, 109].

For a geometry depicted in Figure 64, the Fanning friction factor for flow over an array of tubes is defined by

$$f = \frac{\Delta P}{2\rho U_{\max}^2 N_{row}} \tag{90}$$

where $U_{\max}$ is the average velocity at the minimum area across the flow. The Reynolds number is defined based on the tube diameter (d) as

$$\mathrm{Re} = \frac{\rho U_{\max} d}{\mu} \tag{91}$$

Most of the studies in the literature are limited to long tubes ($8 < h/d$) at transitional and turbulent flow regimes. It has been shown that for long tubes ($8 < h/d$), the friction factor is independent of the height-to-diameter ratio (h/d) at all flow regimes [108]. For intermediate tubes ($4 < h/d < 8$), the friction factor is independent of h/d in transitional and turbulent regimes but it strongly depends on h/d for laminar flow [110].

For short tubes ($h/d < 4$) the studies suggested no or very small dependence of the friction factor on h/d at high Reynolds numbers ($1000 < \mathrm{Re}$); however, similar to the intermediate tubes the friction factor for short tubes depends on h/d for lower Reynolds numbers ($\mathrm{Re} < 1000$).

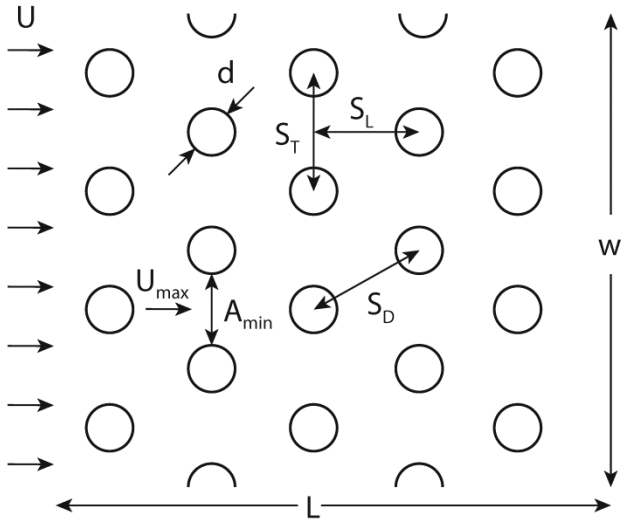

Figure 64: Staggered post arrangement: S_T, S_L, and S_D represent the transverse, longitudinal, and diagonal pitches, respectively. The height of the post is defined by h normal to the page.

In our application, the velocity in the channels is expected to be less than 5 cm/s, the depth of the device less than $100\,\mu m$, and the diameter of the posts around $100-200\,\mu m$. Considering these ranges, the Reynolds number defined based on the diameter of the microposts is less than 16, thus the flow is expected to be laminar.

To the best of the author's knowledge only 4 studies, listed in Table 13, have been conducted on short tubes ($h/d < 4$) at low/moderate Reynolds numbers (Re < 1000). We expect the Reynolds numbers in our microchannel dialyzer device to be less than 16. The presented correlations suggested that the friction factor is a function of the Reynolds number and transverse and longitudinal pitches (S_T and S_L). The dependence on S_T and S_L did not appear in the correlations derived from the experiments with fixed-pitch post arrangements.

Table 13: Friction factor correlations for staggered array of short tubes between parallel plates

Short et al. [110]	Flui	Re	d	h/d	Pitch
	air	175–4500	1.98,1.57 mm	Short tubes $1.9 < h/d < 7.5$	$S_T / d = 1.83 - 3.21$ $S_L / d = 2 - 6.4$
	$f = 35.1\left(\frac{S_L}{d}\right)^{-1.3}\left(\frac{S_T}{d}\right)^{-0.78}\left(\frac{h}{d}\right)^{-0.55}\mathrm{Re}^{-0.65}$				
Moores and Joshi [111]	Fluid	Re	d	h/d	Pitch
	water	200–10000	~ 4 mm	Short tubes $0.5 < h/d < 1$	$S_T / d = 1.3 - 1.36$ $S_L / d = 1.13 - 1.18$
	$f = 4.76\left(\frac{h}{d}\right)^{-0.742}\mathrm{Re}^{-0.502}$				
Kosar et al. [108]	Fluid	Re	d	h/d	Pitch
	water	5–128	50,100 μm	Short tubes $1 < h/d < 2$	$S_T / d = 1.5, 5$ $S_L / d = 1.5, 5$
	$f = \frac{434.75}{\mathrm{Re}^{1.7}}\left(\frac{h/d}{h/d+1}\right)^{1.1}\left(\frac{S_L S_T}{A_c}\right)^{-0.3} + \frac{172.5}{\mathrm{Re}_{hd}}\left(\frac{1}{h/d+1}\right)^{2}\left(\frac{S_L S_T}{A_c}\right)^{-0.3}$ A_c = cross section area of a single post = dh $\mathrm{Re}_{hd} = \frac{\rho u_{\max} d_h}{\mu}, d_h = \frac{4A_{\min}L}{A_{wet}} = \frac{wh - N_{row}dh}{2Lw + N_t\pi(dh - d^2/2)}$				
Prasher et al. [112]	Fluid	Re	d	h/d	Pitch
	water	40–100	50 – 150 μm	Short tubes $1.3 < h/d < 2.8$	$S_T / d = 2.4, 3.6, 2$ $S_L / d = 1.5, 5, 4$
	$f = 169.82\left(\frac{h}{d}\right)^{-0.64}\left(\frac{S_L - d}{d}\right)^{-0.258}\left(\frac{S_T - d}{d}\right)^{-0.283}\mathrm{Re}^{-1.35}$				

It is important to mention that for very short tubes ($h/d < 1$) with open ends, vortex shedding does not occur at Re < 50 [113]. We can expect that separation and vortex shedding will start at even larger Reynolds numbers when the tubes are confined between parallel plates. Therefore, in our device with $h/d \leq 1$ and Re < 16, the occurrence of separation and vortex shedding is not expected.

Kosar et al. [108] and Prasher et al. [112] had lower Reynolds number limits of 5 and 40 respectively in their experiments which are relatively close to the upper Reynolds number limit in our device (Re < 16). To understand if their suggested correlations are valid for our specifications, a 3D CFD model of a staggered geometry has been built in COMSOL, as shown in Figure 65, and the pressure drop along one row over a range of inlet velocities has been measured.

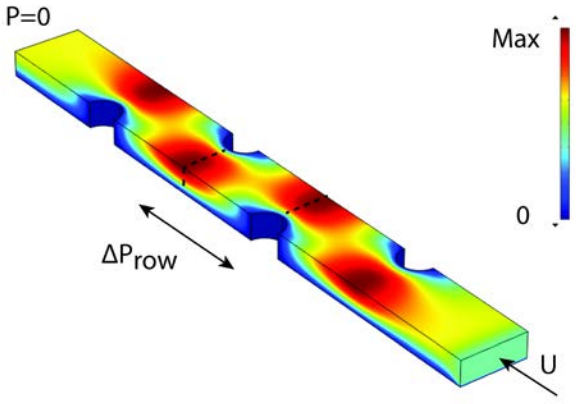

Figure 65: Velocity contour in the simulation domain, the pressure drop over the length of the middle row is measured for a range of inlet velocities

The CFD results showed that Kosar and Prasher correlations overpredict the pressure drop at our lower Reynolds numbers (Re < 16) by an order of magnitude. In those

correlations, the friction factor has a power relationship with the inverse of the Reynolds number. Therefore, for our low Reynolds number system, those correlations overestimated the friction factor and subsequently overpredicted the pressure drop.

Another study specific to creeping and low Reynolds number flows (Re < 8) through microposts is a theoretical study inspired by Darcy's law in porous media. Tamayol et al. [114] worked on square and staggered arrays of microposts embedded in a rectangular minichannel. For low Reynolds number flows in porous media, the Darcy equation describes a linear relationship between the applied pressure drop and the volume averaged velocity

$$\frac{dP}{dx} = -\frac{\mu}{\kappa}U \tag{92}$$

where μ is the fluid viscosity and κ is the permeability of the medium. In applications where a porous material is confined by solid walls, for example microchannels filled with porous media, and when the flow inside the porous medium is boundary driven, the Brinkman equation should be used instead

$$\frac{dP}{dx} = -\frac{\mu}{\kappa}U + \mu_{eff}\frac{d^2U}{dy^2} \tag{93}$$

where μ_{eff} is called the effective viscosity. Previous studies have shown that the viscosity ratio $\mu' = \mu / \mu_{eff}$ varies between 1 and 10. The assumption of $\mu' = 1$ is reasonable for highly porous materials. Tamayol et al. [114] assumed that $\mu' = 1/\phi$,

where ϕ is the porosity of the porous medium. Porosity of an equilateral staggered arrangement $(S_T = S_D)$ is given by

$$\phi = 1 - \frac{\pi d^2}{2\sqrt{3} S_T^{\,2}} \tag{94}$$

The last term in the Brinkman equation enables the solution to fulfill the no-slip boundary condition on solid walls. In the limiting case, where either there is no porous medium inside the channel or the boundary effects are dominant, the Darcy term vanishes and the equation becomes identical to the Stokes equation. On the other hand, in the limit of very dense porous media, the Brinkman equation reduces to the Darcy equation. The Brinkman equation is valid for creeping flow regimes where the inertial effects of the porous media on pressure drop are negligible. This assumption is valid when the Reynolds number defined based on the cylinder diameter is less than 8 [114].

For 2D flow in a porous medium between parallel plates subject to no-slip boundary conditions on the wall, the solution of the Brinkman equation for pressure drop per unit length becomes

$$-\frac{\Delta P}{L} = \frac{\mu Q \sinh\left(\frac{h}{\sqrt{\mu'\kappa}}\right)}{\kappa h \left[2\frac{\sqrt{\mu'\kappa}}{h}\left(-1 + \cosh\left(\frac{h}{\sqrt{\mu'\kappa}}\right)\right) - \sinh\left(\frac{h}{\sqrt{\mu'\kappa}}\right) \right]} \tag{95}$$

where Q is the 2D flow rate and is equal to the velocity multiplied by h [114]. The pressure drop along the length of a single row becomes

$$\Delta P_{row} = \frac{-S_L \mu U \sinh(\frac{h}{\sqrt{\mu'\kappa}})}{\kappa\left[2\frac{\sqrt{\mu'\kappa}}{h}(-1+\cosh(\frac{h}{\sqrt{\mu'\kappa}})) - \sinh(\frac{h}{\sqrt{\mu'\kappa}})\right]} \tag{96}$$

The only unknown in the pressure drop equation is the permeability (κ). Tamayol et al. [115] proposed the following correlation for the permeability in an equilateral staggered arrangement of microposts

$$\frac{\kappa}{d^2} = \frac{0.16\left[\frac{\pi}{2\sqrt{3}\varphi} - 3\sqrt{\frac{\pi}{2\sqrt{3}\varphi}} + 3 - \sqrt{\frac{2\sqrt{3}\varphi}{\pi}}\right]}{\sqrt{1-\varphi}} \tag{97}$$

where post density φ is defined as $1-\phi$ and varies between 0 and 1. Tamayol et al. [114] showed that using the suggested permeability correlations, the pressure drop acquired by the equation is in agreement with numerical and experimental results for five different geometries. However, in their further experimental investigations of additional geometries they reported that the correlation sometimes failed to accurately predict the pressure drop [116].

We have compared the pressure drop through one row of microposts predicted by Tamayol et al. [114] and data obtained by CFD simulations for cases summarized in Table 14. We have also compared the data with an expression for analytical pressure drop through 2D parallel plate geometry, Eq. (60), with the inlet velocity of $U_{\max}$ (average velocity of the flow through contractions). The results are shown in Figure 66.

Table 14: Parameters used in CFD simulations

d (μm)	h (μm)	S_L (μm)	S_T (μm)	U (cm/s)
100	100	350	303	1 – 10
200	100	450	390	1 – 5

The comparison shows that the Tamayol correlation underpredicts the pressure drop while parallel plate estimation overpredicts it. Both correlations can provide us with close enough approximations of the pressure drop per row of a staggered array. In the next section we will see that the range of the pressure drop along each row is essentially much smaller than the clogging pressure of the contractions.

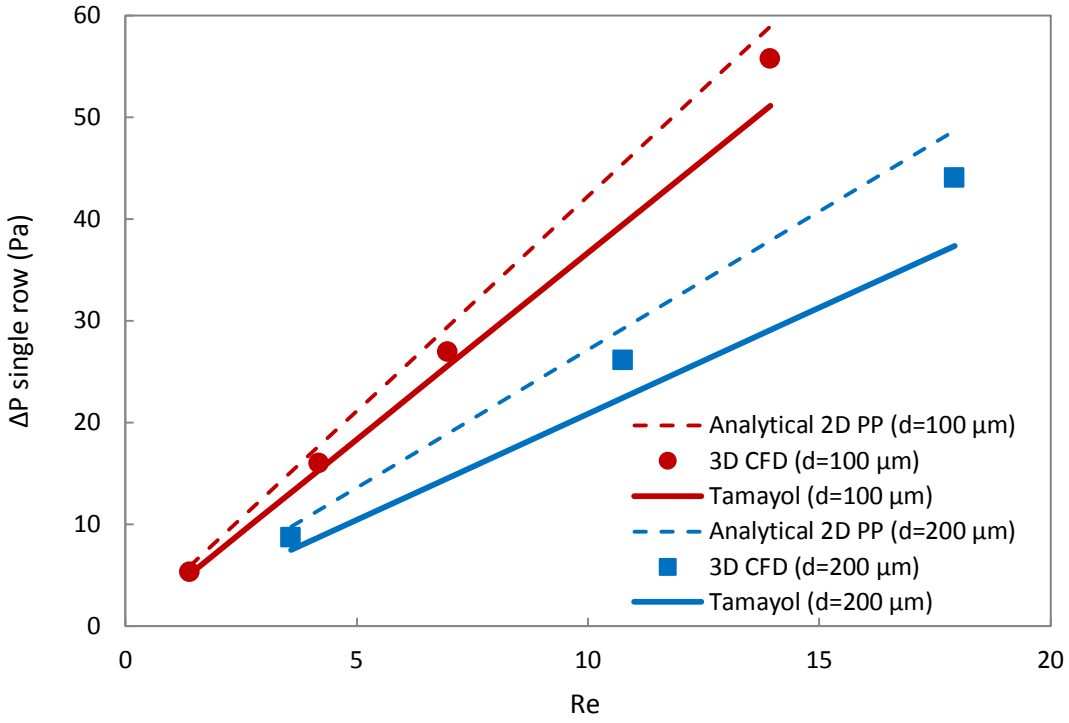

Figure 66: Comparison of pressure drop through a single row in a staggered array from analytical correlation for 2D parallel plates (PP) with the inlet velocity of U_{max}, 3D CFD, and Tamayol et al.'s correlation [114]

7.3 CLOGGING PRESSURE FOR A BUBBLE PASSING A CONTRACTION BETWEEN MICROPOSTS

To the best of the author's knowledge, so far there have not been any studies on the clogging pressure for bubbles passing a contraction within an array of microposts. Such contractions have changing tapering angles, in contrast to channel contractions with a constant tapering angle such as those analyzed in Jensen et al [27].

In order to understand the type of forces acting on the bubbles in a micropost array, we need to categorize the bubbles into different size categories as shown in Figure 67. Small bubbles are the ones which originally had a diameter smaller than the open space between the posts. Medium bubbles are specified as bubbles which fit inside the contraction or extend beyond the contraction area but do not touch more than three posts of the array. Large bubbles, on the other hand, come into contact with more than three posts.

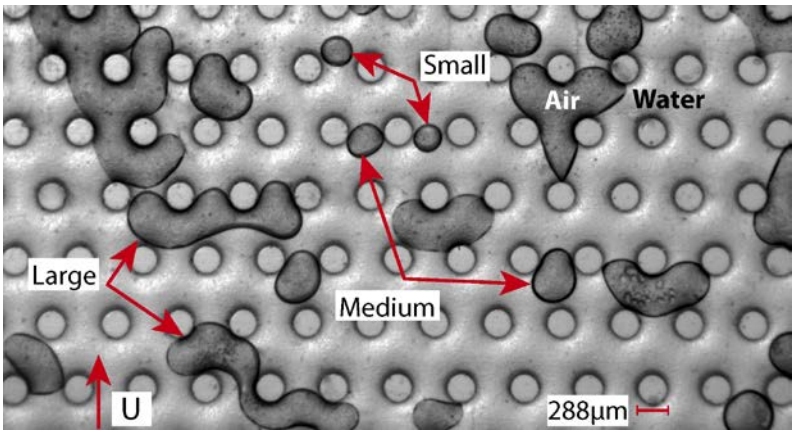

Figure 67: Classification of bubbles based on their size relative to the open space between posts

SMALL BUBBLES: Small bubbles can pass a contraction without experiencing clogging pressure. The velocities are low and bubbles are generally dry in our system. Figure 68 shows the contact angle hysteresis in the front and back contact lines of a small bubble. It is assumed that the planar curvature of the small bubble is constant. Due to the contact angle hysteresis, bubbles experience capillary and pinning forces. The maximum capillary pressure is given by

$$\left|\Delta P_{cap}\right|_{\max} = 2\sigma\left(\frac{\cos\theta_{rec} - \cos\theta_{adv}}{h}\right) \tag{98}$$

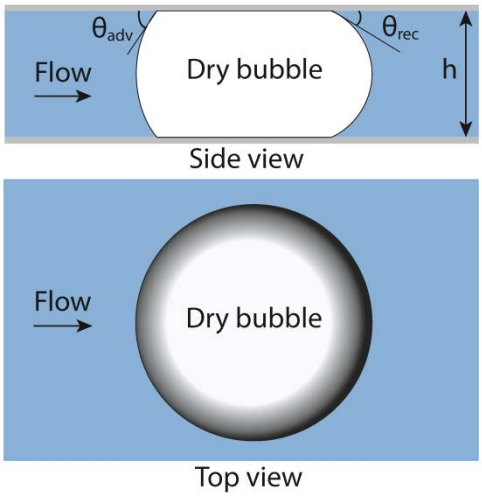

Figure 68: Side and top views of a small dry bubble confined between parallel plates

Eq. (98) suggests that reducing the depth increases the capillary pressure. Reducing the depth also increases the pressure drop per length. The length of a bubble with a constant volume will be larger if we reduce the depth; therefore, it will experience a larger pressure difference across its length. Overall, reducing the depth has a positive influence on the movability of small bubbles (more details in section 4.3). However,

reducing the depth also demands a higher pressure drop and subsequently a higher sealing pressure for the device.

MEDIUM BUBBLES: Medium bubbles must contract to pass through openings between posts as shown in Figure 69. Therefore, they experience an additional capillary pressure or the so-called clogging pressure. The clogging pressure depends on the size of the bubble, the open spacing between the microposts, the radius of the microposts, and the curvature of the bubble outside of the contraction.

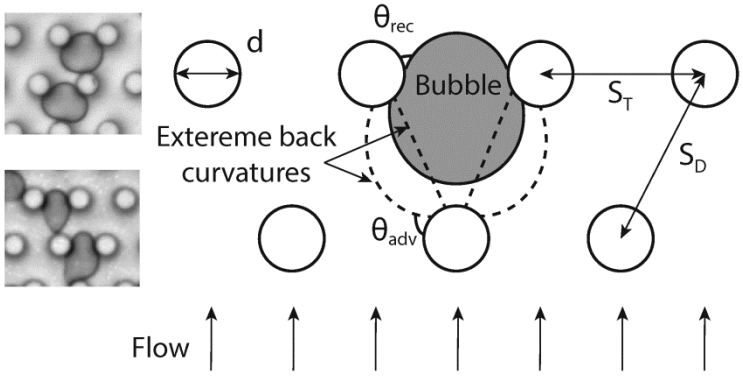

Figure 69: Medium bubbles passing through contractions, bubbles with a flat back interface experience the largest capillary pressure

The front interface curvature varies depending on the location of the front contact line of the bubble and the diameter of the posts. It is easier for the bubble to enter the contraction between posts with smaller diameters. However, the maximum capillary pressure occurs at the narrowest part of the contraction. If we keep the open spacing between the posts constant, the maximum capillary pressure would become

independent of the post diameter. Obviously, increasing the open distance reduces the capillary pressure.

The back curvature of a bubble is not necessarily confined between the posts and its shape depends on the bubble size, geometry, and flow conditions. In practice, the curvature of the bubble interface outside of the contraction is rarely constant. It is possible to make an extreme estimate of the in-plane back curvature of those bubbles that fit inside the contraction or extend beyond the contraction region as shown in Figure 69. In the most extreme scenario, the front and back of the bubble would have the largest and lowest possible curvatures, respectively. The maximum clogging pressure becomes

$$\left|\Delta P_{cap}\right|_{\max} \simeq \underbrace{2\sigma\left(\frac{\cos\theta_{rec}-\cos\theta_{adv}}{h}\right)}_{hysteresis} + \underbrace{2\sigma\left(\frac{\cos\theta_{rec}}{S_T-d}\right)}_{contraction} \tag{99}$$

Assuming $\sigma = 0.072$ N/m, $\theta_{rec} = 5^{\circ}$, $\theta_{adv} = 45^{\circ}$ (contact angles of the PEO coated surface), $d = 100$ μm, $S_T = 350$ μm, and $h = 100$ μm, the maximum clogging pressure becomes about 990 Pa. In shallow geometries, the larger term in the above equation is the depth-wise capillary pressure due to hysteresis which acts on small bubbles as well. For this case, the depth-wise capillary pressure is 416 Pa.

This pressure is an order of magnitude larger than the viscous pressure drop along one row of microposts at low flow rates (see section 7.2). The blockage of one of the contractions increases the flow velocity in the open cross section which increases the

pressure drop along that row. Furthermore, the blockage produces a very low velocity region in front of the contraction which causes the pressure drop between the front and the back of the bubble to be, at its maximum, twice the pressure drop along one row. Even with those considerations, when a medium bubble has only blocked a single contraction in a row of an array of microposts, the pressure drop along the length of the bubble is not even close to the clogging pressure so it will never pass the contraction. Our options for improving the movability of the medium and small bubbles are limited to the following:

a) A gradual increase in the depth of the device is the best geometrical-based solution. It is possible to derive the minimum slope that results in a zero clogging pressure for medium bubbles. A gradual increase of the depth also helps the movement of large bubbles. Unfortunately, manufacturing of plates with variable depth is not yet possible for our group.

b) Making the surfaces more hydrophilic reduces both capillary and pinning forces as discussed in section 2.4. With PEO coating we could achieve $\theta_{rec} = 5^{\circ}$ and $\theta_{adv} = 45^{\circ}$. Further improving the coating quality may lead to further decreases in the contact angles and additional reductions in capillary and pinning forces.

c) From everyday laboratory practice, it is known that one way to purge a microfluidic system is flushing it with a high flow rate pulse. For systems which continuously produce gas bubbles, for example direct methanol fuel cells (DMFC) where gas bubbles are generated as a reaction product, the

purging can be performed periodically [9]. As the microchannel dialyzer device deals with degassing and air ingress continuously, a periodic high flow injection through the duration of the treatment can be successful in terms of removal of small and medium bubbles but it requires extra sealing pressure.

LARGE BUBBLES: The final size category is large bubbles which come into contact with more than three posts. It is impossible to derive a capillary pressure formula for large bubbles since their geometries have too many different curvatures and each bubble has a unique shape.

Those large bubbles that produce enormous blockages also cause a significant pressure buildup behind them. The pressure drop across those large bubbles is generally able to move them. They may pass the contractions in one piece or they may break up and leave smaller fractions (small, medium, or large bubbles) behind. Those large bubbles that do not cause a significant blockage and do not experience enough pressure force remain stagnant.

In a partially hydrophilic system, large bubbles tend to partially enter all the contractions they see along their way. This is due to the positive capillary pressures at the beginning of the contractions (see section 7.1). When a bubble experiences enough driving force by the pressure field to overcome the clogging pressure of one of the contractions it is partially inside, it will pass through that contraction.

In a micropost array, different contraction sizes may exist. The wider contractions result in a smaller curvature for the advancing interface of the bubbles and bubbles prefer to pass through them, as shown in Figure 70. The relative size of the contractions with respect to each other strongly affects the direction of the motion. Using this characteristic, large bubbles have the highest potential for geometry-based management.

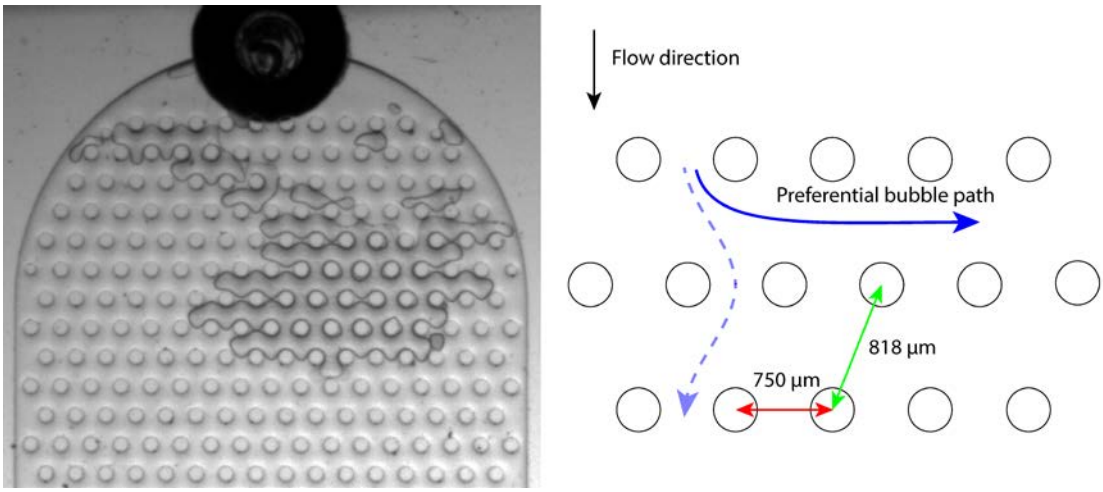

Figure 70: Bubbles prefer to proceed through the larger contractions

7.4 PREFERENTIAL BUBBLE PATHS IN DIFFERENT STAGGERED ARRANGEMENTS

In order to investigate preferential bubble paths in staggered arrangements of microposts, we have characterized the arrangements with hexagonal unit cells, as shown in Figure 71. By changing theta (θ), the top angle of the hexagon, the relative dimensions of the openings (red and green lines) with respect to each other will change.

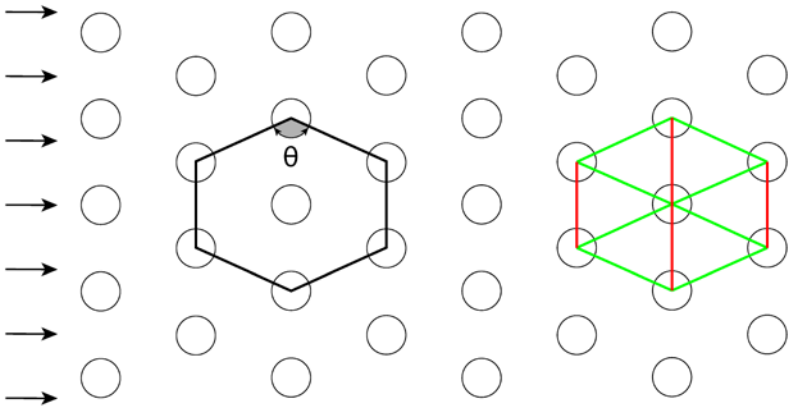

Figure 71: Relative size of openings in a staggered arrangement is determined by the top angle of the hexagon

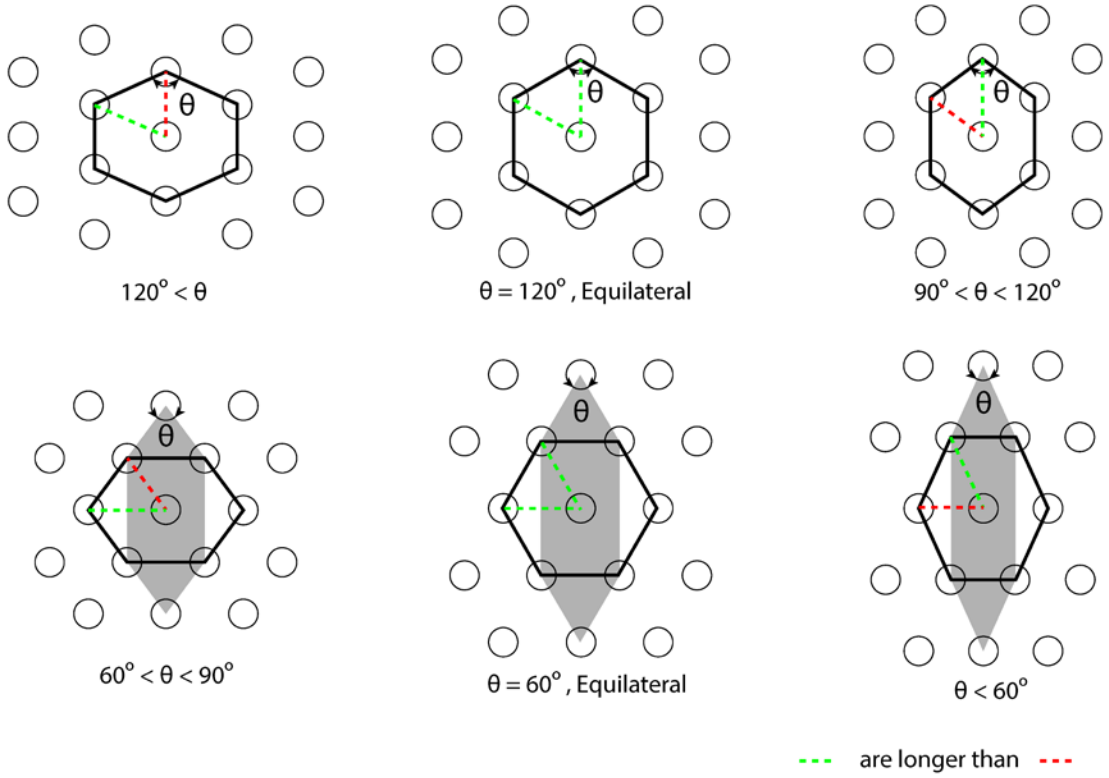

Figure 72: Categorizing staggered arrangements into six groups based on the top angle of the hexagon

Six primary types of post arrangements with θ ranging from 0 to 180 degrees have been defined, as shown in Figure 72. For theta angles smaller than 90 degrees shown in the second row of Figure 72, it makes more sense visually and also in terms of bubble motion to consider hexagons with a black outline as the unit cells rather than the gray hexagons with the theta angles.

For these six designs, we have looked into the preferential bubble paths through the unit cells. The results are presented in Figure 73. Large arrows present the more noticeable bubble trajectories and small arrows shows the less frequent paths.

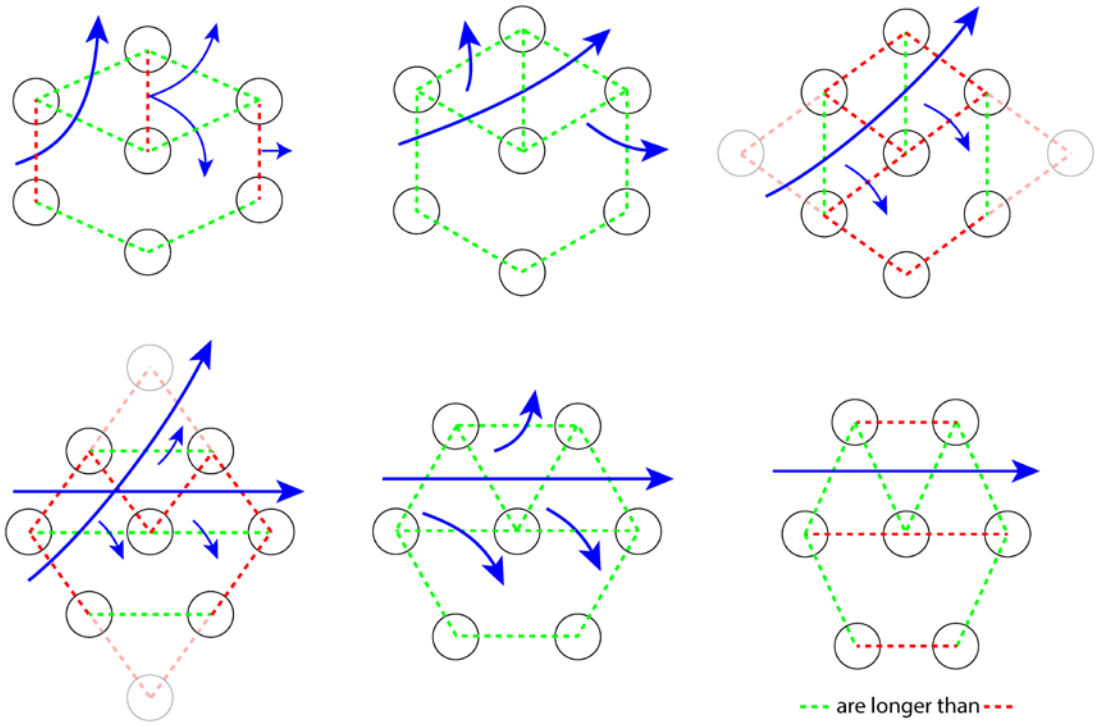

Figure 73: Preferential bubble paths through different arrangements depends on the relative size of openings. Large arrows present the more noticeable bubble trajectories and small arrows shows the less frequent paths. For a given cell, green spacings are larger than the red ones.

Two primary factors influencing the bubble motion have been identified:

a) Bubbles generally take the green and larger opening over the red and smaller opening if they have a choice.
b) If the choice is between openings with the same size, bubbles prefer to continue along their current trajectory because of inertia.

There is a possibility that the ratio of the diagonal spacings to the post diameters (S_D / d) affects the bubble trajectories. The porosity of the array is defined by the fraction of the volume of the voids over the total volume. For any arrangement, the unitless characteristic length (S_D / d) and θ determine the porosity of the array. For very dense arrays where S_D / d is close to 1, the preferential bubble paths may be different from the observed paths in our experiments.

Stagnant bubbles in six example arrangements representing the six primary types of arrangements are presented in Figure 74. The size of the microposts in Figure 74a and Figure 74b is $300\ \mu m$ while it is $364\ \mu m$ in Figure 74c. The depth of the layers is about $100\ \mu m$. The water flow rate at which these three images were taken is 1.3 ml/min. The diagonal distance between the posts for the arrangements in Figure 74a and Figure 74b is $600\ \mu m$ while it is $818\ \mu m$ for the arrangements in Figure 74c.

Figure 74a presents equilateral post arrangements. For the arrangements with $\theta = 120^{\circ}$ oblique advancement of bubbles is frequently observed. Transverse advancement of

bubbles still occurs since all the opening are equal to each other and blockages downstream of a bubble affect the path it would take. For the same reason in equilateral arrangements with $\theta = 60^{\circ}$ longitudinal advancement of bubbles is observed frequently but bubbles are not always restricted between two adjacent rows.

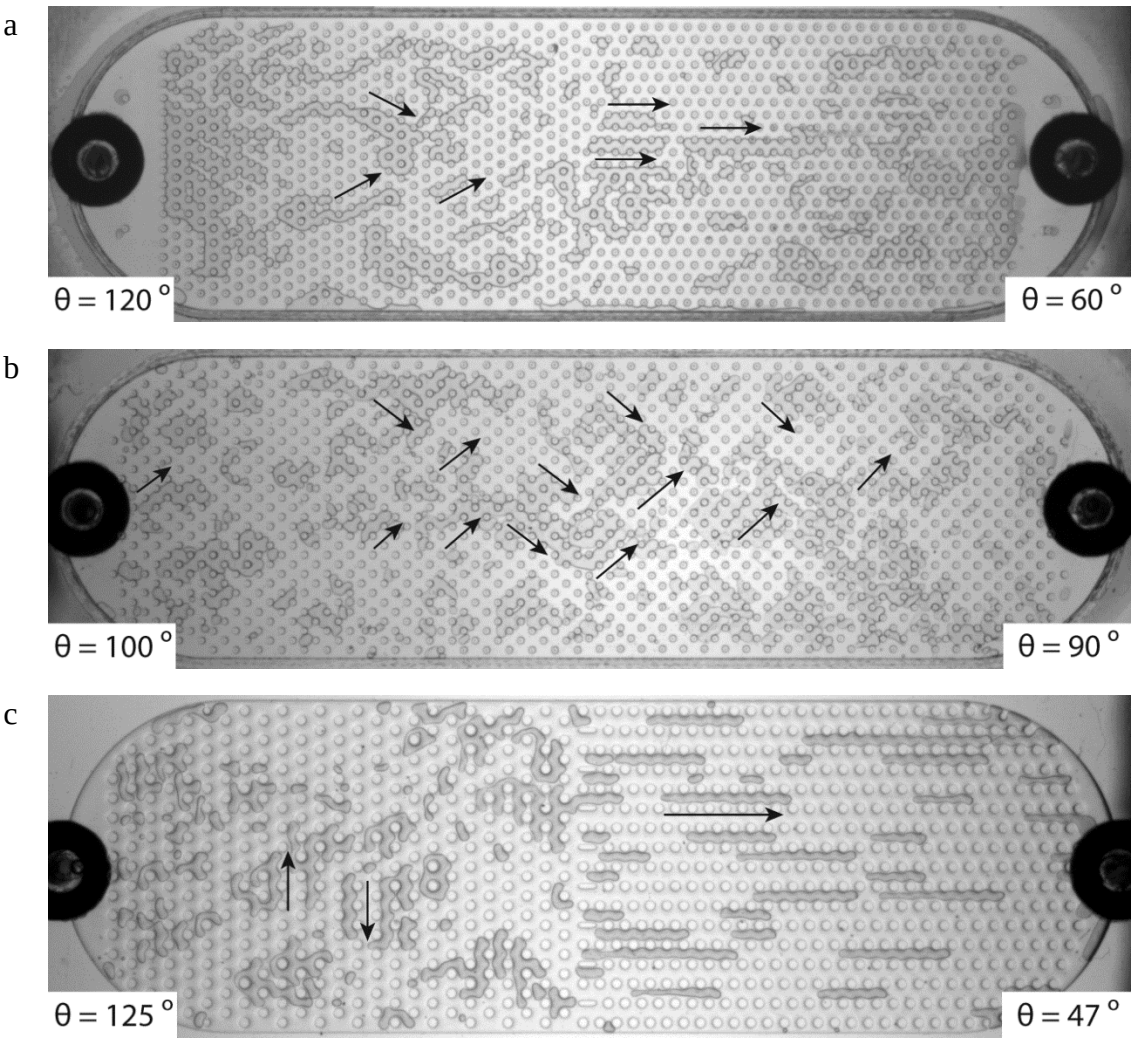

Figure 74: Preferential bubble paths for a) equilateral arrangements, b) arrangements with $60^{\circ} < \theta < 120^{\circ}$, and c) arrangements with $120^{\circ} < \theta$ and $\theta < 60^{\circ}$

Figure 74b presents post arrangements with $60^\circ < \theta < 120^\circ$. In both arrangements, oblique advancement of bubbles is dominant. Longitudinal advancements start occurring at $\theta = 90^\circ$ but they become more frequent and evident for theta angles closer to $\theta = 60^\circ$.

Figure 74c presents post arrangements with extreme theta angles, $\theta < 60^\circ$ and $120^\circ < \theta$. For arrangement with $120^\circ < \theta$, the dominant bubble trajectory is in the transverse direction. Bubbles move longitudinally to the next column of the array after causing significant blockages. For arrangements with $\theta < 60^\circ$ a longitudinal path is the dominant path and *almost always* the only path that bubbles take. This design has a great advantage over the other arrangements: it can keep the bubbles restricted between two adjacent rows and guide them toward the desired destination without forcing them to take meandering paths. The bubble retention behavior in the two extreme cases of arrangements will be compared in the following section.

7.5 STATISTICAL COMPARISON OF BUBBLE RETENTION BETWEEN ARRANGEMENTS WITH $\theta < 60^\circ$ AND $120^\circ < \theta$

In this section, a statistical comparison of bubble retention at different flow rates for the arrangements previously discussed with extreme theta angles, $\theta < 60^\circ$ and $120^\circ < \theta$, is presented.

Figure 75 presents an image of the lamina filled with water, the dimensions of the two arrangements, and a 3D ZeScope image of the metal master used to fabricate the

lamina. The lamina is fabricated using a metal master according to method A described in section 5.2.1. The two arrangements have the same diagonal and transverse spacings and the same post diameter. Therefore, they share the same average velocity at the minimum area (U_{max}) and Reynolds number at any flow rate. The porosities are 0.81 and 0.78 in the left and right arrangement, respectively.

The inevitable variations in the depth of the metal master results in variations in the depth of the lamina. The ZeScope measurements showed that the deepest part of the lamina is around the widest opening with a depth of 105 μm and the shallowest part of the lamina is in the middle of the smaller opening with a depth of $90-100$ μm.

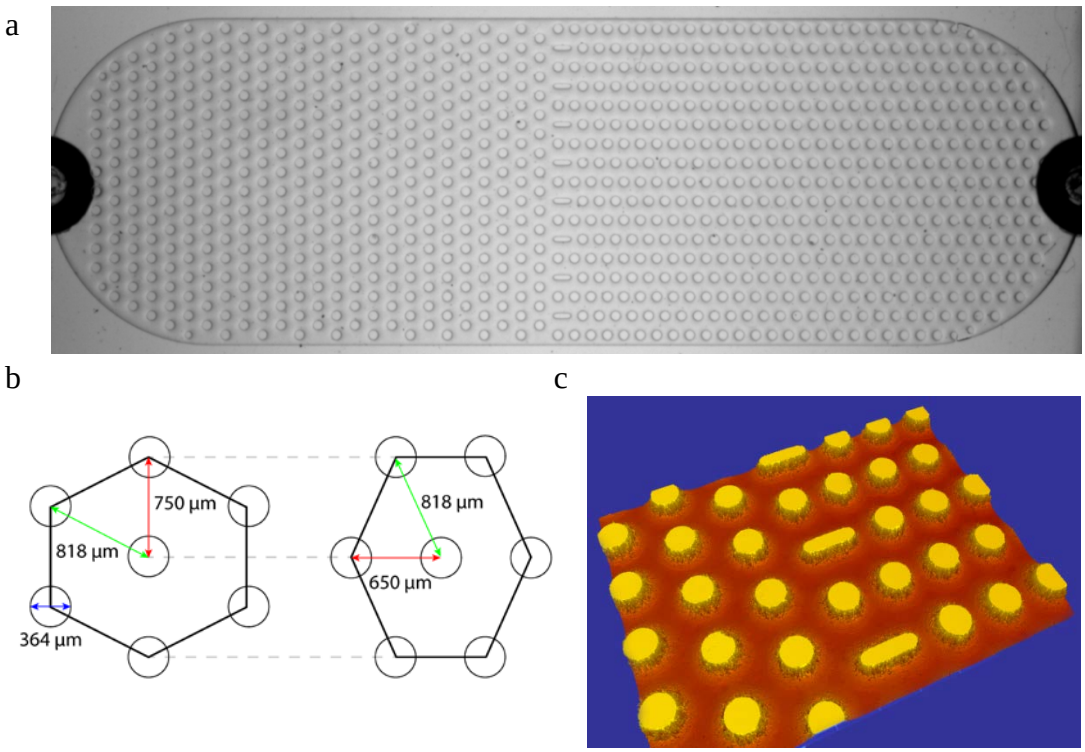

Figure 75: a) Image of the lamina filled with water, b) dimensions of the unit cells in the studied arrangements and c) a Zescope image of the middle part of the lamina connecting the two arrangements

7.5.1 EXPERIMENTAL PROCEDURE

The experimental setup is described in section 5.1. The experiments were performed at water flow rates of 0.65, 1.30, 1.95, and 2.60 ml/min which correspond to average velocities of 2.21, 4.42, 6.63, and 8.84 cm/s at the minimum area $(U_{\max})$, assuming a constant depth of $100\ \mu m$. These velocities correspond to Reynolds numbers of 7.7, 15.4, 23.1, and 30.8 (based on the diameter of the posts). At each flow rate the experiment was repeated 12 – 13 times to produce a large population for a statistical study. A single image of the lamina filled with water in the absence of bubbles was taken before the experiments. This image is used as a *background image* in image processing. For each experiment, a constant volume of air $(0.93 \pm 0.01\ ml)$ was injected into the device while water was pumping into the device. The system became steady after 20 – 30 seconds as no bubble movement occurred. A single image of the remaining stagnant bubbles in the lamina was taken 1 minute after the injection.

After each experiment the remaining bubbles in the system were washed away with a water injection. A few small bubbles usually remained in the system which immediately coalesced with the injected air in the following experiment. Note that the volume of the injected air was more than 10 times larger than the volume of the lamina; the whole lamina was momentarily filled by air after the injection. It is difficult but crucial to obtain high quality images for image processing. Leakage, dust speckles, light refraction from PDMS, and over tightening the clamp screws can all result in unusable images.

7.5.2 IMAGE PROCESSING

In order to obtain statistical data from the images we need to perform image processing. Each bubble has to be recognized as an individual particle. The number of bubbles, their size, and their locations should be documented. The image processing steps are summarized below. The Matlab codes written for processing the images are provided in Appendix F.

a) Import the image containing bubbles and the background image into Matlab (see Figure 76a)
b) Normalize the images
c) Perform intensity based registration of the image containing bubbles on the background image. Due to the environmental vibrations the field of view of each image is slightly different from the others. Since the images have to be subtracted from the background image, they should be registered on the background image first. This step is the most time consuming part of the process.
d) Crop the images and divide each into 5 sub images for accurate thresholding
e) Subtract the image from the background image
f) Normalize the results
g) Import the post mask and the inlet/outlet holes masks into Matlab
h) Threshold each section with a suitable value. The result of the thresholding is a binary image (see Figure 76b and Figure 76c). As the backlighting is not completely uniform, the shadows of the bubble edges in different locations

have different levels of darkness. Choosing the right thresholding value is very important and requires substantial attention. Different threshold values have been tested on one image and the binary bubble outline has been compared with an actual bubble outline in Adobe Photoshop. The chosen thresholding values result in almost exact matches for the outlines.

i) Mask inlet/outlet ports
j) Clean the images. This step involves morphological operations and erasing very small noise particles.
k) Multiply the image by the mask of the posts to regenerate the posts that disappear in the cleaning process
l) Connect the 5 images
m) Label the bubbles (see Figure 76d)
n) Gather the statistics on the bubbles (particles)
o) Categorize the bubbles into two groups based on the micropost arrangement they are in
p) Save the required information about each bubble including label, size, centroid location, and positions of the front and back interfaces on a file.

The rest of the process has been performed manually. Those bubbles which are shared between the two arrangements or which are stopped by the edges of the device have been discarded. This step was performed using the bubble labels. The statistics related to each image such as the number of the bubbles in each arrangement, the average and

median bubble size in each image, the blockage ratio (total area of the bubbles/ total cleared area of each arrangement) have been derived.

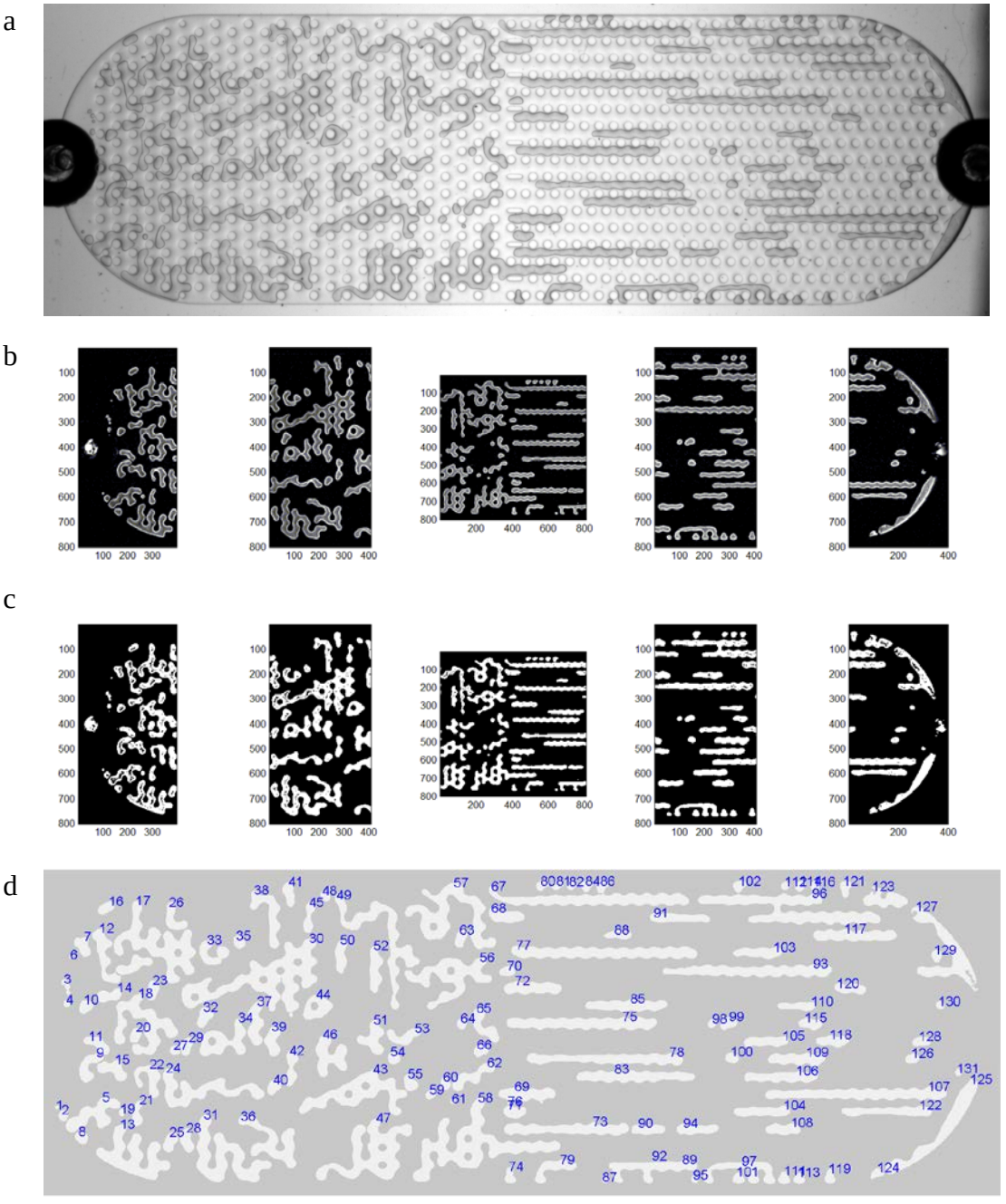

Figure 76: a) Normalized image after cropping, b) normalized five-piece image after subtraction from the background, c) thresholded (binarized) pieces, and d) labeled bubbles

7.5.3 RESULTS

Figure 77 presents images of the remaining bubbles in the system at different flow rates.

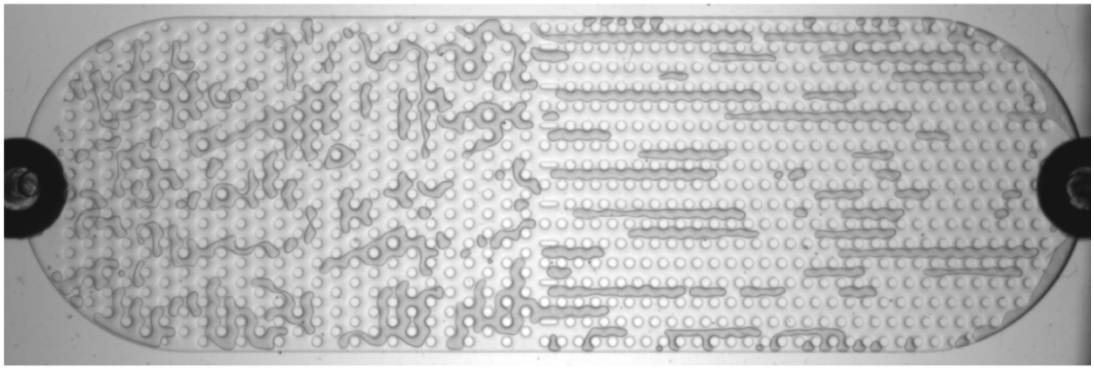

Flow rate = 0.65 ml/min

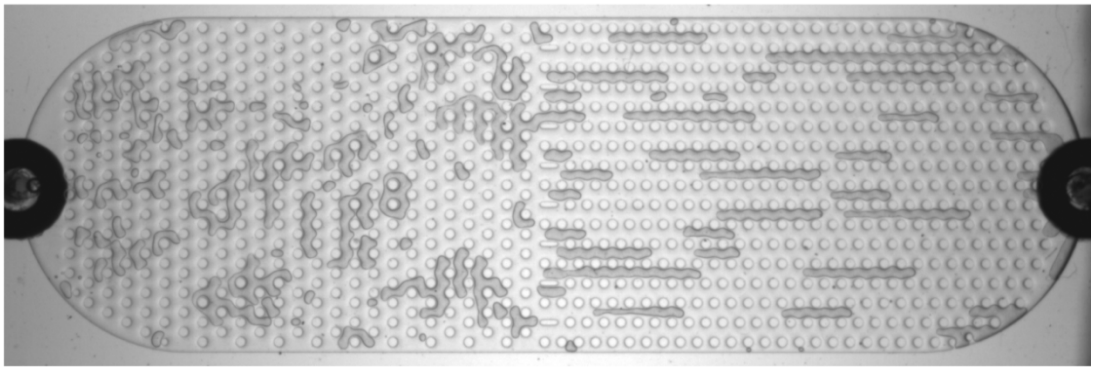

Flow rate = 1.3 ml/min

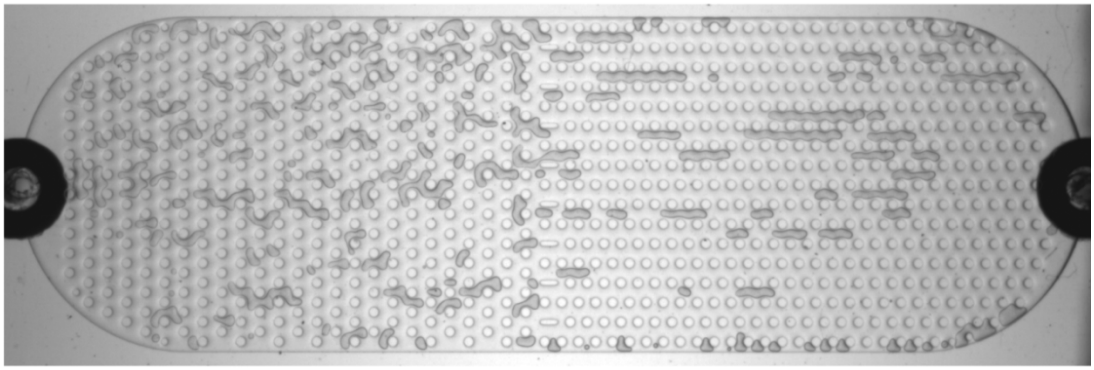

Flow rate = 2.6 ml/min

Figure 77: Remaining bubbles in the lamina at different flow rates

Bubbles take meandering paths in the arrangement on the left while they take straight paths in the arrangement on the right which we refer to as the parallel post arrangement. The images clearly show that by increasing the flow rate, the size of stagnant bubbles in both arrangements decreases.

Figure 78 compares the blockage percentage in the two arrangements. The blockage percentage is defined as the volume occupied by bubbles over the total available volume in each arrangement. The blockage percentage in the right arrangement is 10 to 15% less than the left arrangement. The error bars represent a 95% confidence interval for the average values including the image processing resolution and the standard errors of the measurements in each dataset.

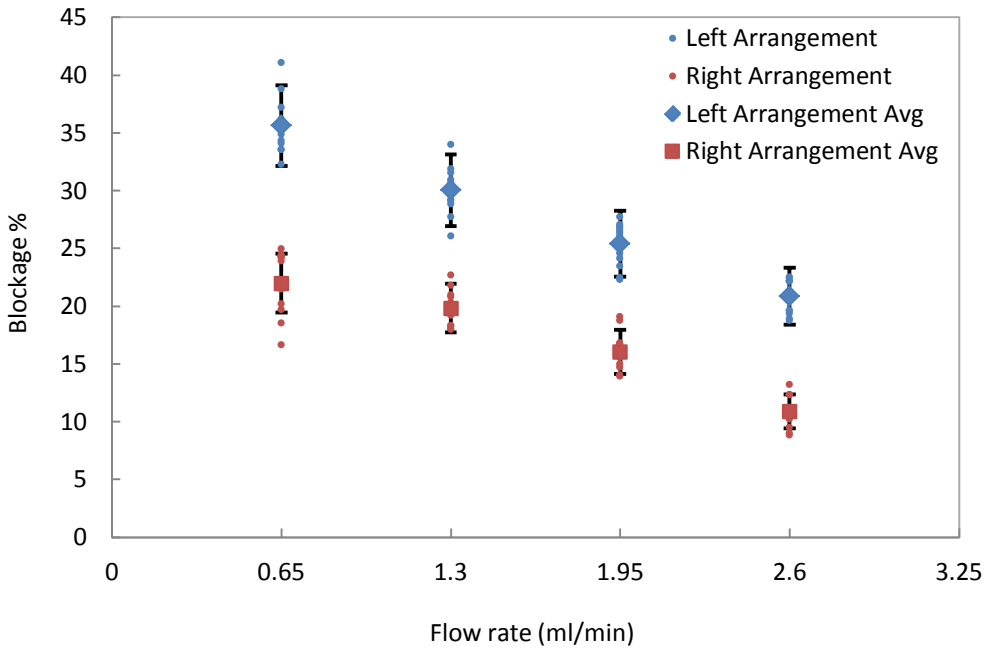

Figure 78: Blockage percentage vs. flow rate, small dots represent the blockage percentages in the set of experiments while large symbols represent the average blockage percentage at each flow rate

Investigating the number of stagnant bubbles in each arrangement and comparing their sizes may reveal the reason behind the lower blockage percentage in the parallel post arrangement. Figure 79 compares the number of stagnant bubbles in the two arrangements; there are fewer stagnant bubbles in the parallel post arrangement. Increasing the flow rate first increases the number of stagnant bubbles in both arrangements. At the highest tested flow rate, the average number of stagnant bubbles remained the same for the left arrangement while it decreased for the right arrangement. The remaining bubbles in the system especially at higher flow rates are products of bubble breakups. The number of breakups is expected to increase with flow rate. The result suggests that at the highest tested flow rate, more broken up bubbles were able to exit the device.

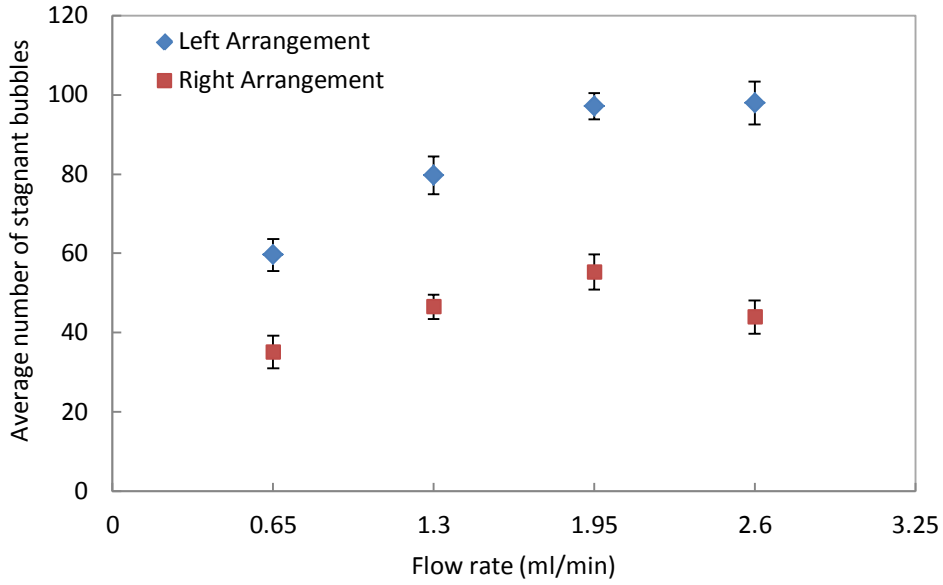

Figure 79: Average number of stagnant bubbles vs. flow rate

Figure 80 presents the average size of the stagnant bubbles in the arrangements. From a statistical point of view, there is no significant difference between the average sizes of stagnant bubbles in the two arrangements. This could be due to the presence of outliers (very large or very small bubbles) in the samples. The average value is not resistant to outliers while the median value is. Therefore, consideration of the median values can be beneficial.

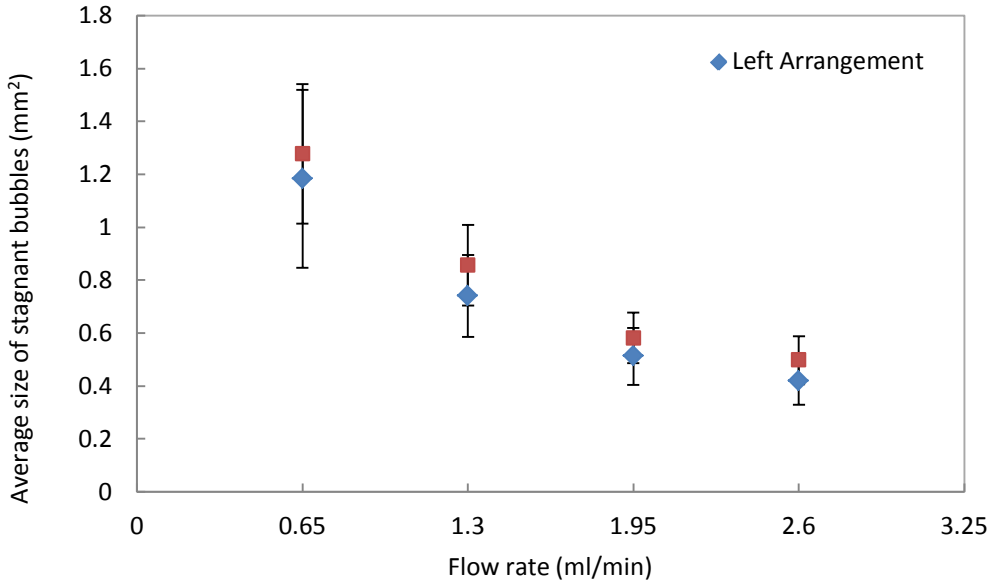

Figure 80: Average size of stagnant bubbles vs. flow rate

Figure 81 presents the median size of the stagnant bubbles in the arrangements vs. the flow rate. Preforming a t-test, at all the tested flow rates the median size of the stagnant bubbles in the parallel micropost array is significantly different from the left arrangement and consistently larger. The results demonstrate that in the left arrangement a larger number of bubble breakups occur and the remaining bubbles are smaller. The results provide hard evidence that when bubbles take meandering path

they break up more often and leave small bubbles behind the posts. Figure 82 shows stagnant bubbles at the high flow rate of 20 ml/min. It is evident that in the left arrangement, where bubbles take meandering paths, that a lot of bubbles were hindered by getting pressed against posts.

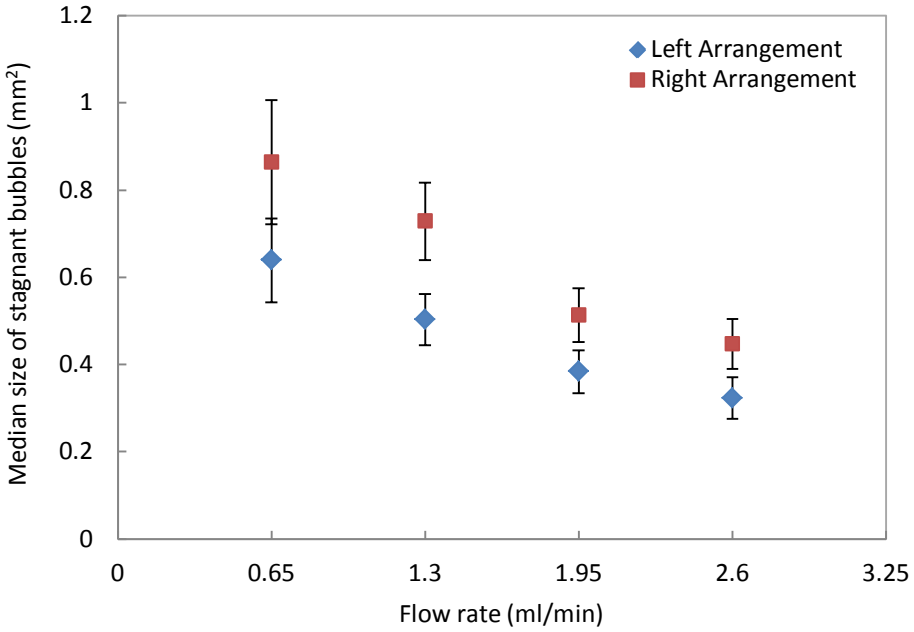

Figure 81: Median size of stagnant bubbles vs. flow rate

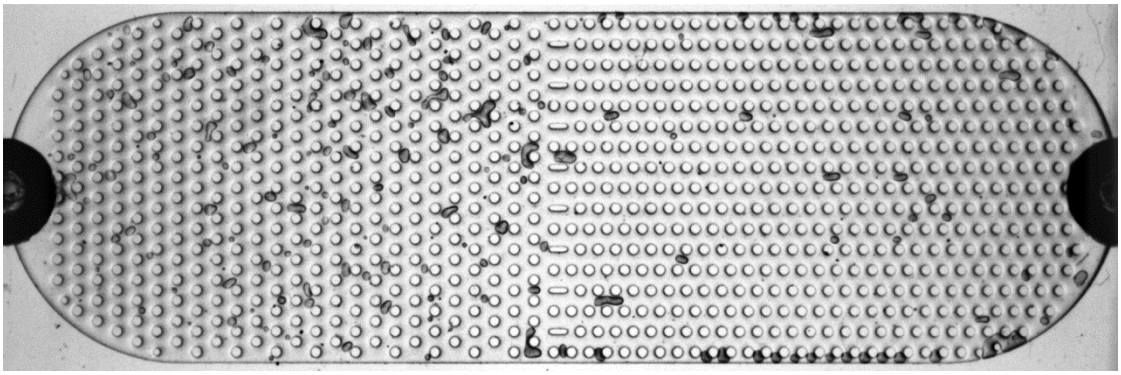

Figure 82: Remaining bubbles in the lamina at the flow rate of 13 ml/min after pausing the flow, note the bubbles that are pressed against the posts in the left arrangement

7.6 BUBBLE BREAKUP AND STAGNATION

In this section, more information on the bubble break up phenomenon and the “sweet spot” for bubble stagnation is provided. In general, bubble breakups may occur due to several reasons such as high shear stress or pressure, turbulent fluctuations or collision, and interfacial instabilities. Herein, to study the effect of geometry on bubble break up, we focus on the effect of shear and normal stresses. When the drag force in the liquid is larger than the surface tension forces, the bubble disintegrates into smaller bubbles. Furthermore, if the difference between gas and liquid pressures becomes smaller than the Laplace pressure, the liquid pressure forces the gas into a narrow thread. The strangling action of the liquid at the neck breaks up the bubble. Figure 83 presents consecutive images of bubble strangling in two different arrangements.

Another circumstance where necking was observed was when the front cap of the bubble moved forward while the back cap remained pinned. In this situation, the pressure difference between the gas and the front liquid was enough to overcome the pinning forces at the front but the pressure difference between the front liquid and the gas was not sufficient to overcome pinning forces at the back. Bubble elongation reduces the gas pressure inside the bubble which leads to breakups.

Bubble breakups occur much more frequently in a micropost arrangement than in microchannels. In a micropost arrangement, bubbles are surrounded by a liquid field with more severe pressure fluctuations due to blockages. Large bubbles that are compressed against a post often break up and leave smaller stagnant bubbles behind

the posts, as shown in Figure 84. In arrangements where bubbles have to take meandering paths, the chances for bubble breakup is significantly higher than the parallel post arrangement in which bubbles remained restricted between two adjacent rows.

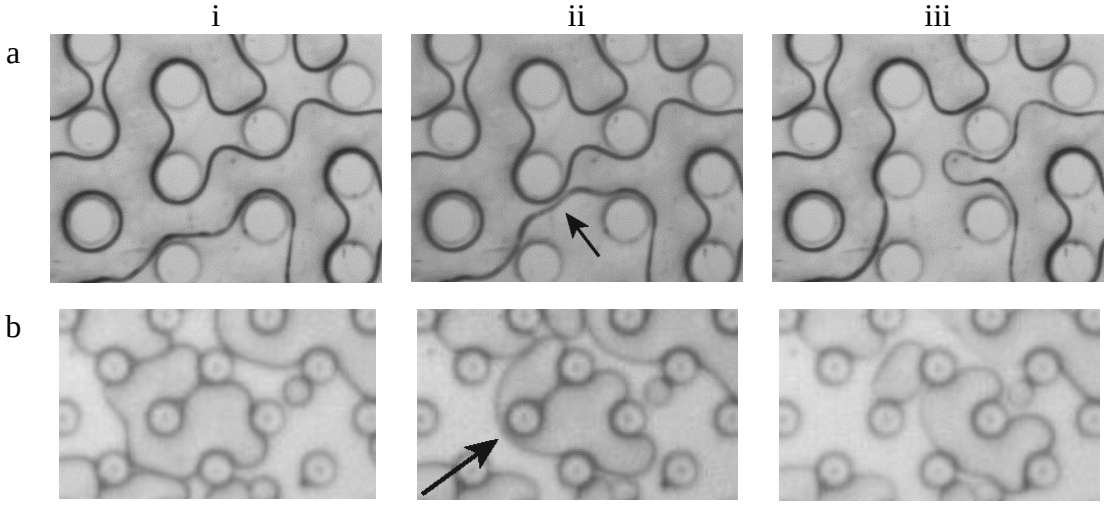

Figure 83: Strangling of a bubble on a post side in a) an arrangement with $120^{\circ} < \theta$ and b) an arrangement with $\theta = 90^{\circ}$ (flow direction: left to right)

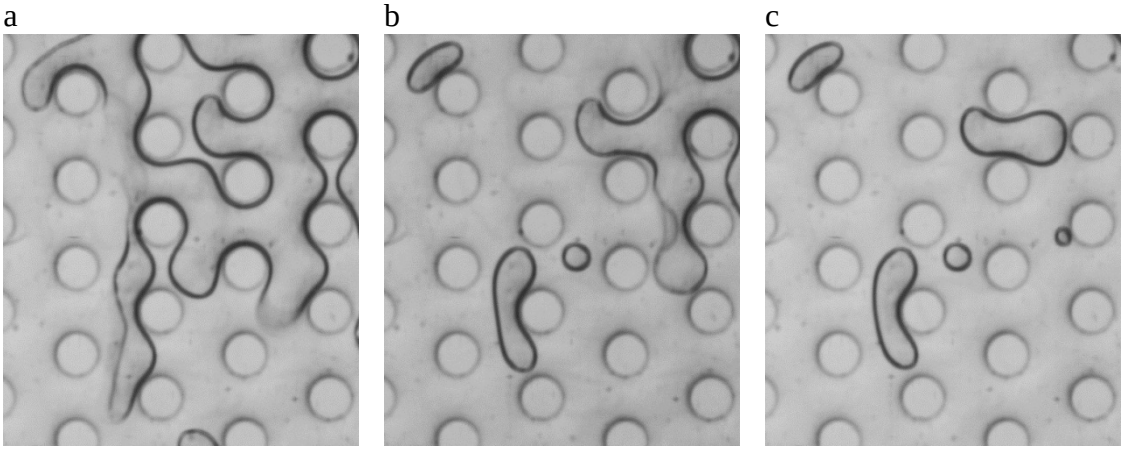

Figure 84 : A large bubble leaving several small and medium bubbles behind (flow direction: left to right). Spaces behind the posts are sweet spots for stagnation when bubbles take meandering paths

Figure 85 presents images of stagnant bubbles in equilateral arrangements at the high flow rate of 20 ml/min. All the *large* remaining bubbles in the lamina are hindered by being pressed against a post. These bubbles would definitely leave the device if they could take a straight path.

a

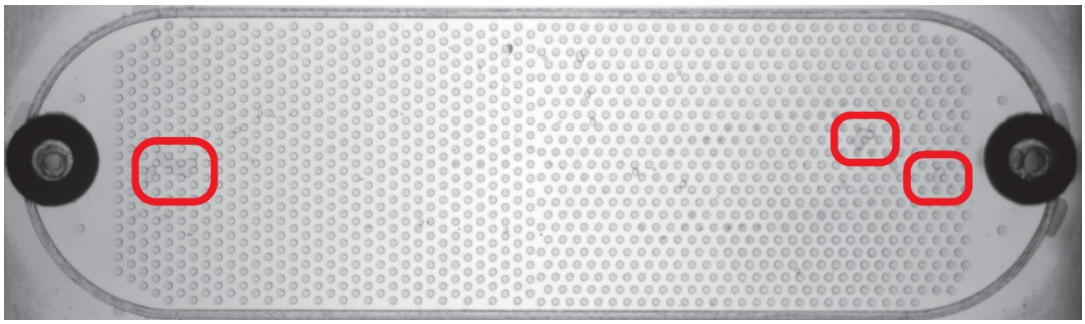

b

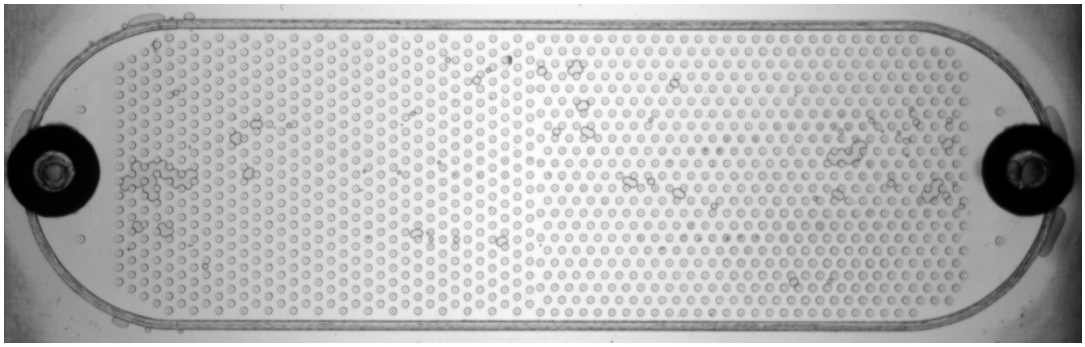

Figure 85: a) Large stagnant bubbles pressed against the posts in equilateral arrangements at a flow rate of 13 ml/min, and b) the same bubbles expanded after pausing the flow

7.7 SIDE PINNING FORCES IN PARALLEL ARRANGEMENT

For bubbles restricted between two adjacent rows of a parallel arrangement, our experimental results have clearly shown that pinning forces act on not only the front and back contact lines but also the side contact lines. Variation in the thickness of the contact line in the images is indicative of the exertion of pinning forces, as shown in

Figure 86. As the contact angle becomes larger the curvature of the bubble interface decreases. The smaller the curvature, the less light refracted at the interface leading to a thinner shadow of the contact line.

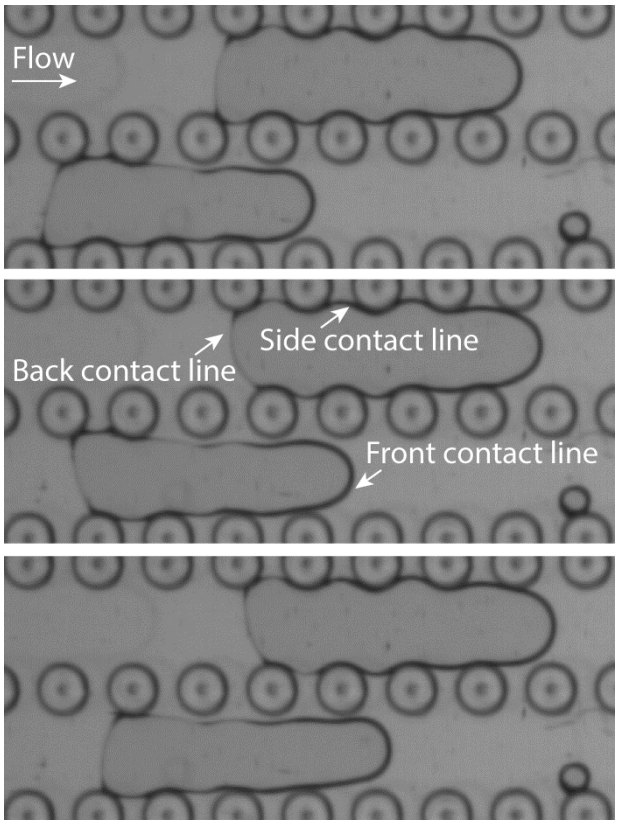

Figure 86: Variation in the thickness of the side contact lines during motion as an indication for the existence of side pinning forces

For the experiments previously discussed in section 7.5, doubling the flow rate should double the pressure drop per length of the device. If pinning forces were to only act on the front and back contact lines of the bubbles and were independent of the bubble length, we would expect doubling the flow rate to reduce the median length of the stagnant bubbles by approximately one half. Figure 87 presents the variations in the

median length of stagnant bubbles vs. flow rate. Doubling the flow rate reduced the median length of stagnant bubbles by only 16%. This is another indication of the existence of side pinning forces. The magnitude of the side pinning forces is a function of bubble length; longer bubbles experience larger resistive forces since they have partially entered a higher number of side contractions.

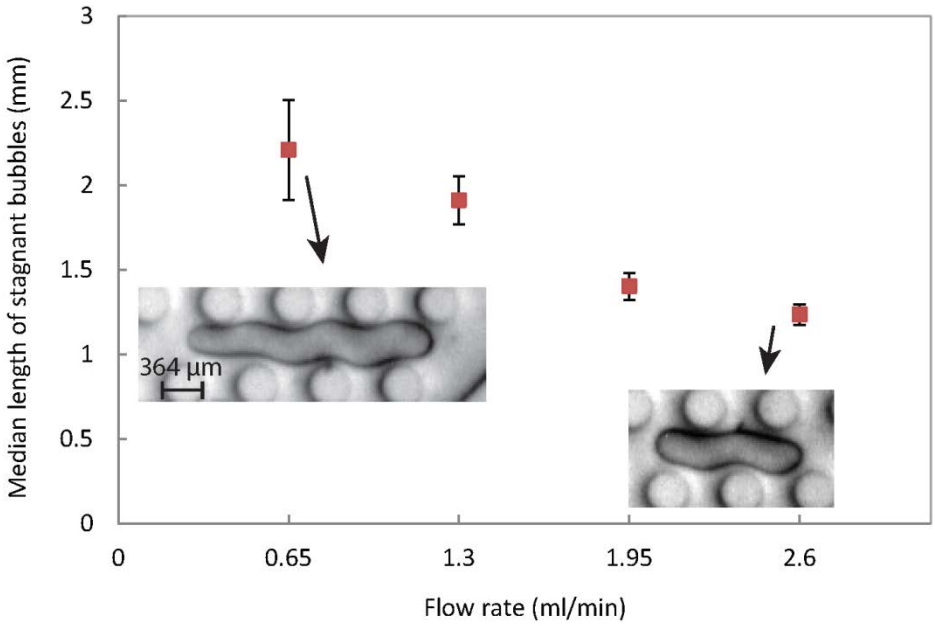

Figure 87: Median length of stagnant bubbles vs. flow rate in parallel arrangement

Understanding the role of side pinning forces triggers important questions: How can we reduce the magnitude of side pinning forces in a parallel micropost arrangement? How can we bring the performance of a parallel micropost arrangement closer to a microchannel in terms of bubble retention and reduce the side pinning forces?

If the magnitude of the side incursion of a bubble into longitudinal openings decreases, it will come out of the contraction more easily because it experiences smaller side pinning forces. Therefore, those designs which reduce the bubble side incursion bring the performance of a parallel micropost arrangement closer to a microchannel. To understand the effect of the geometrical parameters of a parallel array on the side incursion length we have approached the problem analytically.

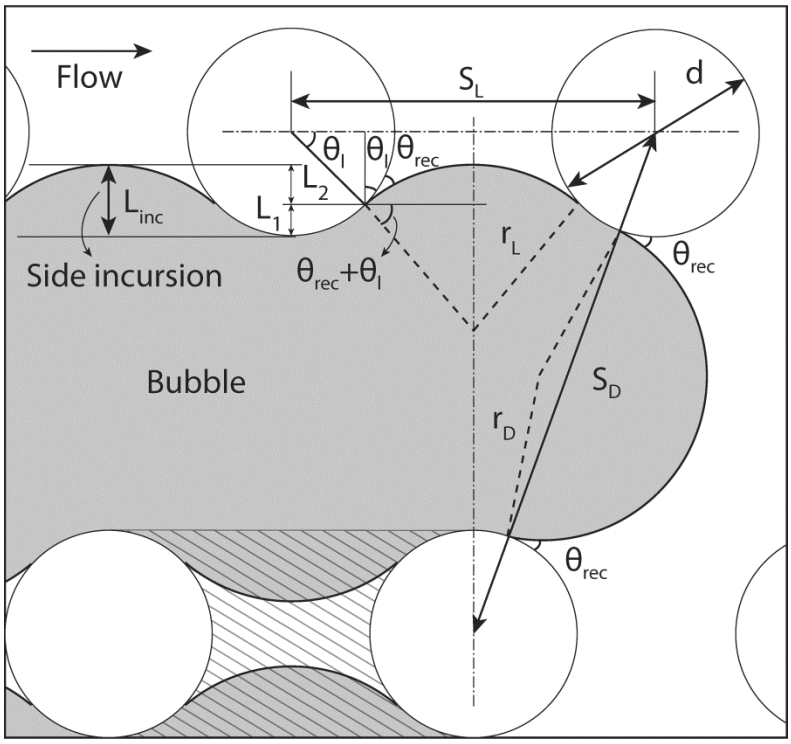

Figure 88: Schematic of a bubble side incursion into longitudinal openings. The interstitial space inside a longitudinal opening is shown with diagonal pattern.

Figure 88 presents a detailed schematic of a bubble side incursion in longitudinal opening. The lateral angle, θ_l, is always less than $\pi/2$; r_D and r_L refer to the radius

of the bubble curvature in the diagonal and longitudinal openings, respectively. At any point, the length of side incursion L_{inc} is equal to $L_1 + L_2$ where

$$L_1 = \frac{d(1-\sin\theta_l)}{2} \tag{100}$$

$$L_2 = r_L\left(1-\sin(\theta_{rec}+\theta_l)\right) \tag{101}$$

Since the diagonal openings are larger than the longitudinal openings bubbles do not fully enter the longitudinal contractions. They may advance to the point where their side curvature becomes equal to the largest front curvature occurring at the narrowest part of the diagonal openings. Beyond that, bubbles prefer to advance from the diagonal opening which does not require extra contraction. The radius of the largest front curvature is given by

$$r_D = \frac{S_D - d}{2\cos\theta_{rec}} \tag{102}$$

The maximum side incursion occurs at $r_L = r_D$. At the maximum side incursion the lateral angle takes its minimum value, $\theta_{l,\min}$. Substituting r_L by r_D from Eq. (102) yields

$$L_{inc,\max} = \frac{d(1-\sin\theta_{l,\min})}{2} + \frac{S_D - d}{2\cos\theta_{rec}}\left(1-\sin(\theta_{rec}+\theta_{l,\min})\right) \tag{103}$$

At any point, the following equation relates the instantaneous lateral angle to the longitudinal spacing:

$$S_L = d\cos\theta_l + 2r_L\cos(\theta_{rec} + \theta_l) \tag{104}$$

Therefore, at the maximum side incursion

$$\begin{aligned} S_L &= d\cos\theta_{l,\min} + \frac{(S_D - d)}{\cos\theta_{rec}}\cos(\theta_{rec} + \theta_{l,\min}) \\ &= d\cos\theta_{l,\min} + (S_D - d)\left(\cos\theta_{l,\min} - \sin\theta_{l,\min}\tan\theta_{rec}\right) \end{aligned} \tag{105}$$

Equation (105) suggests that for a constant diagonal opening $(S_D - d)$ and post diameter, smaller values of longitudinal spacing $(S_L - d)$ result in a larger minimum lateral angle which reduces the side incursion given by Eq. (103). Likewise, for a constant longitudinal opening and post diameter, larger values of diagonal openings result in a smaller side incursion. Investigating the effect of changing the post diameter for constant diagonal and longitudinal openings is more complicated. Subtracting the post diameter from both sides of Eq. (105) results in

$$S_L - d = d(\cos\theta_{l,\min} - 1) + (S_D - d)(\cos\theta_{l,\min} - \sin\theta_{l,\min}\tan\theta_{rec}) \tag{106}$$

Keeping the diagonal and longitudinal openings constant, Eq. (106) suggests that increasing the post diameter results in a smaller minimum lateral angle. According to Eq. (103), for a constant longitudinal opening, larger post diameters and smaller lateral angles both contribute to a larger side incursion. For the special case of $\theta_{rec} \approx 0$, S_L becomes equal to $S_D\cos\theta_{l,\min}$, meaning that the minimum lateral angle is independent of the post diameter. Yet, increasing the post diameter results in a larger side entrance. In summary, increasing the diagonal opening and decreasing the longitudinal opening

or post diameter results in smaller side incursion which has a positive influence on bubble movability.

Scaling the longitudinal opening and the maximum side incursion with respect to the post diameter may give us a better perspective:

$$\frac{S_L - d}{d} = \cos\theta_{l,\min} + \frac{S_D - d}{d}\left(\cos\theta_{l,\min} - \sin\theta_{l,\min}\tan\theta_{rec}\right) - 1 \tag{107}$$

$$\frac{L_{inc}}{d} = \frac{(1-\sin\theta_{l,\min})}{2} + \frac{S_D - d}{d}\frac{1-\sin(\theta_{rec}+\theta_{l,\min})}{2\cos\theta_{rec}} \tag{108}$$

For constant *scaled* values of longitudinal and diagonal openings in Eq. (107), the minimum lateral angle is independent of the post diameter. Under these conditions, the *scaled* length of the side incursion in Eq. (108) becomes independent of the post diameter as well. Therefore, scaling the *longitudinal and diagonal openings* with respect to the *post diameter* is the right scaling approach for this problem.

7.8 MINIMUM REQUIRED POST DIAMETER IN PARALLEL ARRANGEMENT

If the leading edge of a bubble's side interface reaches the middle of a longitudinal contraction the chances of coalescence of restricted bubbles between two adjacent rows becomes high. The resulting bubbles are more resistant to motion since they get pressed against the middle posts. Therefore, the design parameters should be chosen as to prevent side coalescence. The distance between the tip of the side curvature and its lowest point is given

To avoid side coalescence of bubbles at the maximum the side incursion should be smaller than the post radius:

$$\frac{d(1-\sin\theta_{l,\min})}{2}+\frac{S_D-d}{2\cos\theta_{rec}}\left(1-\sin(\theta_{rec}+\theta_{l,\min})\right)<\frac{d}{2} \tag{109}$$

The value of the minimum lateral angle can be obtained by solving Eq. (105) for given diagonal and longitudinal openings and post diameters. For $\theta_{rec}\approx 0$, $\theta_{l,\min}$ becomes equal to $\cos^{-1}(S_L/S_D)$ which simplifies Eq. (109) to

$$1-\sqrt{1-(\frac{S_L}{S_D})^2}<\frac{d}{S_D} \tag{110}$$

For example, according to Eq. (110) for $S_D=600\ \mu\text{m}$ and $S_L=500\ \mu\text{m}$ the post diameter should be larger than $268\ \mu\text{m}$ to avoid the side coalescence of bubbles. For $S_D=600\ \mu\text{m}$ and $S_L=400\ \mu\text{m}$ the post diameter should be larger than $153\ \mu\text{m}$ to avoid side coalescence.

7.9 COMPARISON OF BUBBLE RETENTION IN MANIFOLDS WITH DIFFERENT POST ARRAYS

The goal of the studies presented in this section is to test different ideas for the placement of post arrays in right triangular manifolds and to achieve a better understanding of designing a manifold with a low percentage of bubble blockage by area. All the tested laminas consisted of right triangular manifolds with 40 channels, manifold corner angles of 25° and vertical corner spacings of $500\ \mu\text{m}$. These

variables are defined in chapter 6 and have been chosen based on the results obtained therein. Using even smaller corner angles could still result in a relatively uniform distribution between the channels in the absence of the post in the manifolds in sections 7.4 and 7.5. However, in the presence of posts, the use of smaller corner angles is expected to reduce the ability of the manifold to distribute the flow uniformly. Experimental and numerical studies on manifolds featuring post arrays with smaller corner angles is one of the recommended areas for future studies.

The design concepts developed from the bubble retention studies in micropost arrays are used for the placement of posts in the manifolds. The drawings used for fabrication of the stainless steel masters for the tested laminas are provided in Appendix G. The maximum opening in different designs varies between $292-360\ \mu m$. The average depth of the laminas varies between $90-100\ \mu m$. The deviations between the depths and maximum openings make it difficult to quantitatively compare the performance (blockage percentage) of the designs with each other to draw firm conclusions.

For statistical studies on each design, 6 – 10 experiments at a flow rate of 1.95 ml/min have been performed. This flow rate results in an average flow velocity in the range of $3-4$ cm/s in the channels depending on the channel dimensions in each lamina. For all the experiments, a bubble with a volume of 0.2 ml $\pm$ 0.01 ml (more than five times the volume of the laminas) was injected into the device. All the areas occupied by the bubbles in the manifolds have been taken into account for calculating the blockage

percentage. The rest of the experimental procedure is similar to that described in section 7.5.1.

7.9.1 TRIANGULAR MANIFOLDS WITH ELONGATED POSTS

The design presented in this section was aimed at lowering the side pinning forces acting on the bubbles in a parallel post arrangement. The idea of using elongated posts instead of circular posts has been tested in this design. There is a limit on the minimum size of the posts when the etched metal masters (section 5.2.1) are used for lamina fabrication. Radii of curvature smaller than $75\ \mu m$ cannot be neatly etched on the metal masters. Therefore, we have chosen to use elongated posts with a diameter/thickness around $150\ \mu m$. The thickness of the posts on the studied lamina was the same as the channel spacing and equal to $142\ \mu m$. The maximum open space between posts is almost equal to the channel width, which is $300\ \mu m$.

An image of the remaining bubbles in the system after the air injection is presented in Figure 89. Since a majority of the large bubbles were able to leave the inlet manifold, we can conclude that the design was able to lower the side pinning forces as expected. The presence of many small bubbles in the manifold and also in the channels is indicative of a large number of breakups (see section 7.5.3).

There are significant variations in the direction of flow paths over the area of right triangular manifolds, as shown in Figure 90. With the presence of posts and blocked areas the changes in the flow paths will be even greater. The large number of breakups

can be due to the frequent changes in the flow paths, especially when the stagnant bubbles are relatively restricted between the posts and the flow has to break up bubbles in order to proceed.

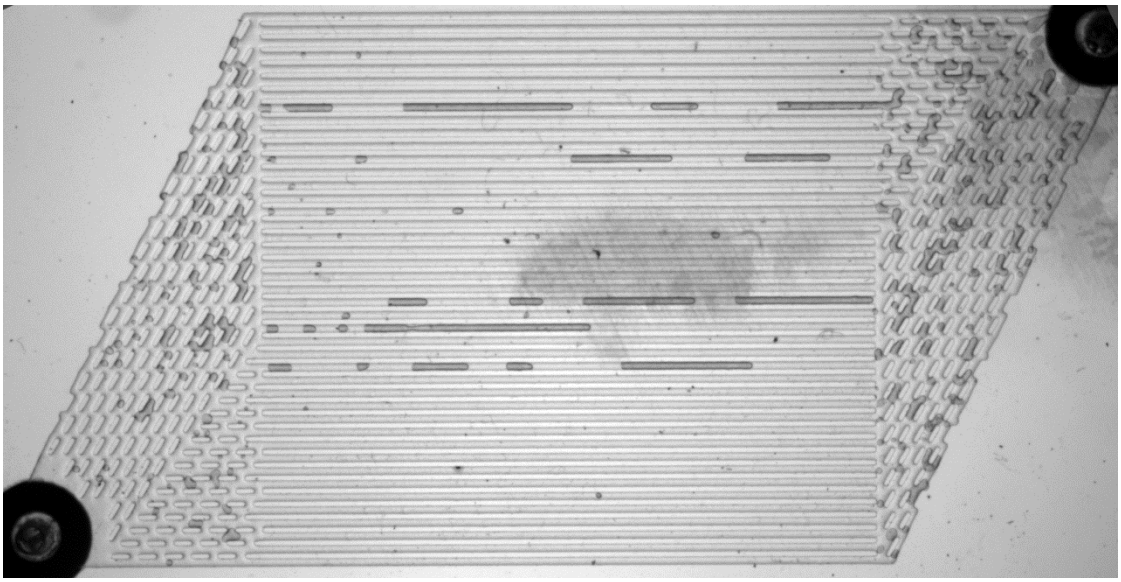

Figure 89: Stationary bubbles in an arrangement with elongated posts, note the large number of small bubbles remaining in the manifolds

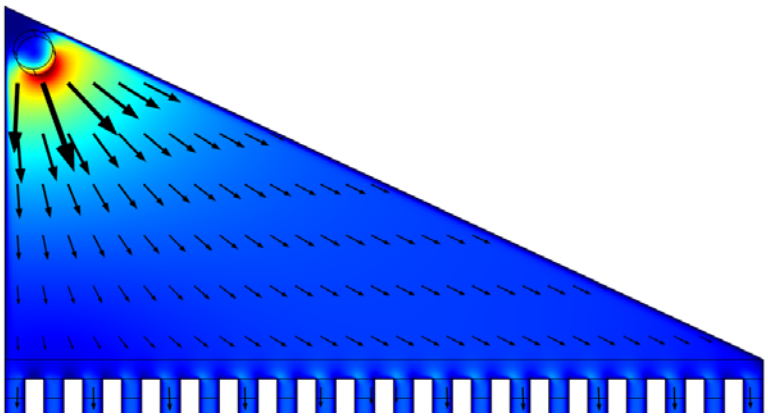

Figure 90: Variations in the direction of the flow paths in a right triangular manifold with a corner angle of 25 degrees and no posts

Small bubbles are the most stubborn bubbles in the system and those designs which produce too many small bubbles should be avoided. For this reason, no statistical study has been performed on this design. Although the use of elongated posts is not a good option for triangular manifolds, it may be more useful in geometries with parallel flow paths.

7.9.2 *TRIANGULAR MANIFOLDS WITH TILTED PARALLEL POST ARRANGEMENTS (TPPA)*

The design presented in this section was aimed at restricting the bubbles between parallel post arrangements and guiding them toward the microchannels (in the inlet manifold) or the device outlet (in the outlet manifold). The triangular manifold is divided into three parts, as shown in Figure 91. Each part consists of a parallel post arrangement aligned with the overall expected flow direction. The diameters of the microposts are $210\ \mu m$. The maximum open distance between posts is $360\ \mu m$.

The blockage percentages in the inlet and outlet manifolds for 6 sets of experiments are $24 \pm 2\%$ and $41 \pm 2\%$, respectively. The blockage percentage in the outlet manifold is significantly larger than the inlet manifold. This can be attributed to the fact that most of the remaining bubbles in the inlet manifold were originally part of the air injected into the system and are produced by bubble breakup. However, the outlet manifold receives smaller bubbles that are products of bubble breakup in the inlet manifold as well. Smaller bubbles are more prone to getting stuck. A higher blockage percentage in the outlet manifold occurs for the designs described in the next sections

as well. Smaller longitudinal openings may stop the bubbles from changing directions. However, changing direction in triangular manifolds may result in a better bubble mobility due to the gradual change in the direction of flow paths over the manifold area.

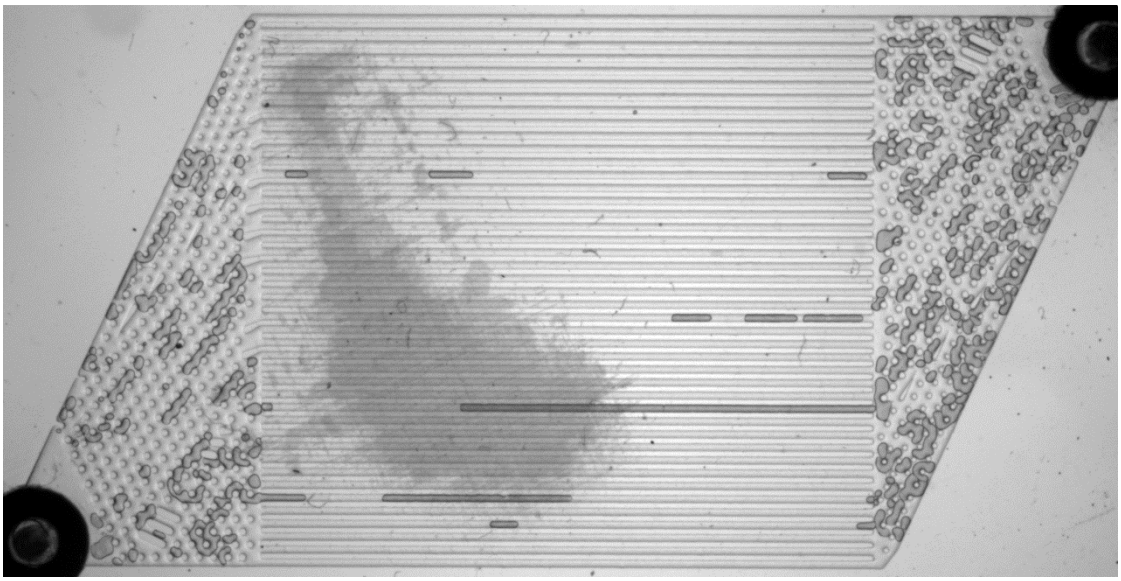

Figure 91: Stationary bubbles in the tilted parallel post arrangement

7.9.3 TRIANGULAR MANIFOLDS WITH PARALLEL POST ARRANGEMENT (PPA)

This design presents a parallel post arrangement in a right triangular manifold aligned with the microchannels, as shown in Figure 92. This goal of this arrangement was to present an ineffective design where bubbles tend to break up frequently. In this arrangement, bubbles spread the space between the parallel rows of microposts because of the larger diagonal opening. However, most of the flow paths are angled with respect to parallel rows and the flow splits up the bubbles. The frequent bubble breakup produces lots of smaller bubbles that tend to remain in the system.

The diameters of the microposts are $260\ \mu m$. The maximum open distance between posts is $290\ \mu m$. This design has narrower channels and subsequently smaller manifolds than other designs. Comparing the performance of this design with the others at the flow rate used for the other designs (1.95 ml/min) will be significantly biased since in a smaller manifold the velocity and pressure drop per unit length are higher. For this reason, the flow rate is scaled in proportion to the ratio of the manifold areas to 1.3 ml/min. At each flow rate, 10 experiments were performed. At a flow rate of 1.3 ml/min, the blockage percentages in the inlet and outlet were $35 \pm 6\%$ and $37 \pm 2\%$, respectively. At the flow rate of 1.95 ml/min, they were $19 \pm 1\%$ and $28 \pm 1\%$.

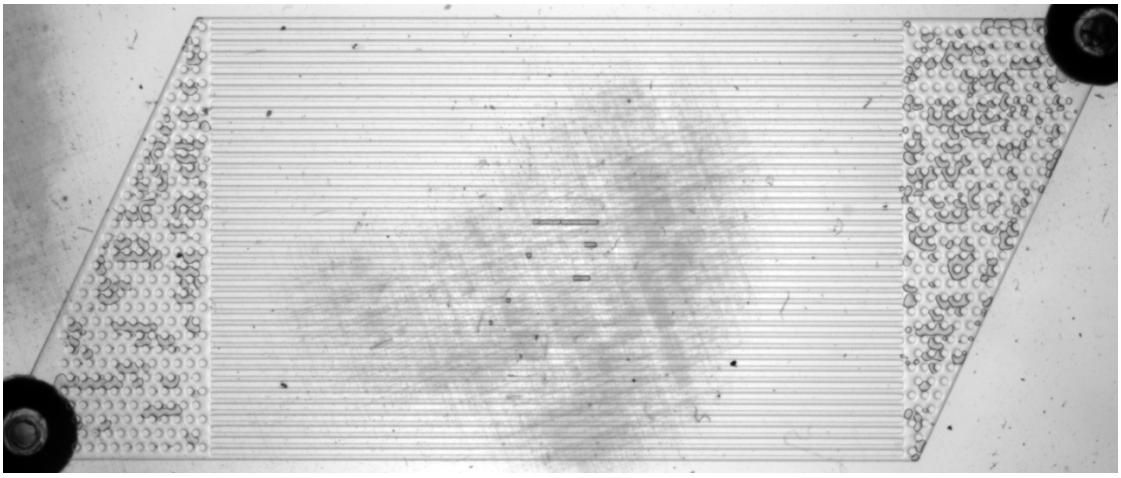

Figure 92: Stationary bubbles in the parallel post arrangement (PPA) at the flow rate of 1.95 ml/min

7.9.4 TRIANGULAR MANIFOLDS WITH EQUILATERAL POST ARRANGEMENT (EPA)

The design presented in this section is an equilateral arrangement of microposts. This design promotes the motion of the bubbles in both horizontal and diagonal directions and also, while having equal openings, does not prevent the bubbles from changing direction. The orientation of the arrangement is in a way that the rows of microposts are aligned with microchannels, as shown in Figure 93. With this orientation for the equilateral arrangement, the chances of bubble breakup are lower than an equilateral arrangement rotated 90 degrees (see section 7.4).

The diameter of the microposts is $212\ \mu m$. The maximum open distance between posts is $308\ \mu m$. The blockage percentages in the inlet and outlet manifolds for 10 sets of experiments are $15 \pm 1\%$ and $22 \pm 2\%$, respectively.

Figure 93: Stationary bubbles in the equilateral post arrangement (EPA)

7.9.5 SUMMARY AND CONCLUSIONS

The sizes of the geometrical features in the studied manifolds are presented in Table 15. Having an equal maximum open distance between microposts would allow us to compare the performance of the manifolds and make more conclusive arguments. In the presented studies, the maximum open distance between the posts differs; however, we are still able to make a qualitative comparison between the performance of parallel post and equilateral post arrangements.

Table 15: Dimensions of the geometrical features in the studied manifolds

Design	Maximum open distance between the posts (μm)	Post diameter (μm)	Channel width (μm)	Channel spacing width (μm)	Average depth (μm)
Tilted parallel post arrangement (7.9.2)	360	210	280	170	100 ± 5
Parallel post arrangement (7.9.3)	292	260	220	180	95 ± 5
Equilateral post arrangement (7.9.4)	308	212	295	155	90 ± 5

The blockage percentages in the inlet and outlet manifolds of the studied designs are presented in Figure 94. The performance of the equilateral arrangement was even better than the performance of the parallel post arrangement at the unscaled flow rate of 1.95 ml/min. In other words, the parallel arrangement at the flow rate of 1.95 ml/min, with a 50% larger flow rate-to-manifold area, still had a lower performance than the equilateral arrangement. The difference between the maximum opening in these two designs was only 16 μm. Therefore, we can conclude that the use

of equilateral arrangements instead of parallel arrangements improves the performance of the manifold and lowers bubble retention.

One consistent finding among all the designs was that the blockage percentage in the outlet manifold was always larger than the one in the inlet manifold. We attributed this to the fact that the outlet manifold receives already broken up and smaller bubbles (see section 7.9.2).

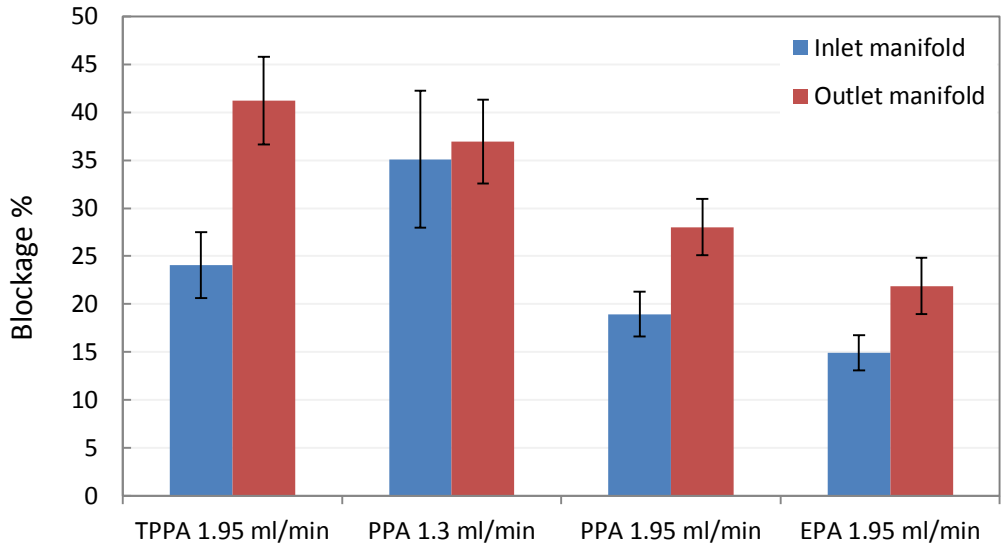

Figure 94: The blockage percentage in the inlet and outlet manifolds of the studied designs: tilted parallel post arrangement (TPPA), parallel post arrangement (PPA), equilibrium post arrangement (EPA)

The fact that the equilateral arrangement with the employed orientation promotes the motion of the bubbles in both horizontal and diagonal directions and also does not prevent the bubbles from changing direction make it a promising design for low bubble retention.

In the presented equilateral arrangement, the diagonal side of the manifold intersects some of the microposts creating dead zones that entrap bubbles. To improve the performance of the future designs, the gaps between the intersecting posts can be filled.

For future comparative studies, the dimensions of the channels and the channel spacings should be equal. More importantly, post arrangements in different designs should have equal post diameters and an equal maximum open distance between the posts. The device should also have uniform depth. These will enable more conclusive comparisons.

8 CONCLUSIONS AND FINAL REMARKS

This chapter summarizes the significant results of this dissertation, followed by a list of the scientific and technical contributions and recommendations for future work.

8.1 SUMMARY

Different aspects of the design of a single lamina of a microchannel dialyzer are presented. The primary intent of the study was to investigate the bubble retention phenomenon in the microchannels and manifold areas and provide design guidelines for reducing bubble blockage.

In chapter 2, it has been shown that the stationary bubbles in the system are always dry and the resistive capillary and pinning forces prevent their motion. For the first time, a theoretical model for the pinning forces acting on dry stationary bubbles in microchannels is proposed. The model estimates the pressure difference required across the length of a stagnant bubble to overcome the contact line forces and stimulate motion. The model correlates the resistive forces to the difference in the cosine of the advancing and receding contact angles of the surface $(\cos\theta_{rec} - \cos\theta_{adv})$. The model has been validated by experimental results.

In the microchannel dialyzer, the laminas will be coated by PEO triblock to inhibit protein adsorption and cell adhesion. The PEO coating was also expected to improve the bubble mobility in the device by increasing the surface hydrophilicity. In chapter 2, the underlying reasons for the positive effect of the PEO coating and in

general a hydrophilic coating on bubble mobility are revealed and explained as following: First, from the theoretical model, we have learned that pinning and capillary forces are proportional to $(\cos\theta_{rec} - \cos\theta_{adv})$; thus more hydrophilic surfaces apply less resistive forces on the bubbles. Second, we have experimentally shown that coating reduces the dewetting velocity of the surface; therefore, bubbles in the coated system have a better chance of remaining lubricated at low flow rates.

One of the considerations for the design is preventing shear-induced blood damage. Microchannel structural parameters and flow velocity determine the magnitude of the shear stress on applied on blood and the duration that blood is exposed to shear stress. After studying the conditions that lead to shear-induced blood damage in chapter 3, a velocity dependent constraint is placed on the depth of the microchannel dialyzer device. For example, based on the provided constraint, for a wide range of velocities up to 10 cm/s, a device depth larger than $16\ \mu m$ does not induce blood hemolysis.

Design of a microchannel dialyzer is a complicated nonlinear problem with several constraints. In chapter 4, potential objective and constraint functions for a design optimization have been suggested. A general guideline that describes the effect of channel structural parameters and flow velocity in each channel on mass transfer, pressure drop, and bubble movability is provided. Design optimization cannot be pursued until all the constraints of the problem become defined as functions of the design parameters in the next stages of the project.

The double magnification imaging system for bubble visualization and the designed and assembled test section have been described in chapter 5. In the assembly of the test section, a novel method for preventing leakage from the polycarbonate lamina in the clamp system was devised by adding PDMS membranes to the assembly.

Flow uniformity is one of the factors affecting the performance of the microchannel dialyzer. In chapter 6, from a comprehensive literature review, we have concluded that right triangular manifolds can distribute the flow more uniformly than other types of manifolds. Through 3D CFD simulations, the impacts of the geometry of the right triangular manifold and the dimensions of microchannels on the desired uniformity have been investigated. Compared to the microchannel dimensions, manifold structural parameters including the corner angle and short vertical corner spacing of the manifold showed more influence on velocity distribution. Including a short vertical spacing at the corner of the manifold was critical to achieving a high level of flow uniformity. The results have been used for the design of the overall manifold geometry.

Structural features must be distributed in the manifold areas to support the membrane and prevent membrane sagging. The geometrical design must exhibit low resistance for bubble mitigation while maintaining a relatively uniform flow distribution between channels. Theoretical analysis provided in chapter 7 indicates that smaller bubbles in the system are more prone to getting stuck in the channels or manifolds since they experience a smaller pressure drop along their length. Through experiments,

preferential bubble paths in different staggered arrangements of microposts have been identified. Statistical studies on staggered post arrangements have shown that when bubbles take meandering paths they are more prone to breakup and produces smaller bubbles. Furthermore, in the arrangements where bubble have to take meandering paths to proceed, they may get pressed against posts and become stagnant. It is concluded that those staggered arrangements that restrict the motion of the bubbles in a straight path and guide them toward the destination exhibit lower bubble retention.

For right triangular manifolds that exhibit variations in the flow path over their area, efforts to restrict the bubble paths in a single direction will not be successful. An equilateral arrangement allows for change of direction without exerting extra resistance that occurs in arrangements with unequal openings. With a proper orientation, an equilateral arrangement promotes the bubble motion in two major directions matching the overall flow paths in most of the manifold areas. Experimental results have shown that such arrangement results in a relatively low bubble blockage percentage in the manifold areas.

8.2 MAJOR CONTRIBUTIONS

- For the first time, a theoretical model was proposed that estimates the pressure difference required across the length of a stagnant bubble with a concave or convex back interface to overcome the contact line forces and stimulate motion. To validate the theory, the pressure required to move a dry bubble in square microchannels exhibiting contact angle hysteresis has been measured.

The experimental results are in good agreement with the model's prediction. The resistive pinning forces acting on dry bubbles have been differentiated from the capillary forces.

- The effect of PEO coating on the hydrophilicity of the polycarbonate lamina and the dewetting velocity of water on it was investigated. The theoretical basis for the positive effect of PEO coating on bubble movability is explained. It has been shown that the stagnant bubbles in the system are dry and there is no thin liquid film around them.
- The effects of channel structural parameters and flow velocity on shear-induced blood damage have been investigated. A velocity-dependent constraint on the depth of the device was proposed that prevents shear-induced blood damage.
- The effects of channel structural parameters and flow velocity in each channel on mass transfer, pressure drop, and bubble movability have been provided using the results of numerical simulations or analytical methods. A general guideline that describes the decision making and optimization process for the future final design have been described.
- Based on a comprehensive literature review on the subject of flow uniformity among an array of microchannels and performing CFD simulations it was concluded that right triangular manifolds can distribute the flow more uniformly than rectangular and obtuse/acute triangular ones. The option of using fractal-like manifolds was eliminated mainly due to the large manifold

area and the subsequent large and costly waste of membrane in the manifold areas.

- The impact of the geometry of the right triangular manifold and the dimensions of the microchannels on the desired uniformity and pressure drop were investigated numerically. A methodical approach was introduced to identify a design that balances low manifold volume and the maintenance of flow uniformity. It has been shown that including a short vertical spacing at the corner of the manifolds is critical to achieving a high level of flow uniformity.
- Preferential bubble paths in different staggered arrangements of microposts have been identified experimentally. The bubble retention behavior in arrangements and the probable frequency of the bubble breakup have been qualitatively linked to the different types of arrangements. It has been also shown that bubbles are less prone to breakup and getting stuck in microchannels than in micropost arrays due to the presence of side pinning forces. The obtained knowledge has been used in designing manifolds featuring micropost arrangements that exhibit low bubble retention.

8.3 RECOMMENDATIONS FOR FUTURE WORK

The PEO-coated laminas featuring micropost arrays in the manifolds have not been tested in this work. Performing experiments on coated laminas will reduce bubble retention and yield better results.

Previous studies on the subject of shear-induced blood damage have investigated the effect of a constant applied shear rate (by Couette viscometers) on hemolysis and platelet aggregation at different exposure times. However, shear rate in a microchannel flow is position dependent meaning that blood cells experience different shear rates depending on their position in the cross sectional area of the channel. Further experimental studies on shear-induced blood damage in microchannels can identify more realistic conditions that lead to hemolysis and platelet aggregation.

The behavior of bubbles in blood flow passing through an array of microposts and microchannels should be studied experimentally and the differences between their behavior in blood and water should be identified.

The removal of toxins (urea, creatinine, etc.) and water from the blood has to be correlated experimentally to channel dimensions (width, height, and length), flow velocity, blood to dialysate ratio, and ultrafiltration pressure. In the final design, the device is required to remove a minimum amount of toxins from the blood in each treatment. Therefore, the amount of removal should be known as a function of the design parameters to allow for performing a design optimization.

A statistical study is required to identify the minimum flow rate for different channel depths that statistically result in no channel blockage in an array of microchannels (i.e. the average number of blocked channels after the injection of a bubble into to the system to be less than 0.5). The width of the channels can be held constant and equal to the maximum allowed channel width.

For determining the design parameters of a single layer of a microchannel dialyzer, it is required to decide on the objective and constraints of the design problem. Putting the objective on minimizing the cost of the device, the other requirements for the design should be clearly defined: desired amount of toxin removal, the maximum allowed pressure drop in each layer, and the limits on the dialysate fluid consumption and duration of treatment. The tolerable blockage in the channels or manifold areas has to be identified as well. Determining the design constraints is an important task for the commercialization of the device.

CFD simulations can be conducted to study the effects of placing microposts in the manifold areas (e.g. the influence of post diameter and the type of arrangement) and also the effect of manifold geometrical parameter including corner angle and corner spacing (in the presence of microposts) on flow uniformity.

Further experimental studies on the arrangement of microposts in the manifold areas will be useful to further decrease bubble retention in the manifolds.

Further experimental investigations on the influence of the corner angle of right triangular manifolds filled with micropost arrays on bubble retention and the blockage of the corner channels will be useful. The triangular manifolds experimentally tested in this work had a corner angle of 25°. The use of smaller corner angles will reduce the size of the manifold and membrane usage. The use of smaller corner angles in the presence of microposts will be helpful if it does not increase the blockage percentage in the manifolds or result in the blockage of the inlet or outlet of the corner channels.

LIST OF PUBLICATIONS AND PRESENTATIONS

Mohammadi, M. and Sharp, K. V., Design of a micropost array for low bubble retention, Journal of Micromechanics and Microengineering (to be submitted)

Coblyn M., Truszkowska A., Mohammadi M., Heintz K., McGuire J., Sharp K., and Jovanovic G., Effect of PEO-coating on bubble behavior within polycarbonate microchannel systems for hemodialysis, Journal of Biomedical Materials Research (to be submitted)

Mohammadi, M. and Sharp, K. V., The Role of Contact Line Forces on Bubble Blockage in Microchannels, Journal of Fluids Engineering (under review)

Mohammadi, M. and Sharp, K. V., 2013, Experimental Techniques for Bubble Dynamics Analysis in Microchannels: A Review, Journal of Fluids Engineering, 135(2), pp. 021202-021202.

Mohammadi, M., Jovanovic, G. N., and Sharp, K. V., 2013, Numerical Study of Flow Uniformity and Pressure Characteristics within a Microchannel Array with Triangular Manifolds, Computers & Chemical Engineering, 52, pp. 134-144

Mohammadi, M. and Sharp, K.V.*, "*The Role of Contact Line Forces on Bubble Blockage in Microchannels,* " 5th International Conference on Heat Transfer and Fluid Flow in Microscale, HTFFM-V 2014, April 22-26, Marseilles, France

Mohammadi, M.*, Sharp, K.V., "*Design of Micropost Array for Low Bubble Retention*, " 66th Annual Meeting of the APS Division of Fluid Dynamics, APS DFD 2013, Nov. 24-26, , Pittsburgh, PA, USA

Mohammadi, M.*, Sharp, K.V., "*Cost Optimization of a Multilayer Microchannel Dialyzer*," Proceedings of the ASME 2013 Summer Bioengineering Conference, SBC 2013, June 26-29, Sunriver, Oregon, USA

Mohammadi, M.*, Jovanovic, G. , Paul, B., Sharp, K. , "*Numerical Study of the Impact of Manifold and Microchannel Geometry on Flow Uniformity and Pressure Characteristics within a Parallel Microchannel Array*," Proceeding of the 10th International Conference on Nanochannels, Microchannels, and Minichannels, ASME 2012, July 8-12, Puerto Rico, USA

BIBLIOGRAPHY

[1] Heintz, K., 2012, "Synthesis and Evaluation of Peo-Coated Materials for Microchannel-Based Hemodialysis. Dissertation," Master of Science, Oregon State University, Corvallis, Oregon.

[2] "U.S. Renal Data System, USRDS 2013 Annual Data Report: Atlas of Chronic Kidney Disease and End-Stage Renal Disease in the United States, National Institutes of Health, National Institute of Diabetes and Digestive and Kidney Diseases," Bethesda, MD, 2013.

[3] Rocco, M. V., 2007, "More Frequent Hemodialysis: Back to the Future?," Adv Chronic Kidney Dis, 14(3), pp. e1-9.

[4] Jovanovic, G. N., Anderson, E. K., and Warner-Tuhy, A. R., "*Micro-Channel Haemo Dialyser*," Proc. MicroNano2008, ASME, pp. 189-190.

[5] Tuhy, A. R., Anderson, E. K., and Jovanovic, G. N., 2012, "Urea Separation in Flat-Plate Microchannel Hemodialyzer; Experiment and Modeling," Biomedical Microdevices, 14(3), pp. 595-602.

[6] Ronco, C., Brendolan, A., Crepaldi, C., Rodighiero, M., and Scabardi, M., 2002, "Blood and Dialysate Flow Distributions in Hollow-Fiber Hemodialyzers Analyzed by Computerized Helical Scanning Technique," Journal of the American Society of Nephrology, 13(suppl 1), pp. S53-S61.

[7] Metz, T., Paust, N., Zengerle, R., and Koltay, P., 2010, "Capillary Driven Movement of Gas Bubbles in Tapered Structures," Microfluid Nanofluid, 9(2-3), pp. 341-355.

[8] Kohnle, J., Waibel, G., Cernosa, R., Storz, M., Ernst, H., Sandmaier, H., Strobelt, T., and Zengerle, R., 2002, "*A Unique Solution for Preventing Clogging of Flow Channels by Gas Bubbles*," The 15th IEEE International Conference on Micro Electro Mechanical Systems, Las Vegas.

[9] Litterst, C., Eccarius, S., Hebling, C., Zengerle, R., and Koltay, P., 2006, "Increasing μDMFC Efficiency by Passive Co2 Bubble Removal and Discontinuous Operation," Journal of Micromechanics and Microengineering, 16(9), pp. S248-S253.

[10] Kandlikar, S., and Balasubramanian, P., 2003, "*Effect of Channel Shape on Flow Pattern During Flow Boiling in Single and Parallel Rectangular Microchannels*," Proc. 5th International Conference on Boiling Heat Transfer, Montego Bay, Jamaica.

[11] Kenny, T. W., Goodson, K. E., Santiago, J. G., Wang, E., Koo, J.-M. O., Jiang, L., Pop, E., Sinha, S., Zhang, L., Fogg, D., Yao, S., Flynn, R., Chang, C.-H., and Hidrovo, C. H., 2006, "Advanced Cooling Technologies for Microprocessors," International Journal of High Speed Electronics and Systems, 16, pp. 301-313.

[12] Kuo, C. Y., and Pan, C., 2009, "The Effect of Cross-Section Design of Rectangular Microchannels on Convective Steam Condensation," Journal of Micromechanics and Microengineering, 19(3), p. 035017.

[13] Litterst, C., Metz, T., Zengerle, R., and Koltay, P., 2008, "Static and Dynamic Behaviour of Gas Bubbles in T-Shaped Non-Clogging Micro-Channels," Microfluid Nanofluid, 5(6), pp. 775-784.

[14] Hibara, A., Iwayama, S., Matsuoka, S., Ueno, M., Kikutani, Y., Tokeshi, M., and Kitamori, T., 2004, "Surface Modification Method of Microchannels for Gas−Liquid Two-Phase Flow in Microchips," Analytical Chemistry, 77(3), pp. 943-947.

[15] Zhu, X., 2009, "Micro/Nanoporous Membrane Based Gas–Water Separation in Microchannel," Microsystem Technologies, 15(9), pp. 1459-1465.

[16] Xu, J., Vaillant, R., and Attinger, D., 2010, "Use of a Porous Membrane for Gas Bubble Removal in Microfluidic Channels: Physical Mechanisms and Design Criteria," Microfluid Nanofluid, 9(4-5), pp. 765-772.

[17] Wong, C. W., Zhao, T. S., Ye, Q., and Liu, J. G., 2005, "Transient Capillary Blocking in the Flow Field of a Micro-DMFC and Its Effect on Cell Performance," Journal of The Electrochemical Society, 152(8), p. A1600.

[18] Rapolu, P., and Son, S. Y., 2011, "Characterization of Wettability Effects on Pressure Drop of Two-Phase Flow in Microchannel," Experiments in Fluids, 51(4), pp. 1101-1108.

[19] Paust, N., Krumbholz, S., Munt, S., Müller, C., Koltay, P., Zengerle, R., and Ziegler, C., 2009, "Self-Regulating Passive Fuel Supply for Small Direct Methanol Fuel Cells Operating in All Orientations," Journal of Power Sources, 192(2), pp. 442-450.

[20] Gravesen, P., Branebjerg, J., and Jensen, O. S., 1993, "Microfluidics-a Review," Journal of Micromechanics and Microengineering, 3, pp. 168-182.

[21] Cubaud, T., and Ho, C. M., 2004, "Transport of Bubbles in Square Microchannels," Physics of Fluids, 16(12), pp. 4575-4585.

[22] de Gennes, P. G., Brochard-Wyart, F., and Quéré, D., 2004, *Capillarity and Wetting Phenomena : Drops, Bubbles, Pearls, Waves*, Springer, New York, pp. 37, 153-174.

[23] Redon, C., Brochard-Wyart, F., and Rondelez, F., 1991, "Dynamics of Dewetting," Physical Review Letters, 66(6), pp. 715-718.

[24] Ajaev, V. S., and Homsy, G. M., 2005, "Modeling Shapes and Dynamics of Confined Bubbles," Annual Review of Fluid Mechanics, 38(1), pp. 277-307.

[25] Wong, H., Morris, S., and Radke, C. J., 1992, "Three-Dimensional Menisci in Polygonal Capillaries," Journal of Colloid and Interface Science, 148(2), pp. 317-336.

[26] Cho, H., Kim, H. Y., Kang, J. Y., and Kim, T. S., 2007, "How the Capillary Burst Microvalve Works," Journal of Colloid and Interface Science, 306(2), pp. 379-385.

[27] Jensen, M. J., Goranovi, G., and Bruus, H., 2004, "The Clogging Pressure of Bubbles in Hydrophilic Microchannel Contractions," Journal of Micromechanics and Microengineering, 14(7), pp. 876-883.

[28] Paust, N., Litterst, C., Metz, T., Eck, M., Ziegler, C., Zengerle, R., and Koltay, P., 2009, "Capillary-Driven Pumping for Passive Degassing and Fuel Supply in Direct Methanol Fuel Cells," Microfluid Nanofluid, 7(4), pp. 531-543.

[29] Jensen, M. J., 2002, "Bubbles in Microchannels. Dissertation," Master of Science, Technical University of Denmark, Lyngby.

[30] Chang, H.-C., 2001, "*Bubble/Drop Transport in Microchannels*," The Mems Handbook, CRC Press.

[31] Kim, H.-Y., Lee, H. J., and Kang, B. H., 2002, "Sliding of Liquid Drops Down an Inclined Solid Surface," Journal of Colloid and Interface Science, 247(2), pp. 372-380.

[32] Miyama, M., Yang, Y., Yasuda, T., Okuno, T., and Yasuda, H. K., 1997, "Static and Dynamic Contact Angles of Water on Polymeric Surfaces," Langmuir, 13(20), pp. 5494-5503.

[33] Della Volpe, C., Maniglio, D., Siboni, S., and Morra, M., 2001, "An Experimental Procedure to Obtain the Equilibrium Contact Angle from the Wilhelmy Method," Oil & Gas Science and Technology Rev IFP, 56(1), pp. 9-22.

[34] Kline, S. J., and McClintock, F. A., 1953, "Describing Uncertainties in Single-Sample Experiments," Mechanical Engineering, 75, pp. 3-8.

[35] Craig, V. S. J., Ninham, B. W., and Pashley, R. M., 1993, "The Effect of Electrolytes on Bubble Coalescence in Water," The Journal of Physical Chemistry, 97(39), pp. 10192-10197.

[36] Merrill, E. W., 1969, "Rheology of Blood," Physiological Reviews, 49(4), pp. 863-888.

[37] Pries, A. R., Neuhaus, D., and Gaehtgens, P., 1992, "Blood Viscosity in Tube Flow: Dependence on Diameter and Hematocrit," American Journal of Physiology - Heart and Circulatory Physiology, 263(6), pp. H1770-H1778.

[38] Hrncir, E., and Rosina, J., 1997, "Surface Tension of Blood," Physiol Res, 46(4), pp. 319-321.

[39] Otake, T., Tone, S., Nakao, K., and Mitsuhashi, Y., 1977, "Coalescence and Breakup of Bubbles in Liquids," Chemical Engineering Science, 32(4), pp. 377-383.

[40] Liao, Z., Lampe, J. W., Ayyaswamy, P. S., Eckmann, D. M., and Dmochowski, I. J., 2011, "Protein Assembly at the Air-Water Interface Studied by Fluorescence Microscopy," Langmuir : the ACS journal of surfaces and colloids, 27(21), pp. 12775-12781.

[41] Ariola, F. S., Krishnan, A., and Vogler, E. A., 2006, "Interfacial Rheology of Blood Proteins Adsorbed to the Aqueous-Buffer/Air Interface," Biomaterials, 27(18), pp. 3404-3412.

[42] Chaudhari, R. V., and Hofmann, H., 1994, "Coalescence of Gas Bubbles in Liquids," Reviews in Chemical Engineering, 10(2), p. 131.

[43] Kroll, M. H., Hellums, J. D., McIntire, L. V., Schafer, A. I., and Moake, J. L., 1996, "Platelets and Shear Stress," Blood, 88(5), pp. 1525-1541.

[44] Hellums, J. D., 1994, "1993 Whitaker Lecture: Biorheology in Thrombosis Research," Ann Biomed Eng, 22(5), pp. 445-455.

[45] Zhao, R., Antaki, J. F., Naik, T., Bachman, T. N., Kameneva, M. V., and Wu, Z. J., 2006, "Microscopic Investigation of Erythrocyte Deformation Dynamics," Biorheology, 43(6), pp. 747-765.

[46] Fedosov, D. A., Caswell, B., Popel, A. S., and Karniadakis, G. E., 2010, "Blood Flow and Cell-Free Layer in Microvessels," Microcirculation, 17(8), pp. 615-628.

[47] Wiedeman, M. P., 1963, "Dimensions of Blood Vessels from Distributing Artery to Collecting Vein," Circulation Research, 12(4), pp. 375-378.

[48] Schaller, J., Gerber, S., Kämpfer, U., Lejon, S., and Trachsel, C., 2008, "*Blood Components*," Human Blood Plasma Proteins, John Wiley & Sons, Ltd, pp. 5-16.

[49] Wheater, P. R., Burkitt, H. G., and Daniels, V. G., 1979, *Functional Histology: A Text and Colour Atlas*, Edinburgh: Churchill Livingstone, New York.

[50] Pitts, K. L., Mehri, R., Mavriplis, C., and Fenech, M., 2012, "Micro-Particle Image Velocimetry Measurement of Blood Flow: Validation and Analysis of Data Pre-Processing and Processing Methods," Measurement Science and Technology, 23(10).

[51] Lima, R., Fernandes, C. S., Dias, R., Ishikawa, T., Imai, Y., and Yamaguchi, T., 2011, "*Microscale Flow Dynamics of Red Blood Cells in Microchannels: An Experimental and Numerical Analysis*," Computational Vision and Medical Image Processing, J. M. R. S. Tavares, and R. M. N. Jorge, eds., Springer Netherlands, pp. 297-309.

[52] Pries, A. R., and Secomb, T. W., 2003, "Rheology of the Microcirculation," Clinical Hemorheology & Microcirculation, 29(3/4), pp. 143-148.

[53] Paul, R., Apel, J., Klaus, S., Schugner, F., Schwindke, P., and Reul, H., 2003, "Shear Stress Related Blood Damage in Laminar Couette Flow," Artif. Organs, 27(6), pp. 517-529.

[54] Kwak, D., and Kiris, C. C., 2010, "*Computation of Viscous Incompressible Flows*," Springer, Dordrecht.

[55] Beissinger, R. L., and Laugel, J.-F., 1987, "Low-Stress Hemolysis in Laminar Blood Flow: Bulk and Surface Effects in Capillaries," AIChE Journal, 33(1), pp. 99-108.

[56] Tomaiuolo, G., Barra, M., Preziosi, V., Cassinese, A., Rotoli, B., and Guido, S., 2011, "Microfluidics Analysis of Red Blood Cell Membrane Viscoelasticity," Lab Chip, 11(3), pp. 449-454.

[57] Lima, R., Wada, S., Tanaka, S., Takeda, M., Ishikawa, T., Tsubota, K., Imai, Y., and Yamaguchi, T., 2008, "In Vitro Blood Flow in a Rectangular PDMS Microchannel: Experimental Observations Using a Confocal Micro-PIV System," Biomedical Microdevices, 10(2), pp. 153-167.

[58] Watanabe, N., Arakawa, Y., Sou, A., Kataoka, H., Ohuchi, K., Fujimoto, T., and Takatani, S., 2007, "Deformability of Human Red Blood Cells Exposed to a Uniform Shear Stress as Measured by a Cyclically Reversing Shear Flow Generator," Physiological Measurement, 28(5), p. 531.

[59] Lee, S. S., Ahn, K. H., Lee, S. J., Sun, K., Goedhart, P. T., and Hardeman, M. R., 2004, "Shear Induced Damage of Red Blood Cells Monitored by the Decrease of Their Deformability," Korea-Australia Rheology Journal, 16(3), pp. 141-146.

[60] Li, J., Lykotrafitis, G., Dao, M., and Suresh, S., 2007, "Cytoskeletal Dynamics of Human Erythrocyte," Proc Natl Acad Sci U S A, 104(12), pp. 4937-4942.

[61] Naito, K., Mizuguchi, K., and Nose, Y., 1994, "The Need for Standardizing the Index of Hemolysis," Artif Organs, 18(1), pp. 7-10.

[62] Iuliano, L., Violi, F., Pedersen, J. Z., Pratico, D., Rotilio, G., and Balsano, F., 1992, "Free Radical-Mediated Platelet Activation by Hemoglobin Released from Red Blood Cells," Arch Biochem Biophys, 299(2), pp. 220-224.

[63] Villagra, J., Shiva, S., Hunter, L. A., Machado, R. F., Gladwin, M. T., and Kato, G. J., 2007, "Platelet Activation in Patients with Sickle Disease, Hemolysis-Associated Pulmonary Hypertension, and Nitric Oxide Scavenging by Cell-Free Hemoglobin," Blood, 110(6), pp. 2166-2172.

[64] Mercier, R., Kameneva, D., and Daly, A., 2004, "An Investigation of Mechanical Blood Trauma in Microfluidic Devices."

[65] "*Medical Device Materials*," Proc. Proceedings of the Materials and Processes for Medical Devices Conference, S. Shrivastava, ed., ASM International, p. 325.

[66] Leverett, L. B., Hellums, J. D., Alfrey, C. P., and Lynch, E. C., 1972, "Red Blood Cell Damage by Shear Stress," Biophysical Journal, 12(3), pp. 257-273.

[67] Heuser, G., and Opitz, R., 1980, "A Couette Viscometer for Short-Time Shearing of Blood," Biorheology, 17(1-2), pp. 17-24.

[68] Giersiepen, M., Wurzinger, L. J., Opitz, R., and Reul, H., 1990, "Estimation of Shear Stress-Related Blood Damage in Heart-Valve Prostheses - Invitro Comparison of 25 Aortic Valves," Int. J. Artif. Organs, 13(5), pp. 300-306.

[69] Carter, J., Hristova, K., Harasaki, H., and Smith, W. A., 2003, "Short Exposure Time Sensitivity of White Cells to Shear Stress," ASAIO Journal, 49(6), pp. 687-691.

[70] Polaschegg, H. D., 2009, "Red Blood Cell Damage from Extracorporeal Circulation in Hemodialysis," Semin Dial, 22(5), pp. 524-531.

[71] Jesty, J., Yin, W., Perrotta, P., and Bluestein, D., 2003, "Platelet Activation in a Circulating Flow Loop: Combined Effects of Shear Stress and Exposure Time," Platelets, 14(3), pp. 143-149.

[72] Corum, L. E., 2011, "Evaluating Surface-Induced Platelet Adhesion and Activation with Surface Patterning and Protein Immobilization Techniques. Dissertation," Doctor of Philosophy, The University of Utah, Salt Lake City.

[73] Maxwell, M. J., Westein, E., Nesbitt, W. S., Giuliano, S., Dopheide, S. M., and Jackson, S. P., 2007, "Identification of a 2-Stage Platelet Aggregation Process Mediating Shear-Dependent Thrombus Formation," Blood, 109(2), pp. 566-576.

[74] Dewitz, T. S., Hung, T. C., Martin, R. R., and McIntire, L. V., 1977, "Mechanical Trauma in Leukocytes," J Lab Clin Med, 90(4), pp. 728-736.

[75] Shah, R. K., and London, A. L., 1978, *Laminar Flow Forced Convection in Ducts*, Academic Press, New York, pp. 196-213.

[76] Cussler, E. L., 2009, *Diffusion Mass Transfer in Fluid Systems*, Cambridge University Press, New York.

[77] Mulder, M., 1996, *Basic Principles of Membrane Technology*, Springer, Dordrecht, The Netherlands, pp. 359.

[78] Ward, D. K., 2013, "Determining the Dimensional Requirements of a Reliable Compression Sealing Method for Use in Microchannel Hemodialysers. Dissertation," Master of Science, Oregon State University, Corvallis.

[79] Gere, J. M., 2004, *Mechanics of Materials*, Thomson, Belmont, CA, pp. 715.

[80] Arora, J. S., 2011, *Introduction to Optimum Design*, Academic Press, Waltham, MA, pp. 412,417,643-653.

[81] Mohammadi, M., and Sharp, K. V., 2013, "Experimental Techniques for Bubble Dynamics Analysis in Microchannels: A Review," Journal of Fluids Engineering, 135(2), pp. 021202-021202.

[82] Mohammadi, M., Jovanovic, G. N., and Sharp, K. V., 2013, "Numerical Study of Flow Uniformity and Pressure Characteristics within a Microchannel Array with Triangular Manifolds," Computers & Chemical Engineering, 52, pp. 134-144.

[83] Liu, H., Li, P. W., and Van Lew, J., 2010, "CFD Study on Flow Distribution Uniformity in Fuel Distributors Having Multiple Structural Bifurcations of Flow Channels," International Journal of Hydrogen Energy, 35(17), pp. 9186-9198.

[84] Commenge, J. M., Falk, L., Corriou, J. P., and Matlosz, M., 2002, "Optimal Design for Flow Uniformity in Microchannel Reactors," AIChe Journal, 48(2), pp. 345-358.

[85] Kim, S., Choi, E., and Cho, Y. I., 1995, "The Effect of Header Shapes on the Flow Distribution in a Manifold for Electronic Packaging Applications," International Communications in Heat and Mass Transfer, 22(3), pp. 329-341.

[86] Anderson, E., 2009, "Prediction of Mass Transfer Performance of Microchannel Dialyzers Using Deconvolution of Impulse-Response Experiments. Dissertation," Master of Science, Oregon State University, Corvallis.

[87] Balaji, S., and Lakshminarayanan, S., 2006, "Improved Design of Microchannel Plate Geometry for Uniform Flow Distribution," Canadian Journal of Chemical Engineering, 84(6), pp. 715-721.

[88] Pan, M., Wei, X., Zeng, D., and Tang, Y., 2010, "Trend Prediction in Velocity Distribution among Microchannels Based on the Analysis of Frictional Resistances," Chemical Engineering Journal, 164(1), pp. 238-245.

[89] Pan, M., Tang, Y., Pan, L., and Lu, L., 2008, "Optimal Design of Complex Manifold Geometries for Uniform Flow Distribution between Microchannels," Chemical Engineering Journal, 137(2), pp. 339-346.

[90] Rebrov, E. V., Schouten, J. C., and de Croon, M., 2011, "Single-Phase Fluid Flow Distribution and Heat Transfer in Microstructured Reactors," Chemical Engineering Science, 66(7), pp. 1374-1393.

[91] Webb, R. L., "*Effect of Manifold Design on Flow Distribution in Parallel Micro-Channels*," Proc. 2003 ASME International Electronic Packaging Technical Conference and Exhibition, IPACK03, ASME, pp. 527-535.

[92] Pan, M., Tang, Y., Yu, H., and Chen, H. Q., 2009, "Modeling of Velocity Distribution among Microchannels with Triangle Manifolds," AIChe Journal, 55(8), pp. 1969-1982.

[93] Saber, M., Commenge, J. M., and Falk, L., 2009, "Rapid Design of Channel Multi-Scale Networks with Minimum Flow Maldistribution," Chemical Engineering and Processing, 48(3), pp. 723-733.

[94] Commenge, J. M., Saber, M., and Falk, L., 2011, "Methodology for Multi-Scale Design of Isothermal Laminar Flow Networks," Chemical Engineering Journal, 173(2), pp. 541-551.

[95] Shah, R. K., and Mueller, A. C., 1985, "*Heat Exchangers*," Handbook of Heat Transfer Applications, W. M. Rohsenow, J. P. Hartnett, and E. N. Ganic´, eds., McGraw-Hill, New York.

[96] Bajura, R. A., and Jones Jr, E. H., 1976, "Flow Distribution Manifolds," Journal of Fluids Engineering, Transactions of the ASME, 98 Ser 1(4), pp. 654-666.

[97] Shah, R. K., and Sekulic, D. P., 2003, *Fundamentals of Heat Exchanger Design*, John Wiley & Sons, Hoboken, New Jersey, pp. 71-73, 380-381, 834-836, 852.

[98] Tonomura, O., Tanaka, S., Noda, M., Kano, M., Hasebe, S., and Hashimoto, L., 2004, "CFD-Based Optimal Design of Manifold in Plate-Fin Microdevices," Chemical Engineering Journal, 101(1-3), pp. 397-402.

[99] Griffini, G., and Gavriilidis, A., 2007, "Effect of Microchannel Plate Design on Fluid Flow Uniformity at Low Flow Rates," Chemical Engineering & Technology, 30(3), pp. 395-406.

[100] Pan, M., Tang, Y., Zhou, W., and Lu, L. S., "*Flow Distribution among Microchannels with Asymmetrical Manifolds*," Proc. 2007 IEEE International Conference on Control and Automation, ICCA, Institute of Electrical and Electronics Engineers Inc., pp. 193-197.

[101] Pan, M., Zeng, D., Tang, Y., and Chen, D., 2009, "CFD-Based Study of Velocity Distribution among Multiple Parallel Microchannels," Journal of Computers, 4(11), pp. 1133-1138.

[102] Mathew, B., John, T. J., and Hegab, H., "*Effect of Manifold Design on Flow Distribution in Multichanneled Microfluidic Devices*," Proc. 2009 ASME Fluids Engineering Division Summer Conference, FEDSM2009, ASME, pp. 543-548.

[103] Solovitz, S. A., and Mainka, J., 2011, "Manifold Design for Micro-Channel Cooling with Uniform Flow Distribution," Transactions of the ASME Journal of Fluids Engineering, 133(5), p. 051103.

[104] Zeng, D., Pan, M., and Tang, Y., 2012, "Qualitative Investigation on Effects of Manifold Shape on Methanol Steam Reforming for Hydrogen Production," Renewable Energy, 39(1), pp. 313-322.

[105] Jang, J.-Y., Huang, Y.-X., and Cheng, C.-H., 2010, "The Effects of Geometric and Operating Conditions on the Hydrogen Production Performance of a Micro-Methanol Steam Reformer," Chemical Engineering Science, 65(20), pp. 5495-5506.

[106] Wiginton, C. L., and Dalton, C., 1970, "Incompressible Laminar Flow in the Entrance Region of a Rectangular Duct," Journal of Applied Mechanics, 37(3), pp. 854-856.

[107] Ahmad, T., and Hassan, I., 2010, "Experimental Analysis of Microchannel Entrance Length Characteristics Using Microparticle Image Velocimetry," Transactions of the ASME Journal of Fluids Engineering, 132(4), p. 041102.

[108] Koşar, A., Mishra, C., and Peles, Y., 2005, "Laminar Flow across a Bank of Low Aspect Ratio Micro Pin Fins," Journal of Fluids Engineering, 127(3), p. 419.

[109] Koşar, A., Schneider, B., and Peles, Y., 2011, "Hydrodynamic Characteristics of Crossflow over Mems-Based Pillars," Journal of Fluids Engineering, 133(8), p. 081201.

[110] Short, B. E., Raad, P. E., and Price, D. C., 2002, "Performance of Pin Fin Cast Aluminum Coldwalls, Part 1: Friction Factor Correlations," Journal of Thermophysics and Heat Transfer, 16(3), pp. 389-396.

[111] Moores, K. A., and Joshi, Y. K., 2003, "Effect of Tip Clearance on the Thermal and Hydrodynamic Performance of a Shrouded Pin Fin Array," Journal of Heat Transfer, 125(6), pp. 999-1006.

[112] Prasher, R. S., Dirner, J., Chang, J.-Y., Myers, A., Chau, D., He, D., and Prstic, S., "*Nusselt Number and Friction Factor of Staggered Arrays of Low Aspect Ratio Micro-Pin-Fins under Cross Flow for Water as Fluid*," Proc. 2006 ASME International Mechanical Engineering Congress and Exposition, IMECE2006, November 5, 2006 - November 10, 2006, American Society of Mechanical Engineers.

[113] Inoue, O., and Sakuragi, A., 2008, "Vortex Shedding from a Circular Cylinder of Finite Length at Low Reynolds Numbers," Physics of Fluids, 20(3), p. 033601.

[114] Tamayol, A., Khosla, A., Gray, B. L., and Bahrami, M., 2012, "Creeping Flow through Ordered Arrays of Micro-Cylinders Embedded in a Rectangular Minichannel," International Journal of Heat and Mass Transfer, 55(15-16), pp. 3900-3908.

[115] Tamayol, A., and Bahrami, M., 2011, "Transverse Permeability of Fibrous Porous Media," Physical Review E, 83(4), p. 046314.

[116] Tamayol, A., Yeom, J., Akbari, M., and Bahrami, M., 2013, "Low Reynolds Number Flows across Ordered Arrays of Micro-Cylinders Embedded in a Rectangular Micro/Minichannel," International Journal of Heat and Mass Transfer, 58(1-2), pp. 420-426.

APPENDICES

Appendix

A. UNCERTAINTY IN PRESSURE MEASUREMENTS AND MODEL'S PREDICTION

If $R = f(x_1, x_2, ..., x_n)$, where x_i are independent variables, then according to Kline and McClintock method [34] estimates the uncertainty in the experimental measurement of *R* as

$$\varepsilon_R = \sqrt{\sum_{i=1}^{n} \left(\frac{\partial R}{\partial x_i} \varepsilon_{x_i} \right)^2} \tag{111}$$

The measured pressure across the bubble length is calculated from

$$\Delta P = P_3 - (P_1 + P_2) \tag{112}$$

where P_1 is the measured pressure at the flow rate of $2\ \mu l/min$ in the absence of a bubble, P_2 is the hydrostatic pressure change ($\rho gh = \rho gQ / \pi r_{reservoir}^2$) due to the change in the water level in the outlet, and P_3 is the measured pressure during the motion of the bubble and image acquisition at the flow rate of $2\ \mu l/min$. The standard error of P_1 and P_3 are associated the pressure transducer presented in Table A-1.

Using Kline and McClintock method the standard error for P_2 becomes

$$\frac{\varepsilon_{P_2}}{P_2} = \frac{2}{r_{reservoir}} \varepsilon_{r_{reservoir}} = \frac{2}{28\ (\text{mm})} 0.1\ (\text{mm}) = 0.007 \tag{113}$$

As P_2 is about 1 to 2 Pa, its standard error becomes completely negligible.

Table A-1: Properties of the pressure transducer

Accuracy	0.08%	2 Pa
Thermal effect	0.0054% /degree F	0.24 Pa for 1.8° F change

According to Kline and McClintock method,

$$\varepsilon_{\Delta P} = \sqrt{\varepsilon_{P_1}^2 + \varepsilon_{P_2}^2 + \varepsilon_{P_3}^2} = \sqrt{(2^2 + 0.24^2) + 2^2 + 0} = 2.84 \tag{114}$$

The concave back model prediction is given by $4\sigma_{lg}(\cos\theta_{rec} - \cos\theta_{adv})/h$ in which $\cos\theta_{rec}$ is replaced by $(\cos\theta_{rec,top} + \cos\theta_{rec,bottom})/2$ and $\cos\theta_{adv}$ is replaced by $(\cos\theta_{adv,top} + \cos\theta_{adv,bottom})/2$. The uncertainty in concave back model's prediction becomes

$$\varepsilon_{\Delta P} = 4\sigma_{\lg}\sqrt{\begin{array}{l}\left(\frac{\sin\theta_{rec,top}}{2h}\varepsilon_{\theta_{rec,top}}\right)^2 + \left(\frac{\sin\theta_{rec,bottom}}{2h}\varepsilon_{\theta_{rec,bottom}}\right)^2 + \\ \left(\frac{\sin\theta_{adv,top}}{2h}\varepsilon_{\theta_{adv,top}}\right)^2 + \left(\frac{\sin\theta_{adv,bottom}}{2h}\varepsilon_{\theta_{adv,bottom}}\right)^2 + \\ \left(\frac{((\cos\theta_{rec,top} + \cos\theta_{rec,bottom}) - (\cos\theta_{adv,top} + \cos\theta_{adv,bottom}))}{h^2}\varepsilon_h\right)^2\end{array}} \tag{115}$$

The convex back model prediction is given by $4\sigma_{lg}(\cos\theta_{rec} - \cos\theta_{equ} - \cos\theta_{adv})/h$. The uncertainty in concave back model's prediction becomes

$$\varepsilon_{\Delta P} = 4\sigma_{\lg}\sqrt{\begin{array}{l}\left(\frac{\sin\theta_{rec,top}}{2h}\varepsilon_{\theta_{rec,top}}\right)^2 + \left(\frac{\sin\theta_{rec,bottom}}{2h}\varepsilon_{\theta_{rec,bottom}}\right)^2 + \\ \left(\frac{\sin\theta_{adv,top}}{2h}\varepsilon_{\theta_{adv,top}}\right)^2 + \left(\frac{\sin\theta_{adv,bottom}}{2h}\varepsilon_{\theta_{adv,bottom}}\right)^2 + \\ \left(\frac{\sin\theta_{equ}}{h}\varepsilon_{\theta_{equ}}\right)^2 + \\ \left(\frac{((\cos\theta_{rec,top} + \cos\theta_{rec,bottom}) - \theta_{equ} - (\cos\theta_{adv,top} + \cos\theta_{adv,bottom}))}{h^2}\varepsilon_h\right)^2\end{array}}$$

The uncertainty in the contact angle reading from the images was $\pm 2.25^{\circ}$. This uncertainty is a function of image resolution and thresholding. The uncertainty in the estimation of the equilibrium contact angle was assigned to be $\pm 2.25^{\circ}$, and the uncertainty in the size of the channel was $\pm 8\ \mu m$.

Appendix

B. DEWETTING VELOCITY MEASURMENT

The variation in the position of a point on the edge of the opening holes during dewetting on the uncoated and coated surfaces are presented in Figure B-1 and Figure B-2. The slope of the position vs. time represents the dewetting velocity. The standard error of the slope is obtained using the LINEST function in Microsoft Excel.

The dewetting velocity on the coated and uncoated surfaces are 1.47 ± 0.02 cm/s and 3.42 ± 0.03 cm/s, respectively.

The marked circle on the surfaces (see Figure 19) with the diameter of 31 mm has been used as a calibrator for the images. The positions have been calculated using Eq. (66). The standard errors on the position measurements are calculated from Eq. (68). The uncertainty due to lens distortion $(\varepsilon_{\Delta x})$ has been neglected.

Table B-1: Data used for the calibration of the dewetting images

Span	31 mm
ε_{span}	0.5 mm
Pixel count	408 pixels
$\varepsilon_{pixel\ count}$	1 pixel

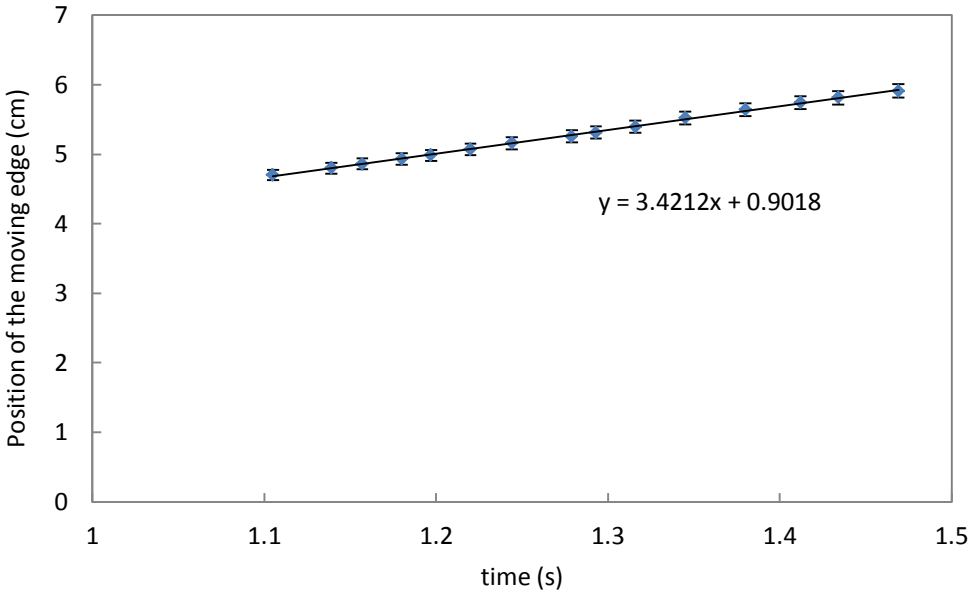

Figure B-1: Dewetting velocity on the uncoated polycarbonate surface

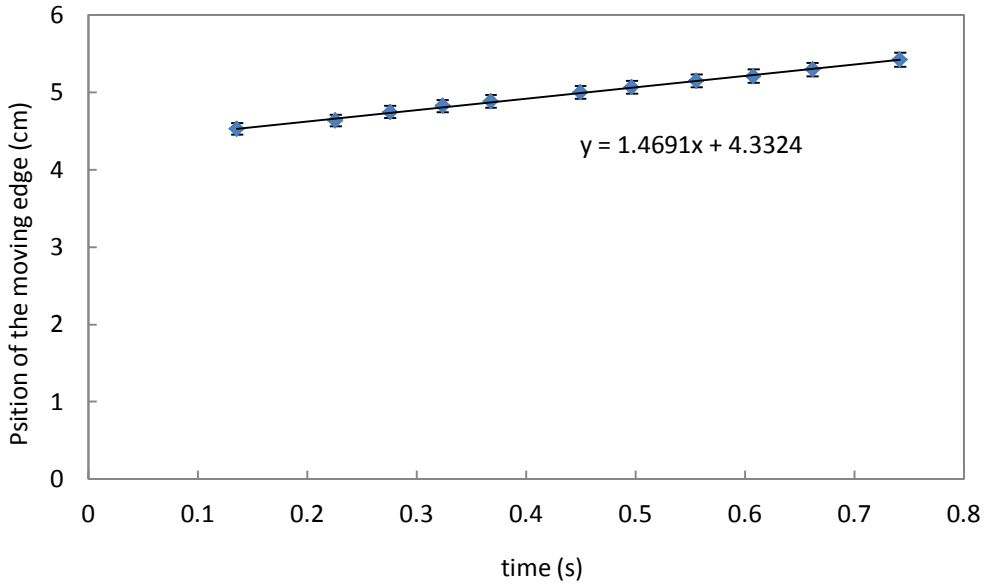

Figure B-2: Dewetting velocity on the PEO coated surface

Appendix

C. SLIP BOUNDARY CONDITION AT BUBBLE INTERFACE

The tangential stress balance at the gas-liquid interface yields

$$\mu_l \frac{\partial u_{x,l}}{\partial y} = \mu_g \frac{\partial u_{x,g}}{\partial y} \tag{116}$$

If we divide the above equation by the dynamic viscosity of the liquid we get

$$\frac{\partial u_{x,l}}{\partial y} = \frac{\mu_g}{\mu_l} \frac{\partial u_{x,g}}{\partial y} \tag{117}$$

As the dynamic viscosity of a gas is small compared to that of a liquid, the right hand side of the equation can be considered negligible and is referred to as the slip boundary condition or the absence of shear stress at the interface.

$$\frac{\partial u_{x,l}}{\partial y} \approx 0 \tag{118}$$

The presence of surfactants in the liquid leads to a no-slip boundary condition. Furthermore, the presented approximation is not valid when the motivating force for the motion of the liquid is the motion of the gas. When gas drags the liquid, the $\partial u_{x,g} / \partial y$ term might be large.

Appendix

D. DRAWINGS OF THE TEST SECTION PIECES

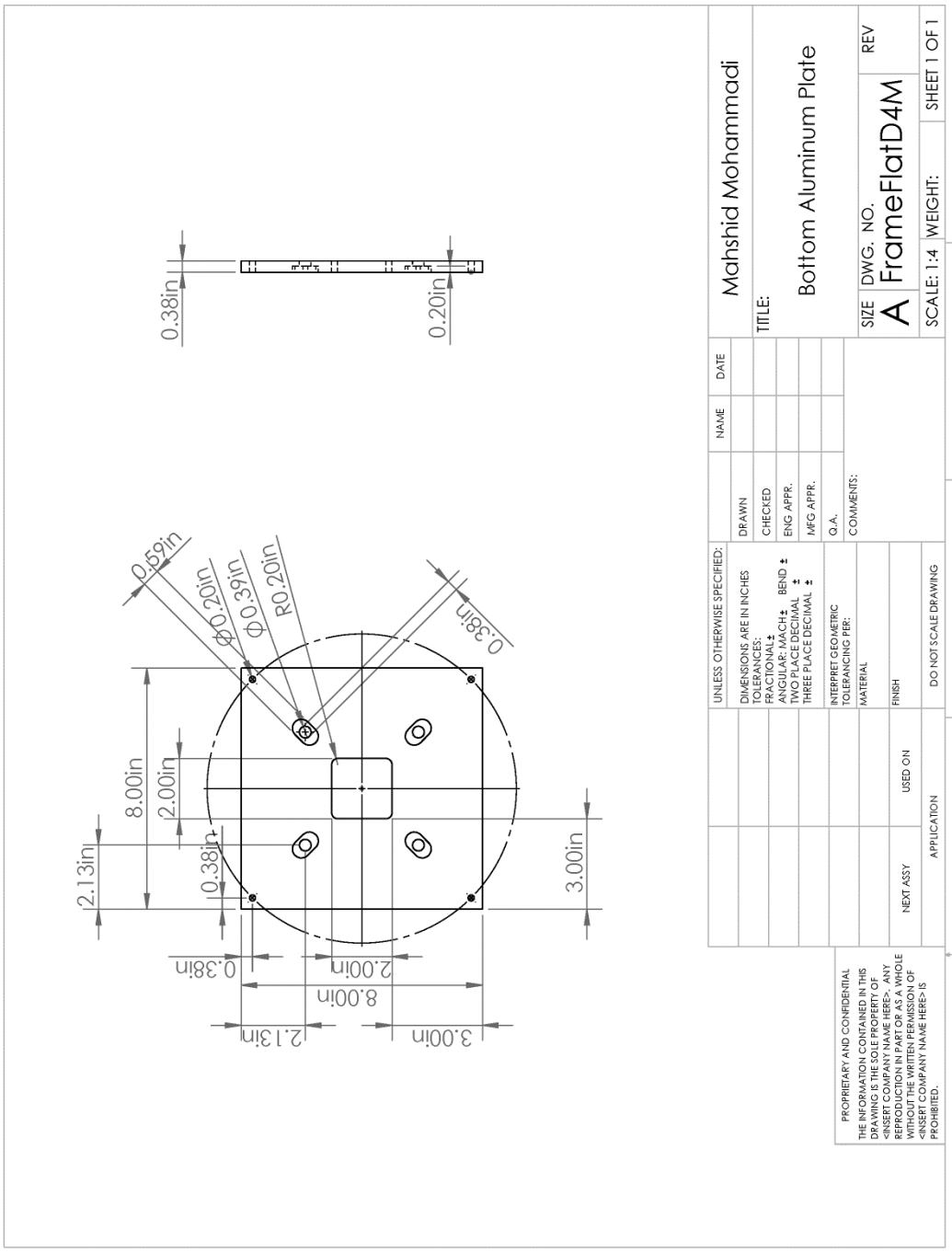
0.38in
0.20in
0.59in
ϕ0.20in
ϕ0.39in
R0.20in
0.38in
8.00in
2.00in
2.13in
0.38in
3.00in
0.38in
2.00in
8.00in
2.13in
3.00in
UNLESS OTHERWISE SPECIFIED:
DIMENSIONS ARE IN INCHES
TOLERANCES:
FRACTIONAL ±
ANGULAR: MACH ± BEND ±
TWO PLACE DECIMAL ±
THREE PLACE DECIMAL ±
INTERPRET GEOMETRIC TOLERANCING PER:
MATERIAL
FINISH
DO NOT SCALE DRAWING
NEXT ASSY
USED ON
APPLICATION
DRAWN
CHECKED
ENG APPR.
MFG APPR.
Q.A.
COMMENTS:
NAME
DATE
Mahshid Mohammadi
TITLE:
Bottom Aluminum Plate
SIZE
A
DWG. NO.
FrameFlatD4M
REV
SCALE: 1:4
WEIGHT:
SHEET 1 OF 1
PROPRIETARY AND CONFIDENTIAL
THE INFORMATION CONTAINED IN THIS DRAWING IS THE SOLE PROPERTY OF <INSERT COMPANY NAME HERE>. ANY REPRODUCTION IN PART OR AS A WHOLE WITHOUT THE WRITTEN PERMISSION OF <INSERT COMPANY NAME HERE> IS PROHIBITED.

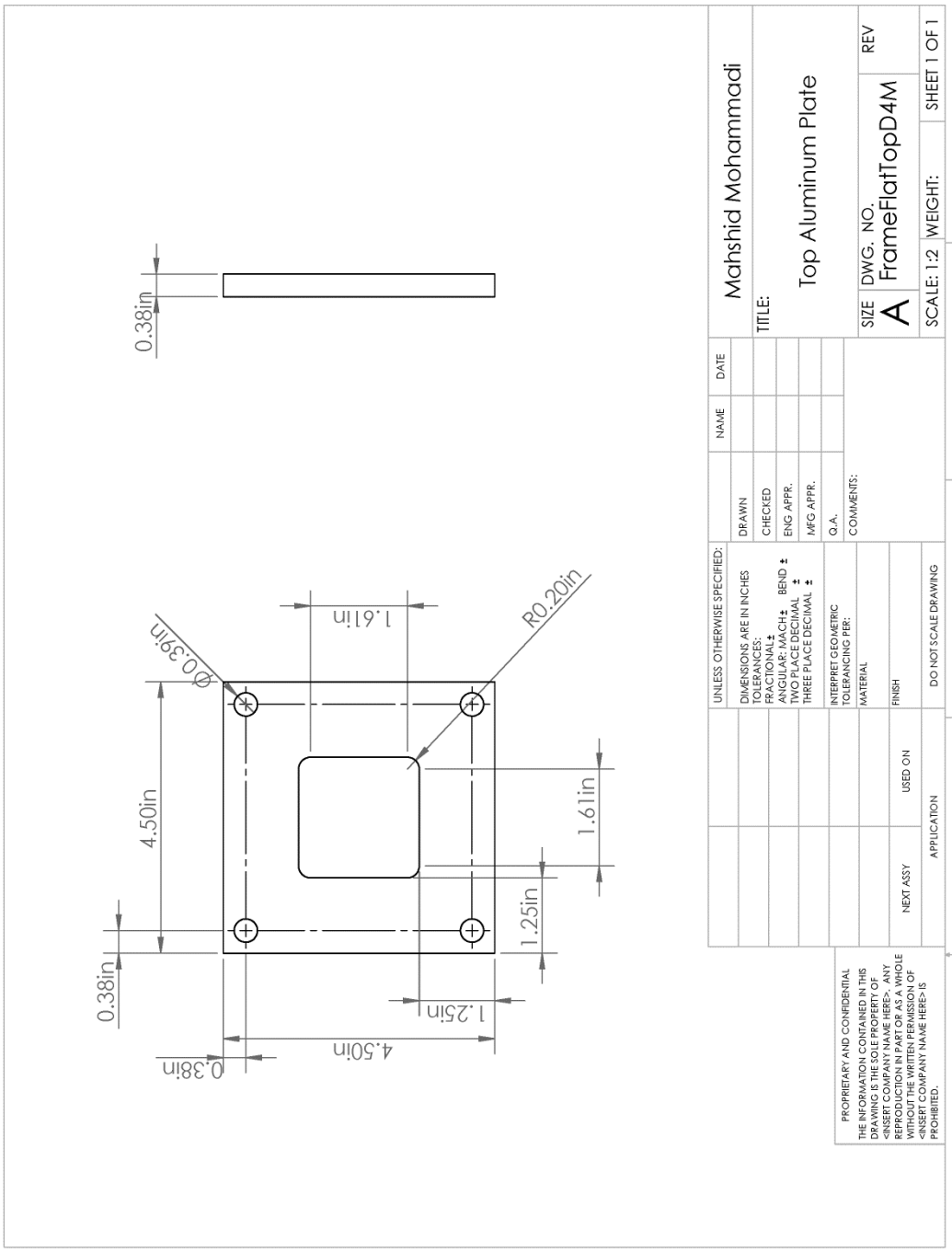
0.38in
R0.20in
Ø0.39in
1.61in
4.50in
0.38in
1.61in
1.25in
1.25in
4.50in
0.38in
Mahshid Mohammadi
TITLE:
Top Aluminum Plate
SIZE
A
DWG. NO.
FrameFlatTopD4M
REV
SCALE: 1:2
WEIGHT:
SHEET 1 OF 1
UNLESS OTHERWISE SPECIFIED:
DIMENSIONS ARE IN INCHES
TOLERANCES:
FRACTIONAL ±
ANGULAR: MACH ± BEND ±
TWO PLACE DECIMAL ±
THREE PLACE DECIMAL ±
INTERPRET GEOMETRIC TOLERANCING PER:
MATERIAL
FINISH
DO NOT SCALE DRAWING
NAME
DATE
DRAWN
CHECKED
ENG APPR.
MFG APPR.
Q.A.
COMMENTS:
NEXT ASSY
USED ON
APPLICATION
PROPRIETARY AND CONFIDENTIAL
THE INFORMATION CONTAINED IN THIS DRAWING IS THE SOLE PROPERTY OF <INSERT COMPANY NAME HERE>. ANY REPRODUCTION IN PART OR AS A WHOLE WITHOUT THE WRITTEN PERMISSION OF <INSERT COMPANY NAME HERE> IS PROHIBITED.

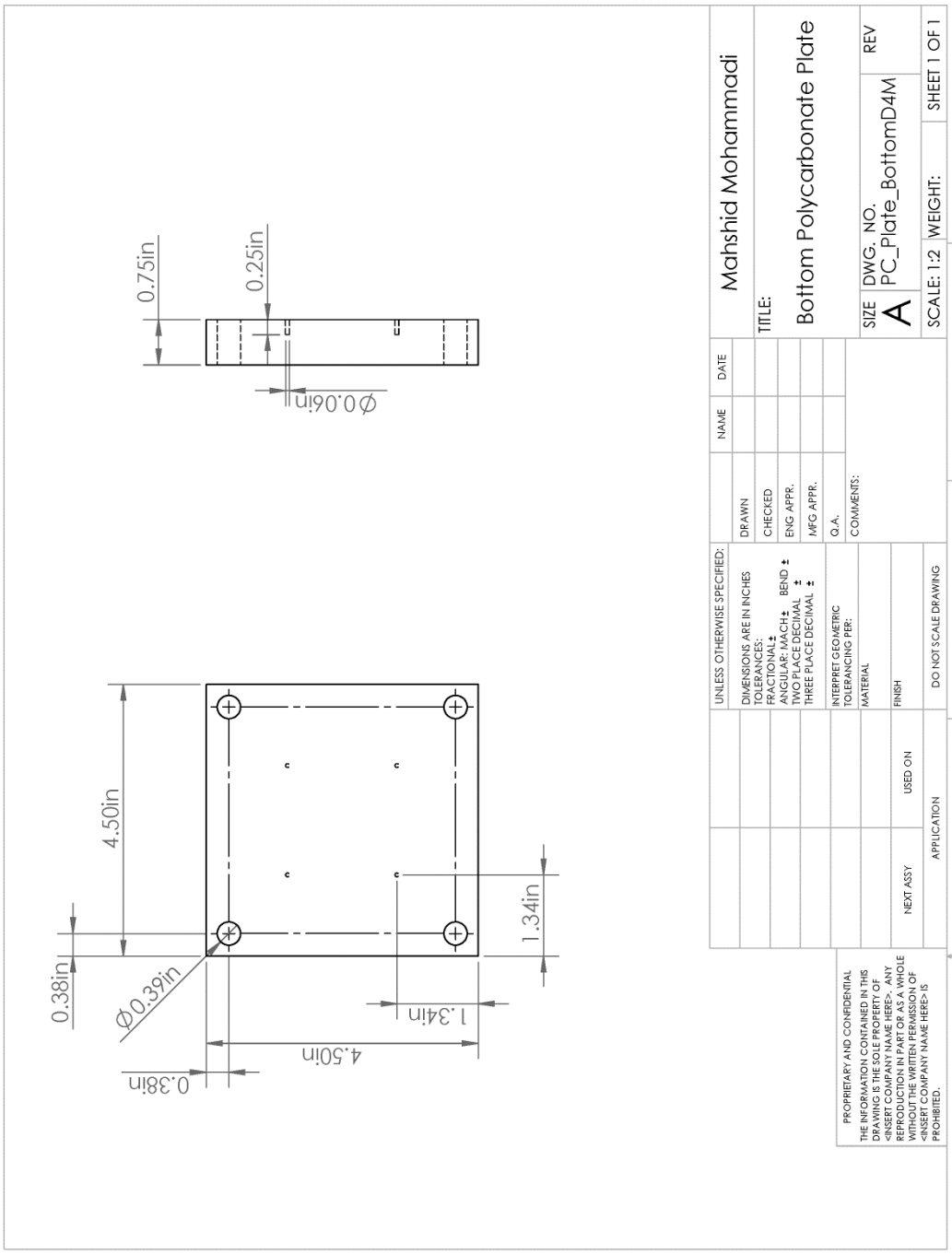
0.75in
0.25in
Ø0.06in
4.50in
0.38in
Ø0.39in
1.34in
4.50in
0.38in
1.34in
UNLESS OTHERWISE SPECIFIED:
DIMENSIONS ARE IN INCHES
TOLERANCES:
FRACTIONAL ±
ANGULAR: MACH ± BEND ±
TWO PLACE DECIMAL ±
THREE PLACE DECIMAL ±
INTERPRET GEOMETRIC TOLERANCING PER:
MATERIAL
FINISH
DO NOT SCALE DRAWING
NEXT ASSY
USED ON
APPLICATION
DRAWN
CHECKED
ENG APPR.
MFG APPR.
Q.A.
COMMENTS:
NAME
DATE
Mahshid Mohammadi
TITLE:
Bottom Polycarbonate Plate
SIZE
A
DWG. NO.
PC_Plate_BottomD4M
REV
SCALE: 1:2
WEIGHT:
SHEET 1 OF 1
PROPRIETARY AND CONFIDENTIAL
THE INFORMATION CONTAINED IN THIS DRAWING IS THE SOLE PROPERTY OF <INSERT COMPANY NAME HERE>. ANY REPRODUCTION IN PART OR AS A WHOLE WITHOUT THE WRITTEN PERMISSION OF <INSERT COMPANY NAME HERE> IS PROHIBITED.

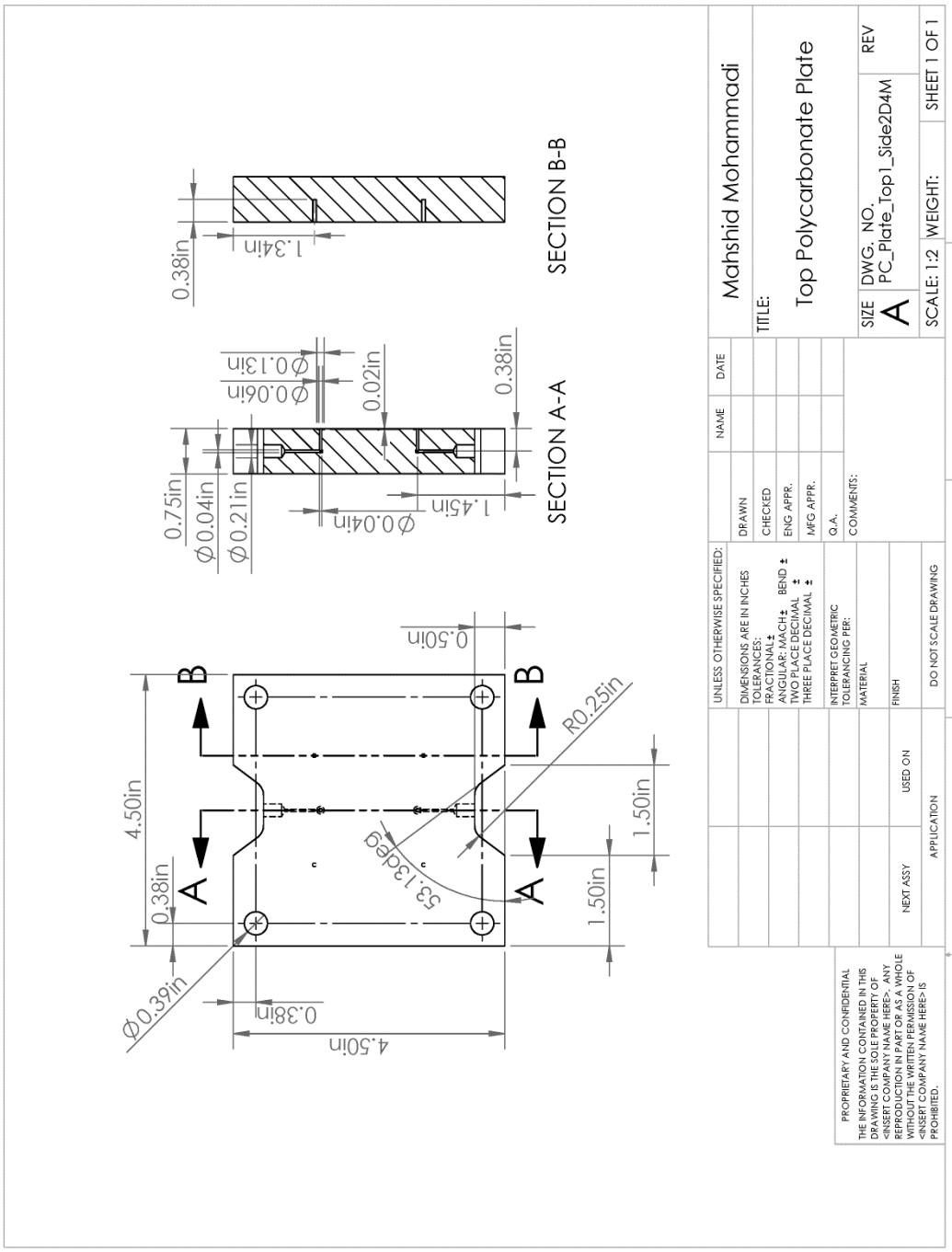
SECTION B-B
SECTION A-A
0.38in
1.34in
0.75in
Ø0.04in
Ø0.21in
Ø0.06in
Ø0.13in
0.02in
0.38in
Ø0.04in
1.45in
4.50in
0.38in
Ø0.39in
0.38in
4.50in
0.50in
R0.25in
53.13deg
1.50in
1.50in
A
B
A
B
UNLESS OTHERWISE SPECIFIED:
DIMENSIONS ARE IN INCHES
TOLERANCES:
FRACTIONAL ±
ANGULAR: MACH ± BEND ±
TWO PLACE DECIMAL ±
THREE PLACE DECIMAL ±
INTERPRET GEOMETRIC TOLERANCING PER:
MATERIAL
FINISH
DO NOT SCALE DRAWING
NEXT ASSY
USED ON
APPLICATION
DRAWN
CHECKED
ENG APPR.
MFG APPR.
Q.A.
COMMENTS:
NAME
DATE
Mahshid Mohammadi
TITLE:
Top Polycarbonate Plate
SIZE
A
DWG. NO.
PC_Plate_Top1_Side2D4M
REV
SCALE: 1:2
WEIGHT:
SHEET 1 OF 1
PROPRIETARY AND CONFIDENTIAL
THE INFORMATION CONTAINED IN THIS DRAWING IS THE SOLE PROPERTY OF <INSERT COMPANY NAME HERE>. ANY REPRODUCTION IN PART OR AS A WHOLE WITHOUT THE WRITTEN PERMISSION OF <INSERT COMPANY NAME HERE> IS PROHIBITED.
1
2
3
4
5

Appendix

E. POSITIVE CAPILLARY PRESSURE AT THE BEGINNING OF A CONTRACTION

To demonstrate why a bubble tends to enter the beginning of a contraction but requires an external clogging pressure to move further, a simple example has been developed. For the described planar geometry in Figure E-1, the position dependent capillary pressure of a bubble which could entirely fit inside the contraction is calculated by Eq. (39). It is assumed that the depth-wise distances are large so the depth-wise curvatures are negligible. A Matlab code is implemented to predict the position of the back interface with the assumption that while moving through the contraction the bubble volume remains constant. The results are shown in Figure E-2 and Figure E-3. The values of the dynamic advancing and receding contact angle have been selected arbitrarily as 60 and 40 degrees. The initial distance between x_R and x_L was $45\ \mu m$.

$$\Delta P_{cap} = \sigma\left(\frac{\cos[\theta_{adv} - \theta_t(x_L)]}{w(x_L)} - \frac{\cos[\theta_{rec} + \theta_t(x_R)]}{w(x_R)}\right) \tag{119}$$

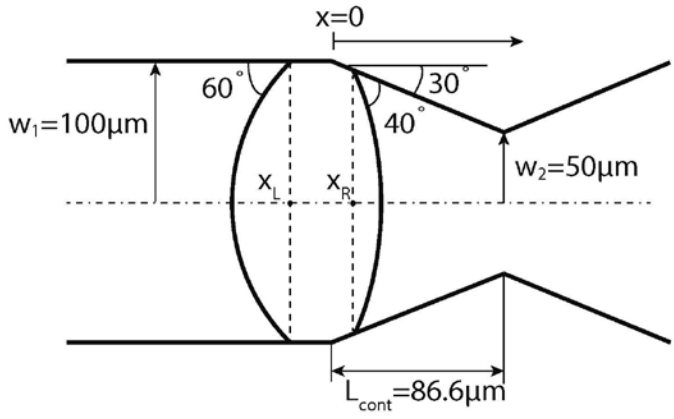

Figure E-1: The top view of the studied geometry

As expected the bubble spontaneously enters the contraction with no pressure requirement $(\Delta P_{cap} > 0)$. Clogging pressure is needed as the front interface moves into the narrower parts and its curvature becomes larger than the curvature of the back interface $(\Delta P_{cap} < 0)$. As it moves further, the backside of the bubble enters the contraction and forms a larger curvature which removes the pressure requirement. In contrast to the bubble front which flattens upon entrance, the back of the bubble swells. The velocity of the back contact line momentarily increases to form the inflated back interface. As the bubble moves further into the contraction, the difference between the back and front curvatures decreases.

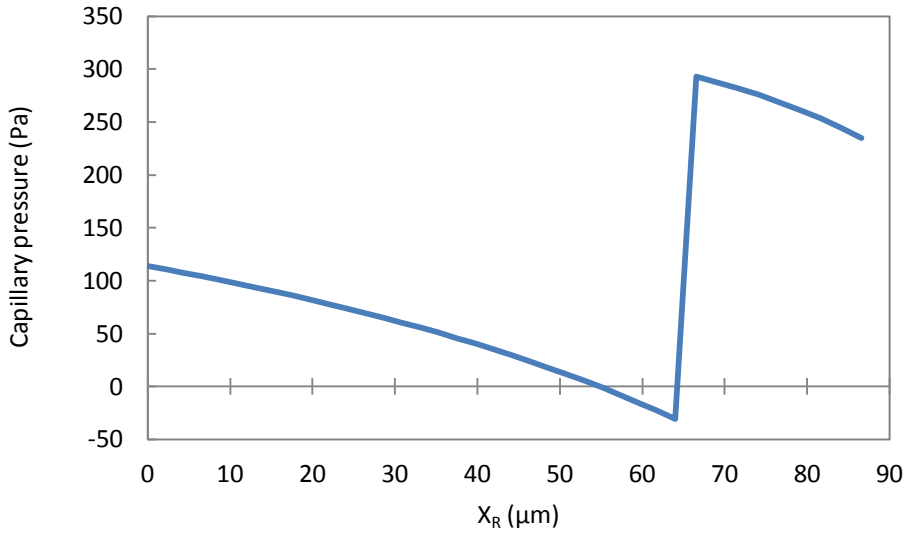

Figure E-2: Variation in the capillary pressure vs. position of the front contact line

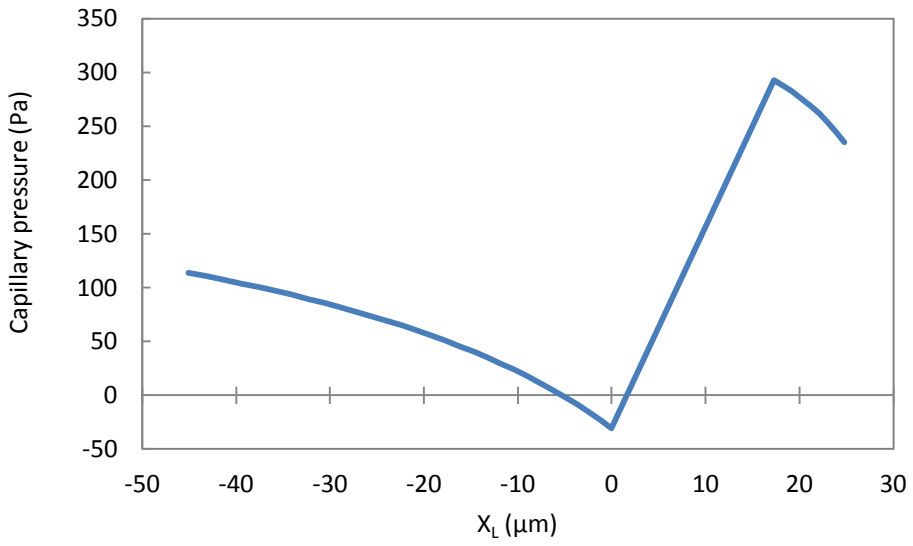

Figure E-3: Variation in the capillary pressure vs. position of the back contact line

Appendix

F. MATLAB IMAGE PROCESSING CODES

Matlab codes for processing the images of bubbles in two arrangements

```
clc, clear all, close all
tic
I_1 = imread('B00001.tif'); %input image
I_2 = imread('bg.tif'); %background
j=1;
k=1;
I1 = imadjust(I_1);
I2 = imadjust(I_2);
I1_c = I_1(615:1415,75:2500); % cropping
I2_c = I_2(615:1415,75:2500);

% Registration of the image over the background
[optimizer metric] = imregconfig('monomodal');
I1_c = imregister(I1_c, I2_c, 'translation', optimizer, metric);

imwrite(I1_c,'cropped registered.tif', 'tif'); %binery image

% Images are broken into five pieces for better thresholding.
LL1 = I1_c(:, 1:399);
LR1 = I1_c(:, 400:808);
C1 = I1_c(:, 809:1617);
RL1 = I1_c(:, 1618:2026);
RR1 = I1_c(:, 2027:2426);

LL2 = I2_c(:, 1:399);
LR2 = I2_c(:, 400:808);
C2 = I2_c(:, 809:1617);
RL2 = I2_c(:, 1618:2026);
RR2 = I2_c(:, 2027:2426);

% Read the mask of microposts
postmask = imread('postmask.tif', 'tif');
postmask = postmask(:,:);
postmask = im2bw(postmask);

% Read the mask of inlet/outlet holes
mask = imread('mask.tif');
ML = mask(:, 1:399);
MR = mask(:, 2027:2426);
ML = im2bw(ML);
MR = im2bw(MR);

figure, subplot(2,5,1), subimage(LL1);
subplot(2,5,2), subimage(LR1);
subplot(2,5,3), subimage(C1);
subplot(2,5,4), subimage(RL1);
subplot(2,5,5), subimage(RR1);
subplot(2,5,6), subimage(LL2)
subplot(2,5,7), subimage(LR2)
subplot(2,5,8), subimage(C2)
subplot(2,5,9), subimage(RL2)
```

```
subplot(2,5,10), subimage(RR2)

% Difference between background and bubble image
LLd = LL2-LL1;
LRd = LR2-LR1;
Cd = C2-C1;
RLd = RL2-RL1;
RRd = RR2-RR1;

% Adjusted difference
LLda = imadjust(LLd);
LRda = imadjust(LRd);
Cda = imadjust(Cd);
RLda = imadjust(RLd);
RRda = imadjust(RRd);

figure, subplot(2,5,1), subimage(LLd)
subplot(2,5,2), subimage(LRd)
subplot(2,5,3), subimage(Cd)
subplot(2,5,4), subimage(RLd)
subplot(2,5,5), subimage(RRd)
subplot(2,5,6), subimage(LLda)
subplot(2,5,7), subimage(LRda)
subplot(2,5,8), subimage(Cda)
subplot(2,5,9), subimage(RLda)
subplot(2,5,10), subimage(RRda)


% Thresholing the adjusted difference.
LLpt = im2bw(LLda, 0.30);
LRpt = im2bw(LRda, 0.30);
Cpt = im2bw(Cda,0.35);
RLpt = im2bw(RLda, 0.35);
RRpt = im2bw(RRda,0.35);

figure, subplot(2,5,1), subimage(LLda)
subplot(2,5,2), subimage(LRda)
subplot(2,5,3), subimage(Cda)
subplot(2,5,4), subimage(RLda)
subplot(2,5,5), subimage(RRda)
subplot(2,5,6), subimage(LLpt)
subplot(2,5,7), subimage(LRpt)
subplot(2,5,8), subimage(Cpt)
subplot(2,5,9), subimage(RLpt)
subplot(2,5,10), subimage(RRpt)


% Mask the inlet outlet holes
LLpt = LLpt.*ML;
RRpt = RRpt.*MR;

% Cleaning up the images.
LLpt = bwareaopen(LLpt, 25); % erases continuous objects smaller than
25 pixels.
```

```
LRpt = bwareaopen(LRpt, 25);
Cpt = bwareaopen(Cpt, 25);
RLpt = bwareaopen(RLpt, 25);
RRpt = bwareaopen(RRpt, 25);

% Connecting all the images
BW = [LLpt LRpt Cpt RLpt RRpt];
BW = imclearborder(BW); %removes lines on the borders due to
registration.
BW = imfill(BW, 'holes');
BW = times(postmask,BW);

% Labeling
[L num] = bwlabel(BW);
bubbles = regionprops(L); % Centroid of labeled objects.

figure, subplot(2,1,1), subimage(I1_c)
subplot(2,1,2), subimage(BW)

h = figure;
vislabels(L)
print(h,'-dpng','-r300','Labeled');
rectangles = zeros(num, 4);
hold on
figure, imshow(BW)
for i = 1:num,
    r     =     rectangle('Position',     [bubbles(i).BoundingBox(1)
bubbles(i).BoundingBox(2)                   bubbles(i).BoundingBox(3)
bubbles(i).BoundingBox(4)]);
    set(r, 'edgecolor', 'r');
end
hold off

% Generating “data1”, containing all the bubbles
for i = 1:num; %extracting area and centroid info.
    data(i,1) = i;
    data(i,2) = bubbles(i).Area;
    data(i,3) = bubbles(i).Centroid(1);
    data(i,4) = bubbles(i).Centroid(2);

   x_min(i,1) = bubbles(i).BoundingBox(1);
   x_max(i,1)          =          bubbles(i).BoundingBox(1)          +
bubbles(i).BoundingBox(3);
   y_min(i,1) = bubbles(i).BoundingBox(2);
   y_max(i,1)          =          bubbles(i).BoundingBox(2)          +
bubbles(i).BoundingBox(4);

% Generating “data2”, containing bubbles on the left
    if bubbles(i).Centroid(2) > 63 && bubbles(i).Centroid(2)<737
        if bubbles(i).Centroid(1) >144 && bubbles(i).Centroid(1)<1202
    data2(j,1) = i;
    data2(j,2) = bubbles(i).Area;
    data2(j,3) = bubbles(i).Centroid(1);
    data2(j,4) = bubbles(i).Centroid(2);
```

```
    data2(j,5) = x_min(i,1);
    data2(j,6) = x_max(i,1);
    data2(j,7) = y_min(i,1);
    data2(j,8) = y_max(i,1);
    j = j+1;
        end

% Generating “data3”, containing bubbles on the right
      if bubbles(i).Centroid(1) >= 1202 && x_max (i,1) <2345
    data3(k,1) = i;
    data3(k,2) = bubbles(i).Area;
    data3(k,3) = bubbles(i).Centroid(1);
    data3(k,4) = bubbles(i).Centroid(2);
    data3(k,5) = x_min(i,1);
    data3(k,6) = x_max(i,1);
    data3(k,7) = y_min(i,1);
    data3(k,8)= y_max(i,1);
    data3(k,9)= x_max(i,1)-x_min(i,1);
    data3(k,10)= y_max(i,1)-y_min(i,1);
    k = k+1;
      end
    end
end

data1 = [data x_min x_max y_min y_max];
imwrite(BW,'BWB00001.tif', 'tif');

% Generating Excel files
header1= {'Bubble No.', 'Area', 'Centroid X', 'Centroid Y','X min',
'X max', 'Y min', 'Y max '};
header2= {'Bubble No.', 'Area', 'Centroid X', 'Centroid Y','X min',
'X max', 'Y min', 'Y max'};
header3= {'Bubble No.', 'Area', 'Centroid X', 'Centroid Y','X min',
'X max', 'Y min', 'Y max','dx', 'dy'};
xlswrite('B00001.xls', data1, 'Sheet1', 'A2');
xlswrite('B00001.xls', header1, 'Sheet1', 'A1');
xlswrite('B00001.xls', data2, 'Sheet2', 'A2');
xlswrite('B00001.xls', header2, 'Sheet2', 'A1');
xlswrite('B00001.xls', data3, 'Sheet3', 'A2');
xlswrite('B00001.xls', header3, 'Sheet3', 'A1');

toc
```

Appendix

G. DRAWINGS OF THE POST ARRANGEMENTS IN THE MANIFOLDS

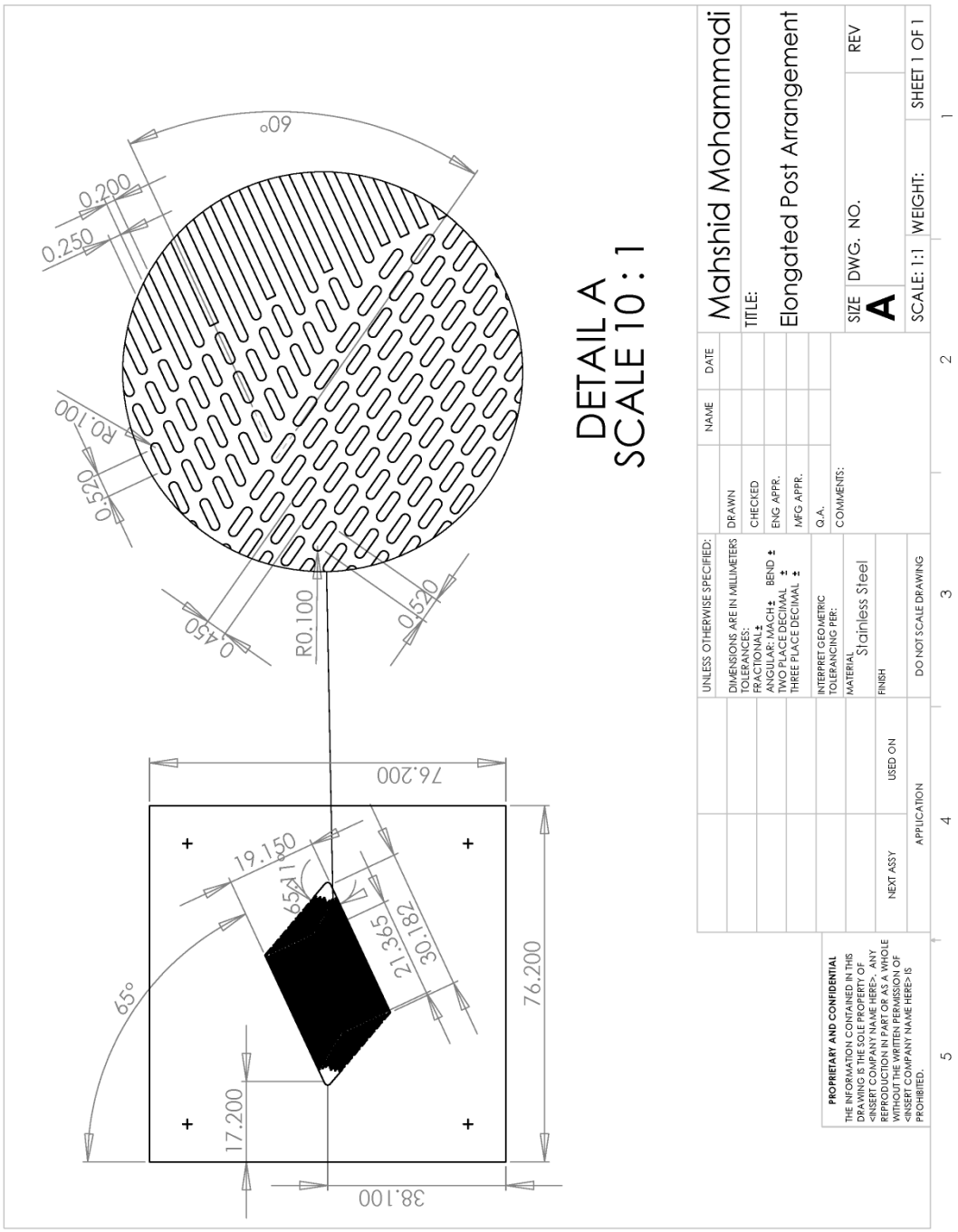
DETAIL A
SCALE 10 : 1
60°
0.200
0.250
R0.100
0.520
0.450
R0.100
0.520
76.200
19.150
65°
21.365
30.182
76.200
65°
17.200
38.100
UNLESS OTHERWISE SPECIFIED:
DIMENSIONS ARE IN MILLIMETERS
TOLERANCES:
FRACTIONAL ±
ANGULAR: MACH ± BEND ±
TWO PLACE DECIMAL ±
THREE PLACE DECIMAL ±
INTERPRET GEOMETRIC TOLERANCING PER:
MATERIAL
Stainless Steel
FINISH
DO NOT SCALE DRAWING
DRAWN
CHECKED
ENG APPR.
MFG APPR.
Q.A.
COMMENTS:
NAME
DATE
Mahshid Mohammadi
TITLE:
Elongated Post Arrangement
SIZE
A
DWG. NO.
REV
SCALE: 1:1
WEIGHT:
SHEET 1 OF 1
NEXT ASSY
USED ON
APPLICATION
PROPRIETARY AND CONFIDENTIAL
THE INFORMATION CONTAINED IN THIS DRAWING IS THE SOLE PROPERTY OF <INSERT COMPANY NAME HERE>. ANY REPRODUCTION IN PART OR AS A WHOLE WITHOUT THE WRITTEN PERMISSION OF <INSERT COMPANY NAME HERE> IS PROHIBITED.

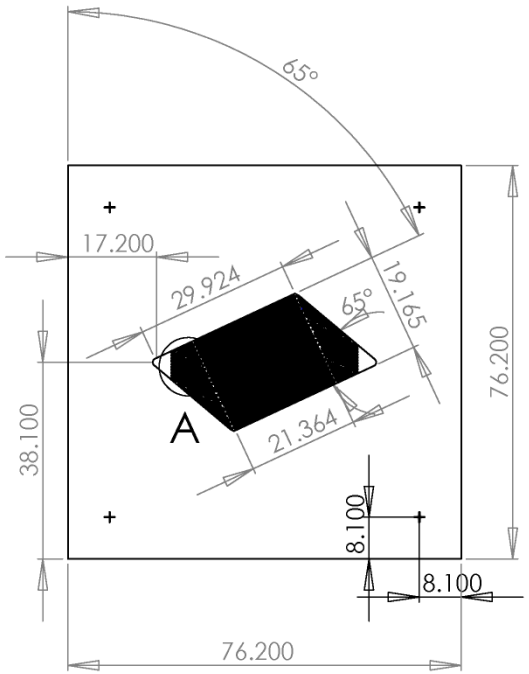

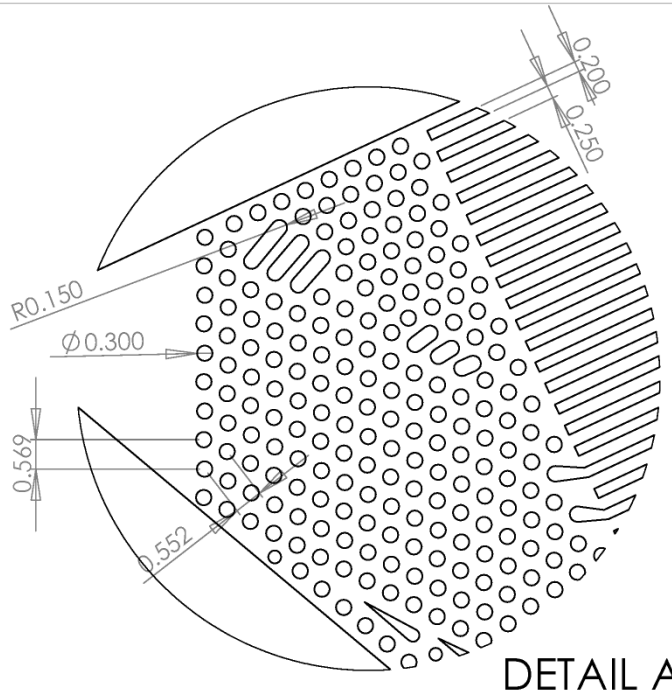

DETAIL A
SCALE 10 : 1

		UNLESS OTHERWISE SPECIFIED:		NAME	DATE
		DIMENSIONS ARE IN MILLIMETERS TOLERANCES: FRACTIONAL ± ANGULAR: MACH ± BEND ± TWO PLACE DECIMAL ± THREE PLACE DECIMAL ±	DRAWN		
			CHECKED		
			ENG APPR.		
			MFG APPR.		
		INTERPRET GEOMETRIC TOLERANCING PER:	Q.A.		
		MATERIAL Stainless Steel	COMMENTS:		
NEXT ASSY	USED ON	FINISH			
APPLICATION		DO NOT SCALE DRAWING			

Mahshid Mohammadi

TITLE:

Staggered Arrangement
three parallel post sections

SIZE	DWG. NO.	REV
A		
SCALE: 1:1	WEIGHT:	SHEET 1 OF 1

5 4 3 2 1

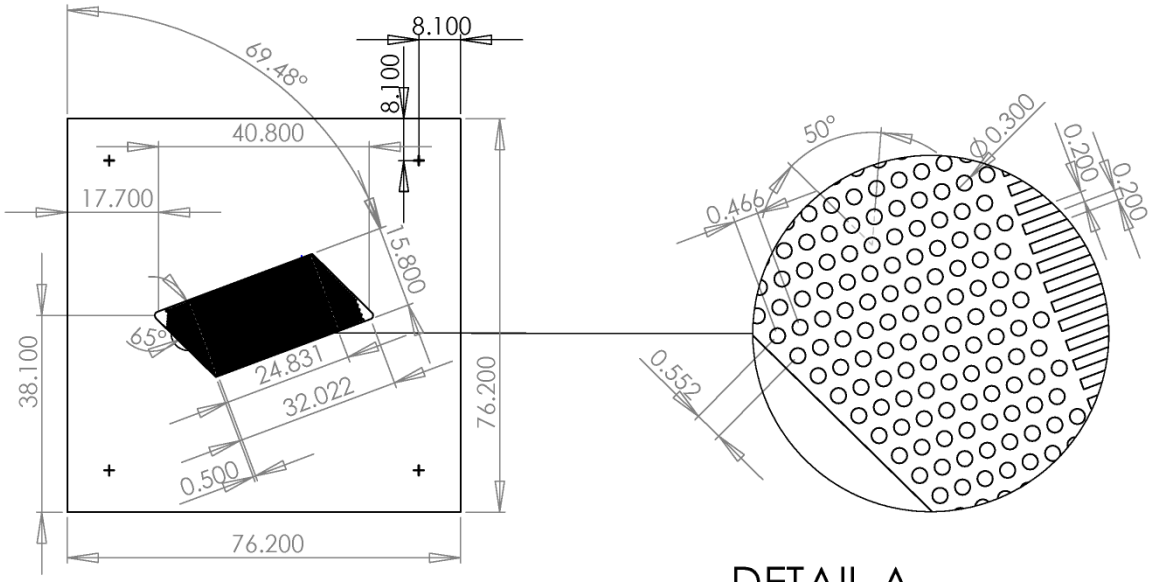

DETAIL A
SCALE 10 : 1

		UNLESS OTHERWISE SPECIFIED:		NAME	DATE
		DIMENSIONS ARE IN MILLIMETERS TOLERANCES: FRACTIONAL ± ANGULAR: MACH ± BEND ± TWO PLACE DECIMAL ± THREE PLACE DECIMAL ±	DRAWN		
			CHECKED		
			ENG APPR.		
			MFG APPR.		
		INTERPRET GEOMETRIC TOLERANCING PER:	Q.A.		
		MATERIAL Stainless Steel	COMMENTS:		
NEXT ASSY	USED ON	FINISH			
APPLICATION		DO NOT SCALE DRAWING			

Mahshid Mohammadi

TITLE:
Staggered Parallel Arrangement
Theta < 60 deg

SIZE	DWG. NO.	REV
A		
SCALE: 1:1	WEIGHT:	SHEET 1 OF 1

5 4 3 2 1

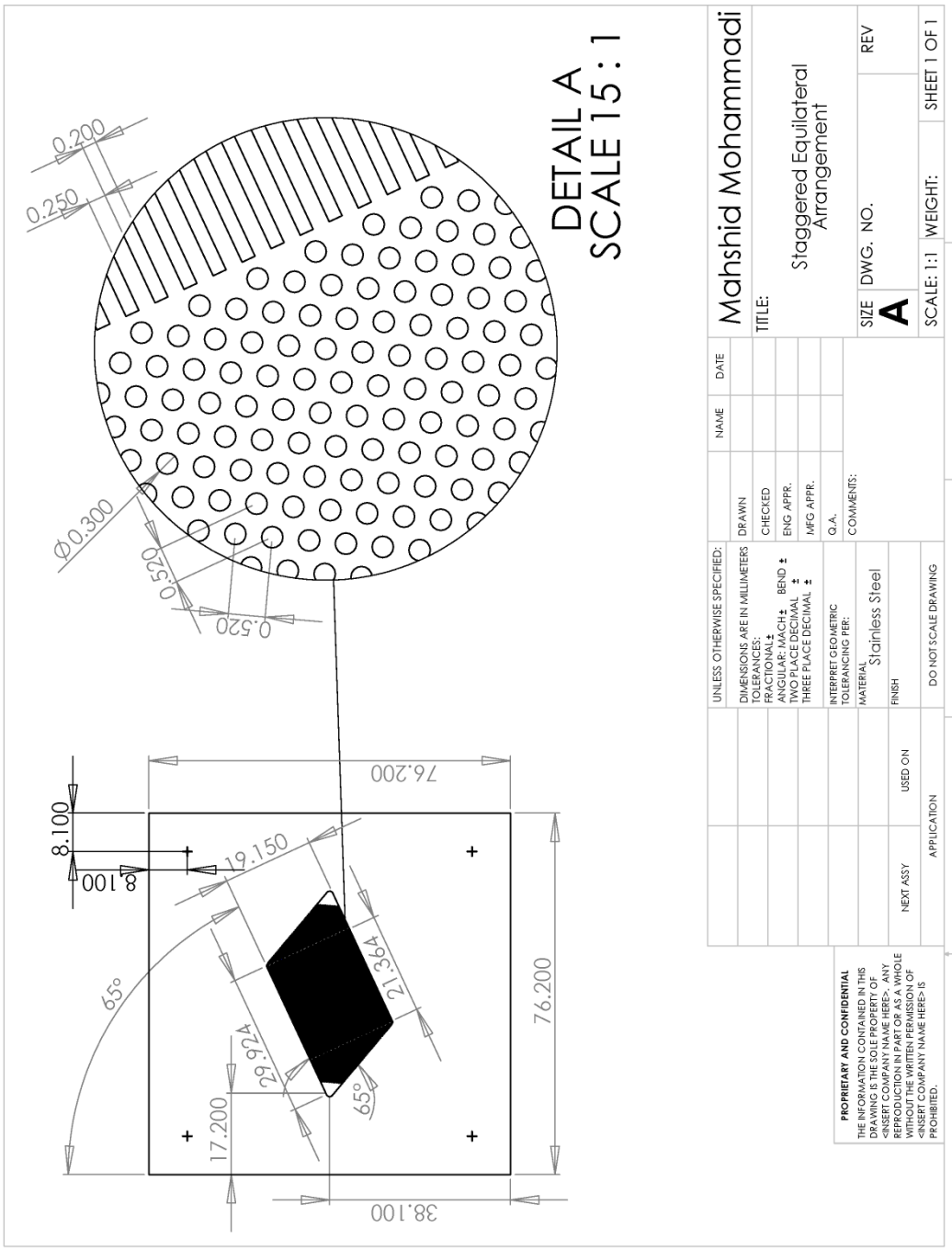
DETAIL A
SCALE 15 : 1
0.200
0.250
Ø0.300
0.520
0.520
76.200
8.100
8.100
19.150
65°
21.364
29.924
65°
17.200
76.200
38.100
UNLESS OTHERWISE SPECIFIED:
DIMENSIONS ARE IN MILLIMETERS
TOLERANCES:
FRACTIONAL ±
ANGULAR: MACH ± BEND ±
TWO PLACE DECIMAL ±
THREE PLACE DECIMAL ±
INTERPRET GEOMETRIC TOLERANCING PER:
MATERIAL
Stainless Steel
FINISH
DO NOT SCALE DRAWING
NEXT ASSY
USED ON
APPLICATION
DRAWN
CHECKED
ENG APPR.
MFG APPR.
Q.A.
COMMENTS:
NAME
DATE
Mahshid Mohammadi
TITLE:
Staggered Equilateral Arrangement
SIZE
A
DWG. NO.
REV
SCALE: 1:1
WEIGHT:
SHEET 1 OF 1
PROPRIETARY AND CONFIDENTIAL
THE INFORMATION CONTAINED IN THIS DRAWING IS THE SOLE PROPERTY OF <INSERT COMPANY NAME HERE>. ANY REPRODUCTION IN PART OR AS A WHOLE WITHOUT THE WRITTEN PERMISSION OF <INSERT COMPANY NAME HERE> IS PROHIBITED.